Study of structured oxide catalysts in Dry Reforming of Methane

by

Seema R. Ghodke
10CC20A26072

A thesis submitted to the
Academy of Scientific & Innovative Research
for the award of the degree of
DOCTOR OF PHILOSOPHY
in
SCIENCE

Under the supervision of
Dr. R. Nandini Devi

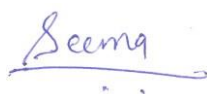**CSIR National Chemical Laboratory, Pune**

Academy of Scientific and Innovative Research
AcSIR Headquarters, CSIR-HRDC campus
Sector 19, Kamla Nehru Nagar,
Ghaziabad, U.P. – 201002, India

October 2023

Certificate

This is to certify that the work incorporated in this Ph.D. thesis entitled, "*Study of structured oxide catalysts in Dry Reforming of Methane"*, submitted by *Seema Rajan Ghodke* to the Academy of Scientific and Innovative Research (AcSIR) in fulfillment of the requirements for the award of the Degree of *Doctor of Philosophy in Science,* embodies original research work carried-out by the student. We, further certify that this work has not been submitted to any other University or Institution in part or full for the award of any degree or diploma. Research material(s) obtained from other source(s) and used in this research work has/have been duly acknowledged in the thesis. Image(s), illustration(s), figure(s), table(s) etc., used in the thesis from other source(s), have also been duly cited and acknowledged.
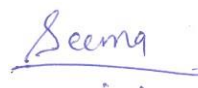
(Signature of Student)
Seema R. Ghodke

Date: 18/10/2023

(Signature of Supervisor)
Dr. R. Nandini Devi
Sr. P. Scientist, CSIR-NCL, Pune
Date:18/10/2023

STATEMENTS OF ACADEMIC INTEGRITY

I Seema R. Ghodke, a Ph.D. student of the Academy of Scientific and Innovative Research (AcSIR) with Registration No. 10CC20A26072 hereby undertake that, the thesis entitled " *Study of structured oxide catalysts in Dry Reforming of Methane"* has been prepared by me and that the document reports original work carried out by me and is free of any plagiarism in compliance with the UGC Regulations on *"Promotion of Academic Integrity and Prevention of Plagiarism in Higher Educational Institutions (2018)"* and the CSIR Guidelines for *"Ethics in Research and in Governance(2020)".*

Seema

Signature of the Student

Date : 18/10/2023

Place : Pune

It is hereby certified that the work done by the student, under my/our supervision, is plagiarism-free in accordance with the UGC Regulations on *"Promotion of Academic Integrity and Prevention of Plagiarism in Higher Educational Institutions (2018)"* and the CSIR Guidelines for *"Ethics in Research and in Governance (2020)".*

Signature of the Supervisor

Name: Dr. R. Nandini Devi

Sr. P. Scientist, CSIR-NCL, Pune

Date: 18/10/2023

Place: Pune

Acknowledgement

I would like to express my immense gratitude and give my warmest thanks to the numerous people who has helped me in my research journey from my family, colleagues and friends. Foremost, I would like to acknowledge my supervisor Dr. R. Nandini Devi, for her constant encouragement, scientific guidance and trust during my thesis work and for giving me complete freedom to establish my idea in my research work.

My Research journey would be incomplete without the guidance of Dr. C.V.V. Satyanarayana, Dr. Paresh Dhepe and Dr. T. Raja in various scientific discussions. I would like to pay gratitude to my seniors Dr. Hanmant Gurav, Dr. Richa Bobade, Dr. Srikanth Dama, Dr. Atul Nagpure, and Dr, Laxmiprasad Guralla, Dr. Pranjal Gogoi for their continues support in scientific activities related to my thesis. I would like to thank my lab mates Dheerendra, Shibin, Sourik, Pavan, Shunottara, Priyanka, Akshay, Chinnu, Shubham, Deepali, Jyoti, Rushikesh, Wasi for making my experience exciting in and out the lab. I sincerely thank my divisional friends Sonia, Shivaprasad, Vipul, Ashwathy, M. prabhu, K. Prabhu, Nagesh, Betsy, Jyoti kadam, Tufiel, Lavanya, Priya, Kalyani, Aakash, Samrudhi, Himanshu, Ravi, Indrajit, Sinduri for their unconditional support during my Ph.D. course.

I extend my straight thanks to Student Academic Office, catalysis division and non-scientific staff for their technical assistance at CSIR-NCL crucial times. I am grateful to CSIR, New Delhi, for awarding the research fellowship and Director, CSIR-National Chemical Laboratory for extending all infrastructural facilities.

Last but not least I would like to thank my parents, family and friends for believing and encouraging me to follow my dreams in various challenging situations during my research period.

Table of Contents

Chapter 1. Introduction and literature survey

Chapter 2.
Synthesis and Screening of Gd based Pyrochlore and defect fluorite catalysts in DRM

Part 2

Effect of active metal concentration in Defect fluorite catalyst ($A_2B_{2-x}Ni_xO_{7-\delta}$ A = Gd, B = Zr, X = 0.2,0.5,0.75) in DRM **64-76**

Part 3

Study of the influential effect of Ce substitution in $Gd_2Zr_{1.8}Ni_{0.2}O_{7-\delta}$ catalyst for Dry reforming of methane **77-113**

Chapter 4 Synthesis and screening of layered metal oxide Na$_2$Ti$_3$O$_7$ catalyst in DRM

List of Figures

List of Tables

List of Abbreviations

DRM	Dry Reforming of Methane
SRM	Steam Reforming of Methane
ATR	Autothermal Reforming
POM	Partial Oxidation of Methane
TRM	Tri Reforming of Methane
DME	Dimethyl ether
FT	Fourier Transform
RWGS	Reverse Water Gas Shift Reaction
GSAS	General Structure Analysis System
ICSD	Inorganic Crystal Structure Database
JCPDS	Joint Committee on Powder Diffraction Standards
BET	Brunauer-Emmett-Teller
SOFC	Solid Oxide Fuel Cell
TGA	Thermo Gravimetric Analysis
XPS	X-ray Photoelectron Spectroscopy
SEM	Scanning Electron Microscopy
EDS	Energy Dispersive X-ray Spectroscopy

Chapter 1

Introduction and literature Survey

1. Introduction

1.1. The Greenhouse effect:

Due to population growth and industrialization, the earth's temperature has changed dramatically in recent decades, resulting in an increasing greenhouse effect [1][2]. Oceans, aquatic species, plants, and humans use the radiation and heat emitted by the sun to survive. The remaining heat reflects towards space, but greenhouse gases (such as carbon dioxide) trap these radiations and heat, allowing the earth's atmosphere to remain warm. The sun's radiations include infrared, ultraviolet, and visible radiations, which are transported to the earth by its atmosphere and reflected back to the sun[3]. Because the earth's atmosphere contains many gases and has been increased by anthropogenic activities particularly greenhouse gases such as carbon dioxide, methane, nitrous oxides, and fluorinated gases, these radiations are absorbed and their departure towards the Sun became limited. This boosted the earth's warmth, resulting in higher temperatures.

1.2. The Greenhouse Gases:

Carbon dioxide, methane, nitrous oxide, and industrial gases such as hydrofluorocarbons (HFCs), perfluorocarbons (PFCs), sulfurhexafluoride (SF_6), and nitrogen trifluoride (NF_3) account for approximately 79.4%, 11.5%, 6%, and 3.0% of the total greenhouse gases that keep the earth's atmosphere warm[4][5] (figure1.1).
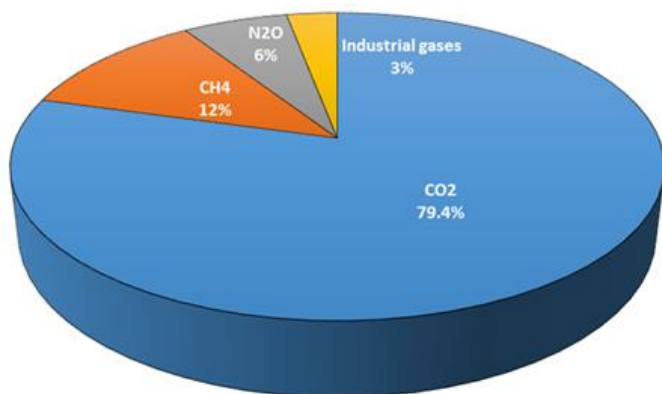
Figure 1.1: Percentage of greenhouse gases

1.2A. Carbon dioxide:

Carbon dioxide is an inert gas that absorbs heat and is the only carbon source for life on Earth. It is present in various forms such as carbonates and bicarbonates and is soluble in water, making it a crucial component of aquatic life [6][7]. Carbon dioxide emissions have recently surpassed their positive threshold. The primary causes of its high discharge are the use of fossil fuels, an exploding population that leads to industrialization and urbanization, which causes climate change, and global warming [8]. Fossil fuel burning accounts for roughly 40% of total CO_2 emissions [9][10]. Transportation, power generation, agriculture, industrial production, and fuel all contributed significantly to increased CO_2 emissions [11][12][13][14][15][16][17][18][19][20]. The increase in CO_2 levels has a significant impact on aquatic life by acidifying the salt water, which alters the chemical equilibrium of the water environment, resulting in the extinction of various aquatic creatures, bacteria and other microorganisms, damaging aquatic life [21][22][23]. Apart from that, higher CO_2 emissions raise the earth's temperature, resulting in global warming, melting ice caps, and rising sea levels, all of which endanger life on Earth.

1.2B. Methane:

Methane is the second most prevalent greenhouse gas, with a 25% greater ability to raise global temperatures than CO_2. It accounts for around 11-15% of total greenhouse gas emissions[24][25][26] Methane is emitted primarily by human activities such as mining, coal processing, combustion of oil, biomass, natural gases, and other industrial treatments such as wastewater treatment caused by the breakdown of organic compounds in water bodies in anaerobic conditions [27][28]. Aside from that, agricultural waste treatment and manure management systems emit significant amounts of methane, and livestock such as sheep, goats, and swine excrete methane. Around 25% of methane emissions are caused by

the combustion of oil and natural gas as a result of urbanization and industrial activities[29][30][31]. Methane mitigation can be accomplished through a variety of methods, including the construction of digesters and their use in a variety of reactions that convert methane into useful industrial products such as syngas through various reforming reactions and by draining marshes and landfills[32][33][34][35][36][37].

1.2C. Nitrous oxide:

According to the IPCC, nitrous oxide gas, also known as "laughing gas," remains in the atmosphere for longer years if it is not removed or utilized, resulting in increasing the earth's temperature and global warming[38][39][40]. Nitrous oxide gas emissions increased fast due to increased usage of fertilizer in agricultural activities, crop and food manufacture, and by deforestation. Furthermore, the upwelling of deep ocean water by sediments of deceased aquatic animals is a source of N_2O emissions. N_2O gas emissions can be reduced by using low nitrogen-containing fertilizers in crop and agricultural areas, or by employing N_2-rich fertilizer substitutes[41][42]. Among the various greenhouse gases CO_2 is the primary cause of global warming and climate change as it accounts for the majority of overall greenhouse gas emissions.

1.3. Current Status of CO_2 emission:

According to recent research, CO_2 emissions have climbed to 421 ppm as a result of population bursts, fossil fuel burning, manufacturing, deforestation and industrialization[43][44][45]. It is anticipated that by the end of the century, it will have risen to 650 ppm, causing a 2 °C increase in global temperature. According to NASA Earth Observatory, the rate of temperature increase in the last 50 years has been 1.2-1.8 °C attributable to human activity. There was a substantial decline in emissions due to Covid, but it skyrocketed after the Covid pandemic[46]. This demonstrated that industrialization and urbanization had a significant impact on global warming. Figure 1.2(a)(b) depicted

recent data on CO_2 emissions and surface temperature hike (figure 1.2).
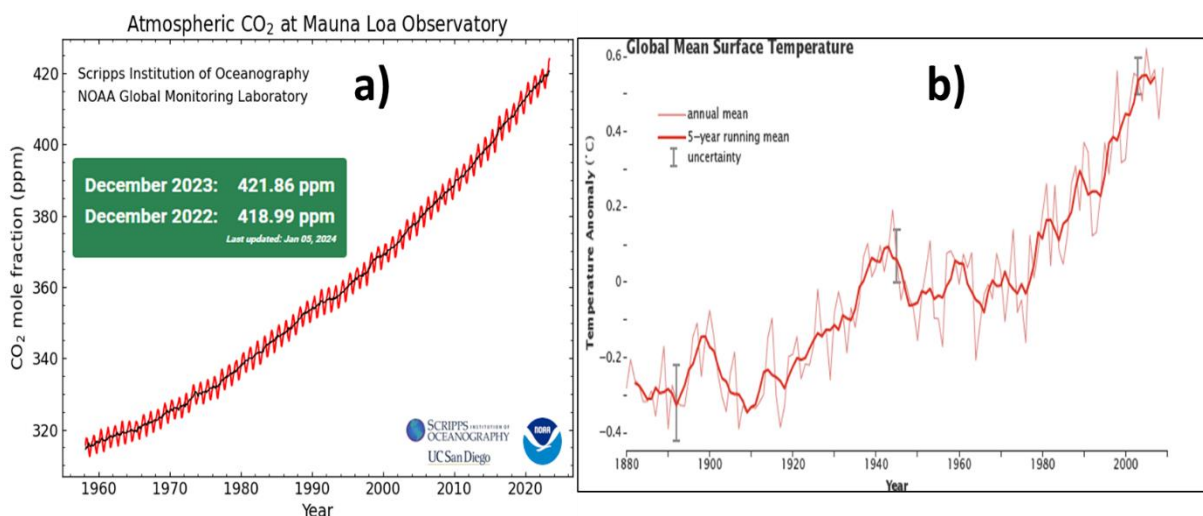
Figure 1.2: a) Recent CO_2 emission b) Increase in global surface temperature data [45]

1.4. CO_2 utilization:

Among all greenhouse gases, rising CO_2 emissions have a significant impact on the lives of living things, climate emergency, depletion of non-renewable energy sources, and on future economic growth resources. Several publications have been published in which considerable work has been done with the goal of utilizing CO_2 via direct utilization, apprehension, and storage of CO_2 and converting it into various valuable molecules via various chemical pathways, implying that CO_2 can be utilized in both physical and chemical ways [47].

1.4A. Physical pathways of CO_2 utilization:

The physical exploitation of CO_2 includes its capture, storage, and direct usage in a variety of industrial processes.CO_2 can be utilized in dry ice, as a refrigerant, fire extinguisher, solvents, and as a welding medium in its gas form without any structural changes. Another physical method of utilizing carbon dioxide is sequestration, which involves injecting CO_2 into existing oil fields to achieve 'improved oil recoveries' and so avoiding CO_2 emissions into the environment[48][49][50][51] (figure 1.3). By boosting oil pressure, CO_2 in oil aids in the free flow of oil toward producing wells. CO_2 is introduced into various gas reservoirs under supercritical conditions (over 31 °C and 7.38 MPa) and adsorbs on reservoir rocks

before being routed to production wells in enhanced gas recoveries (EGR)[52]. EGRs have a CO_2 storage capacity of 390-750 gigatons, which is greater than Enhanced oil recovery (EOR). CO_2 is miscible with other gases such as CH_4, H_2, and N_2 in a specific EGR reservoir, and adsorptive desorption on reservoir rocks commences the sequestration of a large amount of CO_2. Although EGR has various characteristics that may be manipulated, such as the volume of CO_2 used, the separation of CO_2 from other gases makes it less cost-effective than EOR[53][54]. However, gas leakage during pumping and storing CO_2 in reservoirs is extremely dangerous and risky. Furthermore, CO_2 can be sequestered by carbonation, which involves injecting CO_2 into the deep sea, where it combines with seawater to generate carbonic acid. These strategies have proven to be effective in storing CO_2 and lowering emissions into the environment. However, carbonation can have an impact on aquatic life by changing the pH of saltwater, which poses a risk to aquatic species. CO_2 can also be absorbed and neutralized in the aquatic ecosystem in the form of bicarbonates and carbonates[55]. Direct CO_2 conversion and storage in the ocean as carbonates and bicarbonates can positively store CO_2 without harming aquatic life.
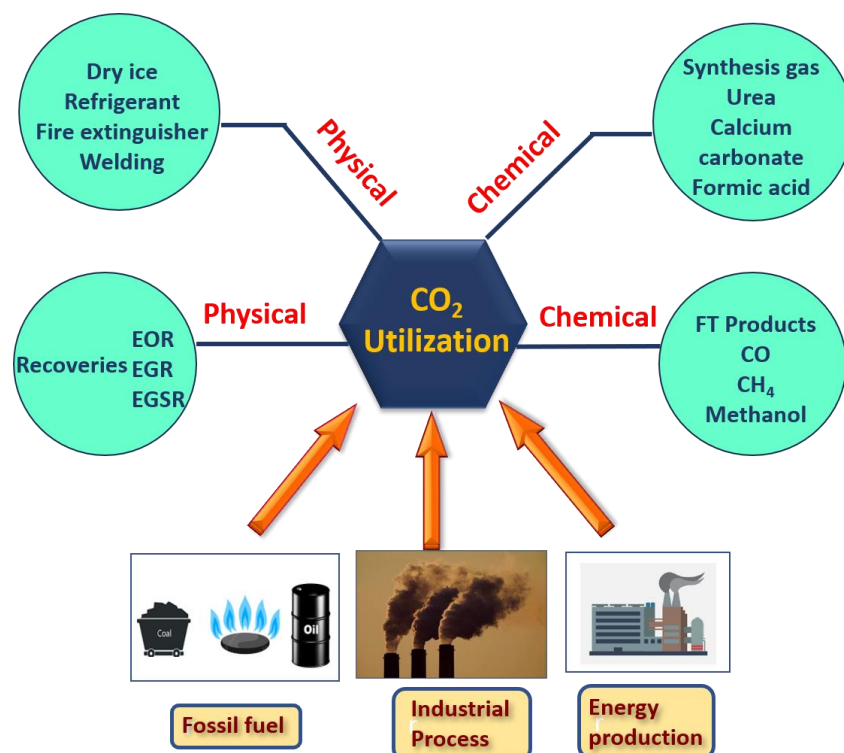
Figure 1.3: CO_2 utilization pathways

1.4B. Chemical pathways of CO_2 utilization:

There are several chemical pathways for utilizing CO_2 by converting it to various value-added products such as syngas, dimethyl ether, methanol, urea, and FT products employing a variety of chemical procedures such as reforming, hydrogenation, and methanation processes at different reaction conditions such as temperature and pressure, with various catalysts[56][57][58][59][60] (figure1.4). The dry reforming of methane (DRM) reaction converts CO_2 into syngas, which is an important intermediate in many reactions and can be transformed into valuable compounds. Historically, apart from DRM, syngas was generated through steam reforming processes, the partial oxidation of hydrocarbons, natural gases, and by waste biomass. Usually, syngas production with high H_2/CO ratio is preferred to convert it into different chemicals like alcohols, acids and gasoline etc. [61][62][63][64].
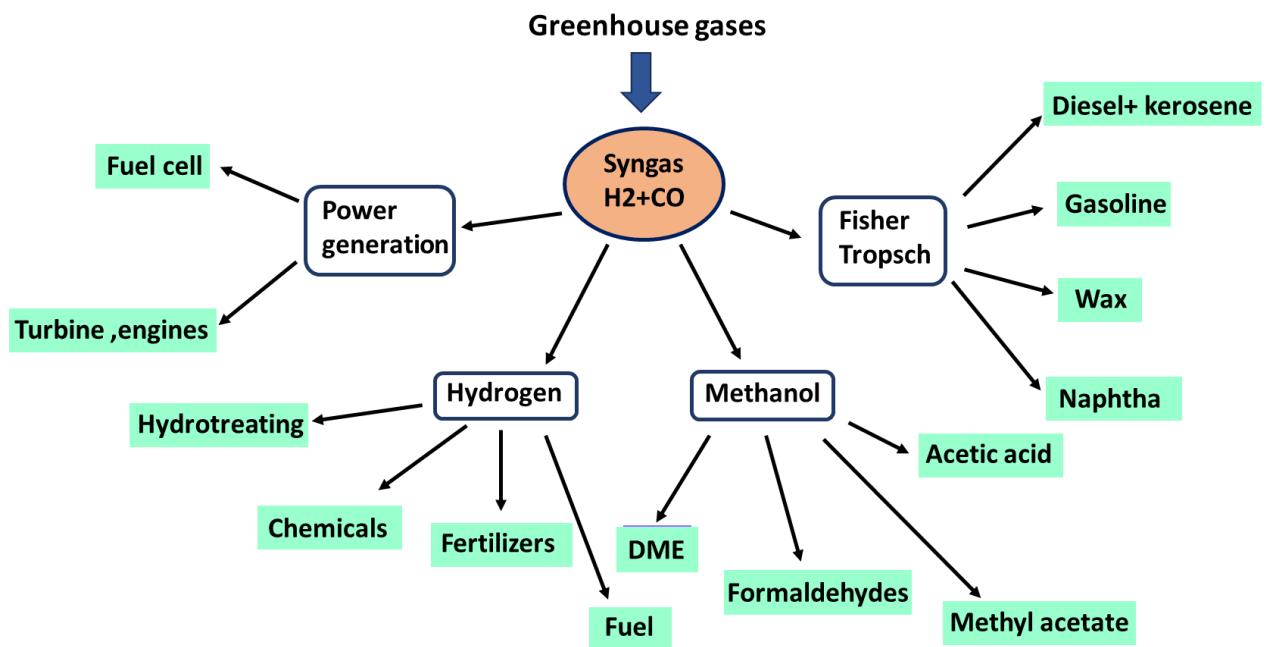
Figure 1.4: Applications of Syngas

1.5. CO_2 Utilization by Reforming Reactions:

One of the important industrial pathways of CO_2 utilization is reforming reactions. There are several reactions by which CO_2 can be converted into desired industrial products.

A. Autothermal reforming

B. Tri reforming of methane

C. Dry reforming of methane

1.5A. Autothermal reforming:

Autothermal reforming is the combination of two reactions: partial oxidation of methane, which is exothermic in nature, generates heat and energy that is used in the subsequent endothermic reaction of methane with CO_2 and H_2O via DRM and SRM reactions to generate syngas with different H_2/CO ratios that can be used in the synthesis of methanol and valuable chemicals such as DME and other biofuels. The ATR reaction occurs at high temperatures ranging from 900 to 1150 °C and pressures ranging from 1 to 30 bar. Change the inlet gas ratio and concentration ranges from 1-2 to change the H_2/CO ratio. The gasification of carbon generated during DRM and steam reforming of methane in the reactor tube and on the catalyst's, surface mitigated by water and oxygen in the reaction zone are the major advantages of autothermal reaction. Moreover, autothermal reaction combines with endothermic reforming reactions consume energy and heat generated by exothermic partial oxidation of methane (a, b, c) and achieves thermodynamic equilibrium in the reaction stream itself [65][66][67][68]. Autothermal reaction has been applied on the industrial level since 2002 in Europe at $H_2O/C = 0.6$ ratio to generate CO-rich syngas and the first industrial setup with 16 autothermal reformers was run in Secunda, South Africa; since then, it has been pushed beyond its limitations in the industrial level[69].

$$CH_4 + 3/2O_2 \rightarrow CO + 2H_2O \qquad\qquad (a)$$

$2CH_4 + O_2 + CO_2 \rightarrow 3H_2 + 3CO + H_2O$ (b)

$4CH_4 + O_2 + 2H_2O \rightarrow 10H_2 + 4CO$ (c)

1.5B. Tri reforming of methane:

Tri reforming of methane is a novel reforming reaction that combines three reactions: steam reforming (1), dry reforming of methane (2), and partial oxidation of methane (3) at 800-850 °C under low pressure [70]. However, in TRM, all inlet gases CO_2, CH_4, O_2, and H_2O are mixed in varied ratios in the reactor tube at high temperatures. Essentially, dry and steam reforming make syngas with a moderate and high H_2/CO ratio, and steam reduces carbon formation on the catalyst surface. The concept of tri-reforming methane combines dry and steam reforming while introducing oxygen into the reaction stream to provide heat in situ, owing to the exothermic nature of the partial oxidation reaction, resulting in increased energy efficiency and carbon mitigation[71]. Several studies have been conducted to investigate the influence of varied inlet gas ratios on catalytic activity and the target H_2/CO ratio. By adjusting the input gas ratio, the appropriate H_2/CO ratio in TRM may be obtained, making it suited for producing value-added compounds such as methanol, DME, and FT. The presence of oxygen in the feed is more effective than H_2O, on CO_2 conversion in TRM. However, larger partial pressures of O_2 have a detrimental impact on CO_2 conversion below 800 °C because CO_2 is generated in greater quantities than it is consumed. Furthermore, at lower temperatures, oxygen lowers the temperature range where carbon production is prominent resulting in less carbon accumulation on active sites [72][73][74][75].

Steam reforming (SR): $\qquad 2CH_4 + 2H_2O \leftrightarrow 2CO + 6H_2$ (1)

Dry reforming of methane (DRM): $\qquad CH_4 + CO_2 \leftrightarrow 2CO + 2H_2$ (2)

Partial oxidation (POX): $\qquad CH_4 + 1/2O_2 \leftrightarrow CO + 2H_2$ (3)

Combustion reaction: $\qquad CH_4 + 2O_2 \leftrightarrow CO_2 + 2H_2O$
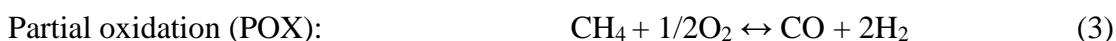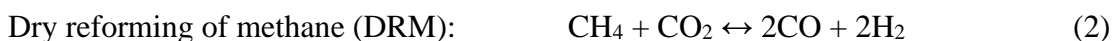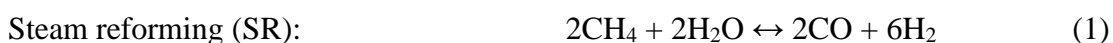
1.5C. Dry reforming of methane:

Dry reforming of methane (DRM), also known as CO_2 reforming, is a reaction that converts two greenhouse gases, CO_2 and CH_4, into syngas at high reaction temperatures with acceptable conversions. In DRM, reactant gases are employed in a 1:1 ratio to produce CO-rich syngas, which is useful in the production of acetic acid. The H_2/CO ratio in the DRM reaction is 1, to make it useful for further chemicals production it is further tuned by the water gas shift reaction by reacting CO with H_2O, and the H_2/CO ratio is attained to 2, which is useful in the FT process and methanol synthesis. Fischer and Tropsch documented the first DRM (2) reaction in 1928 using Ni/Co catalysts with a high quantity of carbon and catalyst deactivation [61].

Dry reforming of methane is a highly endothermic reaction that requires a high temperature to transform CH_4 and CO_2 into syngas since CH_4 is a very stable molecule, it takes a substantial amount of energy to break the C-H bond to convert it into a final product i.e., H_2. Along with DRM, many side reactions such as and methane decomposition reaction (4) reverse water gas shift reaction (5), boudouard reaction (6), happened at these reaction conditions. Energy demand in DRM is little high than other reforming reactions like steam reforming of methane (1), which utilizes methane into CO and hydrogen.

$$CH_4 \rightleftharpoons C + 2H_2 \qquad\qquad \Delta H^{\circ}_{298K} = 75.0 \text{ kJ/mol} \qquad (4)$$

$$CO_2 + H_2 \rightleftharpoons CO + H_2O \qquad\qquad \Delta H^{\circ}_{298K} = 41.0 \text{ kJ/mol} \qquad (5)$$

$$2CO \rightleftharpoons C + CO \qquad\qquad \Delta H^{\circ}_{298K} = -173.0 \text{ kJ/mol} \qquad (6)$$

$$CH_4 + H_2O \rightleftharpoons CO + 3H_2 \qquad\qquad \Delta H^{\circ}_{298K} = +206.0 \text{ kJ/mol}$$

$$CH_4 + CO_2 \leftrightarrow 2CO + 2H_2 \qquad\qquad \Delta H^{\circ}_{298K} = +247.0 \text{ kJ/mol}$$

The H_2/CO ratio in DRM is supposed to be unity with reactant gas CH_4 and CO_2 in a 1:1 ratio, but due to competing side reactions, the H_2/CO ratio is impacted. RWGS reaction produces H_2O below the reaction zone, which is collected in the reactor outflow, resulting

in more CO_2 conversion than CH_4 and a lower H_2/CO ratio than 1.

Aside from that, other side reactions such as methane decomposition and the Boudouard reaction are responsible for producing carbon on the catalyst surface during DRM, resulting blocking active sites for further reaction and deactivation. Most of the reactions are endothermic. Among them SRM (1) is conventional reaction, according to thermodynamic calculations it requires more energy than DRM (2) to produce syngas. Moreover, CO_2 emission intensity is less in DRM than SRM.

1.6. Mechanism of Dry reforming of methane:

Methane dry reforming has mechanistic routes to produce CO and H_2 from methane and CO_2, which include the steps described below:

1.6A. CH₄ decomposition:

At high reaction temperature one of the reactant gases, CH_4, adsorb on the metal surface of the catalyst, resulting in an excess of the CH_x and H species that lead to the final product, H_2. Temperature has a considerable impact on the methane activation stage because temperatures between 400 and 600 °C initiate side reactions such as Boudouard (6) and methane decomposition (4), which result in the creation of carbon on the metal surface and the blocking of active sites for additional methane activation (figure 1.5A). DRM thrives in temperatures ranging from 800 to 850 °C. In the DRM process, methane decomposition is a sluggish and rate-determining stage. The activated CH_x species generates H_2 and carbon species by continuous dissociation on metal surfaces, resulting in carbon accumulation on active sites.
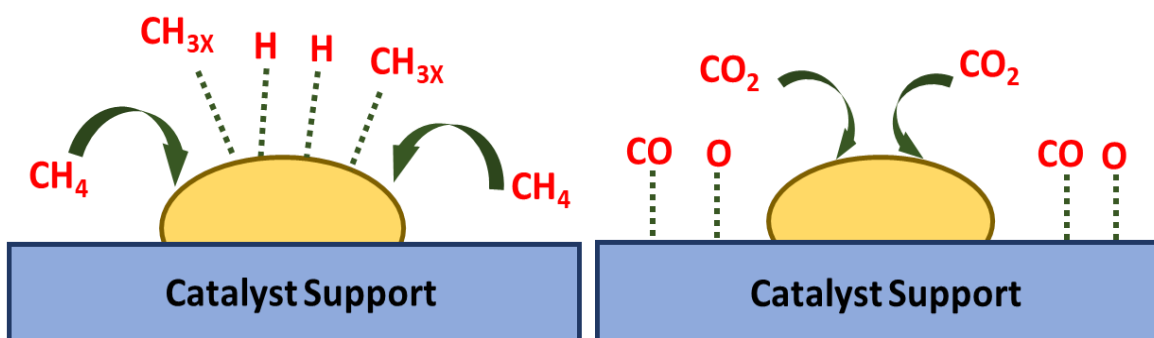
Figure 1.5: Mechanism of DRM: A) CH_4 and CO_2 adsorption on catalyst

1.6B. Dissociative adsorption of CO_2:

The metal support interphase undergoes a transformation to produce CO as the product gas when the second reactant gas, CO_2, is employed on the support. Three processes result in CO_2 adsorption. 1) The metal surface adsorption of C of CO_2. 2) Adsorption of oxygen and carbon atoms, leaving one oxygen atom exposed 3) Coordination of oxygen atoms on both metal and support surfaces during the interphase. The acidic nature of CO_2 makes it attractive to adsorb on metal surfaces having basic sites (figure 1.5B). Adsorption of CO_2 converts into CO and oxygen moieties. So, the characteristics of the support have a significant impact on CO_2 adsorption and desorption in CO[76].
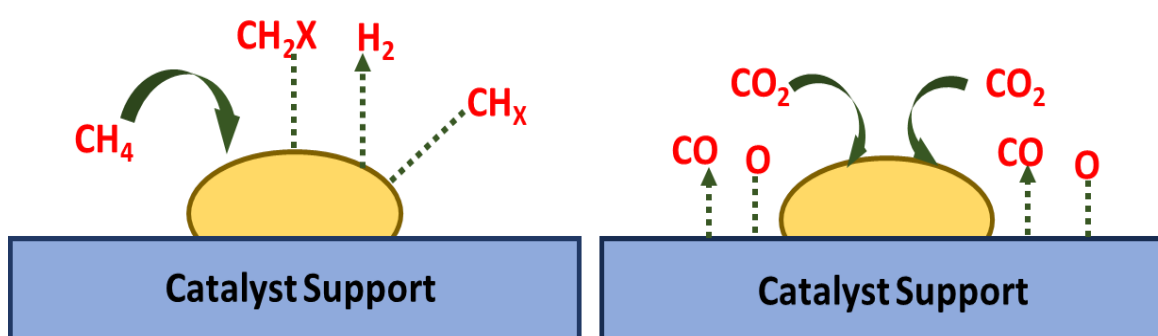
Figure 1.5: Mechanism of DRM: B) Formation of CH_x species and CO desorption

1.6C. Oxygen spillover and hydroxyl species formation:

CO and H_2 are sequentially produced from CO_2 dissociative adsorption and hydrogen from the breakdown of CH_4 respectively. Oxygen atoms and H* moiety spill over onto the

catalyst's surface and form hydroxyl species, which react with CH_x species to create a variety of intermediates like carbonates, bicarbonates, and formates. Additionally, these molecules promoted carbon gasification on metal surfaces by reducing carbon to CO and CO_2. Since CO_2 serves as a major oxidizing agent in DRM, it provides oxygen to gasify the carbon produced by methane decomposition on metal and metal support interphase (figure 1.5C). Aside from that, different supports with redox metals such as Ce create defect-originated oxygen vacancies and active oxygen species to the support, initiating carbon oxidation and keeping active sites available for further reaction [77][78][79].
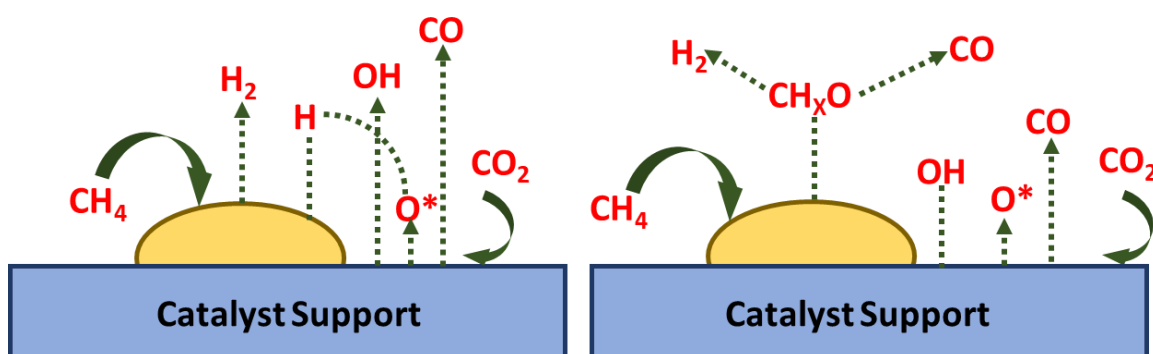
Figure 1.5: Mechanism of DRM: C) Formation of Surface hydroxyl species and oxygen spillover

1.7. DRM catalyst: Design, factors and literature survey

A catalyst is a substance that initiates or accelerates a reaction so that the reactant is converted into a product without being consumed. The primary need of the DRM catalyst is that it is able to withstand difficult reaction conditions for a long period of time without structural change as the dry reforming of methane is a highly endothermic process. Diverse heterogeneous catalysts with various topologies, metal component combinations, and morphologies are of great interest to DRM. Apart from structural aspects other factors like support quality (acid base functionality), active metal sites, and promoters, also have a vital impact on the activity and longevity of DRM catalyst.

1.7A. Active sites:

The locations where reactant dissociation takes place in the final product are known as active sites in catalysts. Methane decomposition for the DRM process occurs at active metal sites, where it transforms into the product gas H_2. By adhering to metal active sites and support sites, CO_2 dissociates into CO gas as a product. Support is a crucial component for CO_2 activation because, according to the literature, CO_2 activation primarily takes place on basic support sites because CO_2 is acidic in nature[80]. While only metal sites experienced methane activation, which led to the sequential production of hydrogen through various intermediates. Ni-based catalysts have been shown to be a promising option for DRM reactions due to its availability and inexpensive price. They are forbidden to be used as industrial catalysts because of their propensity to aggregate at high reaction temperatures over the metal surface and increase the likelihood of carbon production from methane decomposition. As a result, Ni-based catalysts needed other alternatives and modifications for longer and better activity in high-level applications[81][82]. To combat this, researchers have published a number of publications describing how, noble metals like Pt, Pd, Ru, Rh, and Ir and non-noble transition metals like Co and Cu are used with Ni as promoters. These bimetallic systems are thoroughly screened in the dry reforming of methane with good conversions [83][84][85]. According to the reports, Ni-Co-supported catalysts have a greater coke resistant rate and immensely studied as bimetallic catalyst in DRM. Higher conversions and less carbon formation depends on synergetic effect of Ni and Co related to Ni/Co ratio[86]. According to yoontak et al., Ru-Ni/Al_2O_3 catalysts exhibit better activity and less carbon deposition than monometallic Ni/Al_2O_3 catalysts[87]. In addition, the Pt-Ni/Al_2O_3 catalyst converts CH_4 and CO_2 into syngas at a higher rate than monometallic Ni on Al_2O_3 and Pt-Al_2O_3 catalysts[88]. A study found that by making Pt-Ni alloy, Ni metal particle size is reduced, which lowers the development of graphitic carbon. In order to improve conversions and activity with less coke deposition in noble metals, which are sensitive to

coke deposition, alloying with Ni is recommended. Moreover, non-noble metals like alkaline earth metals, and alkali metals (Ca, Sr, Mg, Na, k) are also used with Ni as active centers for methane activation and promoters for coke gasification[89].

1.7B. Support:

Aside from active metals, support is a critical factor in catalytic systems utilized in methane dry reforming. Surface characteristics such as acidity and basicity impede and promote CO_2 adsorption, respectively[90]. Acidic support sites impede CO_2 activation by less adsorption and inhibiting the formation of hydroxyl and active oxygen species unable to oxidize accumulating carbonaceous material on the active metal site, which blocks the active surface responsible for CO_2 adsorption and decreased activity[91]. However, basic sites promote CO_2 chemisorption on the surface by initiating and promoting carbon gasification caused by methane decomposition and the Boudouard reaction, transforming it into carbonates, bicarbonates, and, finally, CO[92][93][94][95]. MgO-supported Ni catalysts with varying Ni ratios demonstrated increased DRM activity. A NiO-MgO-based catalyst aided in the production of a solid solution of NiO and MgO, resulting in reduced coke formation with good activity[96]. The effect of cation substitutions such as Mg^{2+}, Y^{3+}, and La^{2+} on Ni/ZrO_2-based catalysts was investigated and shown to be excellent for DRM due to improved basic sites evaluated by CO_2-TPD and the generation of defect originated oxygen species responsible for decreased carbon deposition[97][98][99][100]. Therefore, the basic feature of the support is a key determinant of the catalyst's persistent action in DRM and increased CO_2 activation. Furthermore, K, Na metal doping in various catalysts also enhance the basic properties of support to initiate CO_2 activation[101].

1.7C. Metal support interaction:

It has been proposed that the metal-support interaction plays a significant role in the improved activity and carbon resistance of supported and non-supported structurally ordered

catalysts. At higher temperatures, there is a considerable risk of metal sintering and agglomeration in the DRM process. DRM activity primarily supports the two-way pathway for methane and CO_2 activation on metal and support, respectively. If the active metal's contact with the support is stronger, there will be less chance for metal particles to move closer together and form larger particles, creating more carbon on the metal surface and blocking the active site for the next methane molecule to break down. Furthermore, the strong metal-support relationship gives thermal resistance to the metal sintering temperatures, which are Huttig and Tamman temperatures, from where the metal agglomerations begin. However, when the support, like SiO_2 with Ni as active species on it having weak metal support interaction, resulting in possibility of metal agglomeration and sintering which leads to attenuated durability in DRM than Ni/Al_2O_3 catalyst. Furthermore, robust metal support contact improves active metal dispersion and pore sizes distribution on the catalyst surface, resulting in less sintering and simultaneous carbon gasification over the catalytic surface[102][103][104][105].

1.7D. Redox property:

The redox potential of the catalysts has been thoroughly explored in the dry reforming of methane to overcome coke deposition and catalyst deactivation. This research in DRM focuses on CeO_2, ZrO_2, and TiO_2-based catalysts. In DRM conditions, the oxidation and reduction of these support materials cause the production of oxygen species and vacancies in the catalysts. The redox behaviour of metals in the support increased the oxygen storage capacity of the catalysts, allowing for continuous flow of oxygen on the catalysts' surfaces and direct oxidation of carbon produced by methane dissociation. Furthermore, the creation of oxygen vacancies promotes CO_2 activation because the oxygen moiety from CO_2 fills these vacancies during CO_2 adsorption. Ce-based catalysts, where oxidation and reduction of Ce^{+3} and Ce^{+4} increase vacancy formation and boost oxygen storage capacity, resulting in

less carbon deposition on the catalyst's surface, greater conversions, and longer activity [106][107][108][109][110] .

1.7E. Synthesis route:

Wet impregnation, dry impregnation, sol-gel technique, solid-state method, co-precipitation, spray pyrolysis, Pechini method, and hydrothermal approach were used to create DRM catalysts[111]. Catalyst synthesis methods modify their physiochemical and morphological properties such as metal support interaction, metal dispersion, pore size volume, particle size distribution, and surface area[112][113].Co-precipitation is a process in which metal precursors are diluted in water and suitable catalysts are precipitated upon the addition of bases such as NaOH and KOH. Co-precipitation consists of the following steps: dissolution of precursors in water, precipitation, filtration of precipitate, drying, and calcination to obtain the necessary catalyst. Although nucleation, uneven shape, and lack of sensitivity are important drawbacks of this technique, moreover, it is a cost-effective method of synthesizing homogenic catalysts[114][115]. Patric da Costa et al. compared the catalytic activity for DRM of Ni/CeO_2-ZrO_2/SBA-15 catalysts synthesized by wet impregnation (sequential and on step) and co-precipitation and discovered that the catalyst synthesized by co-precipitation route has higher conversion than the other two catalysts due to low Ni particle size and distribution [116]. Maleki et al., on the other hand, have distinguished the difference in the catalytic activity of Ni/Al_2O_3-CeO_2 catalyst generated by sol-gel and impregnation technique, demonstrating that the sol-gel method provides small particle size of Ni with high dispersion, leading to superior activity in DRM [117]. Pechini methods, on the other side, are frequently used in heterogeneous catalyst production because liquid precursors are transformed into sol and gel by adding water and chelating agents such as citric and ethylene glycol, respectively[118]. The leftovers from gelation and polyesterification were dried and calcined at various temperatures to produce catalysts with

strong metal support interaction. However, Catalysts synthesized using the sol-gel and Pechini methods, have a reduced surface area because of the high calcination temperature, which leads to less repeatability and unpredictable morphology[119][120][112]. Due to the high firing temperature, catalysts have less impurity and longer stability. Seol et al. synthesized the $Ni/ZrO_2-Al_2O_3$ catalysts using Pechini, which offered strong metal support contact, structural stability, and increased CO_2 adsorption by forming oxygen intermediates rather than hydrolysis and physical mixing approaches, resulting in greater conversion [121]. Other processes, such as hydrothermal and spray pyrolysis, are evidently screened in DRM to regulate active metal particle size. Hydrothermal synthesis was performed in an autoclave with a solution of metal precursors at high temperature and vapour pressure overnight, followed by filtering, drying, and calcination[122]. Spray pyrolysis produces a highly dispersed active metal catalyst with a large surface area and a wide pore-size dispersion[123]. The Ni/Al_2O_3-MgO catalyst synthesized by impregnation and plasma treatment has a greater surface area, no impurities, and a wider pore size distribution than the impregnated catalyst, resulting in enhanced DRM activity[124]. Nonetheless, because they are weakly attached to the support and are prone to deactivation of the catalyst in methane dry reforming, as finely disseminated active metals tend to agglomerate and sinter at high temperatures.

1.8 Catalyst Deactivation

1.8A. Metal sintering

One of the drawbacks of DRM is metal sintering as high reaction temperatures in DRM produce agglomeration of small active metal particles, resulting in the formation of big-sized metal particles. Furthermore, high temperatures cause the melting of active metals, which inhibits the availability of active sites for methane activation and initiates the coke lumps over the metal particles resulting in deactivation of the catalyst. As reported nickel-based

catalysts are extensively used in methane dry reforming, even though they are prone to agglomerate and form large particles, resulting in less dispersion on the catalyst's surface. This leads to less metal support interaction, and favors the formation of more carbon on the metal surface, making it inaccessible for further reaction. According to reports, large particle size of active metal is an important feature to consider in carbon production in DRM processes. Catalysts containing small metal particles, on the other hand, are prone to sintering at high temperatures, but they provide excellent dispersion and strong metal support interaction, leading in high catalytic conversions. According to reports, in order to preserve Ni in low particle size, it was alloyed with other metals known as bimetallic catalysts, which proved to be a good option for carbon suppression in DRM [125][126][127][128]. Furthermore, the preservation of nanosized Ni particles in the core-shell of support materials drew a lot of attention to DRM reactions with great stability and intact structure[129][130][131]. Recently, atomically distributed Ni atoms on a support surface were synthesized and screened in DRM because the C-H bond of methane requires a significant amount of energy to break on metal particles, and other particles give further cleavage of CH_x species to generate H_2. So, prior to the complete dehydrogenation of methane, CH_x species should transform into other oxygenated species in order to gasify the carbon at the same time. As a result, metal sintering and melting are critical issues to consider in the industrial application of DRM with increased carbon resistance[132][133][134][135].

1.8B. Side reactions

Dry reforming of methane at the industrial level remains a challenge attributable to the limited life of the catalyst due to deactivation. Deactivation is caused mostly by carbon deposition on active metal and side reactions such as the Boudouard reaction and methane decomposition reaction at elevated temperatures. Furthermore, carbon accumulation is accelerated by the sintering of active metal at high reaction temperatures, resulting in

minimal metal support contact and poor metal dispersion. Because methane dissociation primarily occurs on metal sites and results in carbon species, these species can be oxidized concurrently by dissociative adsorption of CO_2 on support and metal support interphase. As a result, the support role is essential in coke gasification and DRM activity. Moreover, the stability of catalysts is also important for elevated DRM activity because, during DRM, supported catalysts tend to convert in other crystal phases as an impurity which alters the active site for DRM cycles and declines the conversions. Therefore, in recent times structurally ordered catalysts are more attractive for DRM because of their thermal stability in adverse reaction conditions[136].

1.9. Structured Oxide catalysts:

To achieve high conversions and a long catalytic life, DRM focuses, a variety of supports with different features such as stability, redox behaviour, oxygen spillover capability, oxygen storage ability, and basicity. Additionally, a variety of metal systems, including alloyed and bimetallic metals, are rigorously examined for DRM. Because of its low cost and high conversion rates, Ni is predominantly screened in DRM. In addition to supported catalysts, it has been demonstrated that structurally ordered catalysts with diverse stoichiometry, configurations, and doping of various substituents with various physiochemical properties

are also promising DRM candidates[137]. Over the past ten years, catalysts based on perovskites have been employed inherently with longevity and stability. There are numerous uses for perovskite oxide materials with the ABO_3 formula in various catalytic chemical processes [138][139][140][141][142]. Thermal stability is controlled by site A, whereas catalytic conversion is controlled by site B. Ni-based $SrNiO_3$ and $CeNiO_3$ catalysts were created by Naushad et al., and the catalytic activity was compared[143]. Ce-based catalysts with large surfaces and evenly dispersed Ni atoms have demonstrated superior DRM activity

[144]. LaNiO$_3$ catalysts based on nickel were also studied in DRM, despite the fact that significant coke production was seen. Moreover, to stabilize the structure, partial substitution of Fe in B site is also prepared and investigated and an early deactivation of catalyst was observed[145]. Furthermore, Ni based supported catalysts are prone to more carbon formation then the perovskites with partial substitution of Ni in DRM. According to literature, the A and B sites were reported to be active and stable for DRM conditions with partial doping of rare earth and alkaline earth metals. Small-sized Ni particles are produced during the reduction of perovskite-based Ni catalysts prior to DRM run, which improves dispersion and increases the activity of DRM[146][147][148]. Additionally, the ability of perovskite material to gasify carbon along with its oxygen ion conduction feature has increased interest in DRM. Due to an inherited oxygen vacancy in the structure, pyrochlores-based catalysts have also recently been investigated for DRM. These catalysts showed enhanced activity, coke gasification, and thermal stability[149][150]. La$_2$Zr$_2$O$_7$ catalysts with partial A and B site substitution in the DRM reaction have been examined by Spivey and colleagues, who discovered higher activity and stability[151][152]. The effect of Ca and Sr substitution at A site in Ni substituted La$_2$Zr$_{1.44}$Ni$_{0.56}$O$_{7-d}$ pyrochlore catalyst was also screened in DRM; the Sr substituted La$_{1.95}$Sr$_{0.05}$Zr$_{1.44}$Ni$_{0.56}$O$_{7-d}$ catalyst demonstrated better resistance to coke formation than other catalysts at 800°C owing to high dispersion of Ni on catalyst's surface [153]. In addition, the impact of noble metal (Rh) doping on La$_2$B$_2$O$_7$ (B= Zr, Ti) in DRM was also investigated[154]. The impact of Ce/Zr ratio in pyrochlore catalysts with 10 wt.% Ni loading in DRM has been examined by Yuhan Sun and group members. They discovered that varying Ce/Zr ratios cause the pyrochlore phase to transform into a defect fluorite phase[155]. These structural variations have an impact on the production of surface oxygen species that are capable of gasifying the coke produced during DRM.

1.10. Scope and objective of the thesis:

Methane dry reforming using various catalytic systems has become a crucial tool for converting greenhouse gases into valuable syngas and, ultimately, value-added chemicals. Nevertheless, a number of obstacles such carbon deposition, stability, sintering, and poor conversions drive the creation of various catalysts with structural changes like active metal concentration and the addition of various metals to achieve higher activity and stability. Several structurally ordered catalysts, such as the perovskites and pyrochlores catalysts mentioned in earlier sections, have proven to be effective alternatives to conventional supported catalysts. Additionally, layered catalysts that have been thoroughly tested in electrochemical processes can also be a good candidate for DRM owing to their stability, structural alteration and ion conductivity. Using this as the thesis' goal, the following work has been completed:

1) The Pechini method was used to synthesize Gd-based pyrochlore catalysts that were formulated as Ni substituted $Gd_2X_2O_{7-\delta}$ (X=Zr, Ti). The catalysts were then analyzed using various analytic techniques, and evaluated in methane dry reforming. After figuring out how the support affected DRM activity, next section of this work looked into the impact of Ni concentration on DRM activity in a $Gd_2Zr_2O_{7-\delta}$ catalyst. Moreover, by doping different amounts of Ce in a Ni substituted $Gd_2Zr_2O_{7-\delta}$ catalyst at DRM conditions for 100 hours, the redox behaviour of Ce in the carbon gasification process was further explored.

2) Perovskite-based $SrMnO_3$ catalysts were examined in DRM processes synthesized using the Pechini method. Eu, Sm, and Nd doped catalysts were synthesized, described, and their activity was tested to investigate the effect of rare substitution in A site on DRM in $SrMnO_3$ catalysts. Sm-doped catalyst emerged as a strong competitor with high conversion and was chosen for a 100-hour durability test among all catalysts. The results clearly reveal that the defect generates active surface hydroxyl species that offer carbon gasification and improved DRM action in Sm-doped catalyst.

3) Sodium titanates, a kind of layered oxides designated as $Na_2Ti_3O_7$ with Ni doping was synthesized, and structural modifications were investigated in the furnace under DRM conditions. Following the confirmation of structure stability, the effect of Ni concentration was examined by synthesizing a series of catalysts with higher amounts of Ni. For 100 hours, catalyst with an optimum Ni concentration displayed higher DRM activity. After screening the catalyst for prolonged periods of time, structure changes were discovered, which were substantiated by several characterization techniques. The role of transition metal doping in NTN002 catalysts in the B site was studied further by substituting Co, Cu, and Fe. Cu-based catalysts have shown improved DRM catalytic activity among all. The synergetic effect of Ni with Cu was established in DRM activity

1.11 References:

[1]   Mitchell JFB. THE "GREENHOUSE" EFFECT AND CLIMATE CHANGE. n.d.

[2]   Schneider SH. The Greenhouse Effect: Science and Policy. n.d.

[3]   Fisher R V, Schmincke H, Rocks P. Initial Reports ofthe Deep-Sea Drilling Projec (U.S. Government Printing Of-fice. vol. 282. Wiley; 1979.

[4]   Tuckett R. Greenhouse gases. Encyclopedia of Analytical Science, Elsevier; 2019, p. 362–72. https://doi.org/10.1016/B978-0-12-409547-2.14031-4.

[5]   Feenstra RC, RI and MPT. The Next Generation of the Penn World Table" American Economic Review, n.d.

[6]   Olivier JGJ, Van Aardenne JA, Dentener FJ, Pagliari V, Ganzeveld LN, Peters JAHW. Recent trends in global greenhouse gas emissions:regional trends 1970–2000 and spatial distributionof key sources in 2000. Environ Sci (Ruse) 2005;2:81–99. https://doi.org/10.1080/15693430500400345.

[7]   Rypdal K, Winiwarter W. Uncertainties in greenhouse gas emission inventories-evaluation, comparability and implications. vol. 4. 2001.

[8]   Rietmann N, Hügler B, Lieven T. Forecasting the trajectory of electric vehicle sales and the consequences for worldwide CO_2 emissions. J Clean Prod 2020;261:121038. https://doi.org/10.1016/J.JCLEPRO.2020.121038.

[9]   Köne AI, Büke T. Forecasting of CO_2 emissions from fuel combustion using trend analysis. Renewable and Sustainable Energy Reviews 2010;14:2906–15. https://doi.org/10.1016/J.RSER.2010.06.006.

[10]   Jiang J, Ye B, Liu J. Research on the peak of CO_2 emissions in the developing world: Current progress and future prospect. Appl Energy 2019;235:186–203. https://doi.org/10.1016/J.APENERGY.2018.10.089.

[11]   Quadrelli R, Peterson S. The energy–climate challenge: Recent trends in CO_2 emissions from fuel combustion. Energy Policy 2007;35:5938–52. https://doi.org/10.1016/J.ENPOL.2007.07.001.

[12]   Sumabat AK, Lopez NS, Yu KD, Hao H, Li R, Geng Y, et al. Decomposition analysis of Philippine CO_2 emissions from fuel combustion and electricity generation. Appl Energy 2016;164:795–804. https://doi.org/10.1016/J.APENERGY.2015.12.023.

[13]   Wei L, Geng P. A review on natural gas/diesel dual fuel combustion, emissions and performance. Fuel Processing Technology 2016;142:264–78. https://doi.org/10.1016/J.FUPROC.2015.09.018.

[14]   Chappin EJL, Dijkema GPJ. On the impact of CO_2 emission-trading on power generation emissions. Technol Forecast Soc Change 2009;76:358–70. https://doi.org/10.1016/J.TECHFORE.2008.08.004.

[15]   Doucette RT, McCulloch MD. Modeling the CO_2 emissions from battery electric vehicles given the power generation mixes of different countries. Energy Policy 2011;39:803–11. https://doi.org/10.1016/J.ENPOL.2010.10.054.

[16]   Ozawa A, Kudoh Y, Kitagawa N, Muramatsu R. Life cycle CO_2 emissions from

power generation using hydrogen energy carriers. Int J Hydrogen Energy 2019;44:11219–32. https://doi.org/10.1016/J.IJHYDENE.2019.02.230.

[17] Yoro KO, Daramola MO. CO_2 emission sources, greenhouse gases, and the global warming effect. Advances in Carbon Capture: Methods, Technologies and Applications 2020:3–28. https://doi.org/10.1016/B978-0-12-819657-1.00001-3.

[18] Lee ZH, Sethupathi S, Lee KT, Bhatia S, Mohamed AR. An overview on global warming in Southeast Asia: CO_2 emission status, efforts done, and barriers. Renewable and Sustainable Energy Reviews 2013;28:71–81. https://doi.org/10.1016/J.RSER.2013.07.055.

[19] Pinguelli Rosa L, Kahn Ribeiro S. THE PRESENT, PAST, AND FUTURE CONTRIBUTIONS TO GLOBAL WARMING OF CO_2 EMISSIONS FROM FUELS A Key for Negotiation in the Climate Convention. 2001.

[20] Frölicher TL, Winton M, Sarmiento JL. Continued global warming after CO_2 emissions stoppage. Nat Clim Chang 2014;4:40–4. https://doi.org/10.1038/nclimate2060.

[21] Lodge TP. Materials science: A unique platform for materials design. Science (1979) 2008;321:50–1. https://doi.org/10.1126/science.1159652.

[22] Neale PJ, Williamson CE, Banaszak AT, Häder DP, Hylander S, Ossola R, et al. The response of aquatic ecosystems to the interactive effects of stratospheric ozone depletion, UV radiation, and climate change. Photochemical and Photobiological Sciences 2023;22:1093–127. https://doi.org/10.1007/s43630-023-00370-z.

[23] Wang H, Pilcher DJ, Kearney KA, Cross JN, Shugart OM, Eisaman MD, et al. Simulated Impact of Ocean Alkalinity Enhancement on Atmospheric CO_2 Removal in the Bering Sea. Earths Future 2023;11. https://doi.org/10.1029/2022EF002816.

[24] Bloom AA, Bowman KW, Lee M, Turner AJ, Schroeder R, Worden JR, et al. A global wetland methane emissions and uncertainty dataset for atmospheric chemical transport models (WetCHARTs version 1.0). Geosci Model Dev 2017;10:2141–56.

https://doi.org/10.5194/gmd-10-2141-2017.

[25] Feng L, Palmer PI, Parker RJ, Lunt MF, Bösch H. Methane emissions are predominantly responsible for record-breaking atmospheric methane growth rates in 2020 and 2021. Atmos Chem Phys 2023;23:4863–80. https://doi.org/10.5194/acp-23-4863-2023.

[26] Feng L, Palmer PI, Zhu S, Parker RJ, Liu Y. Tropical methane emissions explain large fraction of recent changes in global atmospheric methane growth rate. Nat Commun 2022;13:1378. https://doi.org/10.1038/s41467-022-28989-z.

[27] Fraser A, Palmer PI, Feng L, Bösch H, Parker R, Dlugokencky EJ, et al. Estimating regional fluxes of CO&lt;sub&gt;2&lt;/sub&gt; and CH&lt;sub&gt;4&lt;/sub&gt; using space-borne observations of XCH&lt;sub&gt;4&lt;/sub&gt::XCO&lt;sub&gt;2&lt;/sub&gt; Atmos Chem Phys 2014;14:12883–95. https://doi.org/10.5194/acp-14-12883-2014.

[28] Fung I, John J, Lerner J, Matthews E, Prather M, Steele LP, et al. Three-dimensional model synthesis of the global methane cycle. J Geophys Res 1991;96:13033. https://doi.org/10.1029/91JD01247.

[29] Janssens-Maenhout G, Crippa M, Guizzardi D, Muntean M, Schaaf E, Dentener F, et al. EDGAR v4.3.2 Global Atlas of the three major greenhouse gas emissions for the period 1970–2012. Earth Syst Sci Data 2019;11:959–1002. https://doi.org/10.5194/essd-11-959-2019.

[30] Landerer FW, Flechtner FM, Save H, Webb FH, Bandikova T, Bertiger WI, et al. Extending the Global Mass Change Data Record: GRACE Follow-On Instrument and Science Data Performance. Geophys Res Lett 2020;47. https://doi.org/10.1029/2020GL088306.

[31] Kvenvolden KA, Rogers BW. Gaia's breath—global methane exhalations. Mar Pet

Geol 2005;22:579–90. https://doi.org/10.1016/j.marpetgeo.2004.08.004.

[32]   Laughner JL, Neu JL, Schimel D, Wennberg PO, Barsanti K, Bowman KW, et al. Societal shifts due to COVID-19 reveal large-scale complexities and feedbacks between atmospheric chemistry and climate change. Proceedings of the National Academy of Sciences 2021;118. https://doi.org/10.1073/pnas.2109481118.

[33]   McNorton J, Bousserez N, Agustí-Panareda A, Balsamo G, Cantarello L, Engelen R, et al. Quantification of methane emissions from hotspots and during COVID-19 using a global atmospheric inversion. Atmos Chem Phys 2022;22:5961–81. https://doi.org/10.5194/acp-22-5961-2022.

[34]   Pandey S, Houweling S, Krol M, Aben I, Monteil G, Nechita-Banda N, et al. Enhanced methane emissions from tropical wetlands during the 2011 La Niña. Sci Rep 2017;7:45759. https://doi.org/10.1038/srep45759.

[35]   Pandey S, Houweling S, Lorente A, Borsdorff T, Tsivlidou M, Bloom AA, et al. Using satellite data to identify the methane emission controls of South Sudan's wetlands. Biogeosciences 2021;18:557–72. https://doi.org/10.5194/bg-18-557-2021.

[36]   Peng S, Lin X, Thompson RL, Xi Y, Liu G, Hauglustaine D, et al. Wetland emission and atmospheric sink changes explain methane growth in 2020. Nature 2022;612:477–82. https://doi.org/10.1038/s41586-022-05447-w.

[37]   Rigby M, Prinn RG, Fraser PJ, Simmonds PG, Langenfelds RL, Huang J, et al. Renewed growth of atmospheric methane. Geophys Res Lett 2008;35:L22805. https://doi.org/10.1029/2008GL036037.

[38]   Cooper MJ, Martin R V., Hammer MS, Levelt PF, Veefkind P, Lamsal LN, et al. Global fine-scale changes in ambient NO2 during COVID-19 lockdowns. Nature 2022;601:380–7. https://doi.org/10.1038/s41586-021-04229-0.

[39]   Janssens-Maenhout G, Crippa M, Guizzardi D, Muntean M, Schaaf E, Dentener F,

et al. EDGAR v4.3.2 Global Atlas of the three major greenhouse gas emissions for the period 1970–2012. Earth Syst Sci Data 2019;11:959–1002. https://doi.org/10.5194/essd-11-959-2019.

[40]   Mao J, Paulot F, Jacob DJ, Cohen RC, Crounse JD, Wennberg PO, et al. Ozone and organic nitrates over the eastern United States: Sensitivity to isoprene chemistry. Journal of Geophysical   Research: Atmospheres   2013;118:11,256-11,268. https://doi.org/10.1002/jgrd.50817.

[41]   Miyazaki K, Bowman K, Sekiya T, Takigawa M, Neu JL, Sudo K, et al. Global tropospheric ozone responses to reduced NO_x emissions linked to the COVID-19 worldwide lockdowns. Sci Adv 2021;7. https://doi.org/10.1126/sciadv.abf7460.

[42]   Chen G, Tam NFY, Ye Y, Chen B. Greenhouse gas emissions from intertidal wetland soils under anthropogenic activities. Carbon Mineralization in Coastal Wetlands: From Litter Decomposition to Greenhouse Gas Dynamics 2022:269–93. https://doi.org/10.1016/B978-0-12-819220-7.00004-2.

[43]   Chopra R, Magazzino C, Shah MI, Sharma GD, Rao A, Shahzad U. The role of renewable energy and natural resources for sustainable agriculture in ASEAN countries: Do carbon emissions and deforestation affect agriculture productivity? Resources Policy 2022;76:102578. https://doi.org/10.1016/J.RESOURPOL.2022.102578.

[44]   Dziejarski B, Krzyżyńska R, Andersson K. Current status of carbon capture, utilization, and storage technologies in the global economy: A survey of technical assessment. Fuel 2023;342:127776. https://doi.org/10.1016/J.FUEL.2023.127776.

[45]   418.64 ppm #CO_2 in the air at Maunakea for the 36th week of 2023 n.d.

[46]   Ziemke JR, Kramarova NA, Frith SM, Huang L, Haffner DP, Wargan K, et al. NASA Satellite Measurements Show Global-Scale Reductions in Free Tropospheric Ozone in 2020 and   again   in   2021   During   COVID-19.   Geophys   Res   Lett   2022;49.

https://doi.org/10.1029/2022GL098712.

[47]   Fu L, Ren Z, Si W, Ma Q, Huang W, Liao K, et al. Research progress on CO_2 capture and utilization technology. Journal of CO_2 Utilization 2022;66:102260. https://doi.org/10.1016/J.JCOU.2022.102260.

[48]   Chai R, Liu Y, Wang J, Liu Q, Rui Z. CO_2 utilization and sequestration in Reservoir: Effects and mechanisms of CO_2 electrochemical reduction. Appl Energy 2022;323:119584. https://doi.org/10.1016/J.APENERGY.2022.119584.

[49]   Hou Z, Luo J, Xie Y, Wu L, Huang L, Xiong Y. Carbon Circular Utilization and Partially Geological Sequestration: Potentialities, Challenges, and Trends. Energies (Basel) 2022;16:324. https://doi.org/10.3390/en16010324.

[50]   Hanifa M, Agarwal R, Sharma U, Thapliyal PC, Singh LP. A review on CO_2 capture and sequestration in the construction industry: Emerging approaches and commercialised technologies. Journal of CO_2 Utilization 2023;67:102292. https://doi.org/10.1016/J.JCOU.2022.102292.

[51]   Yu M, Liu X, Chen Y, Zhang Z, Wang Y, Zhang J, et al. A 4E analysis of a novel coupling process of syngas purification and CO_2 capture, transcritical CO_2 power and absorption refrigeration. Chemical Engineering Journal 2022;445:136757. https://doi.org/10.1016/J.CEJ.2022.136757.

[52]   Zhang L, Cao C, Wen S, Zhao Y, Peng X, Wu J. Thoughts on the development of CO_2-EGR under the background of carbon peak and carbon neutrality. Natural Gas Industry B 2023;10:383–92. https://doi.org/10.1016/J.NGIB.2023.07.007.

[53]   Edouard MN, Okere CJ, Ejike C, Dong P, Suliman MAM. Comparative numerical study on the co-optimization of CO_2 storage and utilization in EOR, EGR, and EWR: Implications for CCUS project development. Appl Energy 2023;347:121448. https://doi.org/10.1016/J.APENERGY.2023.121448.

[54]   YUAN S, MA D, LI J, ZHOU T, JI Z, HAN H. Progress and prospects of carbon dioxide capture, EOR-utilization and storage industrialization. Petroleum Exploration and Development 2022;49:955–62. https://doi.org/10.1016/S1876-3804(22)60324-0.

[55]   Yoo Y, Kim I, Lee D, Yong Choi W, Choi J, Jang K, et al. Review of contemporary research on inorganic CO_2 utilization via CO_2 conversion into metal carbonate-based materials. Journal of Industrial and Engineering Chemistry 2022;116:60–74. https://doi.org/10.1016/J.JIEC.2022.09.007.

[56]   Rafiee A, Khalilpour KR, Milani D. CO_2 Conversion and Utilization Pathways. Polygeneration with Polystorage: For Chemical and Energy Hubs 2019:213–45. https://doi.org/10.1016/B978-0-12-813306-4.00008-2.

[57]   Valluri S, Claremboux V, Kawatra S. Opportunities and challenges in CO_2 utilization. Journal of Environmental Sciences 2022;113:322–44. https://doi.org/10.1016/J.JES.2021.05.043.

[58]   Khojasteh-Salkuyeh Y, Ashrafi O, Mostafavi E, Navarri P. CO_2 utilization for methanol production; Part I: Process design and life cycle GHG assessment of different pathways. Journal of CO_2 Utilization 2021;50:101608. https://doi.org/10.1016/J.JCOU.2021.101608.

[59]   Assaba Fayisa B, Yang Y, Zhen Z, Wang M-Y, Lv J, Wang Y, et al. Engineered Chemical Utilization of CO_2 to Methanol via Direct and Indirect Hydrogenation Pathways: A Review. Industrial & Engineering Chemistry Research 2022;61:10319–35. https://doi.org/10.1021/acs.iecr.2c00402.

[60]   Calzadiaz-Ramirez L, Meyer AS. Formate dehydrogenases for CO_2 utilization. Curr Opin Biotechnol 2022;73:95–100. https://doi.org/10.1016/J.COPBIO.2021.07.011.

[61]   Lavoie JM. Review on dry reforming of methane, a potentially more environmentally-friendly approach to the increasing natural gas exploitation. Front Chem

2014;2. https://doi.org/10.3389/fchem.2014.00081.

[62]   Mondal P, Dang GS, Garg MO. Syngas production through gasification and cleanup for downstream applications — Recent developments. Fuel Processing Technology 2011;92:1395–410. https://doi.org/10.1016/J.FUPROC.2011.03.021.

[63]   Wilhelm DJ, Simbeck DR, Karp AD, Dickenson RL. Syngas production for gas-to-liquids applications: technologies, issues and outlook. Fuel Processing Technology 2001;71:139–48. https://doi.org/10.1016/S0378-3820(01)00140-0.

[64]   Nikitin A, Ozersky A, Savchenko V, Sedov I, Shmelev V, Arutyunov V. Matrix conversion of natural gas to syngas: The main parameters of the process and possible applications. Chemical Engineering Journal 2019;377:120883. https://doi.org/10.1016/J.CEJ.2019.01.162.

[65]   Chen WH, Biswas PP, Ong HC, Hoang AT, Nguyen TB, Dong C Di. A critical and systematic review of sustainable hydrogen production from ethanol/bioethanol: Steam reforming, partial oxidation, and autothermal reforming. Fuel 2023;333:126526. https://doi.org/10.1016/J.FUEL.2022.126526.

[66]   Gao F, Zhan H, Zeng ZY. A methanol autothermal reforming system for the enhanced hydrogen production: Process simulation and thermodynamic optimization. Int J Hydrogen Energy 2023;48:1758–72. https://doi.org/10.1016/J.IJHYDENE.2022.10.067.

[67]   Farsi M. Reforming process design and modeling: Steam, dry, and autothermal reforming. Advances in Synthesis Gas: Methods, Technologies and Applications: Volume 4: Syngas Process Modelling and Apparatus Simulation 2023:123–40. https://doi.org/10.1016/B978-0-323-91879-4.00003-5.

[68]   Assabumrungrat S, Laosiripojana N. FUELS – HYDROGEN PRODUCTION | Autothermal Reforming. Encyclopedia of Electrochemical Power Sources 2009:238–48. https://doi.org/10.1016/B978-044452745-5.00296-3.

[69]   Aasberg-Petersen K, Christensen TS, Dybkjær I, Sehested J, Østberg M, Coertzen RM, et al. Synthesis gas production for FT synthesis. Stud Surf Sci Catal 2004;152:258–405. https://doi.org/10.1016/S0167-2991(04)80461-0.

[70]   Soleimani S, Lehner M. Tri-Reforming of Methane: Thermodynamics, Operating Conditions, Reactor Technology and Efficiency Evaluation—A Review. Energies 2022, Vol 15, Page 7159 2022;15:7159. https://doi.org/10.3390/EN15197159.

[71]   Kozonoe CE, de Abreu TF, de Brito Alves RM, Schmal M. Influence of the material as support for nickel on the product selectivity of the tri-reforming of methane. Mater Today Commun 2023;35:105732. https://doi.org/10.1016/J.MTCOMM.2023.105732.

[72]   P. Nascimento J, de Cássia F. Bezerra R, M. Assaf E, F. Lucredio A, S. Araujo R, D. Saraiva G, et al. Investigation of the Deactivation Behavior of MeMo/La$_2$O$_3$-Al$_2$O$_3$- and MeMo/Nb$_2$O$_5$ Supported Catalysts (Me = Pt, Ni, and Co) in Tri-Reforming of Methane. Energy & Fuels 2023;37:3836–53. https://doi.org/10.1021/acs.energyfuels.2c03120.

[73]   Alli RD, de Souza PAL, Mohamedali M, Virla LD, Mahinpey N. Tri-reforming of methane for syngas production using Ni catalysts: Current status and future outlook. Catal Today 2023;407:107–24. https://doi.org/10.1016/J.CATTOD.2022.02.006.

[74]   Pham XH, Ashik UPM, Hayashi JI, Pérez Alonso A, Pla D, Gómez M, et al. Review on the catalytic tri-reforming of methane - Part II: Catalyst development. Appl Catal A Gen 2021;623:118286. https://doi.org/10.1016/J.APCATA.2021.118286.

[75]   Minh DP, Siang TJ, Vo DVN, Phan TS, Ridart C, Nzihou A, et al. Hydrogen Production From Biogas Reforming: An Overview of Steam Reforming, Dry Reforming, Dual Reforming, and Tri-Reforming of Methane. Hydrogen Supply Chain: Design, Deployment and Operation 2018:111–66. https://doi.org/10.1016/B978-0-12-811197-0.00004-X.

[76]   Lian Z, Olanrele SO, Si C, Yang M, Li B. Critical Role of Interfacial Sites between

Nickel and CeO_2 Support in Dry Reforming of Methane: Revisit of Reaction Mechanism and Origin of Stability. Journal of Physical Chemistry C 2020;124:5118–24. https://doi.org/10.1021/acs.jpcc.9b09856.

[77]   Wittich K, Krämer M, Bottke N, Schunk SA. Catalytic Dry Reforming of Methane: Insights from Model Systems. ChemCatChem 2020;12:2130–47. https://doi.org/10.1002/cctc.201902142.

[78]   Zhang Y, Zu Y, He D, Liang J, Zhu L, Mei Y, et al. The tailored role of "defect" sites on γ-alumina: A key to yield an efficient methane dry reforming catalyst with superior nickel utilization. Appl Catal B 2022;315:121539. https://doi.org/10.1016/J.APCATB.2022.121539.

[79]   Yabe T, Yamada K, Murakami K, Toko K, Ito K, Higo T, et al. Role of Electric Field and Surface Protonics on Low-Temperature Catalytic Dry Reforming of Methane. ACS Sustain Chem Eng 2019;7:5690–7. https://doi.org/10.1021/acssuschemeng.8b04727.

[80]   J. Rostrup-Nielsen. Process for the production of a reforming catalyst. n.d.

[81]   Gadalla AM, Bower B. The role of catalyst support on the activity of Nickel for reforming methane with CO. vol. 43. 1988.

[82]   Akri M, Zhao S, Li X, Zang K, Lee AF, Isaacs MA, et al. Atomically dispersed nickel as coke-resistant active sites for methane dry reforming. Nat Commun 2019;10. https://doi.org/10.1038/s41467-019-12843-w.

[83]   Sasson Bitters J, He T, Nestler E, Senanayake SD, Chen JG, Zhang C. Utilizing bimetallic catalysts to mitigate coke formation in dry reforming of methane. Journal of Energy Chemistry 2022; 68:124–42. https://doi.org/10.1016/J.JECHEM.2021.11.041.

[84]   Yentekakis I V., Panagiotopoulou P, Artemakis G. A review of recent efforts to promote dry reforming of methane (DRM) to syngas production via bimetallic catalyst formulations. Appl Catal B 2021; 296:120210.

https://doi.org/10.1016/J.APCATB.2021.120210.

[85]   Wu X, Xu L, Chen M, Lv C, Wen X, Cui Y, et al. Recent Progresses in the Design and Fabrication of Highly Efficient Ni-Based Catalysts with Advanced Catalytic Activity and Enhanced Anti-coke Performance Toward CO_2 Reforming of Methane. Front Chem 2020;8. https://doi.org/10.3389/fchem.2020.581923.

[86]   Siang TJ, Singh S, Omoregbe O, Bach LG, Phuc NHH, Vo DVN. Hydrogen production from CH_4 dry reforming over bimetallic Ni–Co/Al_2O_3 catalyst. Journal of the Energy Institute 2018; 91:683–94. https://doi.org/10.1016/J.JOEI.2017.06.001.

[87]   Kwon Y, Eichler JE, Floto ME, Mullins CB. The complementary relationship between Ru/Al_2O_3 and Ni/Al_2O_3 catalyst for dry reforming of methane. Chemical Engineering Research and Design 2023; 195:624–36. https://doi.org/10.1016/J.CHERD.2023.06.029.

[88]   García-Diéguez M, Finocchio E, Larrubia MÁ, Alemany LJ, Busca G. Characterization of alumina-supported Pt, Ni and PtNi alloy catalysts for the dry reforming of methane. J Catal 2010; 274:11–20. https://doi.org/10.1016/J.JCAT.2010.05.020.

[89]   Fertout RI, Ghelamallah M, Helamallah M, Kacimi S, López PN, Corberán VC. Nickel Supported on Alkaline Earth Metal–Doped γ-Al_2O_3–La_2O_3 as Catalysts for Dry Reforming of Methane. Russian Journal of Applied Chemistry 2020; 93:289–98. https://doi.org/10.1134/S1070427220020196.

[90]   Ni J, Zhao J, Chen L, Lin J, Kawi S. Lewis Acid Sites Stabilized Nickel Catalysts for Dry (CO_2) Reforming of Methane. ChemCatChem 2016; 8:3732–9. https://doi.org/10.1002/cctc.201601002.

[91]   Ni J, Chen L, Lin J, Kawi S. Carbon deposition on borated alumina supported nano-sized Ni catalysts for dry reforming of CH_4. Nano Energy 2012; 1:674–86. https://doi.org/10.1016/J.NANOEN.2012.07.011.

[92]   Nisa KS, Suendo V, Sophiana IC, Susanto H, Kusumaatmaja A, Nishiyama N, et al. Effect of base promoter on activity of MCM-41-supported nickel catalyst for hydrogen production via dry reforming of methane. Int J Hydrogen Energy 2022; 47:23201–12. https://doi.org/10.1016/J.IJHYDENE.2022.05.081.

[93]   Promotional Effects of Nd2O3 Doped Ni/Al$_2$O$_3$–Y$_2$O$_3$ Catalysts on Oxygen Vacancy and Coking-Resista Rong Zhu XDZLYLLWLZ& YW. Promotional Effects of Nd$_2$O$_3$ Doped Ni/Al$_2$O$_3$–Y$_2$O$_3$ Catalysts on Oxygen Vacancy and Coking-Resistant in Dry Reforming of Methane. Catal Letters 2023;153.

[94]   Liu S, Guan L, Li J, Zhao N, Wei W, Sun Y. CO$_2$ reforming of CH$_4$ over stabilized mesoporous Ni–CaO–ZrO$_2$ composites. Fuel 2008; 87:2477–81. https://doi.org/10.1016/J.FUEL.2008.02.009.

[95]   Song DH, Jung UH, Kim YE, Im HB, Lee TH, Lee KB, et al. Influence of Supports on the Catalytic Activity and Coke Resistance of Ni Catalyst in Dry Reforming of Methane. Catalysts 2022; 12:216. https://doi.org/10.3390/catal12020216.

[96]   Danghyan V, Kumar A, Mukasyan A, Wolf EE. An active and stable NiOMgO solid solution-based catalysts prepared by paper assisted combustion synthesis for the dry reforming of methane. Appl Catal B 2020; 273:119056. https://doi.org/10.1016/J.APCATB.2020.119056.

[97]   Fakeeha A, Kurdi A, Al-Baqmaa Y, Ibrahim A, Abasaeed A, Al-Fatesh A. Performance Study of Methane Dry Reforming on Ni/ZrO$_2$ Catalyst. Energies (Basel) 2022; 15:3841. https://doi.org/10.3390/en15103841.

[98]   Yabe T, Mitarai K, Oshima K, Ogo S, Sekine Y. Low-temperature dry reforming of methane to produce syngas in an electric field over La-doped Ni/ZrO$_2$ catalysts. Fuel Processing Technology 2017;158:96–103. https://doi.org/10.1016/J.FUPROC.2016.11.013.

[99]   Bellido JDA, Assaf EM. Effect of the Y$_2$O$_3$–ZrO$_2$ support composition on nickel

catalyst evaluated in dry reforming of methane. Appl Catal A Gen 2009;352:179–87. https://doi.org/10.1016/J.APCATA.2008.10.002.

[100] Al-Fatesh AS, Fakeeha AH, Ibrahim AA, Abasaeed AE. Ni supported on La$_2$O$_3$+ZrO$_2$ for dry reforming of methane: The impact of surface adsorbed oxygen species. Int J Hydrogen Energy 2021;46:3780–8. https://doi.org/10.1016/J.IJHYDENE.2020.10.164.

[101] Shamsi A. Partial oxidation and dry reforming of methane over Ca/Ni/K(Na) catalysts. Catal Letters 2006;109:189–93. https://doi.org/10.1007/s10562-006-0076-0.

[102] Ewbank JL, Kovarik L, Diallo FZ, Sievers C. Effect of metal–support interactions in Ni/Al$_2$O$_3$ catalysts with low metal loading for methane dry reforming. Appl Catal A Gen 2015;494:57–67. https://doi.org/10.1016/J.APCATA.2015.01.029.

[103] Li K, Pei C, Li X, Chen S, Zhang X, Liu R, et al. Dry reforming of methane over La$_2$O$_2$CO$_3$-modified Ni/Al$_2$O$_3$ catalysts with moderate metal support interaction. Appl Catal B 2020;264:118448. https://doi.org/10.1016/J.APCATB.2019.118448.

[104] Xu. Y, DU.H, LI.J., Weng P, Zhu J, GE J, Zhou J, Song M.Zhu W Y, A comparison of Al$_2$O$_3$ and SiO$_2$ supported Ni-based catalysts in their performance for the dry reforming of methane. J. Fuel Chem. Technol. 2019:2:47. https://doi.org/10.1016/S1872-5813(19)30010-6.

[105] Sung Jeon O, Lee H, Lee K-S, K. Paidi V, Ji Y, Chan Kwon O, et al. Harnessing Strong Metal–Support Interaction to Proliferate the Dry Reforming of Methane Performance by In Situ Reduction. ACS Applied Materials & Interfaces 2022;14:12140–8. https://doi.org/10.1021/acsami.1c20889.

[106] Sun N, Wen X, Wang F, Peng W, Zhao N, Xiao F, et al. Catalytic performance and characterization of Ni–CaO–ZrO$_2$ catalysts for dry reforming of methane. Appl Surf Sci 2011;257:9169–76. https://doi.org/10.1016/J.APSUSC.2011.05.127.

[107] Kim SS, Lee SM, Won JM, Yang HJ, Hong SC. Effect of Ce/Ti ratio on the catalytic

activity and stability of Ni/CeO$_2$–TiO$_2$ catalyst for dry reforming of methane. Chemical Engineering Journal 2015;280:433–40. https://doi.org/10.1016/J.CEJ.2015.06.027.

[108] Rosli SNA, Abidin SZ, Osazuwa OU, Fan X, Jiao Y. The effect of oxygen mobility/vacancy on carbon gasification in nano catalytic dry reforming of methane: A review. Journal of CO$_2$ Utilization 2022;63:102109. https://doi.org/10.1016/J.JCOU.2022.102109.

[109] Damyanova S, Pawelec B, Arishtirova K, Huerta MVM, Fierro JLG. The effect of CeO$_2$ on the surface and catalytic properties of Pt/CeO$_2$–ZrO$_2$ catalysts for methane dry reforming. Appl Catal B 2009;89:149–59. https://doi.org/10.1016/J.APCATB.2008.11.035.

[110] Rodriguez-Gomez A, Lopez-Martin A, Ramirez A, Gascon J, Caballero A. Elucidating the Promotional Effect of Cerium in the Dry Reforming of Methane. ChemCatChem 2021;13:553–63. https://doi.org/10.1002/cctc.202001527.

[111] Perego C, Villa P. Catalyst preparation methods. Catal Today 1997;34:281–305. https://doi.org/10.1016/S0920-5861(96)00055-7.

[112] Chen J, Wang R, Zhang J, He F, Han S. Effects of preparation methods on properties of Ni/CeO$_2$–Al$_2$O$_3$ catalysts for methane reforming with carbon dioxide. J Mol Catal A Chem 2005;235:302–10. https://doi.org/10.1016/J.MOLCATA.2005.04.023.

[113] Abdulrasheed A, Jalil AA, Gambo Y, Ibrahim M, Hambali HU, Shahul Hamid MY. A review on catalyst development for dry reforming of methane to syngas: Recent advances. Renewable and Sustainable Energy Reviews 2019;108:175–93. https://doi.org/10.1016/J.RSER.2019.03.054.

[114] Movasati A, Alavi SM, Mazloom G. Dry reforming of methane over CeO$_2$-ZnAl$_2$O$_4$ supported Ni and Ni-Co nano-catalysts. Fuel 2019;236:1254–62. https://doi.org/10.1016/J.FUEL.2018.09.069.

[115] Na HS, Jeong DW, Jang WJ, Shim JO, Roh HS. The effect of preparation method on

Fe/Al/Cu oxide-based catalyst performance for high temperature water gas shift reaction using simulated waste-derived synthesis gas. Int J Hydrogen Energy 2015;40:12268–74. https://doi.org/10.1016/J.IJHYDENE.2015.07.060.

[116]   Albarazi A, Gálvez ME, Da Costa P. Synthesis strategies of ceria–zirconia doped Ni/SBA-15 catalysts for methane dry reforming. Catal Commun 2015;59:108–12. https://doi.org/10.1016/J.CATCOM.2014.09.050.

[117]   Aghamohammadi S, Haghighi M, Maleki M, Rahemi N. Sequential impregnation vs. sol-gel synthesized Ni/Al_2O_3-CeO_2 nanocatalyst for dry reforming of methane: Effect of synthesis method and support promotion. Molecular Catalysis 2017;431:39–48. https://doi.org/10.1016/J.MCAT.2017.01.012.

[118]   Eshghi J, Haghighi M, Sajjadi SM. Sol-gel synthesis of Co-W promoted $NiAl_2O_4$ spinel nanocatalyst used in combined reforming of methane: Influence of tungsten content on catalytic activity and stability. Ceram Int 2019;45:4596–608. https://doi.org/10.1016/J.CERAMINT.2018.11.147.

[119]   Jana P, De La Peña O'Shea VA, Coronado JM, Serrano DP. Cobalt based catalysts prepared by Pechini method for CO_2-free hydrogen production by methane decomposition. Int J Hydrogen Energy 2010;35:10285–94. https://doi.org/10.1016/J.IJHYDENE.2010.07.125.

[120]   Majid A, Tunney J, Argue S, Wang D, Post M, Margeson J. Preparation of SrFeO~2.85 perovskite using a citric acid assisted Pechini-type method. J Alloys Compd 2005;398:48–54. https://doi.org/10.1016/J.JALLCOM.2005.02.023.

[121]   Shin SA, Noh YS, Hong GH, Park JI, Song HT, Lee KY, et al. Dry reforming of methane over Ni/ZrO_2-Al_2O_3 catalysts: Effect of preparation methods. J Taiwan Inst Chem Eng 2018;90:25–32. https://doi.org/10.1016/J.JTICE.2017.11.032.

[122]   O'Hare D. Hydrothermal Synthesis. Encyclopedia of Materials: Science and

Technology 2001:3989–92. https://doi.org/10.1016/B0-08-043152-6/00701-4.

[123] Shahnazi A, Firoozi S. Improving the catalytic performance of $LaNiO_3$ perovskite by manganese substitution via ultrasonic spray pyrolysis for dry reforming of methane. Journal of CO_2 Utilization 2021;45:101455. https://doi.org/10.1016/J.JCOU.2021.101455.

[124] Estifaee P, Haghighi M, Babaluo AA, Rahemi N, Jafari MF. The beneficial use of non-thermal plasma in synthesis of Ni/Al_2O_3–MgO nanocatalyst used in hydrogen production from reforming of CH_4/CO_2 greenhouse gases. J Power Sources 2014;257:364–73. https://doi.org/10.1016/J.JPOWSOUR.2014.01.128.

[125] Muraza O, Galadima A. A review on coke management during dry reforming of methane. Int J Energy Res 2015;39:1196–216. https://doi.org/10.1002/er.3295.

[126] Han JW, Park JS, Choi MS, Lee H. Uncoupling the size and support effects of Ni catalysts for dry reforming of methane. Appl Catal B 2017;203:625–32. https://doi.org/10.1016/J.APCATB.2016.10.069.

[127] Han JW, Kim C, Park JS, Lee H. Highly coke-resistant Ni nanoparticle catalysts with minimal sintering in dry reforming of methane. ChemSusChem 2014;7:451–6. https://doi.org/10.1002/cssc.201301134.

[128] Liu W, Li L, Zhang X, Wang Z, Wang X, Peng H. Design of $Ni-ZrO_2@SiO_2$ catalyst with ultra-high sintering and coking resistance for dry reforming of methane to prepare syngas. Journal of CO_2 Utilization 2018;27:297–307. https://doi.org/10.1016/J.JCOU.2018.08.003.

[129] Das S, Lim KH, Gani TZH, Aksari S, Kawi S. Bi-functional CeO_2 coated NiCo-MgAl core-shell catalyst with high activity and resistance to coke and H_2S poisoning in methane dry reforming. Appl Catal B 2023;323:122141. https://doi.org/10.1016/J.APCATB.2022.122141.

[130] Zhang J, Li F. Coke-resistant $Ni@SiO_2$ catalyst for dry reforming of methane. Appl

Catal B 2015;176–177:513–21. https://doi.org/10.1016/J.APCATB.2015.04.039.

[131] Wang Y, Fang Q, Shen W, Zhu Z, Fang Y. (Ni/MgAl$_2$O$_4$)@SiO$_2$ core-shell catalyst with high coke-resistance for the dry reforming of methane. Reac Kinet Mech Cat 2018;125:127–39. https://doi.org/10.1007/s11144.

[132] Tang Y, Wei Y, Wang Z, Zhang S, Li Y, Nguyen L, et al. Synergy of Single-Atom Ni1 and Ru1 Sites on CeO$_2$ for Dry Reforming of CH$_4$. J Am Chem Soc 2019;141:7283–93. https://doi.org/10.1021/jacs.8b10910.

[133] Kim S, Lauterbach J, Sasmaz E. Yolk–Shell Pt-NiCe@SiO$_2$ Single-Atom-Alloy Catalysts for Low-Temperature Dry Reforming of Methane. ACS Catal 2021;11:8247–60. https://doi.org/10.1021/acscatal.1c01223.

[134] Akri M, El Kasmi A, Batiot-Dupeyrat C, Qiao B. Highly Active and Carbon-Resistant Nickel Single-Atom Catalysts for Methane Dry Reforming. Catalysts 2020;10:630. https://doi.org/10.3390/catal10060630.

[135] Wu J, Gao J, Lian S, Li J, Sun K, Zhao S, et al. Engineering the oxygen vacancies enables Ni single-atom catalyst for stable and efficient C-H activation. Appl Catal B 2022;314:121516. https://doi.org/10.1016/J.APCATB.2022.121516.

[136] Serrano-Lotina A, Daza L. Influence of the operating parameters over dry reforming of methane to syngas. Int J Hydrogen Energy 2014;39:4089–94. https://doi.org/10.1016/J.IJHYDENE.2013.05.135.

[137] Jabbour K. Tuning combined steam and dry reforming of methane for "metgas" production: A thermodynamic approach and state-of-the-art catalysts. Journal of Energy Chemistry 2020;48:54–91. https://doi.org/10.1016/J.JECHEM.2019.12.017.

[138] Cao D, Luo C, Luo T, Shi Z, Wu F, Li X, et al. Dry reforming of methane by La2NiO4 perovskite oxide, part I: Preparation and characterization of the samples. Fuel Processing Technology 2023;247:107765.

https://doi.org/10.1016/J.FUPROC.2023.107765.

[139]   Kim H, Mane R, Han K, Kim H, Lee C, Jeon Y. In Situ Control of the Eluted Ni Nanoparticles from Highly Doped Perovskite for Effective Methane Dry Reforming. Nanomaterials 2022;12:3325. https://doi.org/10.3390/nano12193325.

[140]   Carrillo AJ, Serra JM. Exploring the Stability of Fe–Ni Alloy Nanoparticles Exsolved from Double-Layered Perovskites for Dry Reforming of Methane. Catalysts 2021;11:741. https://doi.org/10.3390/catal11060741.

[141]   Grabchenko M, Pantaleo G, Puleo F, Vodyankina O, Liotta LF. Ni/La$_2$O$_3$ catalysts for dry reforming of methane: Effect of La$_2$O$_3$ synthesis conditions on the structural properties and catalytic performances. Int J Hydrogen Energy 2021;46:7939–53. https://doi.org/10.1016/J.IJHYDENE.2020.12.026.

[142]   Chava R, Bhaskar Anurag Varma D, Roy B, Appari S. Recent advances and perspectives of perovskite-derived Ni-based catalysts for CO$_2$ reforming of biogas. Journal of CO$_2$ Utilization 2022;65:102206. https://doi.org/10.1016/J.JCOU.2022.102206.

[143]   Ahmad N, Alharthi F, Alam M, Wahab R, Manoharadas S, Alrayes B. Syngas Production via CO$_2$ Reforming of Methane over SrNiO$_3$ and CeNiO$_3$ Perovskites. Energies (Basel) 2021;14:2928. https://doi.org/10.3390/en14102928.

[144]   Lima SM, Assaf JM, Peña MA, Fierro JLG. Structural features of La$_{1-x}$Ce$_x$NiO$_3$ mixed oxides and performance for the dry reforming of methane. Appl Catal A Gen 2006;311:94–104. https://doi.org/10.1016/J.APCATA.2006.06.010.

[145]   Jahangiri A, Aghabozorg H, Pahlavanzadeh H. Effects of Fe substitutions by Ni in La–Ni–O perovskite-type oxides in reforming of methane with CO$_2$ and O$_2$. Int J Hydrogen Energy 2013;38:10407–16. https://doi.org/10.1016/J.IJHYDENE.2013.05.080.

[146]   Damaskinos CM, Zavašnik J, Djinović P, Efstathiou AM. Dry reforming of methane over Ni/Ce$_{0.8}$Ti$_{0.2}$O$_{2-\delta}$: The effect of Ni particle size on the carbon pathways studied by

transient and isotopic techniques. Appl Catal B 2021;296:120321. https://doi.org/10.1016/J.APCATB.2021.120321.

[147] Chaudhary PK, Deo G. Influence of particle size and metal-support interaction on the catalytic performance of Ni-Al$_2$O$_3$ catalysts for the dry and oxidative-dry reforming of methane. Colloids Surf A Physicochem Eng Asp 2022;646:128973. https://doi.org/10.1016/J.COLSURFA.2022.128973.

[148] Qin L, Hu Z, Hu M, Zhao B, Kong L, Chen W, et al. EDTA impregnation assisted synthesis of nickel nanoparticles embedded in activated carbon and its application for dry reforming of methane. Int J Hydrogen Energy 2023;48:13442–51. https://doi.org/10.1016/J.IJHYDENE.2022.12.003.

[149] Jagadeesh P, Varun Y, Himajaa Reddy B, Sreedhar I, Singh SA. A short review on recent advancements of dry reforming of methane (DRM) over pyrochlores. Mater Today Proc 2023;72:361–9. https://doi.org/10.1016/J.MATPR.2022.08.107.

[150] Xu J, Xi R, Xu X, Zhang Y, Feng X, Fang X, et al. A2B2O7 pyrochlore compounds: A category of potential materials for clean energy and environment protection catalysis. Journal of Rare Earths 2020;38:840–9. https://doi.org/10.1016/J.JRE.2020.01.002.

[151] Bhattar S, Krishnakumar A, Kanitkar S, Abedin A, Shekhawat D, J. Haynes D, et al. 110th Anniversary: Dry Reforming of Methane over Ni- and Sr-Substituted Lanthanum Zirconate Pyrochlore Catalysts: Effect of Ni Loading. Industrial & Engineering Chemistry Research 2019;58:19386–96. https://doi.org/10.1021/acs.iecr.9b02434.

[152] Bhattar S, Kanitkar S, Abedin A, Shekhawat D, Haynes DJ, Spivey JJ. Reforming of Methane over Ni and Ca based pyrochlore catalysts to produce syngas Introduction-Natural gas production. n.d.

[153] Bhattar S, Abedin MA, Shekhawat D, Haynes DJ, Spivey JJ. The effect of La substitution by Sr- and Ca- in Ni substituted Lanthanum Zirconate pyrochlore catalysts for

dry reforming of methane. Appl Catal A Gen 2020;602:117721. https://doi.org/10.1016/J.APCATA.2020.117721.

[154] Wu J, Qiao L-Y, Zhou Z-F, Cui G-J, Zong S-S, Xu D-J, et al. Revealing the Synergistic Effects of Rh and Substituted $La_2B_2O_7$ (B = Zr or Ti) for Preserving the Reactivity of Catalyst in Dry Reforming of Methane. ACS Catal 2018;9:932–45. https://doi.org/10.1021/acscatal.8b03319.

[155] Design of Ni-substitute Jieru Bai DrYFWKBPCYSLJWDrJZProfYS. Design of Ni-substituted $La_2(CeZrNi)_2O_7$ Pyrochlore Catalysts for Methane Dry Reforming n.d.

Chapter 2
Synthesis and Screening of Gd based Pyrochlore and defect fluorite catalysts in DRM

In this chapter, structured ternary oxides $A_2B_2O_{7-\delta}$ are synthesized and screened for Dry reforming of methane. Part 1 of this chapter, deals with the effect of B site substitution in Gd based ternary metal oxide catalyst $Gd_2B_{2-x}Ni_xO_{7-\delta}$ (B = Zr, Ti) (x = 0 and 0.2) in the activity of DRM. Secondly, the effect of active metal Ni concentration was also studied in $Gd_2Zr_{2-x}Ni_xO_{7-\delta}$ (0.2, 0.5, 0.75) and lastly, the effect of Ce substitution in $Gd_2Zr_{1.8-x}Ni_{0.2}Ce_xO_{7-\delta}$ (x = 0.1,0.2,0.5,0.75) catalyst and investigated in DRM.

Part 1
Effect of support in Pyrochlore/Defect fluorite $(A_2B_{2-x}Ni_yO_{7-\delta})$ A = Gd, B = Ti /Zr, catalyst in DRM

2.1 Introduction:

The increase in global average temperature is attributed to an alarming upsurge in greenhouse gas emissions, especially CO_2. To address this issue, several reactions converting CO_2 to useful products have been reported, viz., hydrogenation, reforming, methanation, and carboxylation etc,[1]. Among them, CO_2 reforming has attracted more attention since it utilizes two greenhouse gases, CO_2 and methane, to generate valuable syngas (2). In particular, dry reforming of methane (DRM) generates syngas with $H_2/CO \approx$ 1 at thermodynamic equilibrium using CO_2 and CH_4 [2]. Generated syngas can be further used for the synthesis of DME or long-chain hydrocarbons by FT synthesis[3][4].

Ni-based catalysts show superior activity at steam reforming conditions, they are prone to severe coke formation under dry reforming conditions, caused by two reactions, Boudouard reaction (6) and methane cracking (4) at temperatures around 550 °C and 700 °C respectively[5][6]. In DRM Ni based supported catalysts were utilized which gives good conversions and activity. However, the sintering of Ni nanoparticles at high-temperature results in a compromising number of active sites in the catalyst [7]. Several suggestions to minimize these problems are documented and it has been observed that high dispersion and smaller particles of the active Ni with good metal support interaction can limit sintering as well as coke formation [8]. Support characteristics like redox property, basicity, etc. also influence the activity and durability of the catalyst. Recently, the concept of stabilizing active metal sites as ionic lattice sites in stable structured oxides, to prevent sintering and coke formation has been attracting attention.

$A_2B_2O_7$ ternary oxides form a potential family of compounds for various reforming reactions due to their high thermal stability and tolerance to structural variations and lattice site doping. These analogous compounds are known to have various structure types like pyrochlores and defect fluorite. Effect of different parameters viz., A and B site substitutions in these structure types and oxygen vacancies have been studied for gasification, reforming,

etc. Most of the reports are on lanthanum zirconate pyrochlore and noble metals like Rh, Ru, and Pt as well as Ni have been studied as active metals [9][10][11][12][13][14]. Apart from this, the effect of Rh doping in the kinetic parameters of dry and bi-reforming of methane is also analyzed [15][16][17][18].

In this Chapter, Gd-based ternary metal oxides catalyst $Gd_2B_{2-x}Ni_xO_{7-\delta}$ (B = Zr, Ti) (x = 0 and 0.2) has been synthesized by citrate gel method and compared their activity and durability in dry reforming of methane. Structure-activity correlation by various characterization techniques was established.

2.2 Experimental Section:

2.2.1 Synthesis of $Gd_2B_{2-x}Ni_xO_{7-\delta}$ (B = Zr, Ti) (x = 0 and 0.2):

$Gd_2B_{2-x}Ni_xO_{7-\delta}$ (B = Zr, Ti) (x = 0 and 0.2) catalysts were synthesized by conventional Pechini method. Metal nitrate precursors were dissolved in a minimum amount of distilled water separately, mixed together, and then added to the citric acid solution with a ratio of 3:1 (citric acid: nitrate precursors) under constant stirring at 80 °C. For Gd and Ti, Gd_2O_3 and Ti isopropoxide were dissolved in conc. HNO_3 before mixing with citric acid. Gd: B: Ni molar ratio in the solution was 1:0.96:0.099 for Ti compound whereas for Zr analogue, it was 1:0.898:0.099. Ethylene glycol was added to the solution as a polymerizing agent with a molar ratio of 1:1 (EG:CA). The formed gel was dried overnight at 180 °C to promote polyesterification and removal of water. The obtained fluffy material was crushed and calcined at 800 °C for 6h in the air to get the ternary metal oxides.

2.2.2 Catalyst evaluation:

The dry reforming reactions were carried out in a packed-bed tubular down flow reactor made of Inconel HT, placing it in a programmable tubular furnace. All the gases (CH_4, CO_2, and N_2) used for the reaction were regulated by mass flow controllers (Brooks Instruments). 0.5 cm^3 (0.6–0.75g) of 0.3–0.5 mm range catalyst particles were mixed with 0.5 cc of same size quartz pieces and loaded in the reactor tube supported by ceramic wool plugs. The

catalyst bed temperature was measured by a chromel-alumel thermocouple centered in the catalyst bed. Before the reaction, the catalyst was calcined at 700 °C for 5 h and reduced in situ at 700 °C for 5 h using 20% H_2 in an N_2 gas mixture. DRM reaction was carried out using a gas mixture consisting of CH_4, CO_2, and N_2 in the volume ratio of 1:1:1; with a flow rate of 80 mL min-1 with total gas hourly space velocity at 28,800 h^{-1}. The product gas mixture was analyzed by an online gas chromatograph (Chemito 8610) equipped with a Spherocarb packed column (1/8" OD and 8 feet length). CH_4 and CO_2 conversions and the H_2/CO ratio were calculated using the gas composition analyzed by GC and conversions were calculated by the formulae,

CH_4 Conversion:
$$XCH_4 \% = [(FCH_{4\ in} - FCH_{4\ out})/FCH_{4\ in}] \times 100 \tag{A}$$

CO_2 Conversion:
$$XCO_2 \% = [(FCO_{2\ in} - FCO_{2\ out})/FCO_{2\ in}] \times 100 \tag{B}$$

H_2/CO ratio:
$$H_2/CO = [F_{out}\ H_2/F_{out}\ CO] \tag{C}$$

2.3 Result and discussion:

2.3.1 X-Ray Diffraction Analysis and textural properties of $Gd_2B_{2-x}Ni_xO_{7-\delta}$ (B = Zr, Ti) (x = 0 and 0.2):

Phase analysis was carried out by PXRD and figure 2.1 showed $Gd_2Zr_2O_{7-\delta}$ (GZO) crystallized in defect fluorite structure with $Fm\overline{3}m$ space group (PDF 01-080-0471), while $Gd_2Ti_2O_{7-\delta}$ (GTO) crystallized in pyrochlore structure with $Fd\overline{3}m$ space group (PDF 01-073-1698). Ni doping (named as GTNO and GZNO for substitution in Ti and Zr compounds respectively) seems to have minimal effect on the structure type and parent structures are retained, with a small amount of NiO present as impurity outside the lattice as indicated by the peak at 43.2° [19][20]. The XRD patterns also show a small shifting of peaks in Ni-doped catalysts towards high 2θ values, pointing to a contraction of the lattice. This is further confirmed by full pattern refinement by the Rietveld method using GSAS-EXPGUI software [21]. For GZO, refinement was done with defect fluorite $Gd_2Zr_2O_{7-\delta}$ model, with $Fm\overline{3}m$

space group (ICSD collection code - 068265). Refinement went smoothly and resulted in a good fit with cell parameter a = 5.3008 Å, which is in agreement with the literature data [19]. For GTO, the refinement analysis confirmed a face centred cubic lattice system with Fd$\bar{3}$m space group (ICSD collection code- 024207) with cell parameter a = 10.1861 Å. With Ni-doped catalysts, quantitative analysis shows that 1.34 wt% and 0.68 wt% of Ni are present outside the lattice as NiO, in GTNO and GZNO respectively. Refinement studies were carried out by substituting appropriate concentrations of Ni (subtracting the Ni concentration present outside the lattice) in Zr and Ti sites and cell parameters were refined to be 5.2678 and 10.1842 Å for GZNO and GTNO respectively. The decrease in cell parameters of substituted catalysts confirms the incorporation of Ni in Ti and Zr sites. Lattice site substitution of Ni in Ti analog is obviously lower due to the higher concentration of Ti added, which in turn has led to a higher concentration of NiO outside the lattice, in a well dispersed manner. The crystallite size of the main phases was calculated by Lorentian broadening of refined XRD peaks. Refined profiles and parameters are given in figure 2.2 (A-D) and Table 1.1 respectively. Atomic parameters are given in Table 1. 2. In general, the surface area of the materials is low as expected due to the high temperature synthesis (Table 1.3). Substitution of lower valent Ni in the lattice is expected to affect the stoichiometry and hence form and redistribute O occupancy and vacancies. Since scattering parameters of O is low in x-ray diffraction methods, we have refrained from refining O occupancy in Rietveld analysis.
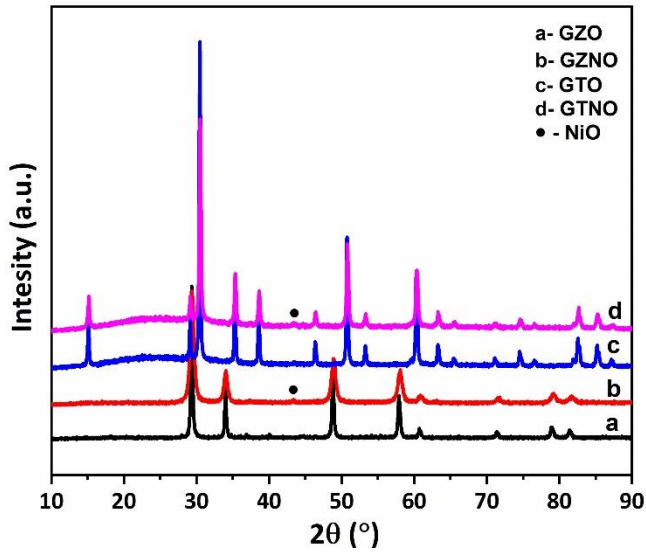
Figure 2.1: XRD pattern of a) GZO b) GZNO c) GTO d) GTNO

Table 1.1: Rietveld refinement data of $A_2B_{2-x}Ni_yO_{7-\delta}$ (A= Gd and B = Zr, Ti)

	$Gd_2Zr_2O_{7-\delta}$	$Gd_2Zr_{1.8}Ni_{0.13}O_{7-\delta}$	$Gd_2Ti_2O_{7-\delta}$	$Gd_2Ti_{1.93}Ni_{0.08}O_{7-\delta}$
$\chi 2$*	3.09	2.32	3.63	3.22
wRp (%)**	4.91	3.77	4.86	4.80
Rp (%) **	3.67	2.99	3.84	3.58
Space group	$Fm\bar{3}m$	$Fm\bar{3}m$	$Fd\bar{3}m$	$Fd\bar{3}m$
a/°A	5.3008	5.2678	10.1861	10.1842
Occupancy	Zr= 0.5000	Zr = 0.4500	Ti = 1.0012	Ti = 0.8926
		Ni = 0.0322		Ni = 0.0370
Impurity phase (wt%)		NiO = 0.68		NiO = 1.34
CrystalliteSize (nm)	54.1	33.1	79.8	55.3

* $\chi^2 = \dfrac{M}{N_{obs}-N_{var}}$ where M is the minimized function during refinement, Nobs is the number of observed intensities and Nvar is the number of refined variables. **Rp and wRp are the residual parameters defined as $R_p = \dfrac{\Sigma|Io-Ic|}{\Sigma I_O}$ and $wR_p == \sqrt{\dfrac{Mp}{\Sigma wIo^2}}$, where Mp is the minimization powder diffraction function, IO and IC are observed and calculated intensities.

Figure 2.2: Rietveld Refinement profile a) GZO, b) GTNO, c) GZO and d) GZNO

Table 1.2: Atomic parameters of $A_2B_{2-x}Ni_yO_{7-\delta}$ (A= Gd and B = Zr, Ti)

Catalyst Name	X	Y	z
$Gd_2Ti_2O_{7-\delta}$			
Gd	0.0	0.0	0.0
Ti	0.5	0.5	0.5
O1	0.125	0.125	0.125
O2	0.44239	0.125	0.125
$Gd_2Ti_{1.93}Ni_{0.08}O_{7-\delta}$			
Gd	0.0	0.0	0.0
Ti	0.5	0.5	0.5
O1	0.125	0.125	0.125
O2	0.43874	0.125	0.125
Ni	0.5	0.5	0.5
$Gd_2Zr_2O_{7-\delta}$			
Gd	0.0	0.0	0.0

Zr	0.0	0.0	0.0
O	0.25	0.25	0.25
$Gd_2Zr_{1.8}Ni_{0.13}O_{7-\delta}$			
Gd	0.0	0.0	0.0
Zr	0.0	0.0	0.0
O	0.25	0.25	0.25
Ni	0.0	0.0	0.0

Table 1.3: BET Surface area of $A_2B_{2-x}Ni_yO_{7-\delta}$ (A= Gd and B = Zr, Ti)

Catalyst	GZO	GZNO	GTO	GTNO
Surface Area(m2/g)	11.1	12.2	10.3	17.1

2.3.2 Raman Analysis of $Gd_2B_{2-x}Ni_xO_{7-\delta}$ (B = Zr, Ti) (x = 0 and 0.2):

an attempt to understand O occupancy and vacancy distribution in the catalysts through Raman spectroscopy was carried out in figure 2.3 Pyrochlore structure is known to have 6 active Raman modes distributed as A1g+Eg+4F2g irreducible presentations[22][23][24]. The A1g mode corresponds to Ti-O stretching, at higher frequencies (515-530 cm^{-1}) and Eg modes are due to O-Ti-O bending motion (330 – 340 cm^{-1}), while the F2g modes are due to O-Ti-O bending (300-320 cm^{-1}) and vibration of Gd-O' lattice (200-250 cm^{-1}). For GTNO catalyst, Raman modes around 215, 310, 449, 519, and 715 cm^{-1} were observed. Bands around 710-750 cm^{-1} are attributed to the defect originated oxygen disorder confirming the occurrence of oxygen vacancy in GTNO catalyst [22]. While in GZNO catalyst, broad Raman bands have been observed in the range of 300-350 cm^{-1}, the broadness of Raman modes confirms the defect fluorite structure of the catalyst [25]. According to Glerup et al., the absence of a broad peak at 750 cm^{-1} confirms the lack of disorder generated oxygen vacancies in GZNO catalyst.
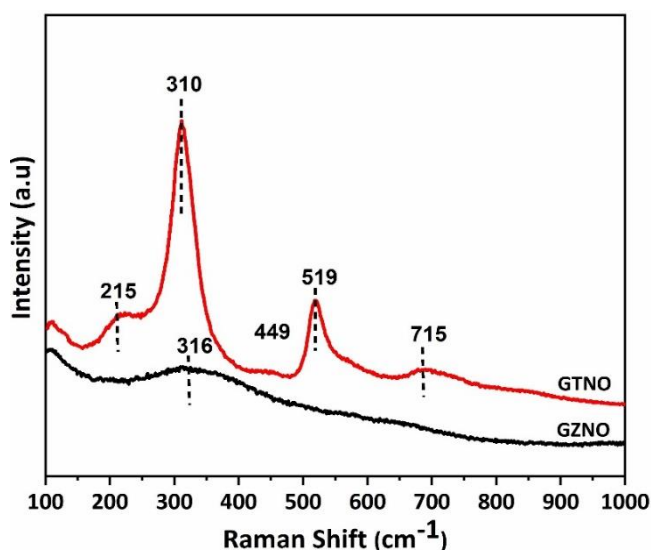
Figure 2.3: Raman spectra of GTNO and GZNO catalysts

2.3.3 Temperature programmed reduction of $Gd_2B_{2-x}Ni_xO_{7-\delta}$ (B = Zr, Ti) (x = 0 and 0.2)

The difference in reducibility of both catalysts was ascertained by TPR analysis. It can be seen from figure 2.4 that, in GZNO two reduction peaks were observed at around 459 ℃ and 559.6 ℃. The first peak corresponds to the reduction of surface NiO particles and the second peak at 559.6 ℃ is owing to the lagged reduction of $Ni^{+2} \rightarrow Ni^0$ present in the sub-surface layers of the support [26][27]. In the case of GTNO, the reduction of NiO particles on the support surface occurs at much lower temperatures in the range of 350 – 410 °C, possibly due to better dispersion. The peak in the range of 480 - 500 °C corresponds to the reduction of NiO, which is strongly interacting with the support. Along with this, reduction peaks centered at 630 °C and 700 °C suggested the reduction of lattice Ni^{2+} into metallic Ni [28].On comparing both the materials, it can be concluded that GTNO has more reducible Ni species over the surface as well as in sub-layers of support.
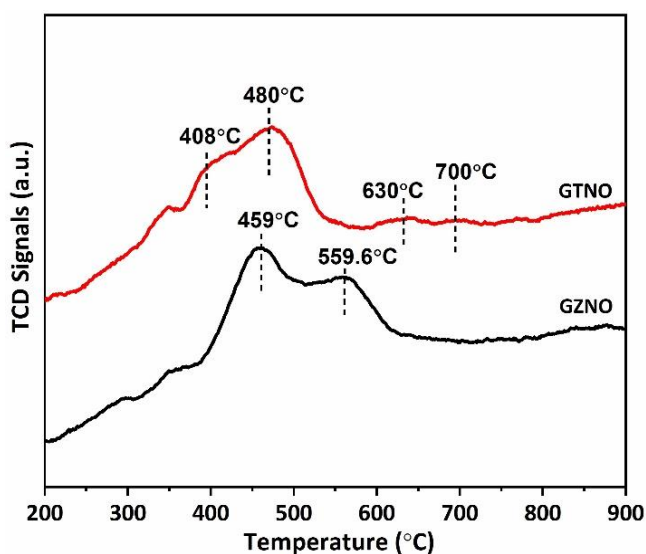
Figure 2.4: TPR Analysis of GTNO and GZNO catalysts

2.3.4 Temperature programmed Desorption of CO_2 in $Gd_2B_{2-x}Ni_xO_{7-\delta}$ (B = Zr, Ti) (x = 0 and 0.2)

Surface acidic/basic nature also plays an important role in DRM, since CO_2 is acidic in nature; the higher the basicity of support, the more CO_2 is adsorbed activating CO formation and further dry reforming of methane. This was estimated by CO_2-TPD experiments showed in figure 2.5. In GTNO, the desorption peaks are observed in lower temperatures as well as in higher temperature ranges which confirms the presence of weak, medium, and strong basic sites facilitating activation of CO_2. While in GZNO catalysts, the broad peaks observed at around 200 °C indicate the presence of weak basic sites resulting in less desorption and activation of CO_2 [29][30].
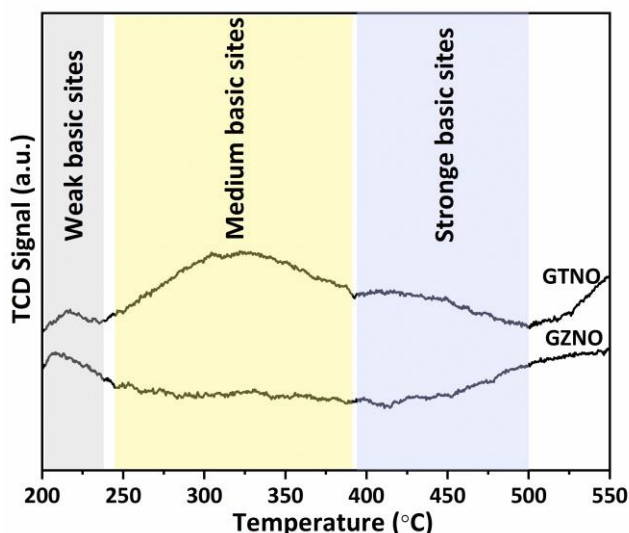
Figure 2.5: CO_2-TPD Analysis of GTNO and GZNO catalysts

2.3.5 XPS Analysis of $Gd_2B_{2-x}Ni_xO_{7-\delta}$ (B = Zr, Ti) (x = 0 and 0.2)

To understand the surface composition of metals in the catalysts, XPS analysis has been carried out in figure 2.6. In GTNO catalyst, Ti 2p XPS spectrum showed the presence of Ti^{+4} through binding energy peaks at 458.1 and 463.8 eV [31](Figure 2.6(A)). Interestingly, we also observed a small peak at 456.6 eV which can be attributed to reduced Ti species [32]. The concentration of this reduced Ti species on the surface, however, decreased on Ni doping. The O 1s spectrum of the GTNO catalyst displays two peaks at 529.2 eV and 531.9 eV corresponding to the surface adsorbed oxygen (O^-) and hydroxyl oxygen (OH^-) species respectively (Figure 2.6 (B)). The ratio of surface adsorbed oxygen (O^-) and the hydroxyl species (O^-: OH^-) was estimated from the area under the peaks and is found to be 9:1 in GTO while in GTNO catalysts it is 7:3. This confirms the enhanced generation of hydroxyl species by Ni substitution in Ti site. In the case of the GZNO catalyst (Figure 2.6(C)), the Zr 3d XPS profile showed peaks at 182.5 eV and 184.9 eV confirming Zr in +4 valence state [33]. The O 1s spectrum shows the binding energy at 529.1 eV indicating only loosely bound surface oxygen species and the lower binding energy peaks correspond to lattice oxygen atoms (Figure 2.6(D)). It is noteworthy that in GZNO, the peak corresponding to hydroxyl oxygen

species at 531.9 eV is missing (Figure 2.6(D)).
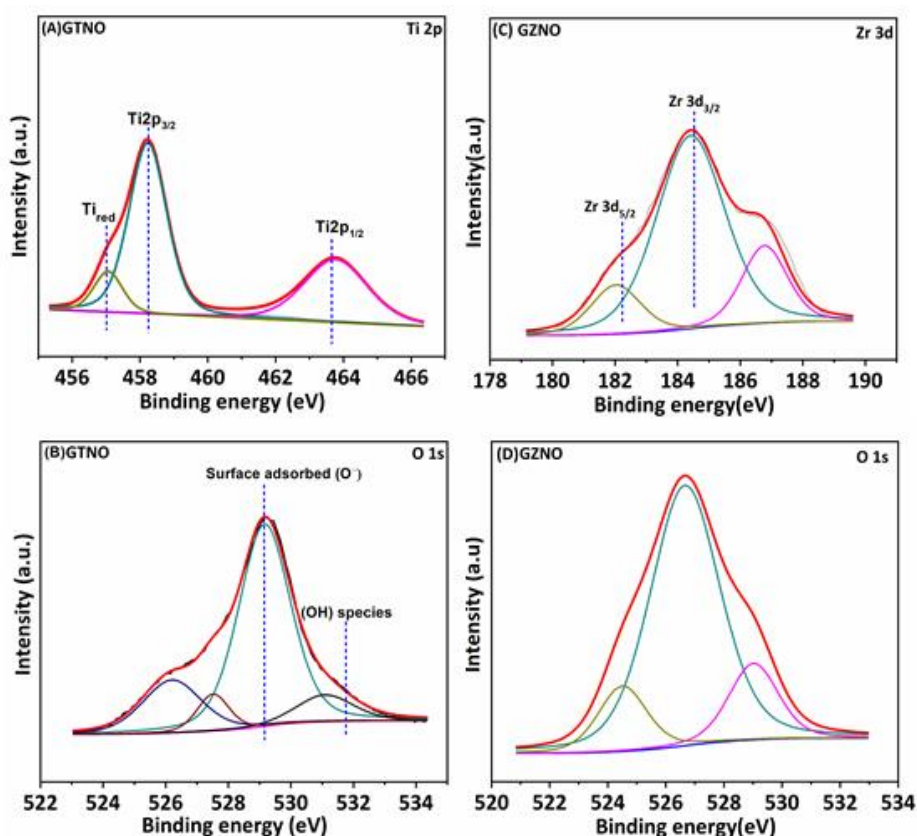
Figure 2.6: Fitted XPS profile of GTNO catalyst (A) Ti 2p (B) O 1s; GZNO catalyst (C) Zr 3d (D) O 1s

2.3.6 DRIFTS Analysis of $Gd_2B_{2-x}Ni_xO_{7-\delta}$ (B = Zr, Ti) (x = 0 and 0.2)

Furthermore, we performed DRIFTS experiments to understand the adsorbed species on the surface of these catalysts upon exposure to CO_2. Before the analysis, the sample was heated inside the DRIFTS cell in N_2 at 400 °C to clean the surface. Following this, the sample was reduced in H_2 (20 mL min^{-1}) for 2 h and later the cell chamber was purged with N_2 at 400 °C for 30 min. H_2 is expected to be homolytically dissociated and adsorbed on the catalytically active sites and the N_2 purge would sweep away any H_2 not anchored on the surface. Then a mixture of N_2 (20 mL min^{-1}) and CO_2 (5 mL min^{-1}) was passed over the sample and spectra were recorded at 400 °C in absorbance mode. The spectra show the presence of carbonates (symmetric stretching O-C-O and C-O) and formate species in the range of 1300-1600 cm^{-1} (Figure 2.7(A)). Formate species are formed because of the interaction between CO_2 and adsorbed H* on the surface. Figure 2.7(B) shows the absorption

bands at 3630 cm^{-1} and 3735 cm^{-1}, which correspond to the hydroxyl species; however, gaseous CO_2 also shows absorption in the same range and hence this cannot be conclusively assigned. The desorbed gaseous CO has been observed at 2143 cm^{-1} in figure. 2.7(C) [34]. The peak at 2143 cm^{-1} is more intense in GTNO than in GZNO catalyst, as the desorption of gaseous CO is more in GTNO catalyst which triggers the fast activation of CO_2. The less desorption of CO in GZNO shows lesser activation of CO_2.
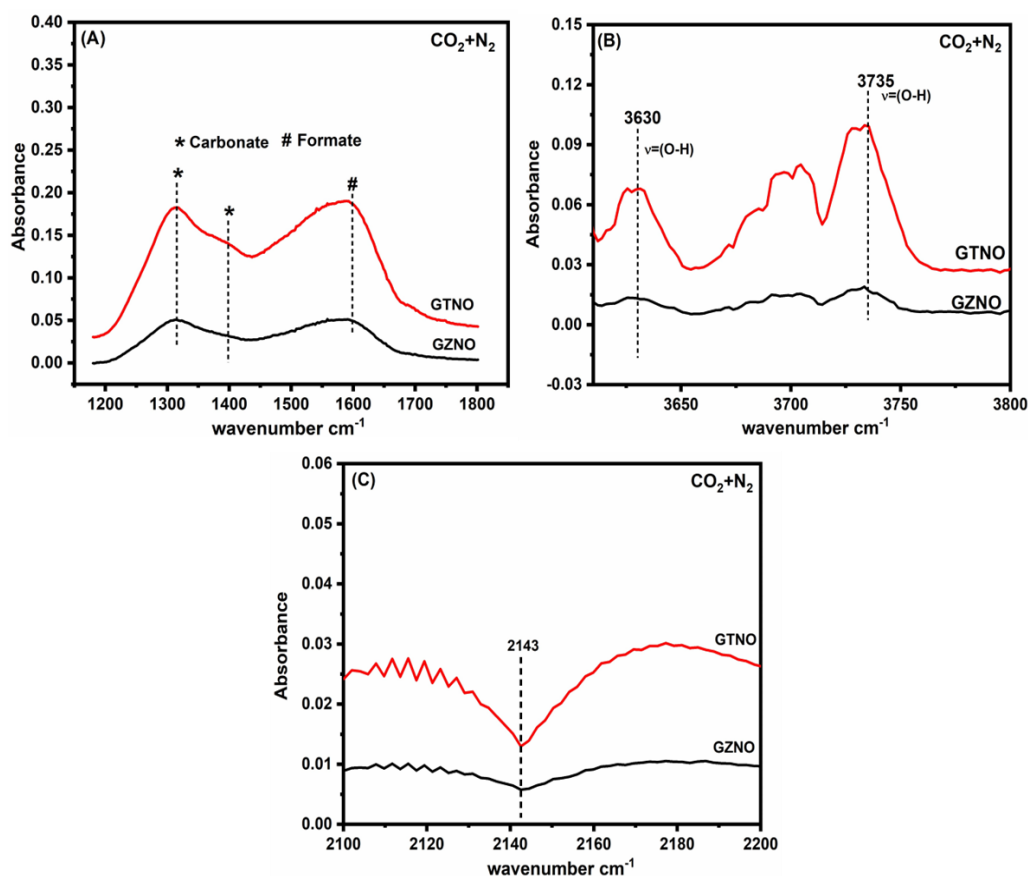
Figure 2.7: in situ FTIR spectra of GTNO and GZNO catalysts with the feed gas 5 mL CO_2+ 20 mL N_2 at 400 °C (A) Formation of carbonate and format species demonstrated by symbols, (B) Variation in desorbed CO intensities in GTNO and GZNO catalysts. (C) Formation of hydroxyl species over the surface of the catalyst.

2.4 Catalytic activity of $Gd_2B_{2-x}Ni_xO_{7-\delta}$ (B = Zr, Ti) (x = 0 and 0.2)

2.4.1 DRM testing at various temperatures and DRM run at 800°C:

The activity for dry reforming of methane of both the Ni substituted catalysts has been studied at various temperatures shown in figure 2.8 and durability was tested at optimized

reaction conditions at 800 °C, 28800 h^{-1} GHSV, CO_2: CH_4: N_2 = 80:80:80 mL min^{-1} and atmospheric pressure for 100 h time on stream (figure 2.9). Among the two catalysts, GTNO showed superior DRM activity. The initial activity of both the catalysts was poor and reached steady state conversions after 35-40 h. The initial poor activity was also accompanied by H_2/CO ratio much less than what is expected of DRM. It has been reported that the decrease in H_2/CO ratio may be because of side reactions like reverse water gas shift reaction (5) and reverse Boudouard reaction (6) at high reaction temperature (800 °C) [35]. In the case of GTNO, the activity recovers to 94% CO_2 and 88% CH_4 conversion and 0.96 (~1) H_2/CO ratio, whereas, GZNO exhibited much lower activity at maximum conversion.
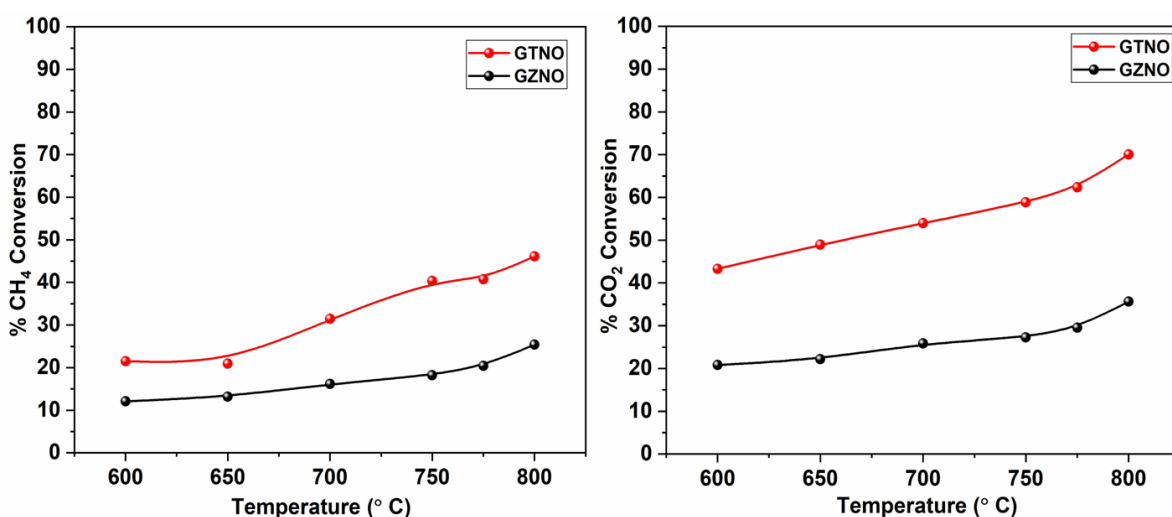
Figure 2.8: Temperature study of GZNO and GTNO catalysts in DRM conditions: CH_4: CO_2: N_2 = 80:80:80 ml/min, 28,800 h^{-1} at atm pressure.
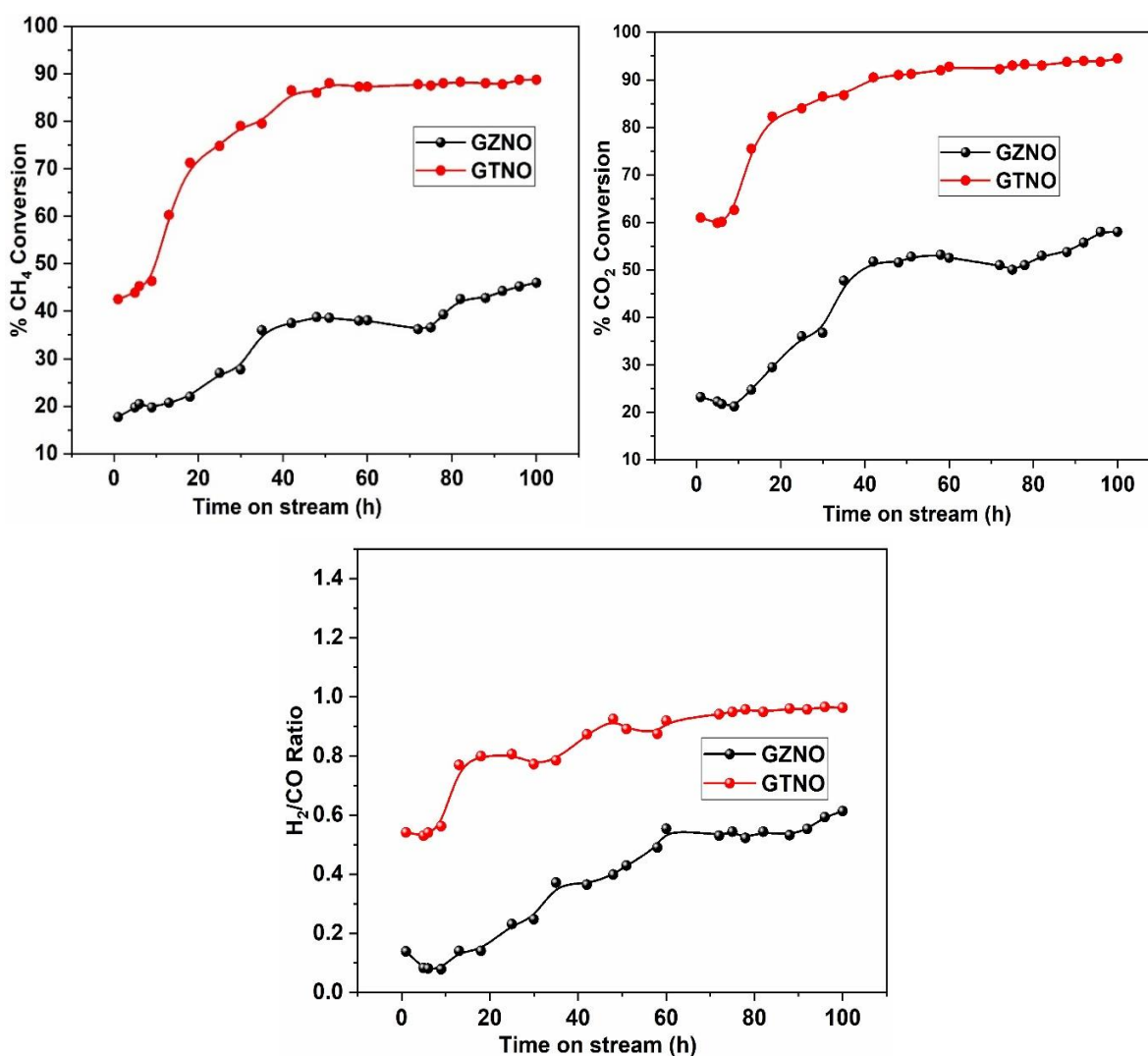
Figure 2.9: Activity analysis of GTNO and GZNO catalysts in DRM conditions: CH_4: CO_2: N_2 = 80:80:80 mL/min, 28,800 h^{-1} GHSV at 800 °C for 100 h time on stream. Conversions and H_2/CO ratios are plotted against time on stream.

It is understood that the surface oxygen species play a key role in the gasification of coke formed during the dry reforming reaction by converting it into CO. The XPS and in situ IR studies confirm the presence of these species, especially hydroxyl in GTNO catalysts. These active groups prevent the blockage of active sites by carbonaceous species and make the active sites available for further reaction. We can anticipate this mechanism of coke removal from the GTNO catalyst surface. The absence of hydroxyl species in the GZNO catalyst may be the reason for its decreased activity by the accumulation of carbonaceous compounds.

2.5 Spent Catalysts Characterization:

2.5.1 XRD analysis of spent catalysts:

In order to check the structural change and the stability of Ni-substituted catalysts after 100 h of reaction, the x-ray diffraction analysis of the spent catalysts was carried out. All two spent catalysts retained their parent structure after 100 h time on stream in DRM conditions (Figure 2.10). An extra peak in the case of GZNO catalyst at 2θ, 26.2° (JCPDS No.75-1621) is attributed to graphitic carbon [35].
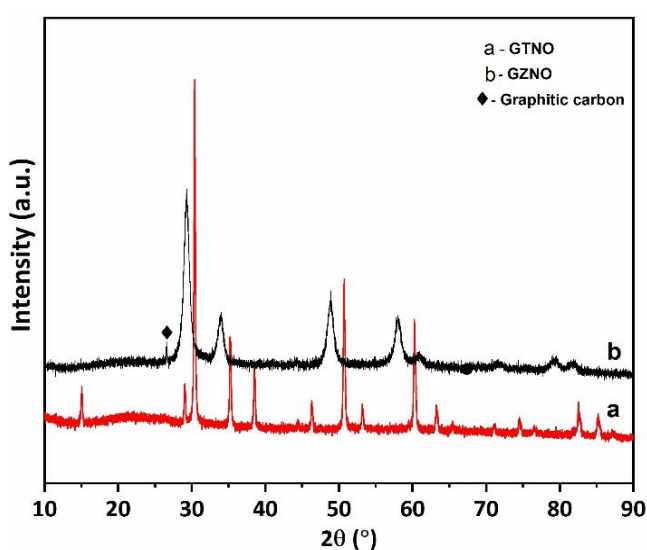
Figure 2.10: XRD pattern of spent GTNO and GZNO catalysts

2.5.2 Raman analysis of spent catalysts:

To further substantiate the presence of graphitic carbon, Raman analysis of spent GTNO and GZNO catalysts was done figure 2.11. Raman spectrum of the GZNO catalyst showed bands at around 1350 cm^{-1} and shoulder peak at 1615 cm^{-1} corresponding to D and G bands of disordered graphitic carbonaceous species. In GTNO catalyst the absence of D and G band confirms the negligible amount of carbon formation on GTNO catalyst [35].
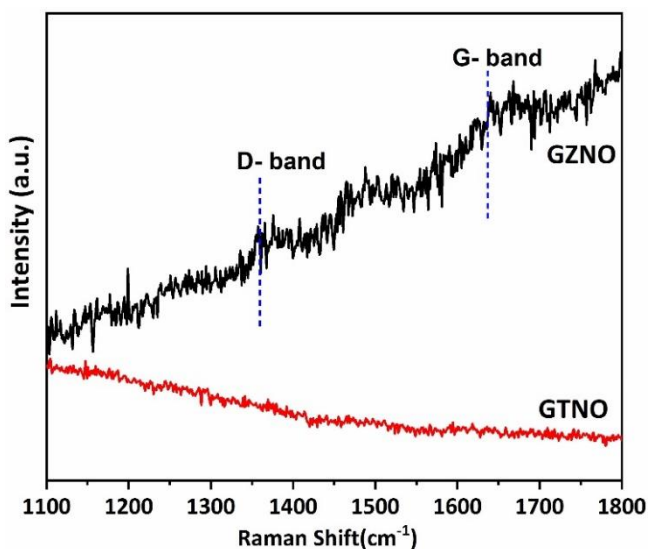
Figure 2.11: Raman analysis of spent GTNO and GZNO catalysts

2.5.3 Thermogravimetric analysis of spent catalysts:

For the estimation of the amount of carbon formed during the dry reforming of methane reaction, thermogravimetric analysis was also done on the spent catalysts. The experiment was carried out under air and oxidized carbon was calculated in moles per gm of catalyst (Figure 2.12). It has been observed that the GZNO showed more coke formation in comparison with GTNO.
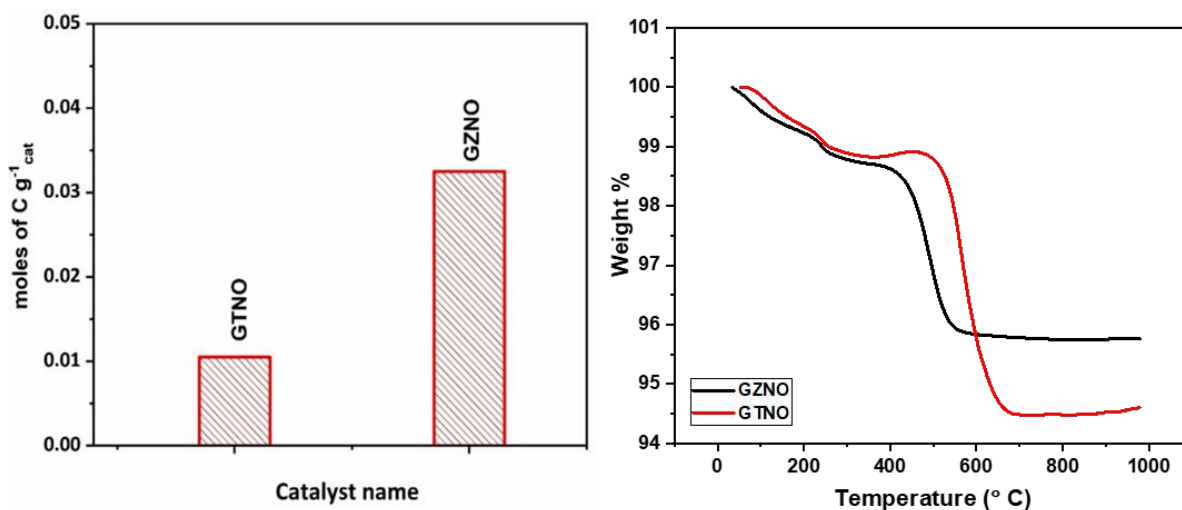
Figure 2.12: TGA analysis of spent GTNO and GZNO catalysts after 100 h of DRM reaction. Moles of carbon formation are plotted per gram of catalyst

2.6. Conclusion:

The Gd based Ni substituted ternary metal Ti and Zr oxide catalysts have been synthesized and tested for dry reforming of methane. The XRD analysis and refinement studies confirm the incorporation of Ni in the lattice as well as presence of reducible NiO over the surface resulting in enhanced activity of the Ti based Ni substituted catalyst. Temperature programmed reduction confirms that the reducibility of this catalyst is more than the Zr analogue, which substantiates the presence of well dispersed NiO particles over the surface and presence of stable active metal ions in the bulk. Strong basicity of GTNO catalyst also results in the promotion of CO_2 adsorption and activation than in GZNO catalyst towards DRM. This is corroborated by in situ IR studies which prove more reductive adsorption and desorption of CO_2 as CO on GTNO. Presence of loosely bound surface oxygen and hydroxyl oxygen species in GTNO catalyst may also be helpful in activation of CO_2 as well as simultaneous coke gasification on the GTNO catalyst surface. Amount of carbon formed in dry reforming of methane is less in GTNO than GZNO catalyst and absence of graphitic carbon shows the simultaneous removal of coke from the surface of GTNO catalyst and availability of active sites for DRM. This study unveils the influence of reducibility, basic strength of support and formation of defect modified oxygen as well as hydroxyl species for the superior and stable activity of GTNO catalyst towards dry reforming of methane.

Part 2
Effect of active metal concentration in Defect fluorite catalyst ($A_2B_{2-x}Ni_xO_{7-\delta}$ A = Gd, B = Zr, X = 0.2,0.5,0.75) in DRM

2.7 Introduction:

The previous part of this chapter studied the effect of support and B site substitution in $Gd_2B_{2-x}Ni_xO_{7-\delta}$ (B = Zr, Ti) (x = 0 and 0.2) catalyst. Ti-based GTNO catalyst has shown superior activity and stability toward the Dry reforming of methane[36]. Support has a crucial role in catalytic behavior in different reforming reactions. There are several reports are available in which the effect of different supports like CeO_2, ZrO_2, TiO_2, Al_2O_3, and MgO has been checked for Dry reforming of methane. Especially, ZrO_2 has enormously been utilized in various reforming reactions due to its thermal stability, acid-base functionality, and strong metal support properties with Ni in the Dry reforming of methane documented in several reports[37][38][39][40][41][42][43]. In structurally ordered catalysts like perovskites, spinals, and pyrochlores Zr is screened in A and B sites of catalysts and proven to be good candidates for reforming reactions with less coke formation. Several perovskite-based structures with Zr in the lattice have been checked with enhanced activity and durability in Dry reforming of methane[44][45][46][47]. Spivey and Coworkers have developed and screened Zr-based pyrochlore catalysts in Dry reforming of methane. Moreover, the substitution of noble metals with Zr in the B site of the pyrochlore catalysts was also studied in Dry reforming of methane[48][49][50]. Furthermore, literature reports exist to indicate that the concentration of Ni in various catalytic systems has an effect on the DRM activity [51][52][53][54]. However, our study found that Zr based Ni substituted $Gd_2Zr_2O_7$ catalyst showed lower activity in DRM. Since there are several factors affecting the catalytic activity like metal to support interaction, the quantity of active metal, the morphology of active metal, and the synergetic effect of active metal with support. One of them is, active metal concentrations which have an enormous effect on the catalytic activity in different reforming reactions. To consider this, we decided to find out the scope for Zr-based $Gd_2Zr_2O_7$ catalyst's lower activity. Hence, this part of the chapter deals with the study of the effect of Ni concentration in $Gd_2Zr_2O_7$ catalyst in Dry reforming of methane.

2.8 Experimental Section:

2.8.1 Synthesis of Gd$_2$Zr$_{2-x}$Ni$_x$O$_{7-\delta}$ (0.2, 0.5, 0.75):

Gd$_2$Zr$_{2-x}$Ni$_x$O$_{7-\delta}$ (0.2, 0.5, 0.75) catalysts were synthesized by conventional citrate gel method. Metal nitrate precursors were dissolved in a minimum amount of distilled water separately, mixed together, and then added to the citric acid solution with a ratio of 3:1 (citric acid: nitrate precursors) under constant stirring at 80 °C. For Gd Gd$_2$O$_3$ was dissolved in conc. HNO3 before mixing with citric acid. The Ni wt. % 1.96, 4.95, and 7.53 was added to the reaction mixture and Ethylene glycol was added to the solution as a polymerizing agent with a molar ratio of 1:1 (EG: CA). The formed gel was dried overnight at 180 °C to promote polyesterification and removal of water. The obtained fluffy material was crushed and calcined at 800 °C for 6 h in the air to get the ternary metal oxides. The added Ni wt. % 1.96, 4.95,7.53 substituted catalysts were denoted as GZN2, GZN5, and GZN75 respectively.

2.9 Result and discussion:

2.9.1 XRD Analysis and textural properties of Gd$_2$Zr$_{2-x}$Ni$_x$O$_{7-\delta}$ (0.2, 0.5, 0.75)
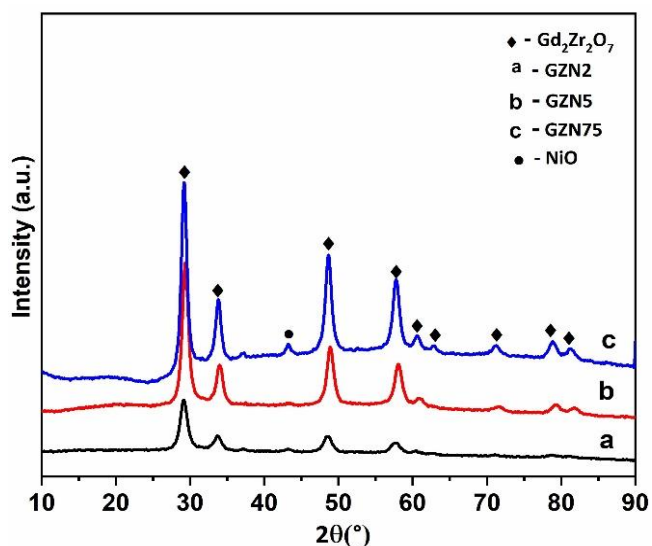
Figure 2.13: XRD pattern of GZN2, GZN5 and GZN75 catalysts

Table 2.1: Rietveld refinement data of $Gd_2Zr_{2-x}Ni_xO_{7-\delta}$ (0.2, 0.5, 0.75)

	$Gd_2Zr_2O_7$	$Gd_2Zr_{1.8}Ni_{0.13}O_{7-\delta}$	$Gd_2Zr_{1.5}Ni_{0.5}O_{7-\delta}$	$Gd_2Zr_{1.25}Ni_{0.75}O_{7-\delta}$
$\chi 2^*$	3.09	2.32	2.08	1.733
wRp (%)**	4.91	3.77	6.40	8.72
Rp (%) **	3.67	2.99	5.18	7.02
Space group	$Fm\overline{3}m$	$Fm\overline{3}m$	$Fd\overline{3}m$	$Fd\overline{3}m$
a/°A	5.3008	5.2678	5.2934	5.3067
Occupancy	Zr= 0.5000	Zr = 0.4500	0.3750	0.3127
		Ni = 0.0322	0.1250	0.1875
Impurity phase (wt%)		NiO = 0.68	2.42	2.38
Crystallite Size (nm)	54.1	33.1	31	28
Surface area(m2/g)	11.1	12.2	10	14

* $\chi^2 = \frac{M}{N_{obs}-N_{var}}$ where M is the minimized function during refinement, Nobs is the number of observed intensities and Nvar is the number of refined variables. **Rp and wRp are the residual parameters defined as $R_p = \frac{\Sigma|Io-Ic|}{\Sigma Io}$ and $wR_p == \sqrt{\frac{Mp}{\Sigma wIo^2}}$, where Mp is the minimization powder diffraction function, IO and IC are observed and calculated intensities.
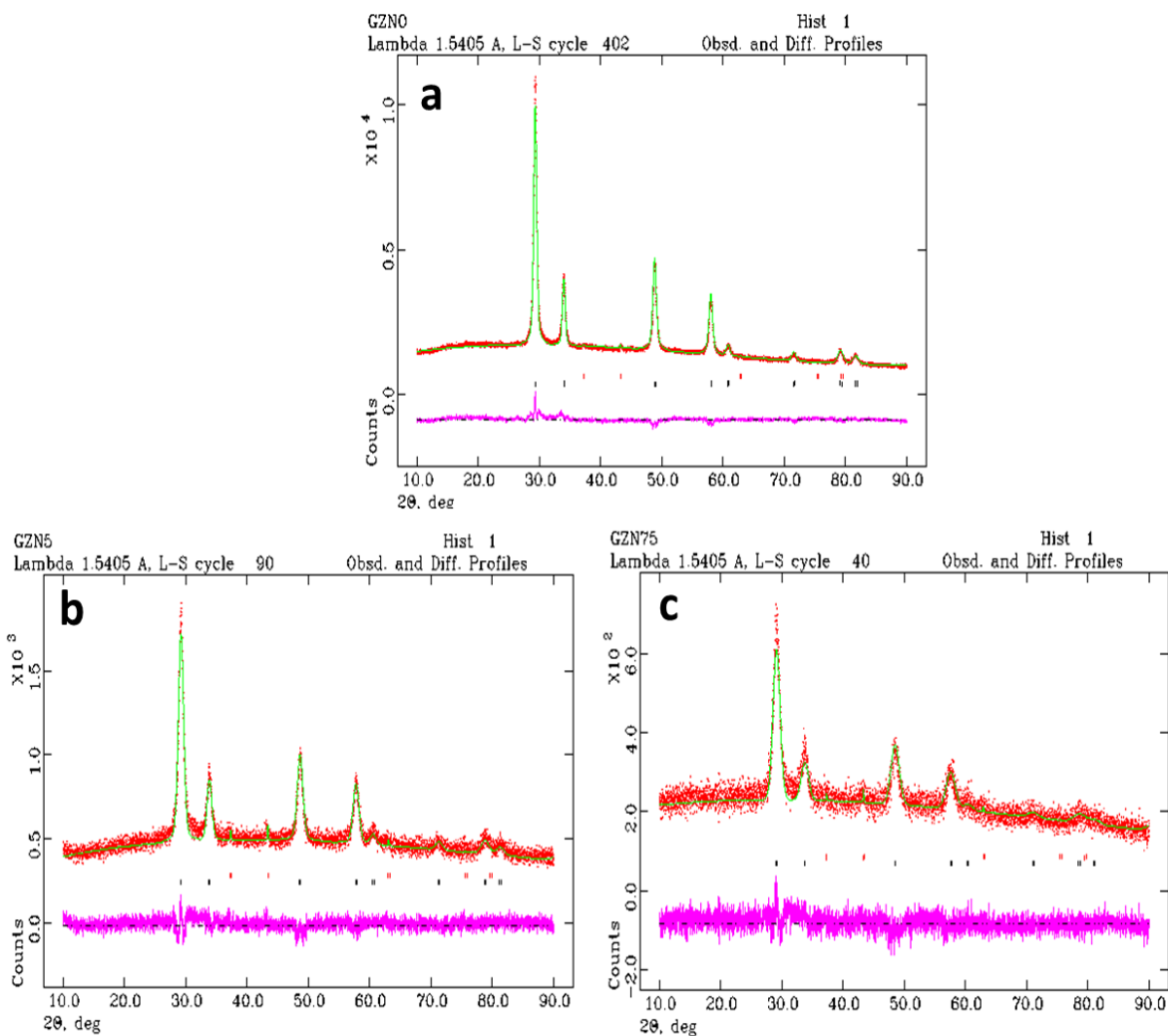
Figure 2.14: Rietveld Refinement profile a) GZNO, b) GZN5, and c) GZN75

Table 2.2: Atomic parameters of $Gd_2Zr_{2-x}Ni_xO_{7-\delta}$ (0.2, 0.5, 0.75)

Catalyst Name	X	Y	z
$Gd_2Zr_2O_{7-\delta}$			
Gd	0.0	0.0	0.0
Zr	0.0	0.0	0.0
O	0.25	0.25	0.25
$Gd_2Zr_{1.8}Ni_{0.13}O_{7-\delta}$			
Gd	0.0	0.0	0.0
Zr	0.0	0.0	0.0
O	0.25	0.25	0.25
Ni	0.0	0.0	0.0
$Gd_2Zr_{1.5}Ni_{0.5}O_{7-\delta}$			
Gd	0.0	0.0	0.0
Zr	0.0	0.0	0.0
O	0.25	0.25	0.25

Ni	0.0	0.0	0.0
$Gd_2Zr_{1.25}Ni_{0.75}O_{7-\delta}$			
Gd	0.0	0.0	0.0
Zr	0.0	0.0	0.0
O	0.25	0.25	0.25
Ni	0.0	0.0	0.0

Figure 2.13 illustrates the XRD pattern of Ni-substituted GZO catalysts named GZN2, GZN5, and GZN75. All three catalysts crystalized in defect fluorite structure with Fm$\overline{3}$m space group. Apart from $Gd_2Zr_2O_7$ phase peaks, a peak corresponding to NiO was observed at 43.2 ° 2θ position. It can be clearly observed that the intensity of NiO is slightly higher in GZN5 and GZN75 catalysts than in GZN2 catalyst. To confirm the structure and quantify the NiO phase Rietveld analysis of all three catalysts was carried out by GSAS software with a standard $Gd_2Zr_2O_7$ model having ICSD collection code 068265[19]. The percentage of surface NiO is higher in GZN75 and GZN5 catalysts than in GZN2 catalyst. Refined profiles and parameters are given in figure 2.14 (a-c) and Table 2.1 respectively. Atomic parameters are given in Table 2.2 With an increased amount of Ni in the parent GZO catalyst, an increase in the surface area was also observed. Moreover, crystallite size for GZN75 catalysts is lower than the other two catalysts which may be responsible for the high surface area of the catalyst.

2.9.2 Raman Analysis of $Gd_2Zr_{2-x}Ni_xO_{7-\delta}$ (0.2, 0.5, 0.75):

Raman analysis of Ni-substituted catalysts has been performed for understanding the structural modifications in substituted catalysts. Figure 2.15 showed the vibrational modes at around 321, 480, 600, and 980 cm-1 confirming the defect fluorite structure[55]. It has been reported that high-temperature treatment initiates the transformation of defect fluorite structure to pyrochlore structure and vice versa but in all Ni substituted catalysts the broadness of peaks sintered at 800 °C temperature confirmed the defect fluorite structure which is corroborated by XRD and Rietveld analysis.
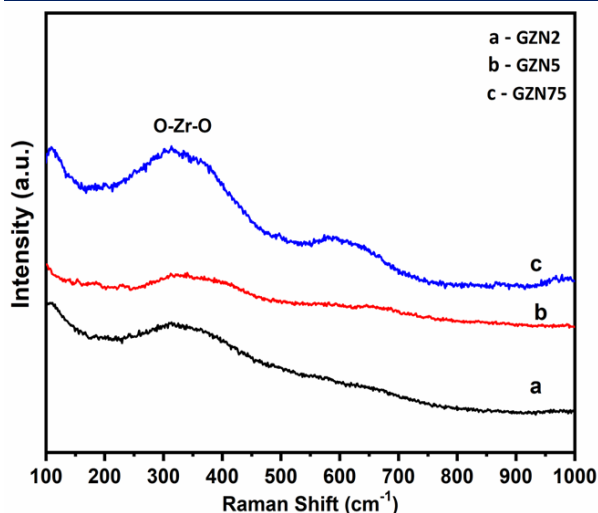
Figure 2.15: Raman analysis of GZN2, GZN5 and GZN75 catalysts

2.9.3 X-Ray photoelectron spectroscopy Analysis of $Gd_2Zr_{2-x}Ni_xO_{7-\delta}$ (0.2, 0.5, 0.75):

To understand the surface environment and oxidation states of metals of all substituted catalysts XPS analysis was employed. In all substituted catalysts oxidation state of Zr is +4 shown in figure 2.16[56] O 1s spectrum of all three catalysts illustrates the presence of three peaks at around 525 eV, 529 eV, and 534 eV corresponding to lattice oxygen, and oxygen of chemisorbed water respectively. Apart from that the peak rendered to the surface hydroxyl species related to defects in the lattice start appearing at 532.2 eV in GZN5 and GZN75 catalysts which are not observed in GZN2 catalyst. The increased amount of Ni in the B site of the parent catalyst initiated the formation of defects in the lattice and the generation of active oxygen and hydroxyl species over the catalyst's surface[57].
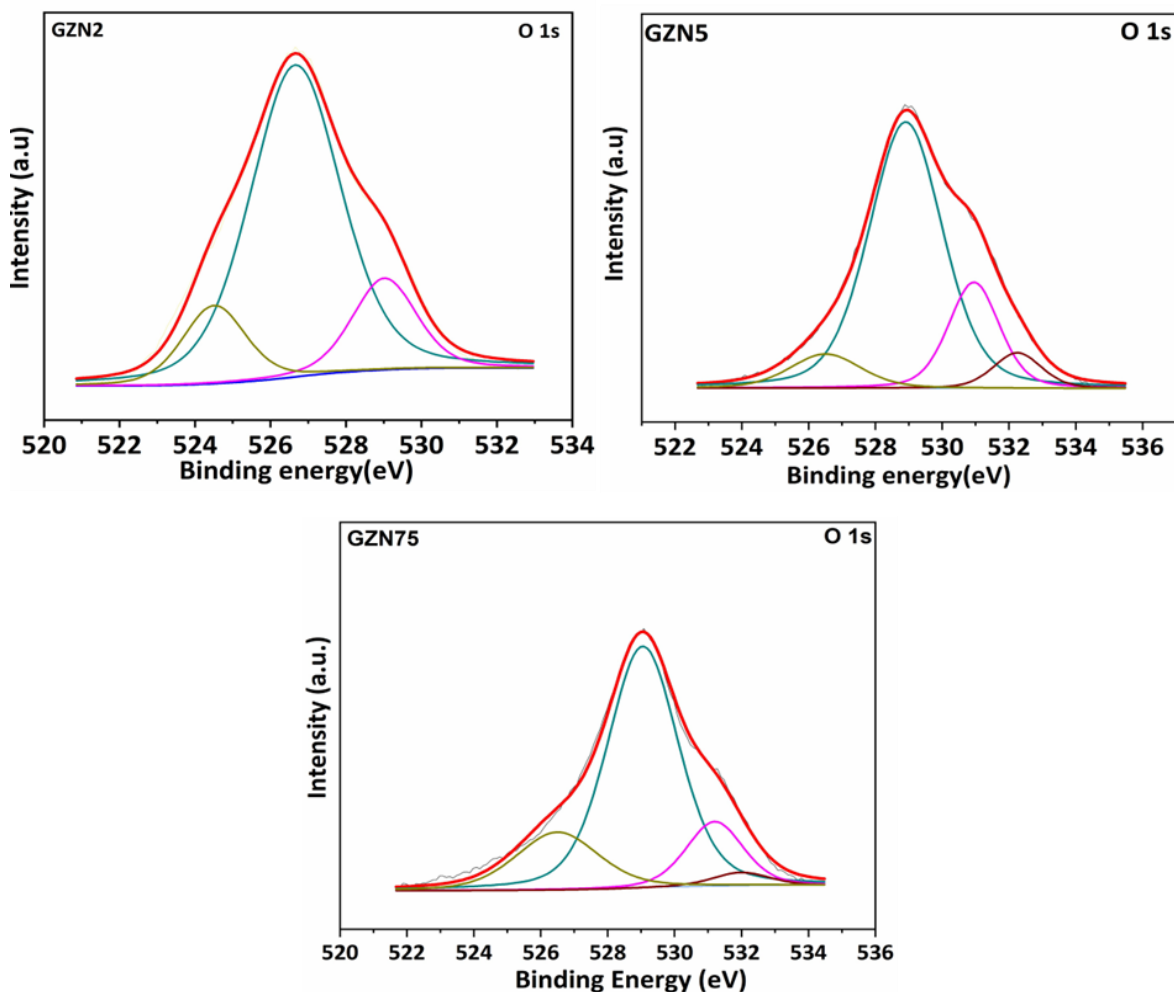
Figure 2.16:   XPS profiles of O1s spectrum of GZN2, GZN5 and GZN75 catalysts

2.9.4 CO$_2$- TPD analysis of Gd$_2$Zr$_{2-x}$Ni$_x$O$_{7-\delta}$ (0.2, 0.5, 0.75):

To activate the CO$_2$ adsorption and desorption as CO, the surface basicity plays a crucial role in Dry reforming reaction. Catalysts with high basic sites on the support enhance the CO$_2$ activation and provide oxygen spillover which initiates the coke gasification over the surface of the catalyst. To illustrate the basic sites of all Ni substituted catalysts CO$_2$ - TPD has been performed. It can be observed in figure 2.17 that in GZN2 catalyst only weak basic sites are present while in GZN5 and GZN75 catalysts along with weak basic sites, medium and strong basic sites are also observed. So higher amount of Ni in the systems alters the basicity of the catalyst which can provide high CO$_2$ activation on the metal support sites with enhanced catalytic activity[58].
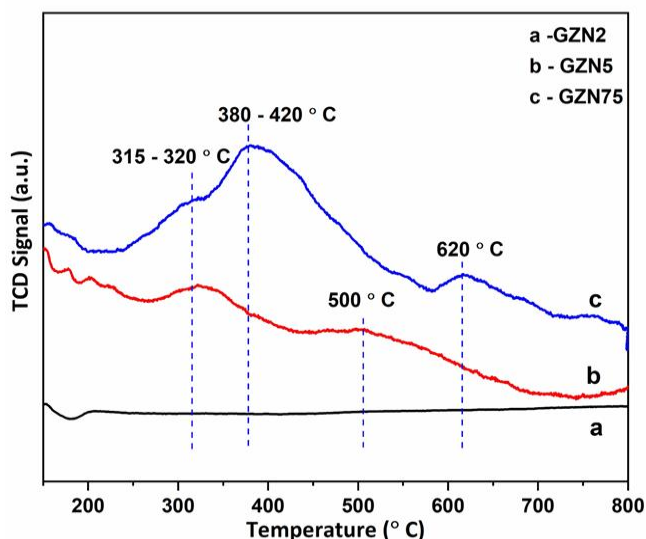
Figure 2.17: CO_2-TPD analysis of GZN2, GZN5 and GZN75 catalysts

2.10 Catalytic activity of $Gd_2Zr_{2-x}Ni_xO_{7-\delta}$ (0.2, 0.5, 0.75):

After characterizing all Ni substituted catalysts with different analytical techniques, they all checked for Dry reforming of methane at 800 °C. It is illustrated in figure 2.18 that initial hours of DRM stream, the conversions were low may be due to the dominance of side reactions. However, after 6-7 h the conversions of CH_4 and CO_2 started increasing and have been checked for 100 h time on stream. The GZN75 catalyst showed superior activity towards Dry reforming of methane with 82 % of CH_4 and 91% of CO_2 with a 0.95 H_2/CO ratio. In other two catalysts, the conversions and H_2/CO ratio are lower. A higher amount of Ni over the surface and the presence of Ni in the lattice increased the strong metal support interaction resulting in superior activity. Although, high Ni content provide enhanced methane activation and decomposition initiating carbon formation. To investigate the structure stability and carbon formation on catalyst after DRM run, all catalysts were analyzed by XRD and TGA analysis.
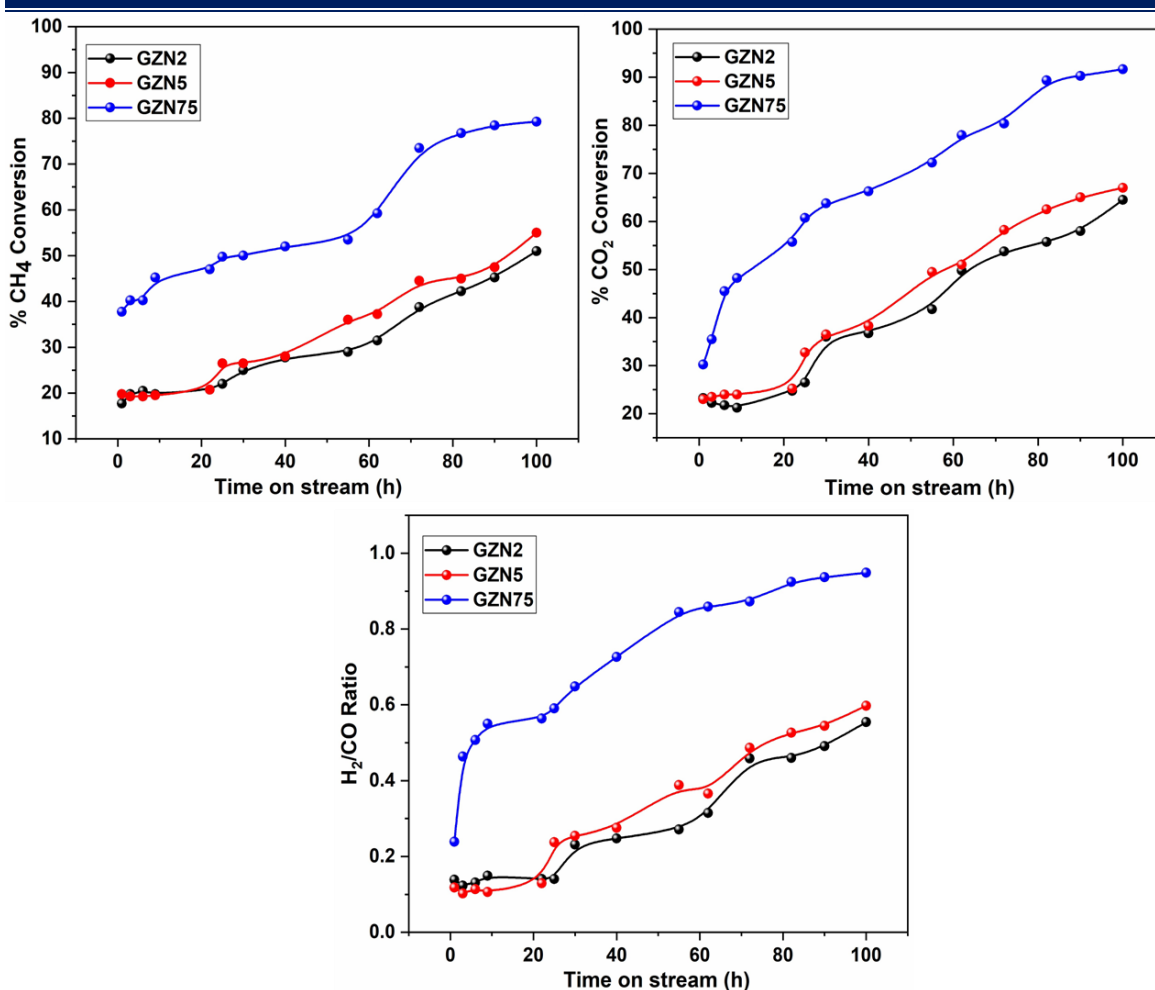
Figure 2.18: Activity analysis of GZN2, GZN5 and GZN75 catalysts in DRM conditions: CH_4: CO_2: N_2 = 80:80:80 mL/min, 28,800 h^{-1} GHSV at 800 °C for 100 h time on stream. Conversions and H_2/CO ratios are plotted against time on stream.

2.11 Spent Catalysts Characterization:

Spent catalysts screened for 100 h of Dry reforming reaction were examined by various techniques.

2.11.1 XRD analysis of spent catalysts:

XRD pattern of spent catalysts was displayed in figure 2.19. The data confirm the retention of parent catalyst after 100 h of reaction and the sharpness of all peaks also increased due to high crystallinity of catalysts. The NiO peak of GZN75 catalysts also got sharp due to the higher amount of Ni in and over the catalyst surface. The presence of carbon over the surface of the catalyst was confirmed by a peak at 26.4° at 2θ position corresponding to graphitic carbon[36]. The peak is more intense in GZN75 catalyst than the other two catalysts. This

may be due to a higher amount of surface NiO confirmed by H_2-TPR analysis prone to carbon formation by methane decomposition (3) and boudouard reactions (2). Quantitative analysis of formed carbon was done by TGA analysis.
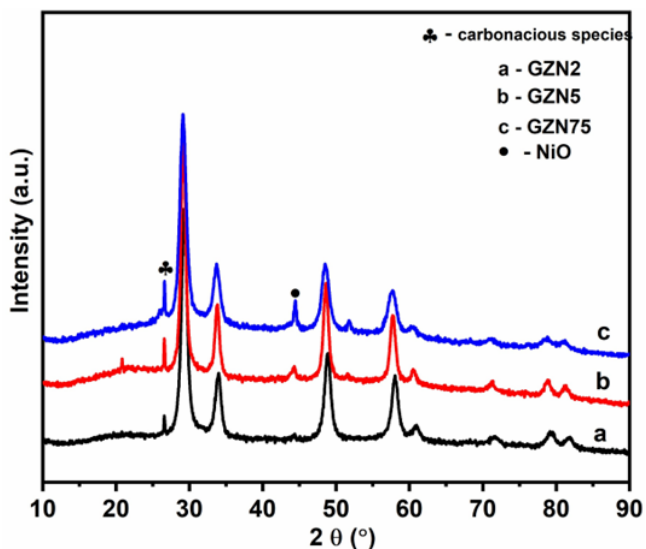
Figure 2.19: XRD pattern of spent GZN2, GZN5 and GZN75 catalysts

2.11.2 Thermogravimetric analysis of spent catalysts:

To estimate the quantity of formed carbon over the catalyst surface TGA analysis has been performed in air atmosphere. The results of TGA analysis shown in figure 2.20 depict the formed moles of carbon per gram of catalyst calculated by weight loss with a temperature range of 30-1000 °C in an air atmosphere. The moles of carbon in GZN75 catalyst are higher than GZN2 and GZN5 catalysts confirming the more carbon formation over the catalyst surface.
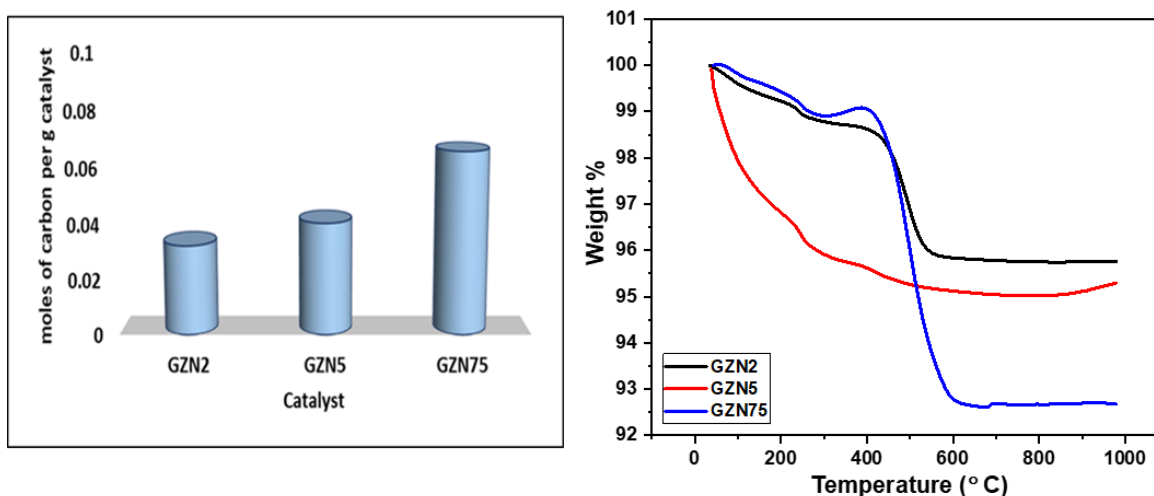
Figure 2.20: TGA Analysis of spent GZN2, GZN5 and GZN75 catalysts

2.12 Conclusions:

Part 2 demonstrates the effect of active metal Ni concentration in GZO catalyst in DRM activity. The commercial citrate gel method was employed to synthesize three catalysts with increased quantity of Ni that are GZN2, GZN5, and GZN75 and the structure was confirmed by XRD and Raman analysis. The retention of catalysts in defect fluorite structure and quantitative analysis of NiO was confirmed by Rietveld analysis. More amount of Ni helped in the creation of defects in the system resulting formation of surface hydroxyl species and enhanced basicity of the GZN75 catalyst was confirmed by XPS and CO_2 – TPD analysis respectively. Apart from that Higher Ni amount in GZN75 catalyst enhanced the conversions of CH_4 and CO_2 in DRM conditions for 100h. This study unveils the positive effect of Ni concentration in DRM activity but also influenced the coke formation over the catalyst surface. However, increased basic sites enhance the CO_2 activation but methane activation is also amplified with high Ni concentration. So, the balance between CO_2 activation with coke gasification and methane activation should be maintained during DRM, increased Ni initiates the defect formation resulting formation of active hydroxyl species on the catalysts surface improving the CO_2 activation and carbon gasification. Nevertheless, high Ni initiates

methane activation and decomposition resulting in more coke accumulation on the catalyst surface. Hence, this study unveils the importance of active metal concentration in maintaining equilibrium between on catalytic activity and coke gasification.

Part 3

Study of the influential effect of Ce substitution in $Gd_2Zr_{1.8}Ni_{0.2}O_{7-\delta}$ catalyst for Dry reforming of methane

2.13 Introduction:

Due to its affordability and availability, Ni-based catalysts have traditionally received significant attention in DRM [59]. However, at high reaction temperatures, Ni nanoparticles have a tendency to sinter, causing C to develop on the catalyst surface and a consequent loss of activity [60][61]. Strong metal support interactions that prevent the active metal from sintering at high reaction temperatures can play a significant role in minimizing coke production in this instance. Furthermore, the support's high surface area, oxygen spillover, oxygen storage capacity, and CO_2 activation produce surface active oxygen species, which help to gasify the carbon that forms on the catalyst surface during DRM [62][63][64][65]. To incorporate these features, different supports like CeO_2, ZrO_2, MgO, Al_2O_3, TiO_2, and La_2O_3 with supported Ni and bimetallic systems have been studied [66][67][68][69][70][71]. Catalyst stability and long-term activity in DRM also have been achieved by using various structurally ordered catalysts like perovskites, layered metal oxides, spinels, and pyrochlores [72][73][36][74][75][46][76][77]. However, a catalyst that activates the reforming cycles on metal surface as well as proficient in oxidizing the coke formed in reforming conditions is still a challenge. Here, the structured and supported mixed metal oxide catalysts with Ce have demonstrated promising abilities in carbon gasification in various reforming reactions with increased activity because of their oxygen storage capability and redox behavior [78][79][80]. We have reported that the Ni substituted $Gd_2Ti_2O_7$ catalyst has outstanding activity and stability correlated to $Gd_2Zr_2O_7$[36]. Because of their great thermal stability and acid-base activity, Zr-based structured oxide catalysts are promising candidates for reforming processes They are, nevertheless, susceptible to C deposition under dry reforming conditions [36]. Hence, the substitution of Ce in B site can be envisaged to mitigate the coke deposition owing to its redox property by generating oxygen species which can gasify the

carbon and provide prolonged activity. In this work, our strategy is to synthesize structured ternary oxide $Gd_2Zr_2O_{7-\delta}$ catalyst with Ni and Ce substituted in B site giving the series $Gd_2Zr_{1.8-x}Ni_{0.2}Ce_xO_{7-\delta}$ (x = 0.1, 0.2,0.50.75) and to examine the influence of Ce in DRM reaction.

2.14 Experimental Section:

2.14.1 Synthesis of $Gd_2Zr_{1.8-x}Ni_{0.2}Ce_xO_{7-\delta}$ (x = 0.1, 0.2,0.50.75):

The traditional Pechini method was used to synthesize all structural catalysts $Gd_2Zr_{1.8-x}Ni_{0.2}Ce_xO_{7-\delta}$ (x = 0.1, 0.2,0.50.75) named as GZN2C1, GZN2C2, GZN2C5, and GZN2C75. Stoichiometric amounts of metal nitrate precursors were dissolved in distilled water separately, combined, and then added to citric acid solution in a 3:1 (citric acid: nitrate precursors) ratio under steady stirring at 80 °C. In a molar ratio of 1:1 (EG:CA), ethylene glycol was added to the solution as a polymerizing agent. To improve polyesterification and water elimination, the gel was dried overnight at 180 °C. The fluffy material was crushed and calcined in air for 6 hours at 800 °C to produce the ternary metal oxides. Gd_2O_3 was dissolved in conc. HNO_3 before being mixed with citric acid. The added weight % of Ni and Ce is tabulated in Table 2.3.

Table 2.3: Catalysts composition of $Gd_2Zr_{1.8-x}Ni_{0.2}Ce_xO_{7-\delta}$ (x = 0.1, 0.2,0.50.75) catalysts

Catalyst Name	Ni wt% added	Ce wt% added
$Gd_2Zr_{1.8}Ni_{0.2}O_7$(GZN2)	1.94	-
$Gd_2Zr_{1.7}Ni_{0.2}Ce_{0.1}O_7$(GZN2C1)	1.94	2.27
$Gd_2Zr_{1.6}Ni_{0.2}Ce_{0.2}O_7$(GZN2C2)	1.94	4.56
$Gd_2Zr_{1.3}Ni_{0.2}Ce_{0.5}O_7$(GZN2C5)	1.94	11.25
$Gd_2Zr_{1.05}Ni_{0.2}Ce_{0.75}O_7$(GZN2C75)	1.94	16.44

2.15 Result and discussion:

2.15.1 X-Ray Diffraction Analysis and textural properties of $Gd_2Zr_{1.8-x}Ni_{0.2}Ce_xO_{7-\delta}$ (x = 0.1, 0.2,0.50.75):

The reported parent compound has Ni inserted in the lattice of $Gd_2Zr_2O_7$ catalyst at Zr site. Our objective was to substitute Ce in $Gd_2Zr_2O_7$ catalyst along with same concentration of Ni in Zr site and examine the synergistic effect of Ce and Ni providing stable structure and improved activity towards DRM [36].
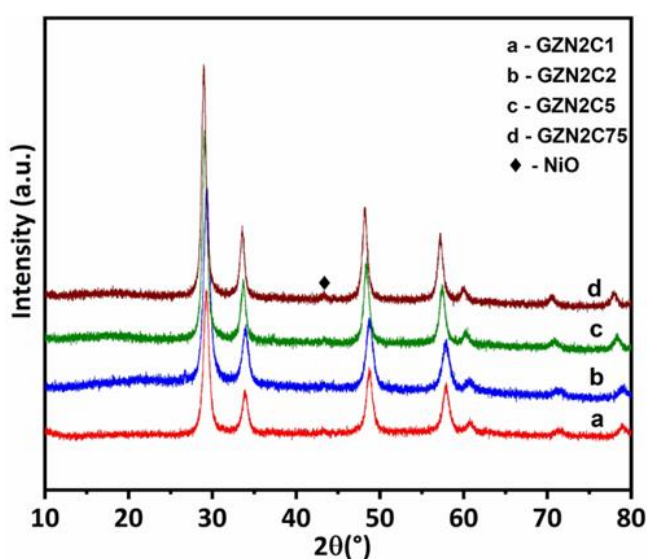
Figure 2.21. XRD patterns of GZN2C1 (a), GZN2C2 (b), GZN2C5 (c), and GZN2C75 (d), with the peak corresponding to NiO denoted by the sign (♦).

PXRD analysis is used to investigate the structural properties of Ce substituted Gd2Zr1.8-xNi0.2CexO7-δ, GZN2C1, GZN2C2, GZN2C5, and GZN2C75 catalysts (Figure 1). All catalysts crystallized in defect fluorite structure with $Fm\overline{3}m$ space group, as shown by the pattern (PDF 01-080-0471)[36][81][82]. This is further supported by the absence of two peaks at $2\theta \approx 14°$ (1 1 1) and 37° (3 3 1) positions corresponding to pyrochlore structure[83]. Additionally, along with confirmation of $Gd_2Zr_2O_{7-\delta}$ phase, a small peak attributing to NiO is observed at 43.2° 2θ position[84]. It is evident that when Ce is substituted in the parent catalyst, no peaks conforming the CeO_2 phase are visible, indicating that Ce has been incorporated into the catalyst's lattice [85][86]. The Rietveld method and GSAS-EXPGUI

software were used to check the effect of doping with full pattern refinement [21]. The cell parameter for $Gd_2Zr_2O_{7-\delta}$ was refined to 5.3008 by using defect fluorite $Gd_2Zr_2O_{7-\delta}$ (ICSD collection code - 068265) as the model [87]. For Ni and Ce substituted catalysts, estimated stoichiometry of Ni and Ce was substituted in Zr site and cell parameters were refined. Table 2.4 summarizes the resultant revised cell parameters and textural features. Quantitative investigation verifies the existence of NiO phase on all catalyst surfaces. Table 2.5 estimates and tabulates the weight percent of Ni substituted inside the lattice as well as NiO present on the surface of catalyst. For each catalyst, the refined fitted patterns are shown in figure 2.22 (A-D), and the resultant parameters are tabulated in Table 2.6. It is observed that as the Ce concentration increases, Ni concertation outside the lattice also increases except in GZN2C2 catalyst. Among all Ce substituted catalysts, GZN2C2 has more amount of Ni inside the lattice. Moreover, the Ce substitution in the lattice was further confirmed by observing the change in cell parameters and cell volume of Ce substituted catalysts. Due to the greater ionic radius of Ce4+, cell size and volume similarly increase with increasing Ce concentration as expected (Figure 2.23).

Table 2.4: Rietveld refinement data of GZN2C1, GZN2C2, GZN2C5 and GZN2C75 catalysts.

Formulae Space group	GZN2C1 Fm-3m	GZN2C2 Fm-3m	GZN2C5 Fm-3m	GZN2C75 Fm-3m
a/Å	5.2831(1)	5.3013(1)	5.3256(1)	5.3537(1)
Rp (%)	3.44	3.92	3.47	3.90
WRp (%)	4.29	4.92	4.37	4.84
Chi^2	1.10	1.62	1.08	1.28
Surface Area (m^2/g)	14.02	15.50	17.58	17.00
Crystallite Size (nm)	22.61	23.16	26.84	39.61
Cell volume	147.4	148.9	151.0	153.4
NiO impurity phase, (wt%)	1.40	1.23	1.70	2.44

* $\chi^2 = \frac{M}{N_{obs}-N_{var}}$, where M is the function that was minimised during refinement, Nobs is

the number of observed intensities, and Nvar is the number of refined variables. **Rp and wRp are residual parameters defined as $R_p = \frac{\Sigma|Io-Ic|}{\Sigma Io}$ and $wR_p == \sqrt{\frac{Mp}{\Sigma wIo^2}}$, where Mp is the powder diffraction function minimization function and IO and IC are observed and computed intensities.
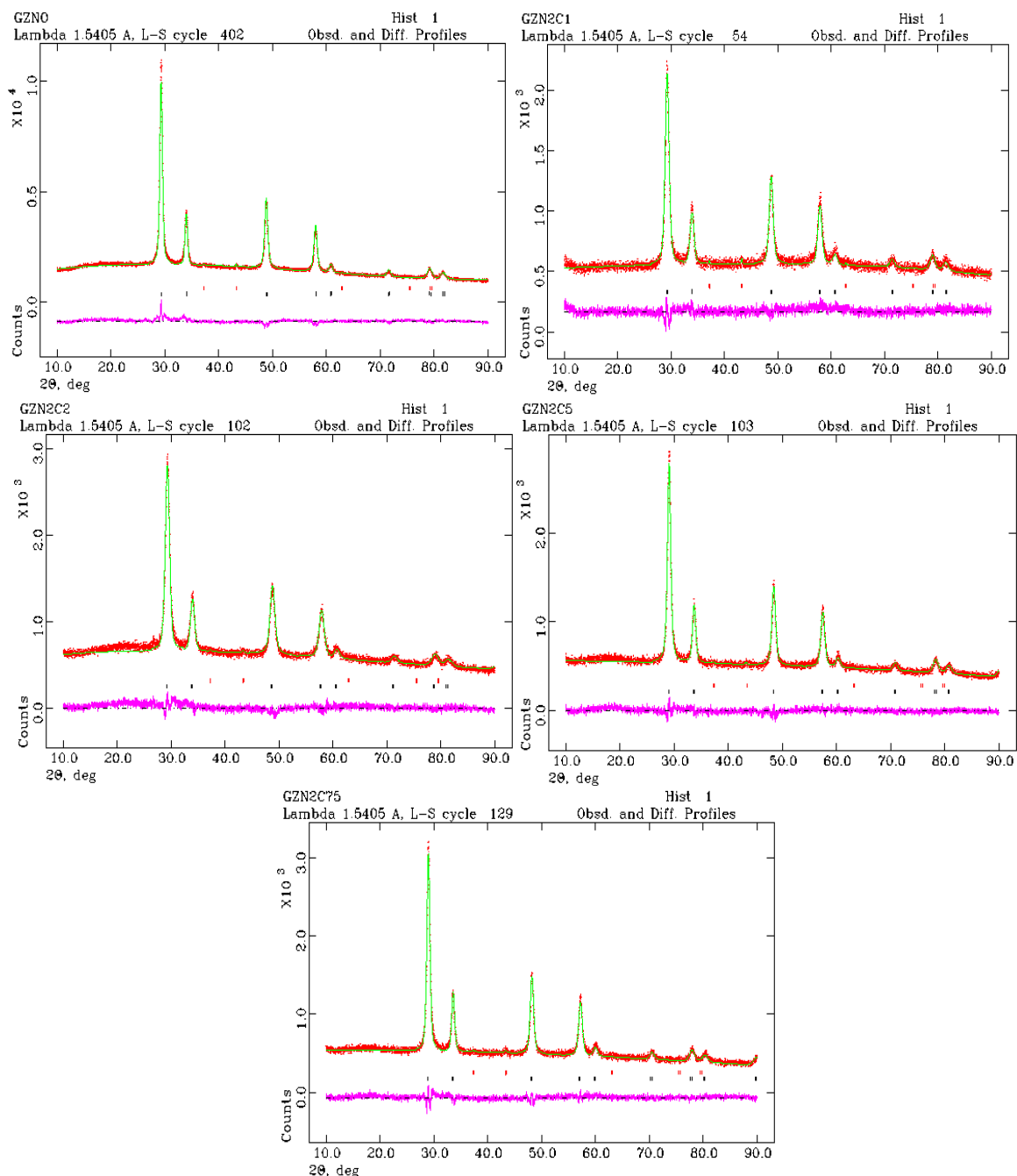
Figure 2.22: Rietveld Refinement profile of GZN2, GZN2C1, GZN2C2, GZN2C5 and GZN2C75 (A-E)

Table 2.5: Quantitative analysis of Ni wt.% obtained from NiO impurity phase by Rietveld refinement analysis.

Catalyst Name	Ni wt% added	Ni wt.% (outside the lattice)	Ni wt.% (inside the lattice)	Ce wt% added
GZN2C1	1.94	1.10	0.84	2.27
GZN2C2	1.94	0.96	0.98	4.56
GZN2C5	1.94	1.33	0.61	11.25
GZN2C75	1.94	1.91	0.03	16.44
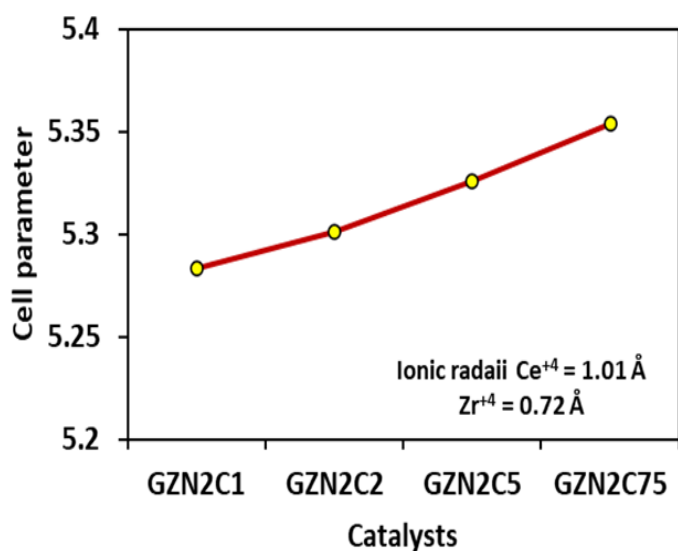
Figure 2.23: Plot of catalysts against cell parameter.

Table 2.6: Atomic parameters of refined $Gd_2Zr_{1.8-x}Ni_{0.2}Ce_xO_{7-\delta}$ (x = 0.1, 0.2,0.50.75) catalysts.

Catalyst Name	X	Y	z
GZN2			
Gd	0.0	0.0	0.0
Zr	0.0	0.0	0.0
O	0.25	0.25	0.25
GZN2C1			
Gd	0.0	0.0	0.0
Zr	0.0	0.0	0.0
O	0.25	0.25	0.25
Ni	0.0	0.0	0.0

Ce	0.0	0.0	0.0
GZN2C2			
Gd	0.0	0.0	0.0
Zr	0.0	0.0	0.0
O	0.25	0.25	0.25
Ni	0.0	0.0	0.0
Ce	0.0	0.0	0.0
GZN2C5			
Gd	0.0	0.0	0.0
Zr	0.0	0.0	0.0
O	0.25	0.25	0.25
Ni	0.0	0.0	0.0
Ce	0.0	0.0	0.0
GZN2C75			
Gd	0.0	0.0	0.0
Zr	0.0	0.0	0.0
O	0.25	0.25	0.25
Ni	0.0	0.0	0.0
Ce	0.0	0.0	0.0

2.15.3 SEM Analysis of $Gd_2Zr_{1.8-x}Ni_{0.2}Ce_xO_{7-\delta}$ (x = 0.1, 0.2,0.50.75):

SEM-EDAX analysis was additionally employed to examine the surface morphology and composition (Figure 2.24 (A-D)). Layers of flakes are seen to be agglomerated in SEM profiles, and the surface composition detected by EDAX agrees with the estimated stoichiometry of the catalysts tabulated in table 2.7. EDAX profile were showed in Figure 2.25.
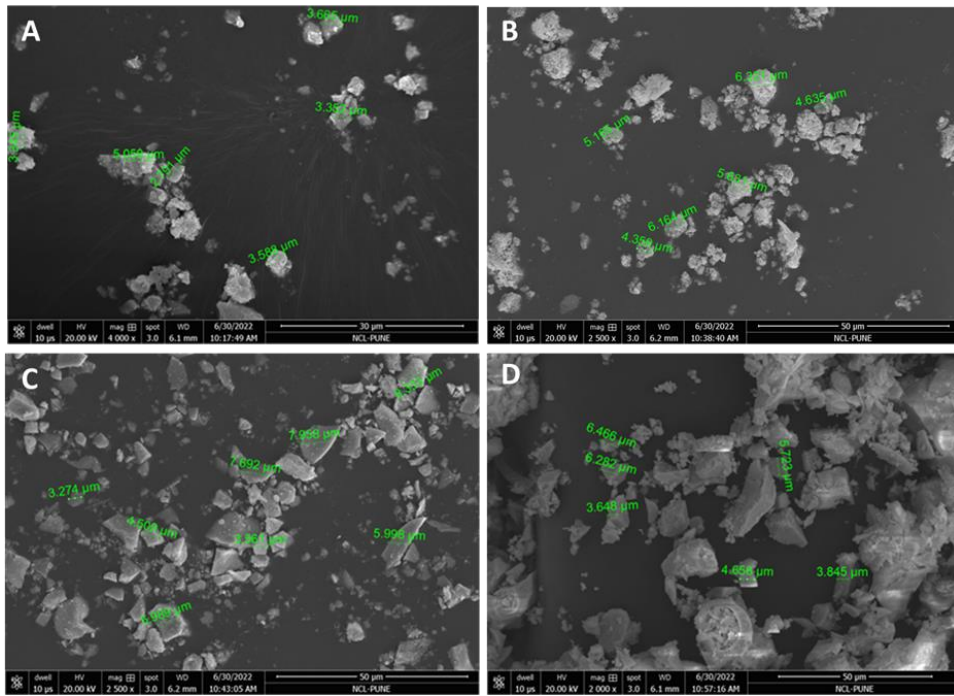
Figure 2.24: SEM images of A) GZN2C1 B) GZN2C2 C) GZN2C5 and D) GZN2C75 catalysts.
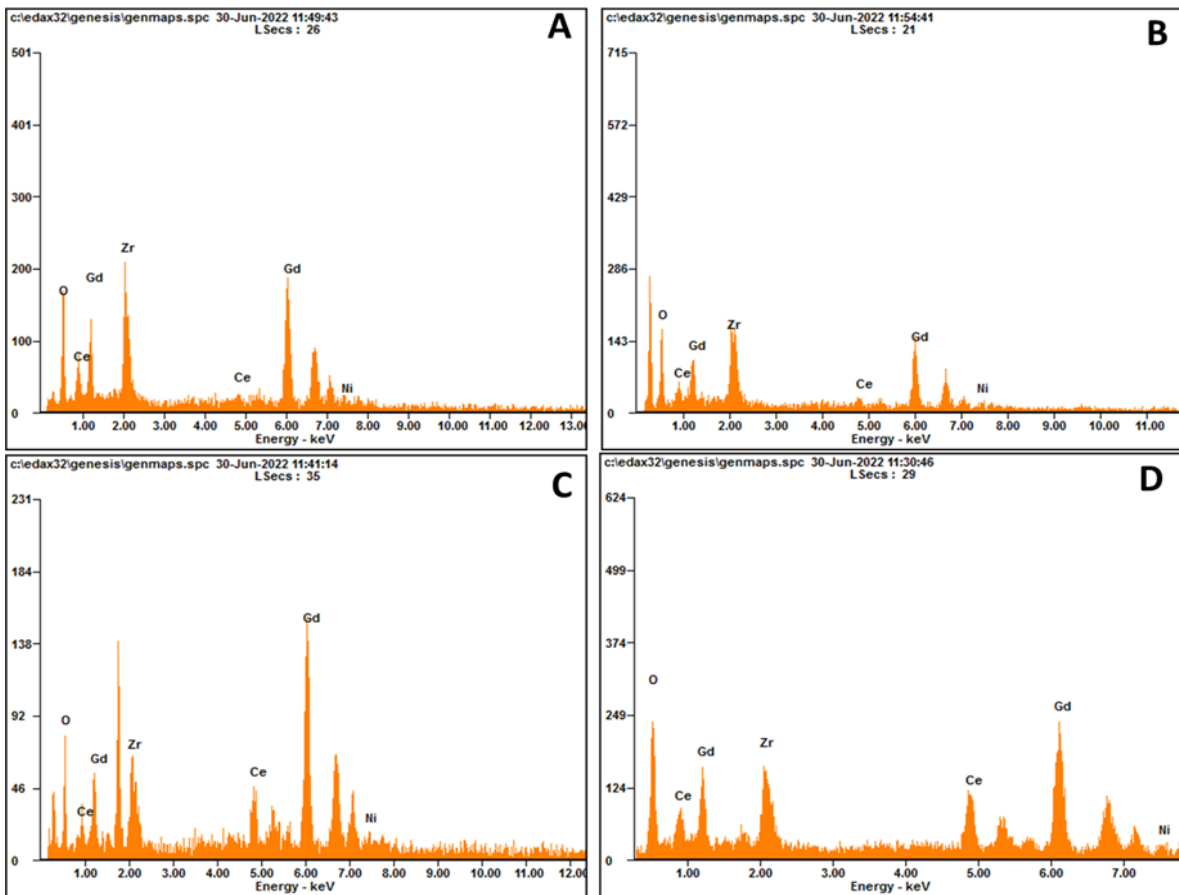
Figure 2.25: EDAX profile of A) GZN2C1 B) GZN2C2 C) GZN2C5 and D) GZN2C75 catalysts.

Table 2.7: EDAX data of A) GZN2C1 B) GZN2C2 C) GZN2C5 and D) GZN2C75 catalysts.

Catalyst	Element	Observed	calculated
GZN2C1	Gd	44.47	52.07
	Zr	25.90	25.69
	Ni	1.87	1.94
	Ce	2.93	2.28
	O	24.83	17.88
GZN2C2	Gd	46.39	51.61
	Zr	24.13	23.95
	Ni	1.81	1.94
	Ce	3.87	4.56
	O	23.80	17.74
GZN2C5	Gd	56.91	50.30
	Zr	14.1	18.98
	Ni	1.89	1.94
	Ce	11.0	11.25
	O	14.79	17.35
GZN2C75	Gd	51.92	49.98
	Zr	12.40	15.04
	Ni	1.79	1.94
	Ce	15.81	16.44
	O	18.08	17.09

2.15.4 Raman Analysis of $Gd_2Zr_{1.8-x}Ni_{0.2}Ce_xO_{7-\delta}$ (x = 0.1,0.2,0.5,0.75):

To understand the structural changes in molecular level by substitution of Ce in parent catalyst, Raman analysis of all the catalysts was performed. It is known that $Gd_2Zr_2O_7$ catalyst with defect fluorite structure has very broad Raman modes at ~331- 400 cm^{-1} along with the absence of 6 active Raman modes (A_{1g} + E_g + $3F_{2g}$ and F_{2g}) corresponding to pyrochlore phase[55]. Figure 2.26 shows that the Raman modes in Ce substituted catalysts are very similar to those of the parent catalyst[36]. Apart from modes at around 331-400 cm^{-1}, broad Raman active bands at 560- 630 cm^{-1} are also observed. The broadening of the bands confirmed the defect fluorite structure for all catalysts[88], corroborated by the XRD analysis. Raman analysis confirms the structure stability of parent $Gd_2Zr_2O_{7-\delta}$ catalyst after

Ni and Ce substitution; doping of Ce can be further supported by absence of Raman mode corresponding to F_{2g} mode of CeO_2 phase at 464 cm^{-1}[89][90].
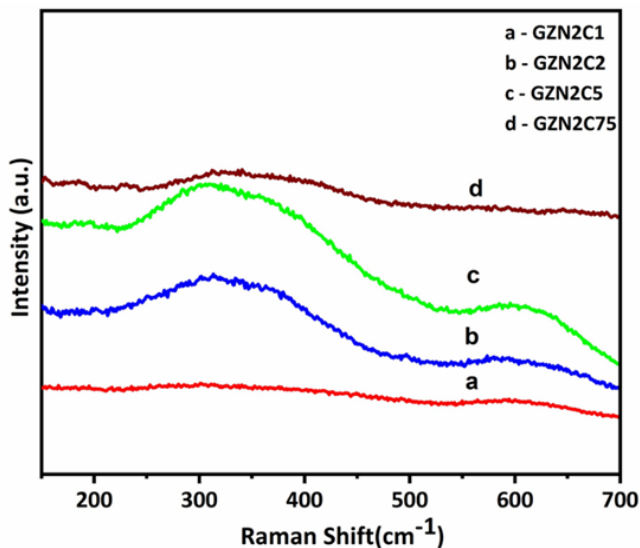
Figure 2.26: Raman spectra of a) GZN2 b) GZN2C1 c) GZN2C2 d) GZN2C5 and e) GZN2C75

2.15.4 H$_2$-Temperature programmed Analysis of Gd$_2$Zr$_{1.8-x}$Ni$_{0.2}$Ce$_x$O$_{7-\delta}$ (x = 0.1,0.2,0.5,0.75):

The TPR approach was employed to investigate the reducibility of Ce substituted catalysts. Ce substitution seems to enhance the reducibility of the catalysts in comparison to the parent compound; The shift of peaks towards lower temperatures reflects the influence of Ce substitution in the Zr site, as it supports the reduction of Ni species in catalysts. The reduction peaks in Ce substituted catalysts in the 420-520 °C range are due to NiO reduction, strongly contacted with the support. The reduction peak at 640 °C is because of lag in the reduction of Ce^{+4} to Ce^{+3}[91][92].
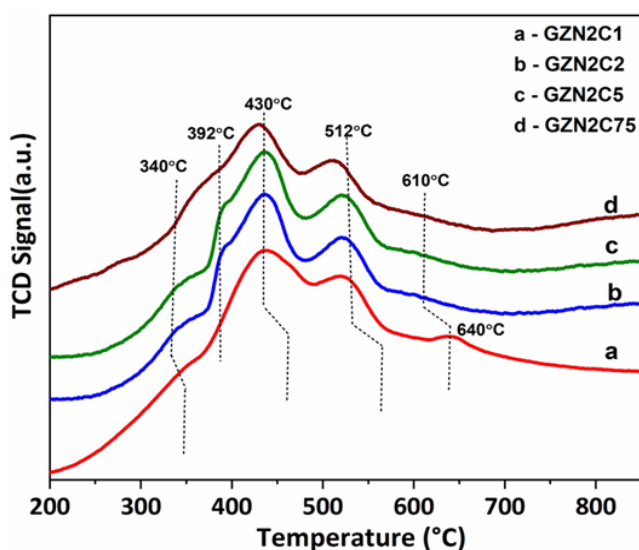
Figure 2.27: TPR analysis of a) GZN2 b) GZN2C1 c) GZN2C2 d) GZN2C5 and e) GZN2C75

2.15.5 X-Ray photoelectron spectroscopy Analysis of $Gd_2Zr_{1.8-x}Ni_{0.2}Ce_xO_{7-\delta}$ (x = 0.1,0.2,0.5,0.75):

In order to gain deep insights to the surface environment of Ce substituted catalysts, XPS analysis of all calcined samples was carried out. All of the catalyst's Zr 3d XP spectra show that Zr is present in the +4 oxidation state[36][57][93](Figure 2.28). The Ce3d spectra of all substituted catalysts are shown in figure 2.29(A), and it can be seen that Ce is present in Ce^{+3} and Ce^{+4} mixed valences[94][95]. It has been proposed that the presence of Ce^{+3} species aids in the creation of oxygen vacancies and other active O species in and on the surface of the catalyst which initiates the CO_2 activation and enhances gasification of accumulated carbon formed during DRM cycles on metal surface and metal support interphase [96][97]. Table 2.8 shows the percentage of Ce^{+3} and Ce^{+4} species derived by relative area. The GZN2C2 catalyst contains the highest concentration of Ce^{+3} species of all the catalysts, most likely due to the higher quantity of Ni in the lattice.

The O 1s (Figure 2.29(B)) spectra of all catalysts, including the parent catalyst, displayed a

peak at BE at 529-530 eV, corresponding to lattice oxygen species, and a peak at 533-534 eV, corresponding to adsorbed oxygen species. Aside from this, the weakly bound surface hydroxyl species are represented by a peak at roughly 531.5-532 eV. The peak corresponding to hydroxyl species is lacking in the parent catalyst GZN2[36], indicating that Ce doping in the parent catalyst's B site induces lattice disorder, resulting in the generation of surface hydroxyl species. Table 2.8 displays the calculated ratio of these species in all of the catalysts. The GZN2C2 catalyst has the largest concentration of hydroxyl species (38.89%), while the GZN2C75 has the lowest (25.8%).
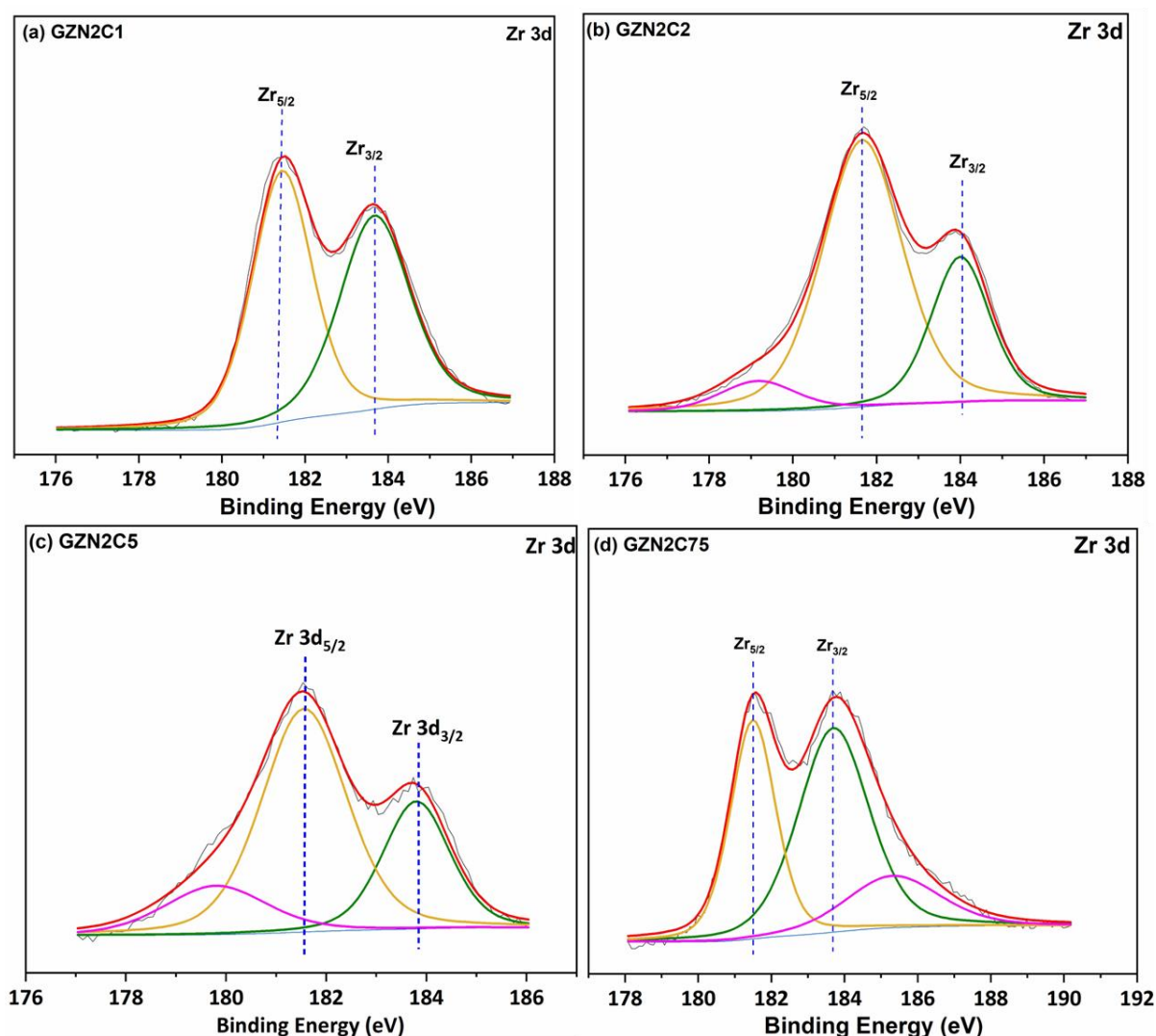
Figure 2.28: Deconvoluted XPS profile of Zr 3d XPS of a) GZN2C1 b) GZN2C2 c) GZN2C5 and d) GZN2C75.
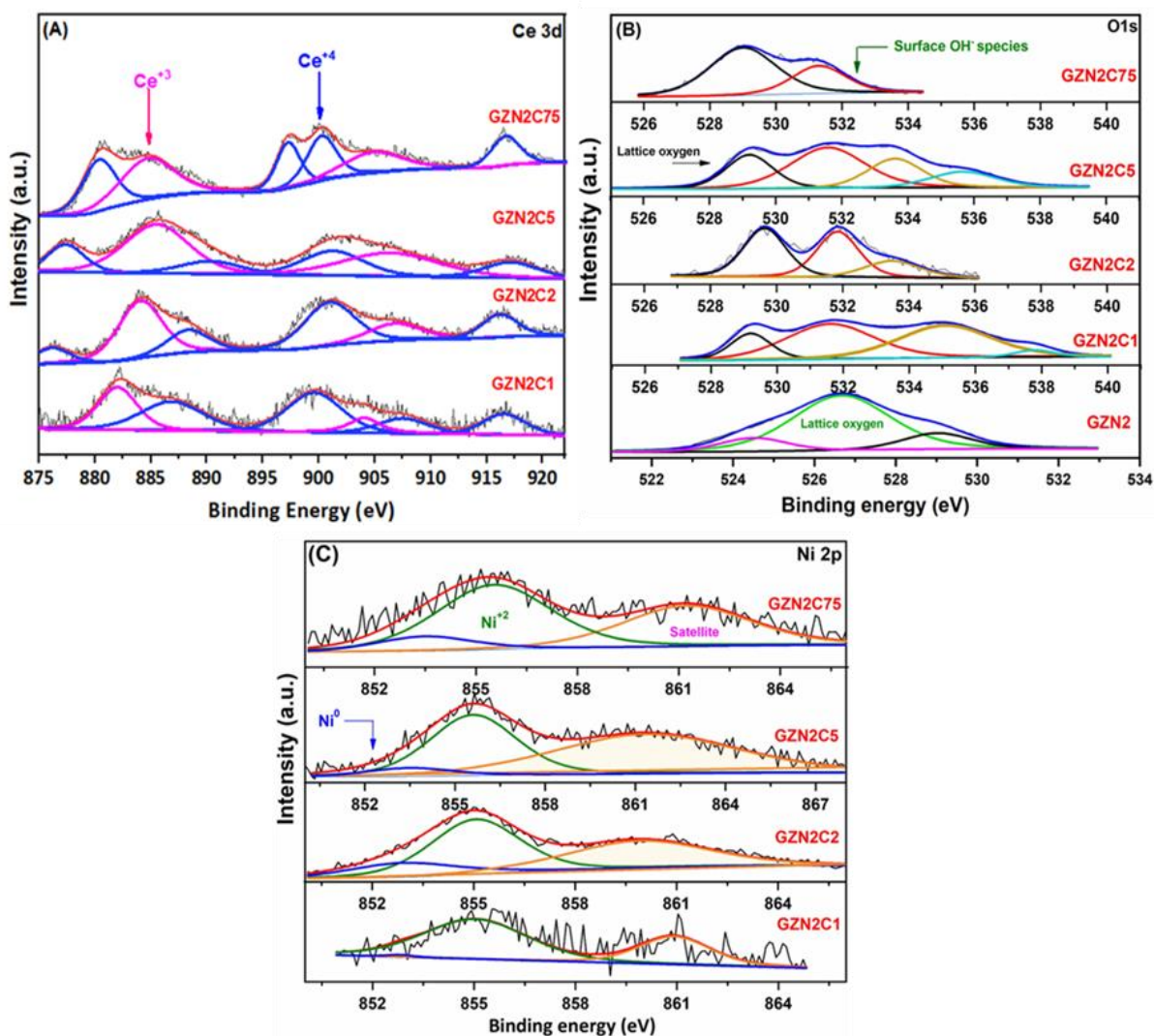
Figure 2.29: (A) XPS Ce 3d, (B) O 1s, (C) Ni 2p spectrum of a) GZN2 b) GZN2C1 c) GZN2C2 d) GZN2C5 and e) GZN2C75.

Table 2.8: % Ratio of Ce^{+3}, OH^- species of GZN2C1, GZN2C2, GZN2C5 and GZN2C75 catalysts.

Catalysts Name	Ce^{+3} BE (eV)	Ce^{+4} BE (eV)	$Ce^{+3}/(Ce^{+3}+Ce^{+4})$ %	OH^- Species BE (eV)	% OH^- species
GZN2C1	881.9, 903.2	888.9,901,907,917	49.2	531.5	30.2
GZN2C2	884.7, 903.0	888.8,901.2,907.1, 917	56.53	531.6	38.89
GZN2C5	884.7, 903.0	888.6, 901, 917	51.73	531.8	34.82
GZN2C75	884.6, 903.0	882.8,898.1,901.0, 917	48.20	531.8	25.8

In the Ni 2p XPS data (Figure 2.29(C)), the peaks observed at 855.5 eV, 861.1 eV and 852.8 eV correspond to Ni^{+2} species, satellite peak and metallic Ni respectively[96][98]. The binding energy corresponding to metallic Ni is observed in all Ce substituted catalysts although GZN2C1 has lowest concentration for the same. This indicates the presence of well-distributed NiO species on the catalyst's surface, resulting in early reduction of surface NiO into Ni^0 and the provision of metallic Ni active sites for the reforming reaction cycle[36][99].

2.15.6 FTIR Analysis of $Gd_2Zr_{1.8-x}Ni_{0.2}Ce_xO_{7-\delta}$ (x = 0.1,0.2,0.5,0.75):

Furthermore, we used DRIFTS analysis to better understand the role of Ce substitution in the generation of surface species in response to CO_2 exposure. Before the experiment, the sample surface was cleaned by heating it within the DRIFTS cell in N_2 at 400 °C. Following that, the sample was reduced in H_2 (20 mL/min) for 2 hours before being purged with N_2 at 400 °C for 30 minutes to sweep off the surplus gas. The material was then passed through a combination of N_2 (20 mL/min) and CO_2 (5 mL/min), and spectra were recorded in absorbance mode at 400 °C. Surface hydroxyl and formate species production was detected in all Ce substituted catalysts, as evidenced by peaks in the 3500-3800 cm^{-1} and approximately 1365 cm^{-1}, 1590 cm^{-1} ranges (Figure 2.30)[100]. Aside from that, the production of several forms of carbonates was seen in the 1200 - 1900 cm^{-1} range. When CO_2 was exposed to the Ce substituted catalysts surface, three types of carbonate species developed (shown in figure 2.31). (i) peaks at 1370 cm^{-1},1515-1520 cm^{-1} correspond to monodentate species, formed by adsorption of CO_2 on basic sites, (ii) peaks at 1570 cm^{-1} and 1635 cm^{-1} can be assigned to bicarbonate species formed by CO_2 adsorption on acid base pair sites like Z^{+4} O^{2-} centres and on OH groups and (iii) peaks at 1442 and 1415 cm^{-1} are attributed to polydentate carbonate species which are formed by the CO_2 adsorption on Zr+4 acidic site[40][101][102]In the FTIR spectra of GZN2C2, monodentate and bidentate carbonate species are more prominent, indicating higher concentration of basic sites over the

surface. Such an activation of CO_2 on the surface of GZN2C2 catalyst can be further corroborated by the presence of desorbed gaseous CO at 2143 cm^{-1}, [103]which is not observed in GZN2C1 catalyst. In GZN2C5 and GZN2C75 catalysts, this feature appears on initial exposure of CO_2 but disappears with time. This confirms the CO_2 adsorption on acidic Zr+4 sites resulting in less desorption of CO_2 as CO. This has been further corroborated by the absence of peak at 2143 cm^{-1} corresponding to the desorbed CO in GZN2 catalyst[36]. Based on these findings, it is obvious that the existence of substantial mono and bidentate carbonate species, as well as surface hydroxyl species, plays a critical role in the ongoing activation of CO_2 and continuous generation of CO in GZN2C2 catalysts over other catalysts [40][104].
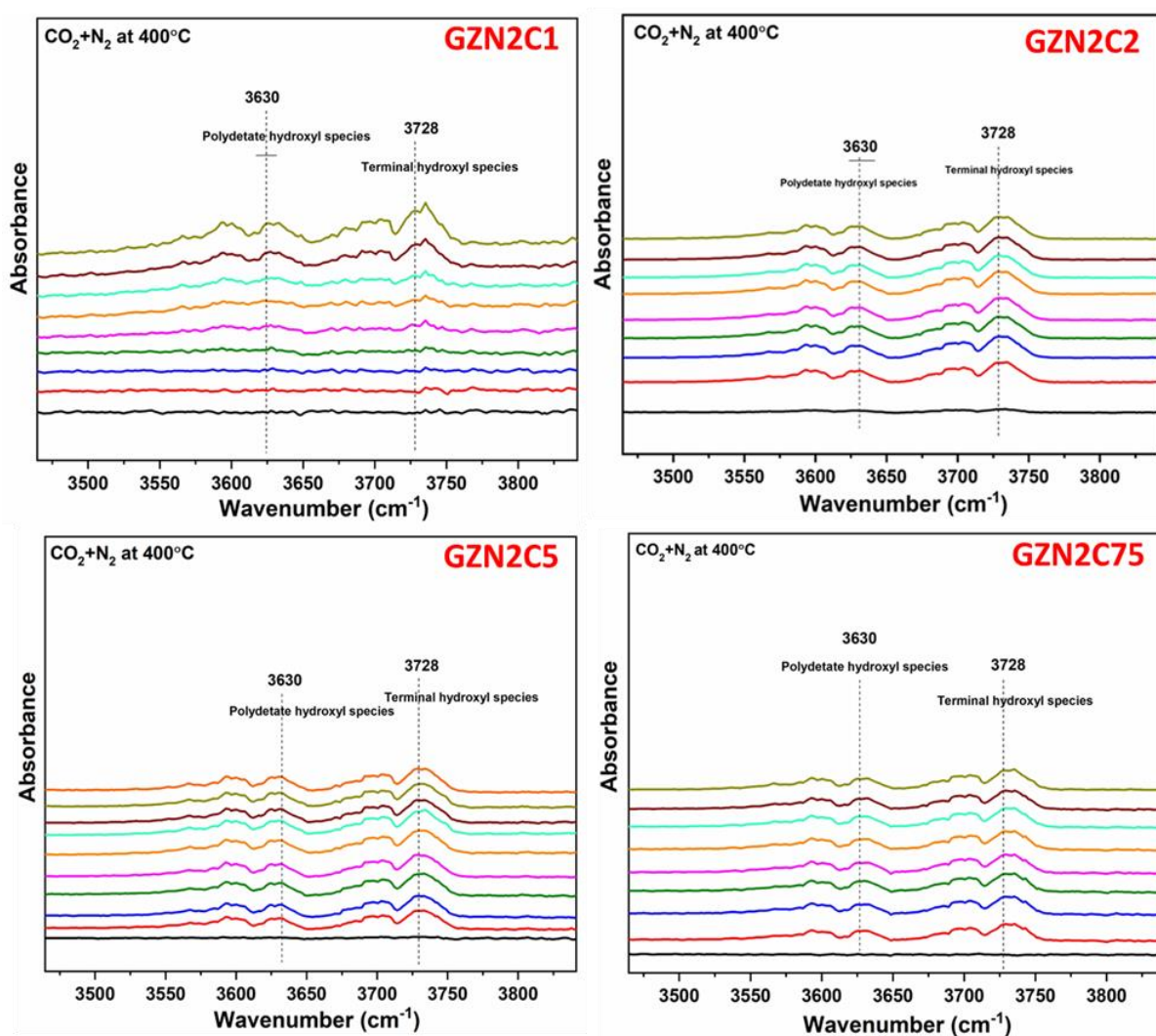
Figure 2.30: in situ FTIR spectra of GZN2C1, GZN2C2, GZN2C5 and GZN2C75 with the

feed gas 5 mL CO_2+ 20 mL N_2 at 400 °C presenting hydroxyl and fotmate species
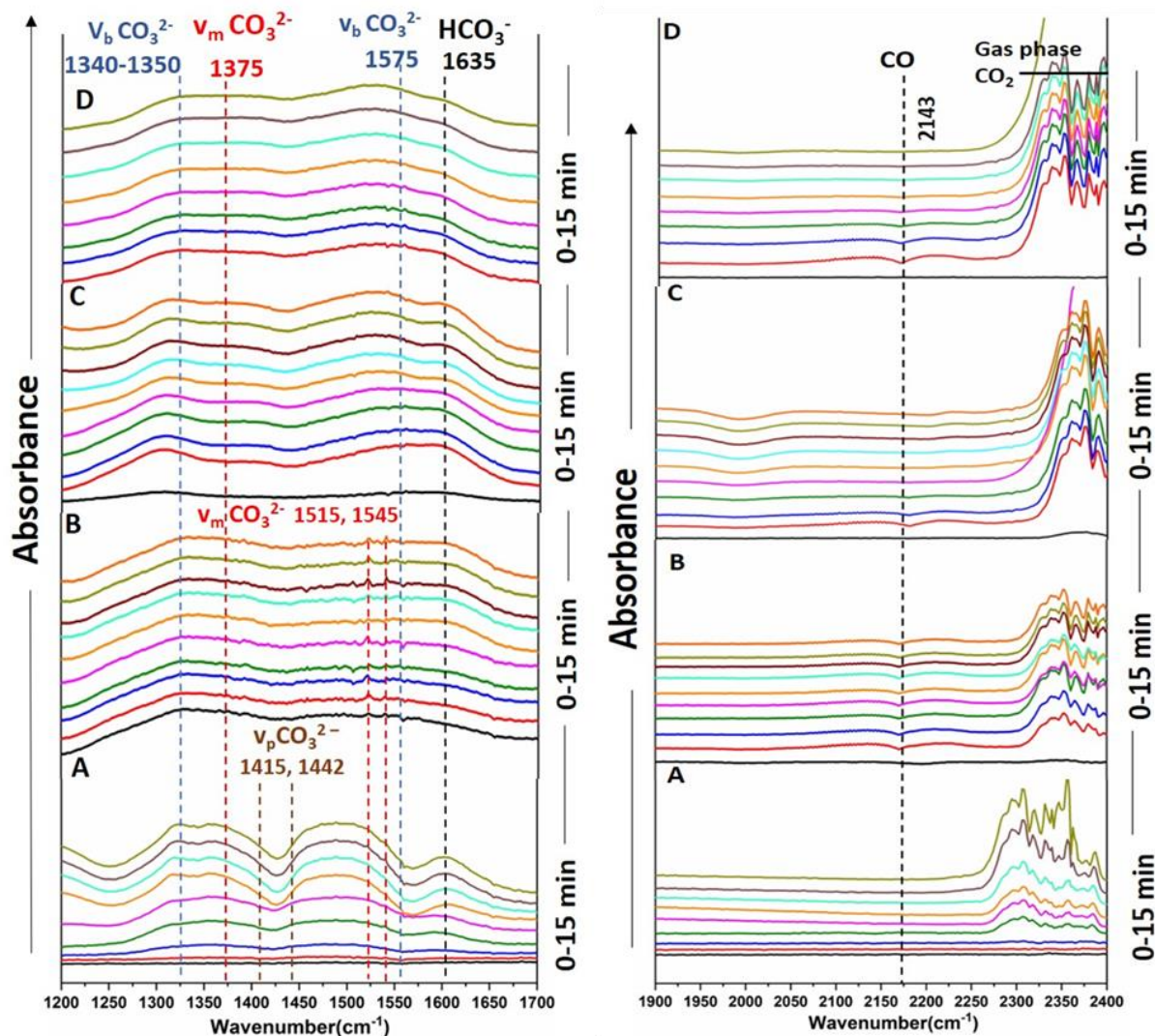
Figure 2.31: FTIR spectra of (A) GZN2C1 B) GZN2C2 C) GZN2C5 D) and GZN2C75.

2.16 Catalytic activity of $Gd_2Zr_{1.8-x}Ni_{0.2}Ce_xO_{7-\delta}$ (x = 0.1,0.2,0.5,0.75):

To check the effect of Ce on conventional DRM activity, all the catalysts were screened for the DRM conditions i.e., CH_4: CO_2: N_2= 1:1:1 as 80:80:80 ml/min with 28,800 h^{-1} GHSV at 800°C in atmospheric pressure (Figure 2.32). Conversion and H_2/CO ratio were initially lower for all catalysts due to the ascendency of side reactions, and improvement in conversion was detected only after 30 hours. Among all the catalysts, GZN2C2 catalyst shows superior activity with 85 % CH_4 and 93.5 % CO_2 conversion with H_2/CO ratio 0.83 after 100 h, whereas lowest activity was observed for GZN2C1. The decreased H_2/CO ratio

could be attributed to the prevalence of side reactions such as the reverse water gas shift reaction (5) and the reverse Boudouard reaction (6). The positive effect of Ce substitution in DRM activity is further confirmed by comparing the activity of GZN2 catalyst with all Ce substituted catalysts as its activity is lowest among all catalysts [36].

$$2CO \leftrightarrow C(s) + CO_2 \qquad (\Delta H°298\ K = +171\ kJ/\ mol) \qquad\qquad (6)$$
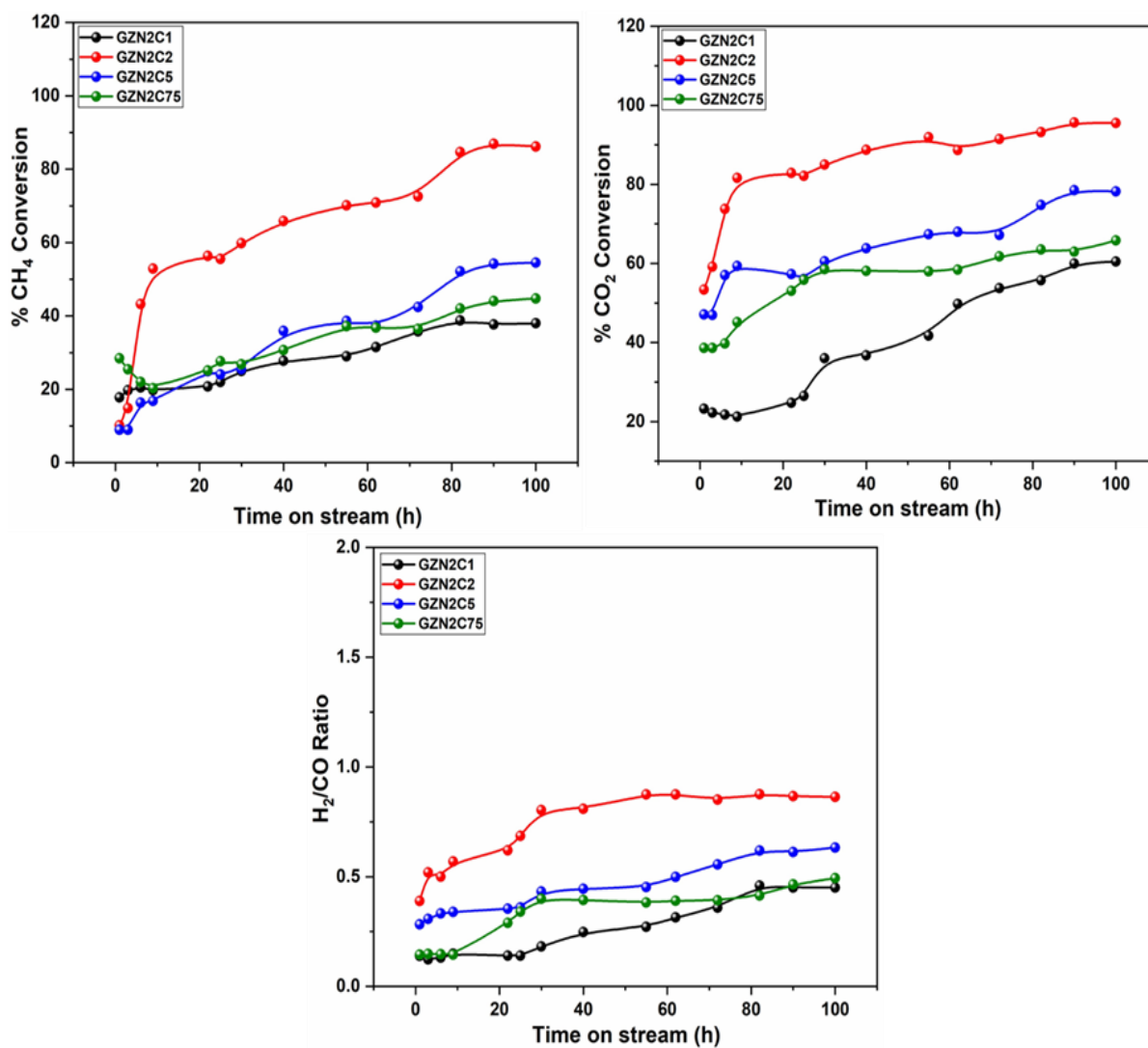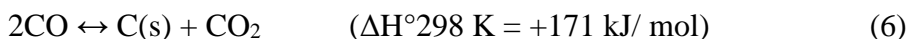
Figure 2.32: Activity analysis of GZN2, GZN2C1, GZN2C2, GZN2C5 and GZN2C75 catalysts in DRM conditions: CH_4: CO_2: N_2 = 80:80:80 mL/min, 28,800 h^{-1} GHSV at 800 °C for 100 h time on stream. Conversions and H_2/CO ratios are plotted against time on stream.

2.17 Spent catalysts Characterization:

2.17.1 XRD analysis of spent catalysts:

XRD was used to examine the structure stability and changes of Ce substituted catalysts

during DRM processes. The XRD plot of spent catalysts in figure 2.33 demonstrated that the original structure was retained. GZN2C1, GZN2C5, and GZN2C75 catalyst patterns show a peak at 26.4° 2θ position that is assigned to graphitic carbon[105]. In the pattern of GZN2C2 catalyst, however, just a minor peak is detected. TGA, HRTEM, and Raman analyses were used to further quantify and investigate the structural properties of produced carbon species in spent catalysts.
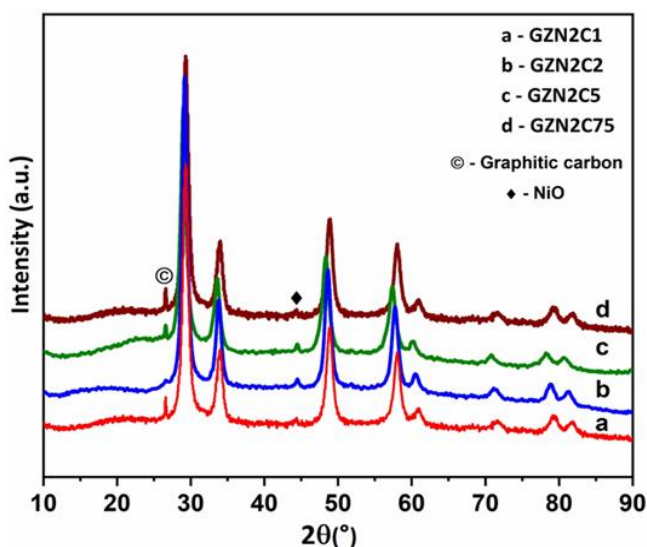
Figure 2.33: XRD patterns of used catalysts a) GZN2C1, b) GZN2C2, c) GZN2C5, and d) GZN2C75, screened in the DRM reaction.

2.17.2 Thermogravimetric analysis of spent catalysts:

TGA analysis in an air atmosphere was used to calculate the amount of carbon produced during the reforming reaction. Figure 2.34 depicts the amount of coke generated during 100 hours of DRM process. The findings show that the GZN2C2 catalyst produces very little coke, but the coke generation trend in other catalysts is GZN2C1> GZN2C75> GZN2C5. In comparison, a significant quantity of coke buildup was detected in the parent GZN2 catalyst in the absence of Ce substitution[36]. Here the effect of Ce substitution has major impact on coke gasification by generation of surface hydroxyl species. Moreover, consistent and stable higher activity and carbon gasification was observed in GZN2C2 catalysts by continuous CO_2 activation with less carbon formation.
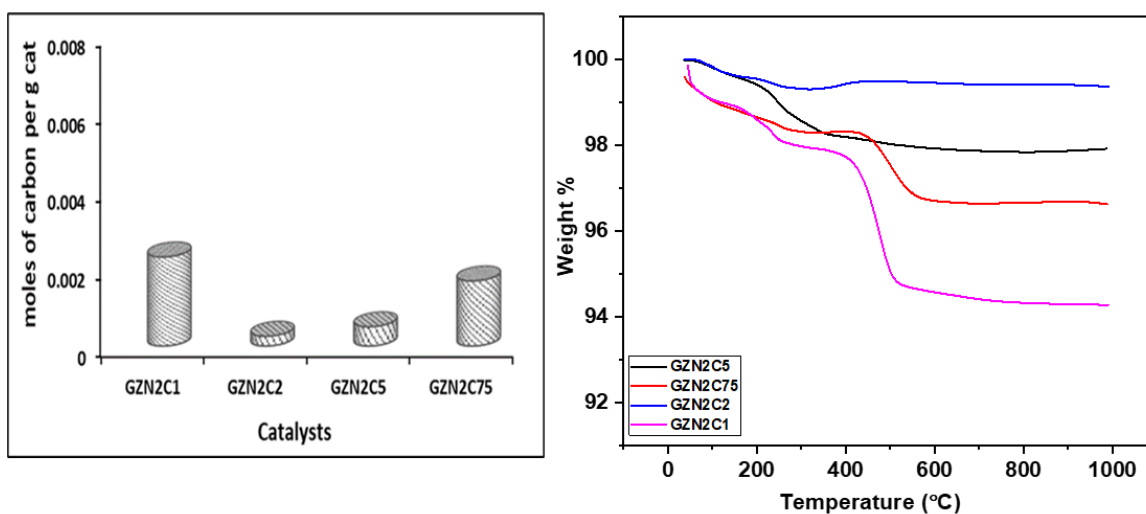
Figure 2.34: TGA analysis of spent catalysts GZN2C1, GZN2C2, GZN2C5 and GZN2C75.

2.17.3 HRTEM analysis of spent catalysts:

The morphology and nature of formed carbon after the reforming reaction was analysed by HRTEM as shown in figure 2.35. After 100 hours of reaction, GZN2C1 catalysts have filamentous graphitic carbon species and multiwalled carbon nanotubes, indicating coke accumulation and deactivation for methane dry reforming (Figure 2.35(A)) [36]. The GZN2C2 catalyst shown in figure 9 (B) has amorphous carbon species which is not responsible for any deactivation as it is simultaneously oxidized by surface adsorbed species, offering higher activity and stability in DRM. Figure 2.35 (C), (D), and (E) show HRTEM micrographs of spent GZN2C5, GZN2C75, and parent GZN2. The GZN2C5 and GZN2C75 catalysts have filamentous carbon and amorphous carbon species. In contrast, GZN2 catalyst has the multiwalled nanotubes with Ni particles embedded in CNTs making it unavailable for further DRM reaction resulting in lower activity and deactivation.
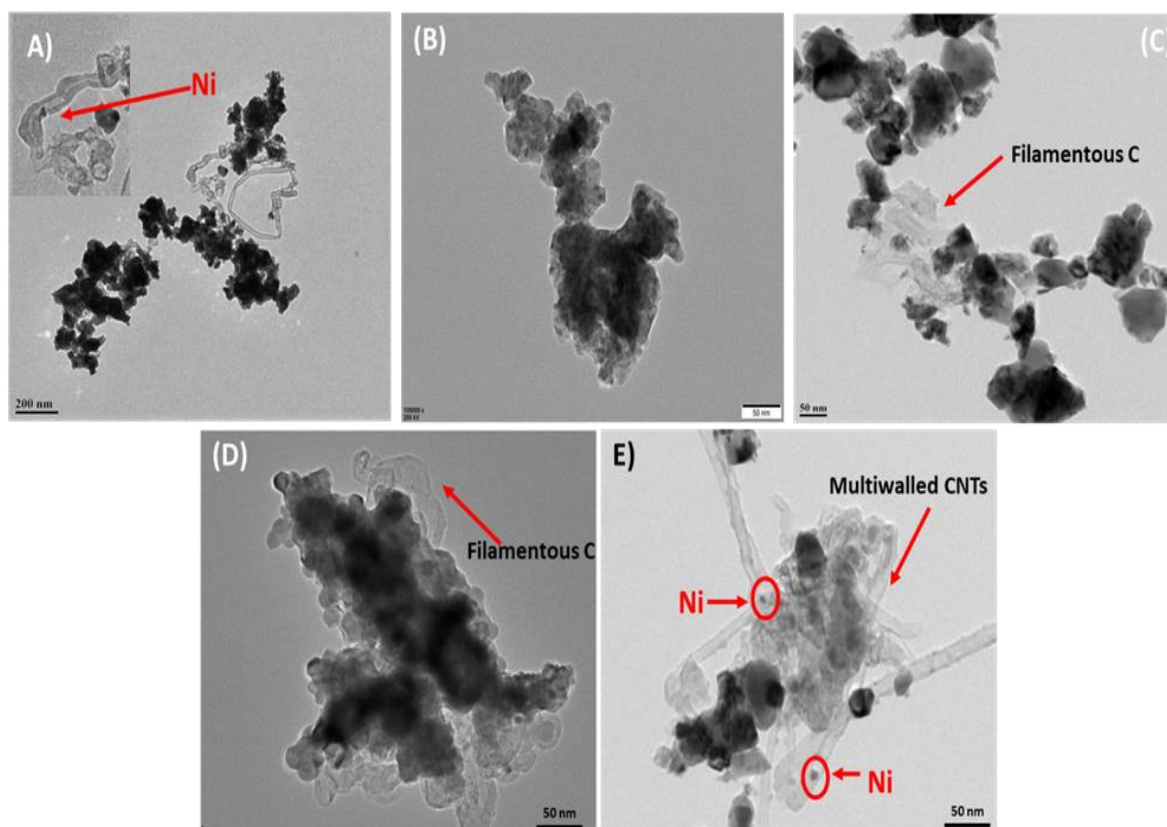
Figure 2.35: TEM micrographs of spent catalysts (A) GZN2C1, (B) GZN2C2, (C) GZN2C5, (D) GZN2C75, and (E) GZN2.

2.17.4 Raman analysis of spent catalysts:

Raman spectroscopy is a useful tool for determining the types of carbon generated during reforming events. Carbon production occurs mostly in reforming reactions as a result of methane degradation (4) on the metal surface and the Boudouard reaction in low temperature regimes (3)[106]. Carbon can form as carbon nanotubes, synthetic diamond carbon, and carbon films on the catalyst's surface[107]. Figure 2.36 displays the Raman spectra of the spent catalysts. The spectra depict two peaks at around 1350 cm^{-1} and 1590 cm^{-1} which attributed to D- band and G- band in GZN2C1 catalyst. The D band ascribed to defect originated band in carbonaceous material while G band arises because of E2g mode attributed to stretching vibrations of sp2 carbon in graphitic carbon species[108][109][110]. The Raman spectra of the parent GZN2 spent catalyst displays D and G bands, confirming the existence of graphitic carbon[36].
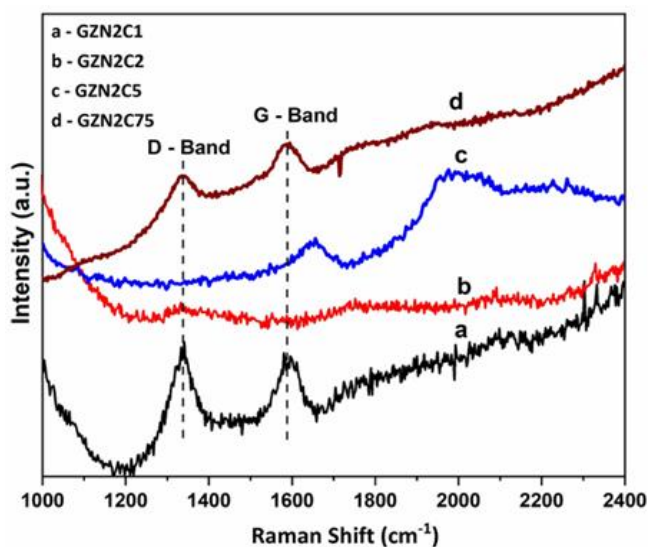
Figure 2.36: Raman spectra of spent catalysts GZN2C1, GZN2C2, GZN2C5, and GZN2C75.

2.18 Conclusions:

Ce substituted $Gd_2Zr_{1.8-x}Ni_{0.2}Ce_xO_{7-\delta}$ (x = 0.1,0.2,0.5,0.75) catalysts were synthesized and tested in methane dry reforming. The identification of the structure, inclusion of Ce in the Zr site, and concentration of Ni substituted in the lattice and present on the surface as NiO particles were examined and validated by XRD and Rietveld refinement analysis. The Raman analysis further confirmed the structural stability after Ce substitution in parent catalyst. TPR analysis confirms the enhanced reducibility of active metal (Ni) of catalyst by Ce substitution in Zr site, Describes the existence of dispersed NiO on the surface as well as the bulk residence of active metal species (Ni) and Ce in the catalyst. The XPS analysis showed the highest amount of reduced Ce^{+3} over the surface of GZN2C2 catalyst which helped in formation of surface hydroxyl species more than other catalysts. Also, GZN2C2 catalyst has prominent monodentate and bidentate carbonates and bicarbonates species, as observed in DRIFTS studies, which provide continuous enhanced CO_2 activation resulting in high conversions in DRM. The spent catalyst characterization illustrates the formation of graphitic carbon in parent and all Ce substituted catalysts except GZN2C2 catalyst with structure retention. Quantification of carbon species in catalysts by TGA analysis suggest

more C formation in GZN2C1 and GZN2C75 catalysts. The doping of more Ni in the lattice in case of GZN2C2 creates more defects resulting in excess of Ce^{+3} which initiates the formation of increased amount of surface hydroxyl species and possible O vacancies. This facilitates the coke gasification with higher and durable activity of GZN2C2 catalyst for 100 h of DRM reaction. The influence of moderate Ce concentration and a higher amount of active metal species Ni inside the lattice in the case of GZN2C2 on the blockage of active sites of catalysts by continuous coke oxidation is established in this work. This appears to provide a balance between the chemical cycle and concomitant gasification of carbon across the surface of the catalyst by hydroxyl species, resulting in enhanced DRM activity.

2.19 Reference:

[1]   A. Saravanan et al., "A comprehensive review on different approaches for CO_2 utilization and conversion pathways," Chem Eng Sci, vol. 236, p. 116515, Jun. 2021, doi: 10.1016/J.CES.2021.116515.

[2]   L. Guczi et al., "Methane dry reforming with CO_2: A study on surface carbon species," Appl Catal A Gen, vol. 375, no. 2, pp. 236–246, Mar. 2010, doi: 10.1016/j.apcata.2009.12.040.

[3]   Z. Zhang and X. E. Verykios, "Mechanistic aspects of carbon dioxide reforming of methane to synthesis gas over Ni catalysts," 1996.

[4]   L. Kapokova et al., "Dry reforming of methane over $LnFe_{0.7}Ni_{0.3}O_{3-\delta}$ perovskites: Influence of Ln nature," Catal Today, vol. 164, no. 1, pp. 227–233, Apr. 2011, doi: 10.1016/J.CATTOD.2010.10.086.

[5]   U. Olsbye, T. Wurzel, and L. Mleczko, "Kinetic and Reaction Engineering Studies of Dry Reforming of Methane over a $Ni/La/Al_2O_3$ Catalyst," Industrial & Engineering Chemistry Research, vol. 36, no. 12, pp. 5180–5188, Dec. 1997, doi: 10.1021/ie970246l.

[6]   H. E. Curry-Hyde and J. R. Rostrup-Nielsen, "Aspects of CO,-reforming of Methane."

[7]   A. J. Brungs, A. P. E. York, J. B. Claridge, C. Márquez-Alvarez, and M. L. H. Green, "Dry reforming of methane to synthesis gas over supported molybdenum carbide catalysts," 2000.

[8]   C. H. Bartholomew, "Carbon Deposition in Steam Reforming and Methanation," Catalysis Reviews, vol. 24, no. 1, pp. 67–112, Jan. 1982, doi: 10.1080/03602458208079650.

[9]   D. J. Haynes, D. A. Berry, D. Shekhawat, and J. J. Spivey, "Catalytic partial oxidation of n-tetradecane using Rh and Sr substituted pyrochlores: Effects of sulfur," Catal Today, vol. 145, no. 1–2, pp. 121–126, Jul. 2009, doi: 10.1016/J.CATTOD.2008.05.014.

[10]   J. Xu et al., "$A_2B_2O_7$ pyrochlore compounds: A category of potential materials for clean energy and environment protection catalysis," Journal of Rare Earths, vol. 38, no. 8, pp. 840–849, Aug. 2020, doi: 10.1016/J.JRE.2020.01.002.

[11]   J. Xu et al., "Constructing $La_2B_2O_7$ (B = Ti, Zr, Ce) Compounds with Three Typical Crystalline Phases for the Oxidative Coupling of Methane: The Effect of Phase Structures, Superoxide Anions, and Alkalinity on the Reactivity," ACS Catal, vol. 9, no. 5, pp. 4030–4045, Mar. 2019, doi: 10.1021/acscatal.9b00022.

[12]   A. C. Roger, C. Petit, and A. Kiennemann, "Effect of Metallo-organic Precursors on the Synthesis of Sm–Sn Pyrochlore Catalysts: Application to the Oxidative Coupling of Methane," J Catal, vol. 167, no. 2, pp. 447–459, Apr. 1997, doi: 10.1006/JCAT.1997.1601.

[13]   D. Pakhare, C. Shaw, D. Haynes, D. Shekhawat, and J. Spivey, "Effect of reaction temperature on activity of Pt- and Ru-substituted lanthanum zirconate pyrochlores ($La_2Zr_2O_7$) for dry (CO_2) reforming of methane (DRM)," Journal of CO_2 Utilization, vol. 1, pp. 37–42, Jun. 2013, doi: 10.1016/J.JCOU.2013.04.001.

[14]   S. Bhattar et al., "110th Anniversary: Dry Reforming of Methane over Ni- and Sr-Substituted Lanthanum Zirconate Pyrochlore Catalysts: Effect of Ni Loading," Industrial & Engineering Chemistry Research, vol. 58, no. 42, pp. 19386–19396, Sep. 2019, doi: 10.1021/acs.iecr.9b02434.

[15]   F. Polo-Garzon, M. He, and D. A. Bruce, "Ab initio derived reaction mechanism for the dry reforming of methane on Rh doped pyrochlore catalysts," J Catal, vol. 333, pp. 59–70, Jan. 2016, doi: 10.1016/J.JCAT.2015.10.017.

[16]   F. Polo-Garzon, D. Pakhare, J. J. Spivey, and D. A. Bruce, "Dry Reforming of Methane on Rh-Doped Pyrochlore Catalysts: A Steady-State Isotopic Transient Kinetic Study," ACS Catal, vol. 6, no. 6, pp. 3826–3833, May 2016, doi: 10.1021/acscatal.6b00666.

[17]   N. Kumar et al., "Bi-reforming of methane on Ni-based pyrochlore catalyst," Appl Catal A Gen, vol. 517, pp. 211–216, May 2016, doi: 10.1016/J.APCATA.2016.03.016.

[18]   X. Fang et al., "Highly active and stable $Ni/Y_2Zr_2O_7$ catalysts for methane steam reforming: On the nature and effective preparation method of the pyrochlore support," Int J Hydrogen Energy, vol. 41, no. 26, pp. 11141–11153, Jul. 2016, doi: 10.1016/J.IJHYDENE.2016.04.038.

[19]   Y. Wang, B. Gao, Q. Wang, X. Li, Z. Su, and A. Chang, "$A_2Zr_2O_7$ (A = Nd, Sm, Gd, Yb) zirconate ceramics with pyrochlore-type structure for high-temperature negative temperature coefficient thermistor," J Mater Sci, vol. 55, no. 32, pp. 15405–15414, Nov. 2020, doi: 10.1007/s10853-020-05104-5.

[20]   S. Ćulubrk, Ž. Antić, V. Lojpur, M. Marinović-Cincović, and M. D. Dramićanin, "Sol-gel derived Eu^{3+}-doped $Gd_2Ti_2O_7$ pyrochlore nanopowders," J Nanomater, vol. 2015, 2015, doi: 10.1155/2015/514173.

[21]   B. H. Toby and IUCr, "EXPGUI, a graphical user interface for GSAS," J Appl Crystallogr, vol. 34, no. 2, pp. 210–213, Apr. 2001, doi: 10.1107/S0021889801002242.

[22]   M. T. Vandenborre, E. Husson, J. P. Chatry, and D. Michel, "Rare-earth Titanates and Stannates of Pyrochlore Structure; Vibrational Spectra and Force Fields."

[23]   S. Saha et al., "High-pressure Raman and x-ray study of the spin-frustrated pyrochlore $Gd_2Ti_2O_7$," Phys Rev B, vol. 74, no. 6, p. 064109, Aug. 2006, doi: 10.1103/PhysRevB.74.064109.

[24]   S. P. S. Porto, P. A. Fleury, and T. C. Damen, "Raman Spectra of TiO_2, Mg F_2 , ZnF_2, FeF_2 ,and MnF_2," Physical Review, vol. 154, no. 2, pp. 522–526, Feb. 1967, doi: 10.1103/PhysRev.154.522.

[25]   A. F. Fuentes, S. M. Montemayor, M. Maczka, M. Lang, R. C. Ewing, and U. Amador, "A Critical Review of Existing Criteria for the Prediction of Pyrochlore Formation and Stability," Inorg Chem, vol. 57, no. 19, pp. 12093–12105, Sep. 2018, doi: 10.1021/acs.inorgchem.8b01665.

[26]   C. Ding et al., "Coking resistant $Ni/ZrO_2@SiO_2$ catalyst for the partial oxidation of methane to synthesis gas," Int J Hydrogen Energy, vol. 40, no. 21, pp. 6835–6843, Jun. 2015, doi: 10.1016/j.ijhydene.2015.03.094.

[27]   M. A. Ebiad, D. R. Abd El-Hafiz, R. A. Elsalamony, and L. S. Mohamed, "Ni supported high surface area CeO_2-ZrO_2 catalysts for hydrogen production from ethanol steam reforming," RSC Adv, vol. 2, no. 21, pp. 8145–8156, 2012, doi: 10.1039/c2ra20258a.

[28]   Y. Lin, Y. Zhu, X. Pan, and X. Bao, "Modulating the methanation activity of Ni by the crystal phase of TiO_2," Catal Sci Technol, vol. 7, no. 13, pp. 2813–2818, 2017, doi: 10.1039/c7cy00124j.

[29]   F. Meng, Y. Song, X. Li, Y. Cheng, and Z. Li, "Catalytic methanation performance in a low-temperature slurry-bed reactor over Ni–ZrO_2 catalyst: effect of the preparation method," J Solgel Sci Technol, vol. 80, no. 3, pp. 759–768, Dec. 2016, doi: 10.1007/s10971-016-4139-4.

[30]   J. L. Falconer' And and A. E. Zagli, "Adsorption and Methanation of Carbon Dioxide on a Nickel/Silica Catalyst," 1980.

[31]   W. Zhang, Y. Tao, and C. Li, "Sol-gel synthesis of $Gd_2Ti_2O_7$/HZSM-5 composite photocatalyst for ofloxacin degradation," J Photochem Photobiol A Chem, vol. 364, pp. 787–793, Sep. 2018, doi: 10.1016/j.jphotochem.2018.07.022.

[32]   J. Pouilleau, D. Devilliers, H. Groult, and P. M. Arcus, "Surface study of a titanium-

based ceramic electrode material by X-ray photoelectron spectroscopy," 1997.

[33]   J. Chen and X. Wang, "Fabrication and characterization of novel excellent thermal-protection $Gd_2Zr_2O_7/ZrO_2$ composite ceramic fibers with different proportions of $Gd_2Zr_2O_7$," Ceram Int, vol. 46, no. 15, pp. 24029–24037, Oct. 2020, doi: 10.1016/j.ceramint.2020.06.180.

[34]   S. Xu et al., "CO Poisoning of Ru Catalysts in CO_2 Hydrogenation under Thermal and Plasma Conditions: A Combined Kinetic and Diffuse Reflectance Infrared Fourier Transform Spectroscopy–Mass Spectrometry Study," ACS Catal, vol. 10, no. 21, pp. 12828–12840, Oct. 2020, doi: 10.1021/acscatal.0c03620.

[35]   S. Dama, S. R. Ghodke, R. Bobade, H. R. Gurav, and S. Chilukuri, "Active and durable alkaline earth metal substituted perovskite catalysts for dry reforming of methane," Appl Catal B, vol. 224, pp. 146–158, May 2018, doi: 10.1016/j.apcatb.2017.10.048.

[36]   S. R. Ghodke, S. Thundiyil, P. Dongapure, and R. Nandini Devi, "Effect of B site substitution in $Gd_2B_{2-x}Ni_yO_{7-\delta}$ (B= Ti, Zr) ternary metal oxide catalysts in dry reforming of methane," Molecular Catalysis, vol. 522, Apr. 2022, doi: 10.1016/j.mcat.2022.112242.

[37]   K. Tanabe, "Surface and catalytic properties of ZrO_2," Mater Chem Phys, vol. 13, no. 3–4, pp. 347–364, Sep. 1985, doi: 10.1016/0254-0584(85)90064-1.

[38]   Y. Lou et al., "Design of stable Ni/ZrO_2 catalysts for dry reforming of methane," J Catal, vol. 356, pp. 147–156, Dec. 2017, doi: 10.1016/J.JCAT.2017.10.009.

[39]   Y. Han, Y. Tan, N. Tsubaki, Q. Zhang, and X. Zhang, Influence of Zirconia Phase on the Performance of Ni/ZrO_2 for Carbon Dioxide Reforming of Methane. 2015. doi: 10.1021/bk-2015-1194.ch006.

[40]   X. Zhang, Q. Zhang, N. Tsubaki, Y. Tan, and Y. Han, "Carbon dioxide reforming of methane over Ni nanoparticles incorporated into mesoporous amorphous ZrO_2 matrix," Fuel, vol. 147, pp. 243–252, May 2015, doi: 10.1016/J.FUEL.2015.01.076.

[41]   Y. Wang et al., "Synergy of Oxygen Vacancies and Ni^0 Species to Promote the

Stability of a Ni/ZrO$_2$ Catalyst for Dry Reforming of Methane at Low Temperatures," ACS Catal, vol. 13, no. 10, pp. 6486–6496, Apr. 2023, doi: 10.1021/acscatal.2c06412.

[42]   M. Zhang et al., "Insight into the effects of the oxygen species over Ni/ZrO$_2$ catalyst surface on methane reforming with carbon dioxide," Appl Catal B, vol. 244, pp. 427–437, May 2019, doi: 10.1016/J.APCATB.2018.11.068.

[43]   M. Zhang, X. Zhou, J. Yang, T. Yang, Z. Liu, and Y. Han, "Deciphering the ZrO$_2$ phase engineering effects on dry reforming of methane over the Ni/ZrO$_2$ catalysts," Fuel, vol. 349, p. 128705, Oct. 2023, doi: 10.1016/J.FUEL.2023.128705.

[44]   M. S. Lanre et al., "Modification of CeNi$_{0.9}$Zr$_{0.1}$O$_3$ Perovskite Catalyst by Partially Substituting Yttrium with Zirconia in Dry Reforming of Methane," Materials, vol. 15, no. 10, p. 3564, May 2022, doi: 10.3390/ma15103564.

[45]   P. K. Yadav and T. Das, "Study of the perovskite-type catalysts 40LaNi$_{0.75}$Fe$_{0.25-X}$ MXO$_3$/SiO$_2$ (M=Ce, Zr) for the dry reforming of methane," Reaction Kinetics, Mechanisms and Catalysis, vol. 132, no. 1, pp. 279–300, Feb. 2021, doi: 10.1007/s11144-021-01926-9.

[46]   S. Dama, S. Ghodke, R. Bobade, H. Gurav, and S. Chilukuri, "Tuning the dimensionality of layered Sr$_{n+1}$Ti$_{n-x}$Ni$_x$O$_{3n+1}$ perovskite structures for improved activity in syngas generation," J Catal, vol. 360, pp. 27–39, Apr. 2018, doi: 10.1016/J.JCAT.2018.01.015.

[47]   J. L. Martín-Espejo, L. P. Merkouri, J. Gándara-Loe, J. A. Odriozola, T. R. Reina, and L. Pastor-Pérez, "Nickel-based cerium zirconate inorganic complex structures for CO$_2$ valorisation via dry reforming of methane," Journal of Environmental Sciences, Jan. 2023, doi: 10.1016/J.JES.2023.01.022.

[48]   S. Gaur, D. J. Haynes, and J. J. Spivey, "Rh, Ni, and Ca substituted pyrochlore catalysts for dry reforming of methane," Appl Catal A Gen, vol. 403, no. 1–2, pp. 142–151, Aug. 2011, doi: 10.1016/J.APCATA.2011.06.025.

[49]   X. Fang et al., "Dry reforming of methane on active and coke resistant Ni/Y$_2$Zr$_2$O$_7$

catalysts treated by dielectric barrier discharge plasma," Journal of Energy Chemistry, vol. 25, no. 5, pp. 825–831, Sep. 2016, doi: 10.1016/J.JECHEM.2016.06.002.

[50]   D. J. Xu et al., "Doping low amount of Zirconium in Rh-LTO to prepare durable catalysts for dry reforming of methane," Molecular Catalysis, vol. 535, p. 112822, Jan. 2023, doi: 10.1016/J.MCAT.2022.112822.

[51]   E. Akbari, S. M. Alavi, and M. Rezaei, "Synthesis gas production over highly active and stable nanostructured NiMgOAl$_2$O$_3$ catalysts in dry reforming of methane: Effects of Ni contents," Fuel, vol. 194, pp. 171–179, Apr. 2017, doi: 10.1016/J.FUEL.2017.01.018.

[52]   A. H. K. Owgi et al., "The preferable Ni quantity to boost the performance of FSA for dry reforming of methane," Fuel, vol. 332, p. 126124, Jan. 2023, doi: 10.1016/J.FUEL.2022.126124.

[53]   R. Babakouhi, S. M. Alavi, M. Rezaei, E. Akbari, and M. Varbar, "Combined CO$_2$ reforming and partial oxidation of methane over mesoporous nanostructured Ni/M-Al2O3 catalyst: Effect of various support promoters and nickel loadings," Journal of CO$_2$ Utilization, vol. 70, p. 102427, Apr. 2023, doi: 10.1016/J.JCOU.2023.102427.

[54]   Z. Alipour, M. Rezaei, and F. Meshkani, "Effect of Ni loadings on the activity and coke formation of MgO-modified Ni/Al$_2$O$_3$ nanocatalyst in dry reforming of methane," Journal of Energy Chemistry, vol. 23, no. 5, pp. 633–638, Sep. 2014, doi: 10.1016/S2095-4956(14)60194-7.

[55]   L. Zhou et al., "Thermal-Driven Fluorite–Pyrochlore–Fluorite Phase Transitions of Gd$_2$Zr$_2$O$_7$ Ceramics Probed in Large Range of Sintering Temperature," Metall Mater Trans A Phys Metall Mater Sci, vol. 47, no. 1, pp. 623–630, Jan. 2016, doi: 10.1007/s11661-015-3234-4.

[56]   G. Wei et al., "Immobilization mechanism of Gd$_2$Zr$_2$O$_7$ ceramic for nuclear waste treatment," Ceram Int, vol. 48, no. 24, pp. 37164–37173, Dec. 2022, doi: 10.1016/J.CERAMINT.2022.08.292.

[57]   S. K. Gupta, P. S. Ghosh, C. Reghukumar, N. Pathak, and R. M. Kadam, "Experimental and theoretical approach to account for green luminescence from $Gd_2Zr_2O_7$ pyrochlore: Exploring the site occupancy and origin of host-dopant energy transfer in $Gd_2Zr_2O_7$:Eu^{3+}," RSC Adv, vol. 6, no. 50, pp. 44908–44920, 2016, doi: 10.1039/c6ra05113h.

[58]   E. T. Kho, S. Jantarang, Z. Zheng, J. Scott, and R. Amal, "Harnessing the Beneficial Attributes of Ceria and Titania in a Mixed-Oxide Support for Nickel-Catalyzed Photothermal CO_2 Methanation," Engineering, vol. 3, no. 3, pp. 393–401, Jun. 2017, doi: 10.1016/J.ENG.2017.03.016.

[59]   L. Huang et al., "Optimization of Ni-Based Catalysts for Dry Reforming of Methane via Alloy Design: A Review," Energy & Fuels, vol. 36, no. 10, pp. 5102–5151, May 2022, doi: 10.1021/acs.energyfuels.2c00523.

[60]   J. R. Rostrup-Nielsen and J. H. Bak Hansen, "CO_2-Reforming of Methane over Transition Metals," J Catal, vol. 144, no. 1, pp. 38–49, Nov. 1993, doi: 10.1006/JCAT.1993.1312.

[61]   Z. Zou et al., "Controllable Preparation of Nano-Ni to Eliminate Step Edges of Carbon Deposition on Ni-Based Catalysts for Methane Dry Reforming," Industrial & Engineering Chemistry Research, vol. 62, no. 15, pp. 6039–6051, Apr. 2023, doi: 10.1021/acs.iecr.2c04333.

[62]   N. Laosiripojana and S. Assabumrungrat, "Catalytic dry reforming of methane over high surface area ceria," Appl Catal B, vol. 60, no. 1–2, pp. 107–116, Sep. 2005, doi: 10.1016/J.APCATB.2005.03.001.

[63]   A. G. S. Hussien and K. Polychronopoulou, "A Review on the Different Aspects and Challenges of the Dry Reforming of Methane (DRM) Reaction," Nanomaterials, vol. 12, no. 19, p. 3400, Sep. 2022, doi: 10.3390/nano12193400.

[64]   S. Corthals et al., "Influence of composition of $MgAl_2O_4$ supported $NiCeO_2ZrO_2$

catalysts on coke formation and catalyst stability for dry reforming of methane," Catal Today, vol. 138, no. 1–2, pp. 28–32, Oct. 2008, doi: 10.1016/J.CATTOD.2008.04.038.

[65]   I. V. Yentekakis, P. Panagiotopoulou, and G. Artemakis, "A review of recent efforts to promote dry reforming of methane (DRM) to syngas production via bimetallic catalyst formulations," Appl Catal B, vol. 296, p. 120210, Nov. 2021, doi: 10.1016/J.APCATB.2021.120210.

[66]   E. Ruckenstein and Y. H. Hu, "Role of Support in CO_2 Reforming of CH_4 to Syngas over Ni Catalysts," J Catal, vol. 162, no. 2, pp. 230–238, Sep. 1996, doi: 10.1006/JCAT.1996.0280.

[67]   M. Shah and P. Mondal, "Optimization of CO_2 reforming of methane process for the syngas production over Ni–Ce/TiO_2–ZrO_2 catalyst using the Taguchi method," Int J Hydrogen Energy, vol. 46, no. 44, pp. 22799–22812, Jun. 2021, doi: 10.1016/j.ijhydene.2021.04.091.

[68]   Z. Zuo et al., "Dry Reforming of Methane on Single-Site Ni/MgO Catalysts: Importance of Site Confinement," ACS Catal, vol. 8, no. 10, pp. 9821–9835, Sep. 2018, doi: 10.1021/acscatal.8b02277.

[69]   V. Stivenson Sandoval-Bohórquez, E. M. Morales-Valencia, C. O. Castillo-Araiza, L. M. Ballesteros-Rueda, and V. G. Baldovino-Medrano, "Kinetic Assessment of the Dry Reforming of Methane over a Ni–La_2O_3 Catalyst," ACS Catal, vol. 11, no. 18, pp. 11478–11493, Sep. 2021, doi: 10.1021/acscatal.1c02631.

[70]   N. D. Charisiou et al., "An indepth investigation of deactivation through carbon formation during the biogas dry reforming reaction for Ni supported on modified with CeO_2 and La_2O_3 zirconia catalysts," Int J Hydrogen Energy, vol. 43, no. 41, pp. 18955–18976, Oct. 2018, doi: 10.1016/J.IJHYDENE.2018.08.074.

[71]   M. A. Salaev, L. F. Liotta, and O. V. Vodyankina, "Lanthanoid-containing Ni-based catalysts for dry reforming of methane: A review," Int J Hydrogen Energy, vol. 47, no. 7,

pp. 4489–4535, Jan. 2022, doi: 10.1016/J.IJHYDENE.2021.11.086.

[72]   P. B. Managutti et al., "Exsolution of Ni Nanoparticles from A-Site-Deficient Layered Double Perovskites for Dry Reforming of Methane and as an Anode Material for a Solid Oxide Fuel Cell," ACS Applied Materials & Interfaces, vol. 13, no. 30, pp. 35719–35728, Jul. 2021, doi: 10.1021/acsami.1c08158.

[73]   A. H. Khoja et al., "Thermal dry reforming of methane over La_2O_3 co-supported Ni/MgAl2O4 catalyst for hydrogen-rich syngas production," Research on Chemical Intermediates, vol. 46, no. 8, pp. 3817–3833, Aug. 2020, doi: 10.1007/s11164-020-04174-z.

[74]   P. K. Yadav and T. Das, "Production of syngas from carbon dioxide reforming of methane by using $LaNi_xFe_{1-x}O_3$ perovskite type catalysts," Int J Hydrogen Energy, vol. 44, no. 3, pp. 1659–1670, Jan. 2019, doi: 10.1016/J.IJHYDENE.2018.11.108.

[75]   F. Touahra et al., "Enhanced catalytic behaviour of surface dispersed nickel on $LaCuO_3$ perovskite in the production of syngas: An expedient approach to carbon resistance during CO_2 reforming of methane," Int J Hydrogen Energy, vol. 41, no. 4, pp. 2477–2486, Jan. 2016, doi: 10.1016/J.IJHYDENE.2015.12.062.

[76]   M. H. Aghaali and S. Firoozi, "Enhancing the catalytic performance of Co substituted $NiAl_2O_4$ spinel by ultrasonic spray pyrolysis method for steam and dry reforming of methane," Int J Hydrogen Energy, vol. 46, no. 1, pp. 357–373, Jan. 2021, doi: 10.1016/J.IJHYDENE.2020.09.157.

[77]   S. Andraos et al., "Production of hydrogen by methane dry reforming over ruthenium-nickel based catalysts deposited on Al_2O_3, $MgAl_2O_4$, and YSZ," Int J Hydrogen Energy, vol. 44, no. 47, pp. 25706–25716, Oct. 2019, doi: 10.1016/J.IJHYDENE.2019.08.081.

[78]   N. D. Charisiou, A. Iordanidis, K. Polychronopoulou, I. V. Yentekakis, and M. A. Goula, "Studying the stability of Ni supported on modified with CeO_2 alumina catalysts for

the biogas dry reforming reaction," Mater Today Proc, vol. 5, no. 14, pp. 27607–27616, Jan. 2018, doi: 10.1016/J.MATPR.2018.09.081.

[79]   S. Das et al., "Silica–Ceria sandwiched Ni core–shell catalyst for low temperature dry reforming of biogas: Coke resistance and mechanistic insights," Appl Catal B, vol. 230, pp. 220–236, Aug. 2018, doi: 10.1016/J.APCATB.2018.02.041.

[80]   M. L. Chaudhary et al., "Promotional effect of addition of ceria over yttria-zirconia supported Ni based catalyst system for hydrogen production through dry reforming of methane," Int J Hydrogen Energy, vol. 47, no. 48, pp. 20838–20850, Jun. 2022, doi: 10.1016/J.IJHYDENE.2022.04.199.

[81]   A. Panghal, Y. Kumar, F. Singh, and N. L. Singh, "Role of structural ordering on the radiation response of $Gd_2Zr_2O_7$ pyrochlore," Ceram Int, vol. 49, no. 8, pp. 12191–12200, Apr. 2023, doi: 10.1016/J.CERAMINT.2022.12.071.

[82]   Y. H. Lee, H. S. Sheu, J. P. Deng, and H. C. I. Kao, "Preparation and fluorite–pyrochlore phase transformation in $Gd_2Zr_2O_7$," J Alloys Compd, vol. 487, no. 1–2, pp. 595–598, Nov. 2009, doi: 10.1016/J.JALLCOM.2009.08.021.

[83]   B. P. Mandal, N. Garg, S. M. Sharma, and A. K. Tyagi, "Solubility of ThO_2 in $Gd_2Zr_2O_7$ pyrochlore: XRD, SEM and Raman spectroscopic studies," Journal of Nuclear Materials, vol. 392, no. 1, pp. 95–99, Jul. 2009, doi: 10.1016/J.JNUCMAT.2009.03.050.

[84]   M. Alagiri, S. Ponnusamy, and C. Muthamizhchelvan, "Synthesis and characterization of NiO nanoparticles by sol-gel method," Journal of Materials Science: Materials in Electronics, vol. 23, no. 3, pp. 728–732, Mar. 2012, doi: 10.1007/s10854-011-0479-6.

[85]   D. Parimi, V. Sundararajan, O. Sadak, S. Gunasekaran, S. S. Mohideen, and A. Sundaramurthy, "Synthesis of Positively and Negatively Charged CeO_2 Nanoparticles: Investigation of the Role of Surface Charge on Growth and Development of Drosophila melanogaster," ACS Omega, vol. 4, no. 1, pp. 104–113, Jan. 2019, doi:

10.1021/acsomega.8b02747.

[86]   N. Ishikawa et al., "Study of structural change in CeO_2 irradiated with high-energy ions by means of X-ray diffraction measurement," Nucl Instrum Methods Phys Res B, vol. 266, no. 12–13, pp. 3033–3036, Jun. 2008, doi: 10.1016/J.NIMB.2008.03.159.

[87]   Y. Wang, B. Gao, Q. Wang, X. Li, Z. Su, and A. Chang, "$A_2Zr_2O_7$ (A = Nd, Sm, Gd, Yb) zirconate ceramics with pyrochlore-type structure for high-temperature negative temperature coefficient thermistor," J Mater Sci, vol. 55, no. 32, pp. 15405–15414, Nov. 2020, doi: 10.1007/s10853-020-05104-5.

[88]   A. F. Fuentes, S. M. Montemayor, M. Maczka, M. Lang, R. C. Ewing, and U. Amador, "A Critical Review of Existing Criteria for the Prediction of Pyrochlore Formation and Stability," Inorg Chem, vol. 57, no. 19, pp. 12093–12105, Sep. 2018, doi: 10.1021/acs.inorgchem.8b01665.

[89]   C. Schilling, A. Hofmann, C. Hess, and M. Verónica Ganduglia-Pirovano, "Raman Spectra of Polycrystalline CeO2: A Density Functional Theory Study," The Journal of Physical Chemistry C, vol. 121, no. 38, pp. 20834–20849, Sep. 2017, doi: 10.1021/acs.jpcc.7b06643.

[90]   S. Wang, W. Wang, J. Zuo, and Y. Qian, "Study of the Raman spectrum of CeO_2 nanometer thin films," 2001.

[91]   M. A. Ebiad, D. R. Abd El-Hafiz, R. A. Elsalamony, and L. S. Mohamed, "Ni supported high surface area CeO_2-ZrO_2 catalysts for hydrogen production from ethanol steam reforming," RSC Adv, vol. 2, no. 21, pp. 8145–8156, 2012, doi: 10.1039/c2ra20258a.

[92]   P. Hongmanorom et al., "Zr–Ce-incorporated Ni/SBA-15 catalyst for high-temperature water gas shift reaction: Methane suppression by incorporated Zr and Ce," J Catal, vol. 387, pp. 47–61, Jul. 2020, doi: 10.1016/J.JCAT.2019.11.042.

[93]   J. Chen and X. Wang, "Fabrication and characterization of novel excellent thermal-protection $Gd_2Zr_2O_7$/ZrO_2 composite ceramic fibers with different proportions of

Gd$_2$Zr$_2$O$_7$," Ceram Int, vol. 46, no. 15, pp. 24029–24037, Oct. 2020, doi: 10.1016/J.CERAMINT.2020.06.180.

[94]   J. Pang, W. Li, Z. Cao, J. Xu, X. Li, and X. Zhang, "Mesoporous Cu $_2$ O–CeO$_2$ composite nanospheres with enhanced catalytic activity for 4-nitrophenol reduction," Appl Surf Sci, vol. 439, pp. 420–429, May 2018, doi: 10.1016/j.apsusc.2018.01.055.

[95]   J. Lian, P. Liu, C. Jin, Z. Shi, X. Luo, and Q. Liu, "Perylene diimide-functionalized CeO 2 nanocomposite as a peroxidase mimic for colorimetric determination of hydrogen peroxide and glutathione," Microchimica Acta, vol. 186, no. 6, Jun. 2019, doi: 10.1007/s00604-019-3439-0.

[96]   R. P. Ye et al., "High-performance of nanostructured Ni/CeO$_2$ catalyst on CO$_2$ methanation," Appl Catal B, vol. 268, p. 118474, Jul. 2020, doi: 10.1016/J.APCATB.2019.118474.

[97]   J. Fan, X. Wu, X. Wu, Q. Liang, R. Ran, and D. Weng, "Thermal ageing of Pt on low-surface-area CeO$_2$-ZrO$_2$-La$_2$O$_3$ mixed oxides: Effect on the OSC performance," Appl Catal B, vol. 81, no. 1–2, pp. 38–48, May 2008, doi: 10.1016/j.apcatb.2007.11.022.

[98]   B. P. Payne, M. C. Biesinger, and N. S. McIntyre, "Use of oxygen/nickel ratios in the XPS characterisation of oxide phases on nickel metal and nickel alloy surfaces," J Electron Spectros Relat Phenomena, vol. 185, no. 5–7, pp. 159–166, Aug. 2012, doi: 10.1016/J.ELSPEC.2012.06.008.

[99]   P. Salunkhe, A. V. Muhammed Ali, and D. Kekuda, "Investigation on tailoring physical properties of Nickel Oxide thin films grown by dc magnetron sputtering," Mater Res Express, vol. 7, no. 1, 2020, doi: 10.1088/2053-1591/ab69c5.

[100]   S. C. Yang et al., "Synergy between Ceria Oxygen Vacancies and Cu Nanoparticles Facilitates the Catalytic Conversion of CO$_2$ to CO under Mild Conditions," ACS Catal, vol. 8, no. 12, pp. 12056–12066, Dec. 2018, doi: 10.1021/acscatal.8b04219.

[101]   K. Lorber et al., "CO$_2$ Activation over Nanoshaped CeO$_2$ Decorated with Nickel for

Low-Temperature Methane Dry Reforming," ACS Appl Mater Interfaces, vol. 14, no. 28, pp. 31862–31878, Jul. 2022, doi: 10.1021/acsami.2c05221.

[102]   G. N. Vayssilov, M. Mihaylov, P. S. Petkov, K. I. Hadjiivanov, and K. M. Neyman, "Reassignment of the vibrational spectra of carbonates, formates, and related surface species on ceria: A combined density functional and infrared spectroscopy investigation," Journal of Physical Chemistry C, vol. 115, no. 47, pp. 23435–23454, Dec. 2011, doi: 10.1021/jp208050a.

[103]   Z. Liu et al., "Highly Active Ceria-Supported Ru Catalyst for the Dry Reforming of Methane: In Situ Identification of $Ru^{\delta+}$-Ce^{3+} Interactions for Enhanced Conversion," ACS Catal, vol. 9, no. 4, pp. 3349–3359, Apr. 2019, doi: 10.1021/acscatal.8b05162.

[104]   X. Zhang, Y. Su, C. Pei, Z. J. Zhao, R. Liu, and J. Gong, "Chemical looping steam reforming of methane over Ce-doped perovskites," Chem Eng Sci, vol. 223, p. 115707, Sep. 2020, doi: 10.1016/J.CES.2020.115707.

[105]   M. González-castaño et al., "Article nickel phosphide catalysts as efficient systems for CO_2 upgrading via dry reforming of methane," Catalysts, vol. 11, no. 4, Apr. 2021, doi: 10.3390/catal11040446.

[106]   A. M. Gadalla and B. Bower, "The role of catalyst support on the activity of nickel for reforming methane with CO_2," Chem Eng Sci, vol. 43, no. 11, pp. 3049–3062, Jan. 1988, doi: 10.1016/0009-2509(88)80058-7.

[107]   C. Klinke, R. Kurt, J.-M. Bonard, and K. Kern, "Raman Spectroscopy and Field Emission Measurements on Catalytically Grown Carbon Nanotubes," J Phys Chem B, vol. 106, no. 43, pp. 11191–11195, Oct. 2002, doi: 10.1021/jp0215217.

[108]   L. M. Cornaglia, J. Múnera, S. Irusta, and E. A. Lombardo, "Raman studies of Rh and Pt on La2O3 catalysts used in a membrane reactor for hydrogen production," Appl Catal A Gen, vol. 263, no. 1, pp. 91–101, May 2004, doi: 10.1016/J.APCATA.2003.12.003.

[109]   Y. Zhou, D. Haynes, J. Baltrus, A. Roy, D. Shekhawat, and J. J. Spivey, "Methane

steam reforming at low steam-to-carbon ratio: The effect of Y doping in Rh substituted lanthanum zirconates," Appl Catal A Gen, vol. 606, Sep. 2020, doi: 10.1016/j.apcata.2020.117802.

[110] E. Le Saché et al., "Multicomponent Ni-CeO$_2$ nanocatalysts for syngas production from CO$_2$/CH$_4$ mixtures," Journal of CO$_2$ Utilization, vol. 25, pp. 68–78, May 2018, doi: 10.1016/j.jcou.2018.03.012.

Chapter 3
Synthesis and screening of Perovskite-based catalyst (ABO₃) in DRM

3.1 Introduction:

 The perovskite material was first discovered as a mineral of $CaTiO_3$ by Gustav Ross and named after mineralogist L.A. Perovski. Perovskite formulates as ABX_3 where A and B are positively charged ions and X, mostly oxide ions with a negative charge. Structure comprised of A ions generally larger in size than B which are 12-fold cuboctahedron coordinates and 6-fold coordinates surrounded by octahedra of anions respectively[1]. A cations of perovskite materials play as support usually incorporated with alkaline metals, alkaline earth metals and rare earth metals while B is generally transition and Nobel metals utilized as catalytic sites[2]. Perovskite materials need high calcination temperatures to attain their structure usually crystallized in a cubic phase; however, different metal substitutions, doping, and synthesis processes alter the structure in various phases like orthorhombic, monoclinic, and rhombohedral[3]. To attain neutrality and stable crystallite phase, various oxidation states of A and B site cations provide variety of possible distributions like $A_IB_VO_3$, $A_{II}B_{IV}O_3$, $A_{III}B_{III}O_3$, $A_{IV}B_{III}O_3$ [4]. These structural variations make perovskites attractive for different industrial applications like sensors, solar cells, fuel cells, electrochemical, photocatalysis, and in various catalytic reactions. Syngas synthesis by dry reforming reactions using perovskite-based catalysts has been studied immensely due to their thermal stability, structural and physiochemical properties[5][6][7][8][9][10][11]. Conventional supported catalysts are widely used for dry reforming reactions but deactivate within few hours due to active metal species agglomeration and carbon accumulation during methane activation at elevated reaction temperature. To overcome these challenges, structured perovskite-based catalysts are investigated and proved to be good candidates in coke gasification with higher and stable activity in DRM owing to high temperature stability. Even though, high thermal stability causes low surface area, exsolution of metal particles over the catalyst surface provides more active sites for continuous and high activity in dry reforming reaction[12].

"*A*" site substitution plays a crucial role in carbon suppression as it generates defects in the lattice by doping of different metals with different ratios, triggers the formation of oxygen vacancies and enhances the ionic conductivity of oxygen ions resulting in gasification of carbon providing prolonged activity in dry reforming reaction. These defects produce surface hydroxyl and active oxygen species which improve the dissociative adsorption of CO_2 as CO and oxidation of carbon formed during CH_4 activation on the metal surface and metal support interphase. Moreover, alkaline earth metals like Ca, Sr, Mg and Y as A site substituent are studied as promoters in dry reforming reactions as they enhance the basic sites on the catalyst surface, and promotes the adsorption of acidic CO_2. While *B* site substitution affects the successive methane decomposition and hydrogen generation. Ni-substituted perovskite materials are majorly screened in dry reforming reactions because of their ability to cleave C-H bond of methane due to higher electron cloud density, low cost and abundance[13]. However, metal sintering and carbon formation is high with Ni-based catalysts at high reaction temperatures resulting in fast deactivation of the catalyst. Nevertheless, along with Ni, different noble metals like Ru, Rh, Pt and transition metals like Co, Fe, Cu were also substituted in perovskite structure and proved to be highly stable and active for DRM with the synergetic effect of bimetals in the structure[14]. Apart from that, redox properties of transition and rare earth metals hop in different oxidation states, boost the defect formation and ion mobility in the catalyst which surpass the coke agglomeration on active metals of the catalyst[15][16]. Currently, MnOx has been immensely utilized in dry reforming of methane as promoter providing basic sites to the support and enhance CO_2 adsorption. Moreover, the addition of Mn in the support stabilizes the Ni in metallic form and enhance the reducibility of catalyst[17][18]. So, a catalyst with good catalytic activity, stability and carbon resistant capabilities in DRM is crucial. Hence, in this chapter, Ni substituted $SrMnO_3$ perovskite-based catalyst was synthesized and screened in dry reforming reaction. Additionally, the effect of rare earth substitution in A site of

$SrMn_{0.8}Ni_{0.2}O_3$ catalyst on DRM activity was also investigated.

3.2 Experimental Section:

3.2.1 Synthesis of $Ln_{0.2}Sr_{1-x}Mn_{0.8}Ni_{0.2}O_3$ (Ln= Nd, Sm, Eu):

The rare earth substituted $Ln_{0.2}Sr_{1-x}Mn_{0.8}Ni_{0.2}O_3$ (X= Nd, Sm, Eu) perovskite-type catalysts was synthesized by the citrate gel method. The metal nitrates Sr $(NO_3)_2$, Ni $(NO_3)_2.6H_2O$, and lanthanide nitrates were mixed in distilled water separately and mixed together at room temperature. This solution was added to the citric acid solution with a 3:1 (citric acid: nitrate precursor) ratio and stirred at 180 °C till foam-like material was obtained. Afterward, this material is kept in the oven at 180°C overnight for water removal and polyesterification. The dried material was crushed in powder form and calcined at 800 °C for 6h in an air atmosphere.

3.2.2 Catalyst evaluation:

Dry reforming of methane (DRM) was conducted in a packed-bed tubular reactor made up of quartz and reaction procedure has been followed as mentioned in chapter 2.

3.3 Result and discussion:

3.3.1 Structural analysis of $Ln_{0.2}Sr_{1-x}Mn_{0.8}Ni_{0.2}O_3$ (Ln= Nd, Sm, Eu):

The XRD pattern of $Ln_{0.2}Sr_{1-x}Mn_{0.8}Ni_{0.2}O_3$ (Ln= Nd, Sm, Eu) catalysts as shown in Figure 3.1 confirmed the formation of $SrMnO_{3-\delta}$ catalyst with hexagonal phase and matched with standard ICSD code 00-024-1213 having P63/mmc space group [19][20][21]. Along with $SrMnO_{3-\delta}$ identical peaks, some impurity peaks of $SrCO_3$ and Mn_3O_4 were also observed in Ni-substituted catalysts[22]. Although, for activity comparison purposes, wt.% of Ni was kept similar in all catalysts. Lanthanide-substituted catalysts also crystallized in hexagonal phase with impurity peaks of $SrCO_3$ and Mn_3O_4 and no peak corresponding to lanthanide oxides were observed in lanthanide-substituted catalysts. Moreover, peak corresponding to Mn_3O_4 was observed after the doping of Ni in the B site of the catalysts confirming the

substitution of Ni in the lattice. Textural properties and the amount of Ni and rare earth metals added were tabulated in Table 3.1. Due to the high calcination temperature, surface area of $SrMnO_{3-\delta}$ is very less but substituted catalysts have little high surface area than parent catalyst.

Table 3.1: Textural property of $Ln_{0.2}Sr_{1-x}Mn_{0.8}Ni_{0.2}O_3$ (Ln= Nd, Sm, Eu)

Catalyst Name	Ni wt% added	RE wt% added	Surface area(m^2/g)
$SrMnO_{3-\delta}$		-	4.5
$SrMn_{0.8}Ni_{0.2}O_{3-\delta}$ (SMN2)	5.8		6.1
$Nd_{0.2}Sr_{0.8}Mn_{0.8}Ni_{0.2}O_{3-\delta}$ (NdSMN2)	5.8	11.2	10.2
$Sm_{0.2}Sr_{0.8}Mn_{0.8}Ni_{0.2}O_{3-\delta}$ (SmSMN2)	5.8	11.0	9.5
$Eu_{0.2}Sr_{0.8}Mn_{0.8}Ni_{0.2}O_{3-\delta}$ (EuSMN2)	5.8	11.5	13
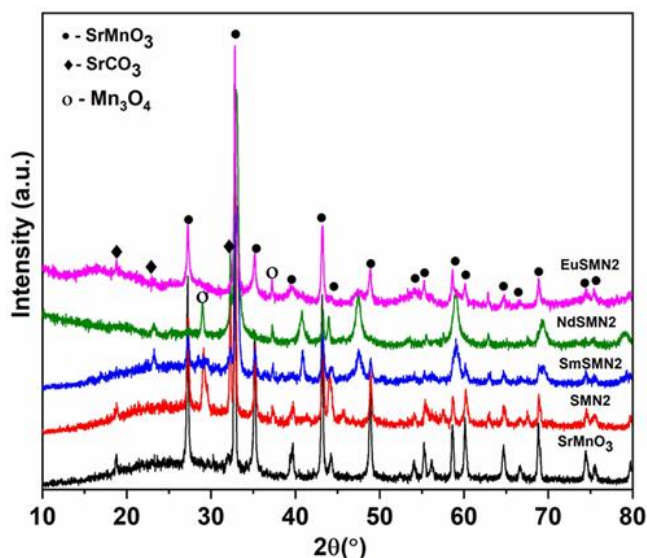
Figure 3.1: XRD pattern of $Ln_{0.2}Sr_{1-x}Mn_{0.8}Ni_{0.2}O_3$ (Ln= Nd, Sm, Eu) catalysts

3.3.2 Temperature programmed reduction of $Ln_{0.2}Sr_{1-x}Mn_{0.8}Ni_{0.2}O_3$ (Ln= Nd, Sm, Eu):

It was reported that Mn enhances the reducibility of Ni in catalysts by stabilizing it in the metallic form. Moreover, rare earth metal substitution enhances the reducibility of Ni-based catalysts because of their electron transfer capacity. To check the reducibility of all substituted catalysts, H_2 - TPR analysis has been employed. Figure 3.2 illustrates that

hydrogen consumption was observed at 200-210 °C in NdSMN2 and SmSMN2 catalysts which is due to the reduction of surface NiO. In all substituted catalysts, a second reduction peak was observed at 400-450 °C owing to the reduction of NiO which is present in sub-layers of support. In Nd and Sm based catalysts high-temperature reduction peaks were observed because of the reduction of bulk NiO and Ni^{+2} into metallic Ni. Low-temperature reduction peaks confirmed the presence of nicely dispersed NiO over the catalysts was also corroborated by XRD data as at 43.2° 2θ position peak corresponding to NiO is observed. Moreover, the high-temperature reduction peaks in Sm substituted SMN2 catalyst disclose that the doping of rare earth in the catalysts strengthens the metal support interaction leading to the reduction of bulk Ni^{+2} into metallic Ni [23].
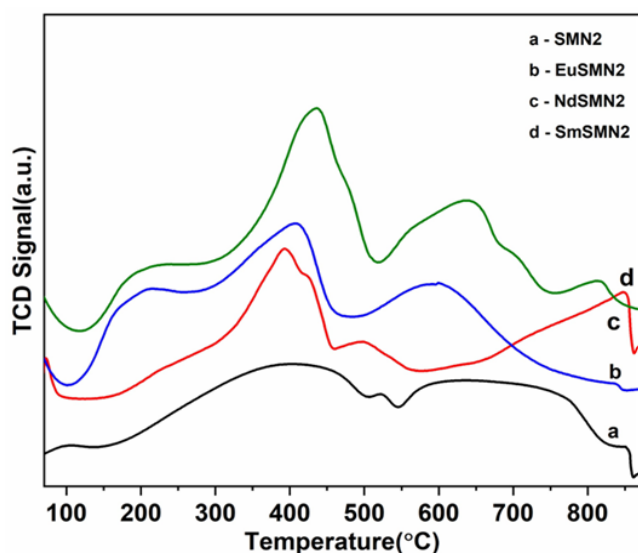
Figure 3.2: TPR Analysis of $Ln_{0.2}Sr_{1-x}Mn_{0.8}Ni_{0.2}O_3$ (Ln= Nd, Sm, Eu) catalysts

3.3.3 X- Ray photoelectron spectroscopy of $Ln_{0.2}Sr_{1-x}Mn_{0.8}Ni_{0.2}O_3$ (Ln= Nd, Sm, Eu):
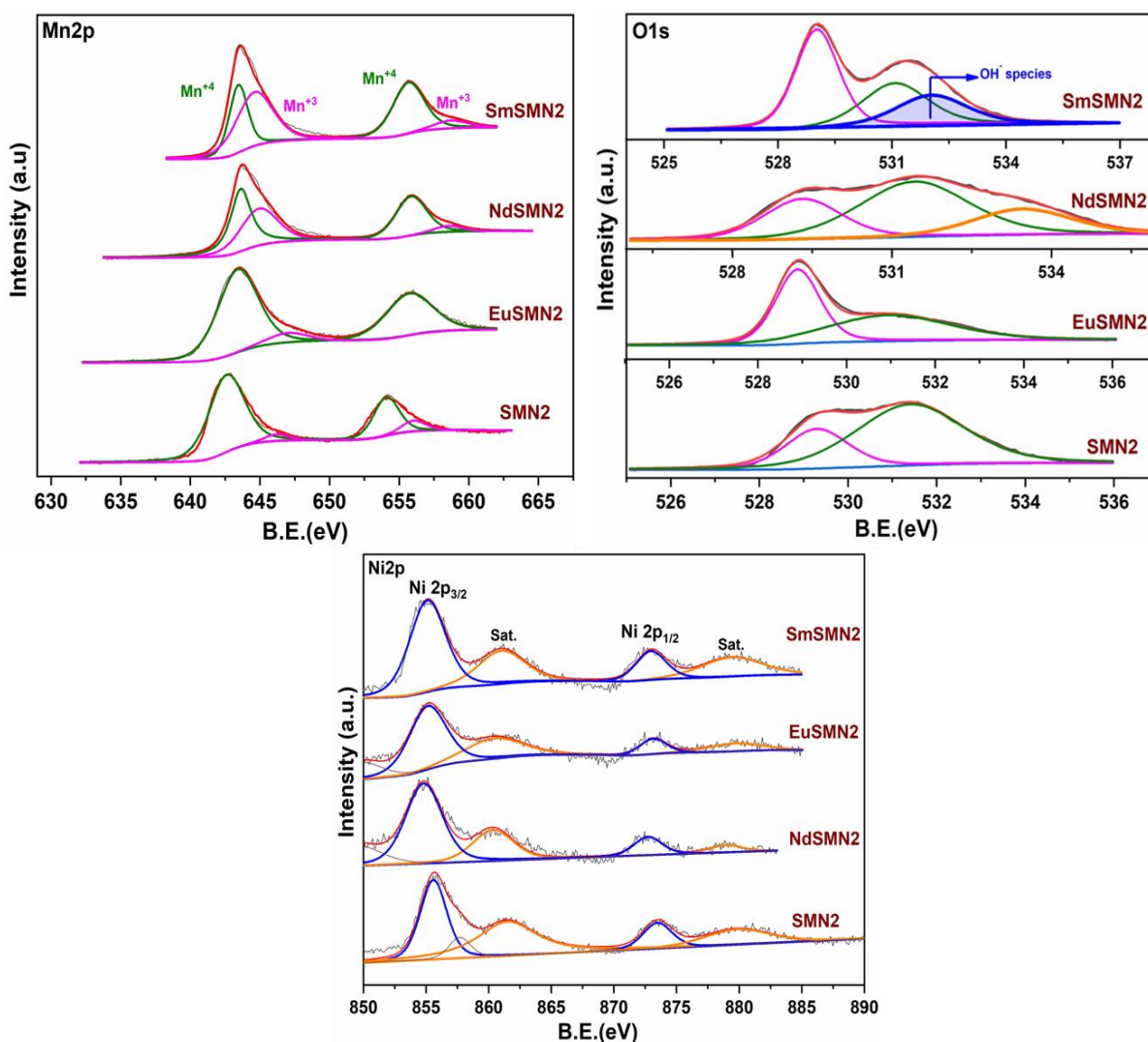
Figure 3.3: XPS spectra of Mn2p and O1s of SMN2, EuSMN2, NdSMN2 and SmSMN2 catalysts

XPS spectra of Mn 2p shown in Figure 3.3 illustrate the presence of Mn in a mixed valence state that is +3 and +4 in all substituted $SrMnO_{3-\delta}$ catalysts. In O1s spectrum, all catalysts have peaks corresponding to lattice oxygen and chemisorbed oxygen at 529.6 eV, and 531.4 eV respectively. However, in SmSMN2 catalysts along with these species the extra peak was observed at 532.6 eV binding energy is attributed to surface hydroxyl species. These species are formed due to defect originated oxygen vacancies. The Ni 2p spectrum showed the core level Ni2p$_{3/2}$ at 855.6 eV and satellite peak at 861.2 eV and Ni2p$_{1/2}$ at 873.5 eV and 879.6

eV (satellite) confirming the +2 oxidation state Ni and presences of of nickel oxide and hydroxide in substituted $SrMnO_{3-\delta}$ catalysts[24][25][26][27].

3.4 Catalytic activity of $Ln_{0.2}Sr_{1-x}Mn_{0.8}Ni_{0.2}O_3$ (Ln= Nd, Sm, Eu):
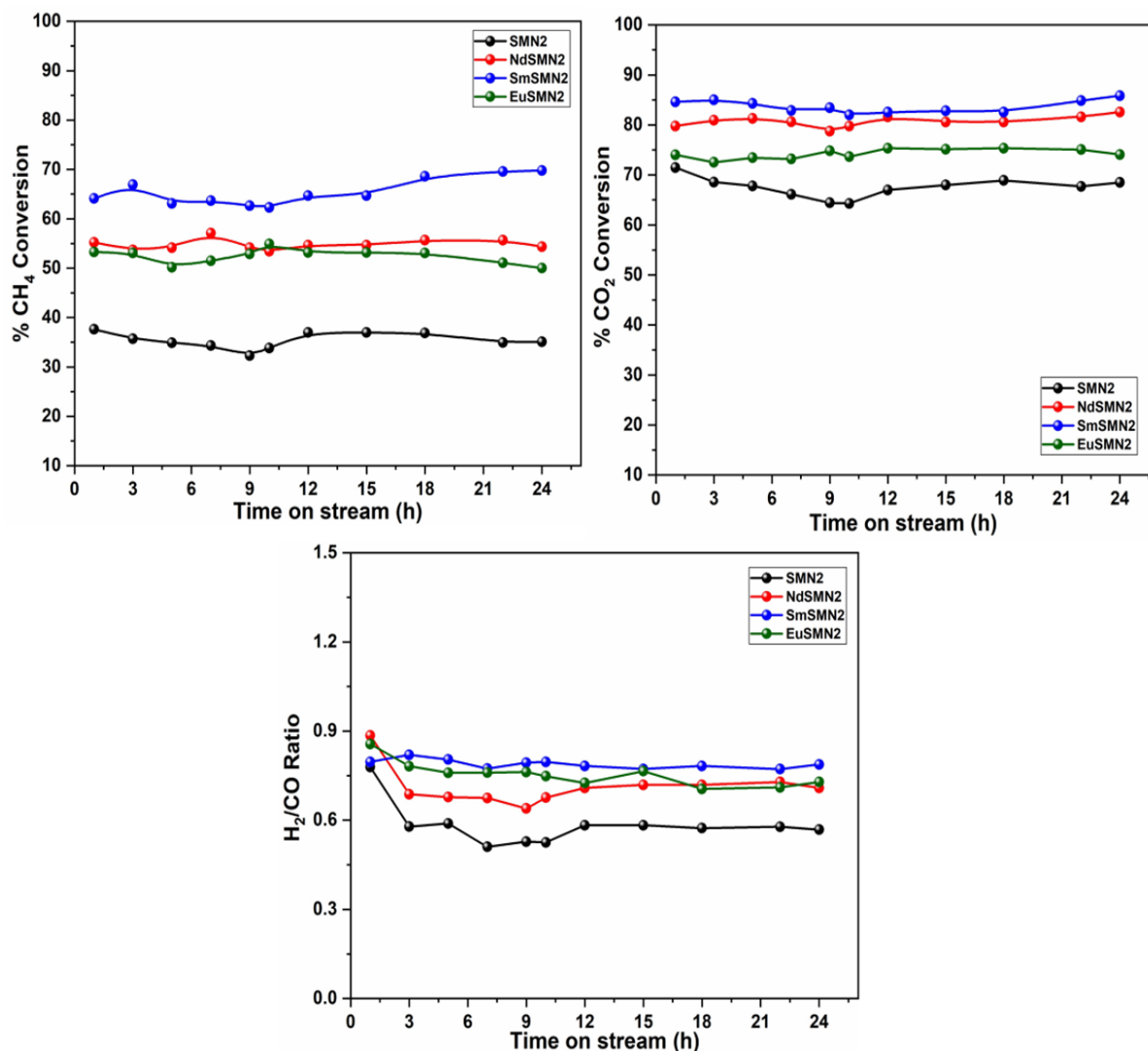
Figure 3.4: Activity analysis of SMN2, EuSMN2, NdSMN2 and SmSMN2 catalysts in DRM conditions: CH_4: CO_2: N_2 = 80:80:80 mL/min, 28,800 h^{-1} GHSV at 800 °C for 24 h time on stream. Conversions and H_2/CO ratios are plotted against time on stream

The catalytic activity of substituted $SrMnO_{3-\delta}$ catalysts has been checked for 24 h and results are plotted in figure 3.4. The rare earth metals substitution has shown a positive impact on the catalytic activity as the conversion of rare earth metal doped catalysts is higher than parent catalyst. For the parent catalyst SMN2 H_2/CO ratio is around 0.6 for 24 h which has been steadily increasing for rare earth doped catalysts. Among all catalysts, SmSMN2

catalysts have shown excellent activity towards DRM with around 70% of CH_4 and 85% of CO_2, and H_2/CO ratio was near unity which is 0.75. The low H_2/CO ratio is may be due to the ascendency of side reactions like reverse water gas shift reaction (4) and reverse Boudouard reaction (5). After evaluation of all catalysts, SmSMN2 catalyst has been chosen for durability test in DRM conditions.

3.4.1 Durability test of $Ln_{0.2}Sr_{1-x}Mn_{0.8}Ni_{0.2}O_3$ (Ln= Nd, Sm, Eu):

Since SmSMN2 showed stable and superior activity in optimum Dry reforming reaction conditions at 800 °C for 24 h, its activity was monitored for 100 h to check its durability. The conversion of CH_4 and CO_2 are stable at 70 and 85%. The H_2/CO ratio is also observed at 0.7. The stable activity may be due to continuous carbon gasification over the surface of the catalyst during the reaction and formed carbon is unable to block the active sites of the catalyst and keep the conversion stable. Probably, Sm substitution generates the hydroxyl species and enhanced the metal support interactions in the catalyst and helps in carbon removal, and kept the catalyst active for the long run.
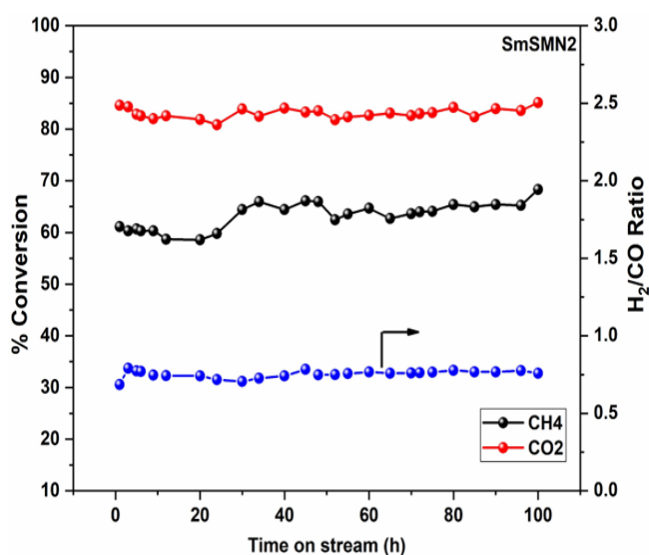
Figure 3.5: Durability analysis of SmSMN2 catalyst for 100h in DRM conditions: CH_4: CO_2: N_2 = 80:80:80 mL/min, 28,800 h^{-1} GHSV at 800 °C.

3.5 Spent catalysts characterization:

3.5.1 XRD analysis of spent catalysts:

To check the structure modifications after 24 h of DRM run, spent catalysts were analyzed by XRD and results are shown in figure 3.6. After the reaction, hexagonal structure was retained in all substituted catalysts. Apart from $SrMnO_{3-\delta}$ phase, additional peak of $SrCO_3$ was observed and a peak positioned at 26.4 ° 2θ corresponding to graphitic carbon was observed. From the data, it can be seen that peaks attributed to $SrCO_3$ are more intense than fresh catalysts, and the carbon which formed in the interlayer of support and metal was moulded in different carbon species observed in XRD data. Apart from that in parent SMN2 catalyst, a shoulder peak is also observed which may be due to the presence of amorphous carbon species on the catalyst surface[28][29]. The quantification of carbon species was carried out by TGA analysis.
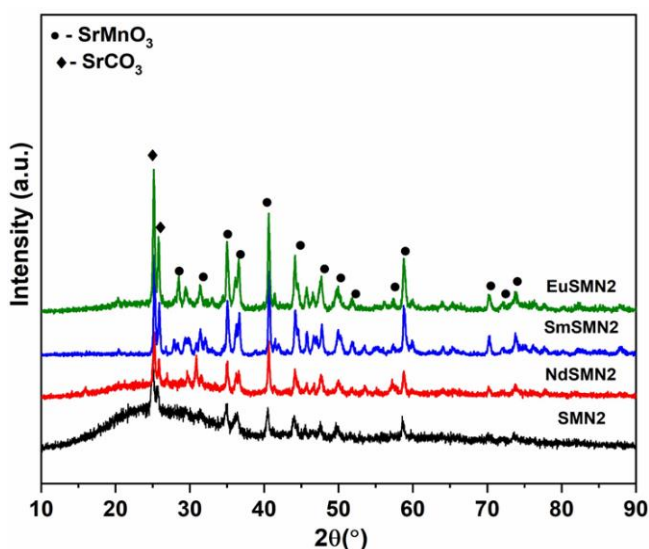
Figure 3.6: XRD analysis of spent catalysts screened for DRM.

3.5.2 TGA analysis of spent catalysts:

To calculate the amount of carbon formed after DRM screening, TGA analysis was employed in air atmosphere from a temperature range of 40-1000 °C and results were shown in figure 3.7. The plot indicates that the rare earth substitution has a positive impact on carbon suppression. The coke was formed more in the parent SMN2 catalyst. Among all rare earth substituted catalysts, Sm based catalyst has the lowest amount of carbon species.
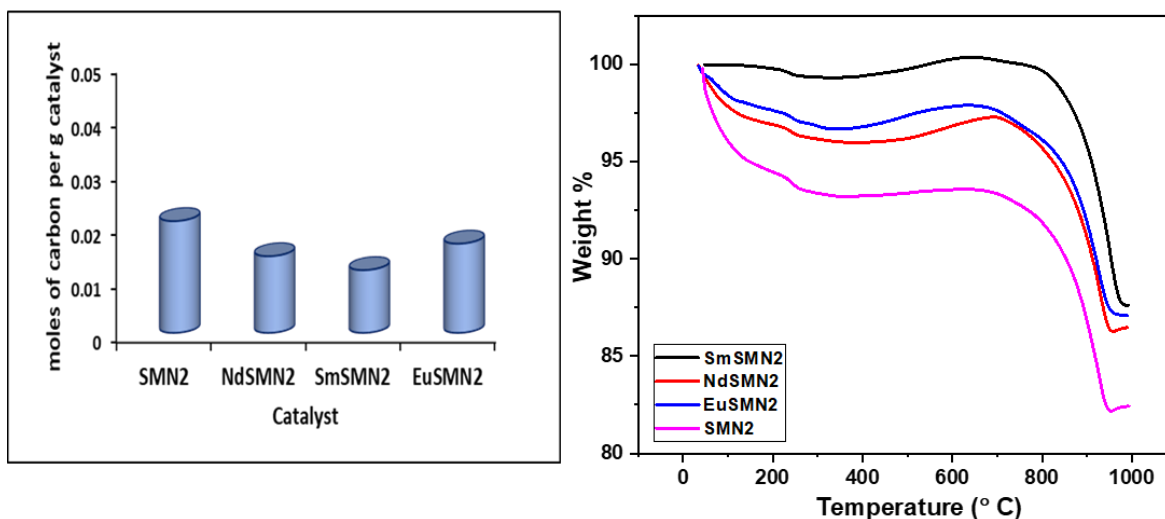
Figure 3.7: TGA analysis of spent catalysts screened for DRM.

3.6 Conclusion:

Perovskite-based $SrMnO_3$ was synthesized by citrate gel method and characterized by XRD, H_2-TPR, BET surface area technique, and XPS analysis. XRD analysis confirmed the formation of a hexagonal phase with P63/mmc space group.H_2-TPR studies confirmed the better reducibility of SmSMN2 catalyst compared to other catalysts as the catalyst has high reduction temperature peak along with lower reduction temperature peaks confirming the presence of surface NiO and the presence of Ni in sub-layers of support and in bulk as well with high metal support interaction. XPS data elucidate the presence of mixed valency of Mn in the +4 and +3 oxidation states. The O 1s spectrum showed the formation of hydroxyl species in SmSMN2 catalyst providing better and stable activity in DRM for 100 h time on stream with less carbon formation. Spent catalyst characterization like XRD and TGA analysis confirm the retention of parent phase and carbon formation. A higher amount of carbon was seen in SMN2, NdSMN2, and EuSMN2 catalysts while SmSMN2 has a lower quantity of carbon species elucidating the simultaneous carbon gasification and strong metal support interaction for longer hours of DRM.

3.7 References:

[1]   L. G. Tejuca, J. L. G. Fierro, and J. M. D. Tascón, "Structure and Reactivity of Perovskite-Type Oxides," Advances in Catalysis, vol. 36, no. C, pp. 237–328, Jan. 1989, doi: 10.1016/S0360-0564(08)60019-X.

[2]   M. Muraleedharan Nair and S. Kaliaguine, "Structured catalysts for dry reforming of methane," New Journal of Chemistry, vol. 40, no. 5, pp. 4049–4060, 2016, doi: 10.1039/C5NJ03268G.

[3]   S. Bhattar, M. A. Abedin, S. Kanitkar, and J. J. Spivey, "A review on dry reforming of methane over perovskite derived catalysts," Catal Today, vol. 365, pp. 2–23, Apr. 2021, doi: 10.1016/J.CATTOD.2020.10.041.

[4]   F. A. Kröger and H. J. Vink, "Relations between the Concentrations of Imperfections in Crystalline Solids," Solid State Physics - Advances in Research and Applications, vol. 3, no. C, pp. 307–435, Jan. 1956, doi: 10.1016/S0081-1947(08)60135-6.

[5]   L. G. Tejuca, J. L. G. Fierro, and J. M. D. Tascón, "Structure and Reactivity of Perovskite-Type Oxides," Advances in Catalysis, vol. 36, no. C, pp. 237–328, Jan. 1989, doi: 10.1016/S0360-0564(08)60019-X.

[6]   C. B. Alcock, R. C. Doshi, and Y. Shen, "Perovskite electrodes for sensors," Solid State Ion, vol. 51, no. 3–4, pp. 281–289, Apr. 1992, doi: 10.1016/0167-2738(92)90210-G.

[7]   S. Ahmad, A. Husain, M. M. Ali, K. I. Khana, A. Khancd, and A. M. Asiricd, "Perovskite-based material for sensor applications," Hybrid Perovskite Composite Materials: Design to Applications, pp. 135–145, Jan. 2021, doi: 10.1016/B978-0-12-819977-0.00005-6.

[8]   T. Salim, S. Sun, Y. Abe, A. Krishna, A. C. Grimsdale, and Y. M. Lam, "Perovskite-based solar cells: Impact of morphology and device architecture on device performance," J Mater Chem A Mater, vol. 3, no. 17, pp. 8943–8969, May 2015, doi: 10.1039/c4ta05226a.

[9]   G. Hodes, "Perovskite-based solar cells," Science, vol. 342, no. 6156. American

Association for the Advancement of Science, pp. 317–318, 2013. doi: 10.1126/science.1245473.

[10]   J. Sunarso, S. S. Hashim, N. Zhu, and W. Zhou, "Perovskite oxides applications in high temperature oxygen separation, solid oxide fuel cell and membrane reactor: A review," Prog Energy Combust Sci, vol. 61, pp. 57–77, Jul. 2017, doi: 10.1016/J.PECS.2017.03.003.

[11]   Z. Zhuang et al., "Reversely trapping atoms from a perovskite surface for high-performance and durable fuel cell cathodes," Nat Catal, vol. 5, no. 4, pp. 300–310, Apr. 2022, doi: 10.1038/s41929-022-00764-9.

[12]   F. Schrenk et al., "Impact of nanoparticle exsolution on dry reforming of methane: Improving catalytic activity by reductive pre-treatment of perovskite-type catalysts," Appl Catal B, vol. 318, Dec. 2022, doi: 10.1016/j.apcatb.2022.121886.

[13]   Z. Bian, Z. Wang, B. Jiang, P. Hongmanorom, W. Zhong, and S. Kawi, "A review on perovskite catalysts for reforming of methane to hydrogen production," Renewable and Sustainable Energy Reviews, vol. 134, p. 110291, Dec. 2020, doi: 10.1016/J.RSER.2020.110291.

[14]   K. Mabhouti, P. Norouzzadeh, and M. Taleb-Abbasi, "Effects of Fe, Co, or Ni substitution for Mn on $La_{0.7}Sr_{0.3}MnO_3$ perovskite: Structural, morphological, and optical analyses," J Non Cryst Solids, vol. 610, Jun. 2023, doi: 10.1016/j.jnoncrysol.2023.122283.

[15]   S. S. Mabaleha, F. Gholizadeh, and P. Kalita, "Recent advances in Ni-based stable catalysts for methane dry reforming: Stable catalysts' preparation review," Molecular Catalysis, vol. 547, p. 113398, Aug. 2023, doi: 10.1016/J.MCAT.2023.113398.

[16]   X. Zhang, Y. Su, C. Pei, Z. J. Zhao, R. Liu, and J. Gong, "Chemical looping steam reforming of methane over Ce-doped perovskites," Chem Eng Sci, vol. 223, p. 115707, Sep. 2020, doi: 10.1016/J.CES.2020.115707.

[17]   L. Yao, M. Elena Galvez, C. Hu, and P. Da Costa, "Synthesis Gas Production via Dry Reforming of Methane over Manganese Promoted Nickel/Cerium–Zirconium Oxide

Catalyst," Industrial & Engineering Chemistry Research, vol. 57, no. 49, pp. 16645–16656, Nov. 2018, doi: 10.1021/acs.iecr.8b04183.

[18]   X. Gao, W. Lin, Z. Ge, H. Ge, and S. Kawi, "Modification Strategies of Ni-Based Catalysts with Metal Oxides for Dry Reforming of Methane," Methane, vol. 1, no. 3, pp. 139–157, Jun. 2022, doi: 10.3390/methane1030012.

[19]   K. Sugahara, K. Kamata, S. Muratsugu, and M. Hara, "Amino Acid-Aided Synthesis of a Hexagonal $SrMnO_3$ Nanoperovskite Catalyst for Aerobic Oxidation," ACS Omega, vol. 2, no. 4, pp. 1608–1616, Apr. 2017, doi: 10.1021/acsomega.7b00146.

[20]   N. Pandey and A. K. Thakur, "Studies on structural and electrical properties of $SrMnO_{3-\delta}$," Advances in Applied Ceramics, vol. 109, no. 2, pp. 83–90, Feb. 2010, doi: 10.1179/174367509X12503626841433.

[21]   P. G. R. Achary, A. A. Nayak, R. K. Bhuyan, R. N. P. Choudhary, and S. K. Parida, "Effect of cerium dopant on the structural and electrical properties of $SrMnO_3$ single perovskite," J Mol Struct, vol. 1226, Feb. 2021, doi: 10.1016/j.molstruc.2020.129391.

[22]   S. K. Abbas, S. Atiq, S. Riaz, and S. Naseem, "Thermally activated variations in conductivity and activation energy in $SrMnO_3$," Journal of Materials Science: Materials in Electronics, vol. 28, no. 10, pp. 7171–7176, May 2017, doi: 10.1007/s10854-017-6397-5.

[23]   S. Mahammadunnisa, P. Manoj Kumar Reddy, N. Lingaiah, and C. Subrahmanyam, "$NiO/Ce_{1-x}Ni_xO_{2-\delta}$ as an alternative to noble metal catalysts for CO oxidation," Catal Sci Technol, vol. 3, no. 3, pp. 730–736, Mar. 2013, doi: 10.1039/c2cy20641b.

[24]   L. Yao, M. E. Galvez, C. Hu, and P. Da Costa, "Synthesis Gas Production via Dry Reforming of Methane over Manganese Promoted Nickel/Cerium-Zirconium Oxide Catalyst," Ind Eng Chem Res, vol. 57, no. 49, pp. 16645–16656, Dec. 2018, doi: 10.1021/acs.iecr.8b04183.

[25]   C. Chen, X. T. Wang, J. H. Zhong, J. Liu, G. I. N. Waterhouse, and Z. Q. Liu, "Epitaxially Grown Heterostructured $SrMn_3O_{6-x}$-$SrMnO_3$ with High-Valence Mn3+/4+ for

Improved Oxygen Reduction Catalysis," Angewandte Chemie - International Edition, vol. 60, no. 40, pp. 22043–22050, Sep. 2021, doi: 10.1002/anie.202109207.

[26]   J. Yue et al., "Effect of Nd doping on structure, magnetic properties and microwave absorption performance of $SrMnO_3$," Journal of Rare Earths, Mar. 2023, doi: 10.1016/J.JRE.2023.03.002.

[27]   F. Wang et al., "Oxygen vacancy formation, crystal structures, and magnetic properties of three $SrMnO_{3-\delta}$ films," Appl Phys Lett, vol. 109, no. 5, Aug. 2016, doi: 10.1063/1.4960463.

[28]   Z. Asgari-Fard, M. Sabet, and M. Salavati-Niasari, "Synthesis and characterization of strontium carbonate nanostructures via simple hydrothermal method," High Temperature Materials and Processes, vol. 35, no. 2, pp. 215–220, Feb. 2016, doi: 10.1515/htmp-2014-0232.

[29]   B. Manoj and A. G. Kunjomana, "Study of Stacking Structure of Amorphous Carbon by X-Ray Diffraction Technique," 2012. [Online]. Available: www.electrochemsci.org

Chapter 4

Synthesis and screening of layered metal oxide Na$_2$Ti$_3$O$_7$ catalyst in DRM

4.1 Introduction:

Layered metal oxides are a category of heterogeneous catalysts with stacks of metal oxide layers interleaved by cations and anions. This class of metal oxides covers several interlayered catalytic systems with different metals, structures, properties, and various arrangements of composite elements. For example, layered perovskites formulated as ABX_3, where A cations are arranged in cuboctahedral cavity of oxygen ions, whereas B is present in octahedra of 6 oxygen ions, are further sub-categorized in Ruddlesden Popper phase and Dion Jacobson phase [1][2][3]. Another class of oxygen-deficient layered perovskite is brownmillerites with different arrangements of constituent metals with formula $A_2B_2O_5$ having alternate layers of oxygen octahedra and tetrahedra, extensively been utilized in electrochemical applications [4][5]. Additionally, another class of layered metal oxides is double-layered hydroxides (LDHs) with metal oxides sheets separated by anions. The LDHs can be represented by the general formula: $[M_{2+1-x}M_{3+x}(OH)_2]_x+(A_{n-})_{x/n}.mH_2O$, where M^{2+} and M^{3+} are the divalent and trivalent cations, An- is the interlayer anion with n- charge. In these types of structures when divalent cations are replaced by trivalent cations for different applications, the charge compensation and structure stability are achieved by insertion of negatively charged hydrated anions[6].

A new class of layered titanates with the general formula $A_2Ti_nO_{2n+1}$ (n=3 or 8, and A=Na, K, Li) crystalizes in a monoclinic crystal structure. This class of titanium based layered oxides has various compounds like Na_2TiO_4, α-Na_2TiO_3, β- Na_2TiO_3, γ- Na_2TiO_3, $Na_4Ti_5O_{12}$, $Na_2Ti_6O_{13}$, and $Na_2Ti_3O_7$ based on their metal arrangement [7]. Na_2TiO_3 has Ti atoms that are bounded to oxygen atoms in trigonal bipyramidal coordination, arranged in c axis while sodium atoms are surrounded by five oxygen atoms and form a 3-dimensional structure[8]. $Na_4Ti_5O_{12}$ crystallizes in trigonal and monoclinic phase with edge-sharing TiO_6

octahedron with two-dimensional sodium ion pathway. Moreover, in monoclinic phase 2D channels have partially occupied four sodium sites with more space for intercalation wherein trigonal phase has fully occupied sodium sites [9]. $Na_2Ti_6O_{13}$, another class of titanates have tunnel like structure crystalize in monoclinic phase. Na ion in this category of layered oxides bonded to six oxygen atoms in the range of 2.46-2.89 Å bond length, while Ti +4 bonded to six oxygen atoms form edge and corner sharing octahedra in which corner sharing octahedra titled with different angles arranged in a way to form a tunnel with interstitial space having Na ions in it. The typical structure of $Na_2Ti_3O_7$ consists of distorted octahedra of Ti ion surrounded by anions distanced around 1.98-1.99 Å. Three edge-sharing octahedra form a ribbon like structure extending towards the b-axis. These ribbons connected through the adjacent ribbons with oxygen ions of octahedra located in the edges give the step-like layers which are parallel to the ab axis linked by Na+ cations in the c axis [10]. The layer-like structure of $Na_2Ti_3O_7$ have good ion exchange capacity with a wide range of applications in different areas like photocatalysis, sensors, and in electrochemistry as energy storage devices, etc [11][12][13][14][15]. Sodium based layered titanates are widely utilized in sodium-ion batteries as low-voltage oxide anode material and as a matrix. In this chapter, Ni substituted $Na_2Ti_3O_7$ layered titanates were synthesized and screened in DRM. Moreover, the effect of transition metal substitution in $Na_2Ti_{2.8}Ni_{0.2}O_7$ catalysts on DRM activity was also examined.

Part 1
Optimization of Ni concentration in Na$_2$Ti$_3$O$_7$ catalyst for Dry Reforming of Methane

In DRM, at high temperatures, carbon formation is prominent due to side reactions like methane decomposition and the Boudouard reaction. Several studies are documented with Ti-based materials in catalytic reforming reactions because of their stability, strong metal support interactions, and acid-base properties [14][15]. Hence $Na_2Ti_3O_7$-based materials can be envisaged to be good candidates for DRM due to higher stability and coke removal capacity providing higher conversions and prolonged activity. Moreover, Na as an alkali promoter, provides basic strength to the support and increases the CO_2 activation into CO dissociation resulting in high conversions towards DRM [16][17][18].

To consider this, we decided to study the $Na_2Ti_3O_7$ catalyst in the dry reforming of methane reaction. In this part of the chapter, we have studied the effect of active metal species, i.e., Ni, concentration in $Na_2Ti_3O_7$ on DRM activity.

4.2 Experimental Section:

4.2.1 Synthesis of $Na_2Ti_3O_7$:

$Na_2Ti_3O_7$ catalyst was synthesized by the sol-gel method by the addition of Ti isopropoxide (18 mmoles), NaOH (12.6 mmol), and H_2O_2 (30%) (18 ml) in 100 ml of distilled water. The solution is stirred at 85 ℃ till complete evaporation of water. Afterward, the residue was kept in the oven at 150 ℃ overnight for complete drying. The dried material was crushed in powder form and kept for calcination in the furnace at 800 ℃ for 6h in an air atmosphere [19].

4.2.2 Synthesis of $Na_2Ti_{3-x}Ni_xO_7$ (X= 0.02, 0.05,0.1,0.2)

Optimization of Ni concentration in $Na_2Ti_3O_7$ catalyst is done by synthesizing the catalysts by adding the calculated amount of Ni nitrate in the reaction mixture and other precursors by sol-gel route. In this context, four catalysts with different amounts of Ni wt. % (0.38, 0.97, 1.94, and 3.80) named NTN002, NTN005, NTN01, and NTN02 respectively were synthesized by the above-mentioned steps like the parent catalyst. All the substituted

catalysts were calcined at 800 °C for 6h in an air atmosphere.

4.3 Catalyst evaluation:

Before performing the DRM experiment in the reactor tube NTN002 catalyst was subjected to all pre-treatment and DRM reaction conditions to evaluate its structural stability; this was done in a programmable ceramic tube furnace. 0.5 cc catalyst was kept in the ceramic tube (ID = 2.5 cm, OD = 3.5 cm) furnace and pre-treatment like calcination and reduction was carried out at 750 °C for 6 h. Then a mixture of CO_2 and CH_4 (CO_2 = 20 CH_4 = 20 ml/min) was passed for 2 h at different temperatures 500 °C, 600 °C, and 800 °C and the spent catalyst was further characterized. After this, the DRM experiment was carried out as mentioned before.

4.4 Result and discussion:

4.4.1 X-Ray Diffraction Analysis and textural properties of $Na_2Ti_{3-x}Ni_xO_7$ (X= 0.02, 0.05,0.1,0.2):

X-ray diffraction pattern of Ni substituted $Na_2Ti_3O_7$ (NTO) are shown in figure 4.1. NTO catalyst crystallized in monoclinic phase with P21/m space group with JCPDS No. 31-1329[19]. Characteristic peaks at around 2θ = 11°, 26° and 30° corresponding to 001, 011 and 300 respectively, confirmed the monoclinic phase of $Na_2Ti_3O_7$. Substitution of Ni (0.38 wt.%) does not change the structure of the parent catalyst as no impurity peaks were observed in the NTN002 diffraction pattern.
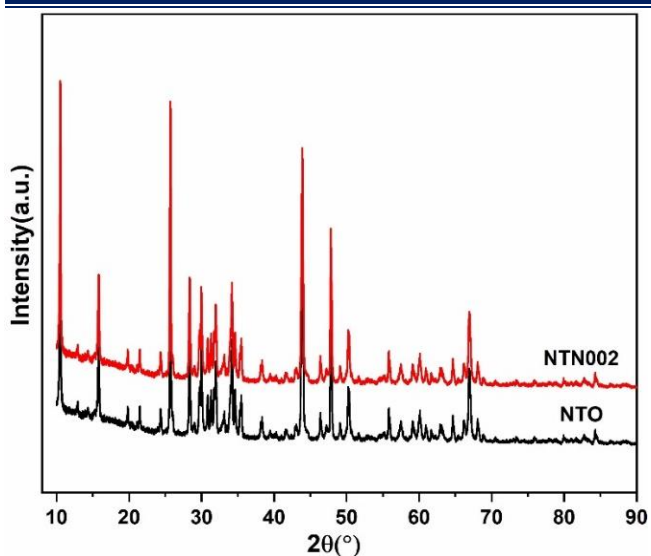
Figure: 4.1 XRD of NTO and NTN002 catalysts.

After confirming the structure stability of the catalyst on Ni substitution, NTN002 was subjected to pre-treatment (calcination and reduction) and DRM conditions at different temperatures in the tube furnace. After this, structural modifications were analysed by XRD (Figure 4.2). The calcined and reduced catalysts retained the parent structure at 750 °C. After passing reactant gases CH_4 and CO_2 at different temperatures for 2 h, no impurity peaks or phase change was observed in the NTN002 catalyst. Although in XRD of catalyst treated at 600 °C in DRM conditions have some extra peaks and amorphous background were observed due to structural modifications and corresponding to $Na_2Ti_{12}O_{25}$ phase.
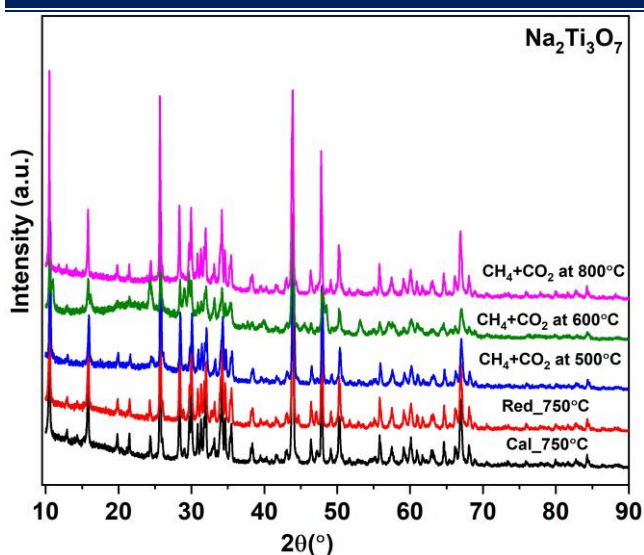
Figure: 4.2 XRD of NTN002 catalysts after different pre-treatment and DRM conditions.

Furthermore, catalysts with different amounts of Ni in the NTO parent catalyst, namely NTN002, NTN005, NTN01, and NTN02 with 2,5,10 and 20 wt.% respectively was analysed by XRD (Figure 4.3). It can be clearly observed that all catalysts were indexed in monoclinic phase, identical with standard JCPDS No. 31-1329 without any impurity peaks. All peaks are very sharp confirming the high-order crystallinity for all catalysts. The retention in structure confirmed the insertion of Ni into the lattice without any impurity of NiO over the surface of the catalysts. In Table 4.1, the textural properties of Ni-substituted catalysts were tabulated. The specific surface area of all catalysts is analysed by the N_2 physisorption method. The surface area of all catalysts is low because of the high calcination temperature to get the desired structure. After Ni substitution there is a slight increase in specific surface area was observed.

Table 4.1: Textural properties of $Na_2Ti_{3-x}Ni_xO_7$ (X= 0.02, 0.05,0.1,0.2)

Catalyst	Ni wt. %	Surface area(m2/g)	Pore volume (cc/g)
NTO	-	8.2	0.032
NTN002	0.38	10.65	0.044
NTN005	0.97	9.56	0.042
NTN01	1.94	4.53	0.024
NTN02	3.80	8.18	0.011
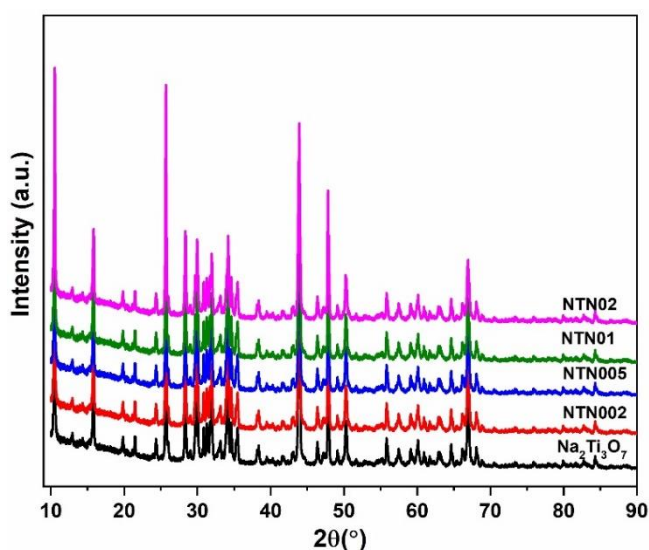
Figure 4.3: XRD of NTN002, NTN005, NTN01 and NTN02 catalysts

4.4.2 Raman Analysis of $Na_2Ti_{3-x}Ni_xO_7$ (X= 0.02, 0.05,0.1,0.2):

XRD of all synthesized catalysts showed the formation of a monoclinic structure which has been further confirmed by Raman analysis, demonstrated in figure 4.4. Typically, $Na_2Ti_3O_7$ has 36 vibrational modes which are Raman active. The spectra of NTO, NTN002, NTN005, NTN01, and NTN02 reveal all identical Raman modes which confirmed the monoclinic phase of synthesized samples [20][21]. Some modes are not observed may be due to low polarizability in Ni-substituted catalysts. In the spectra high-intensity peaks were observed at 301, 850, and 885 cm^{-1} corresponding to the different stretching and vibrational modes of Ti-O bond confirming the formation of layered stepped $Na_2Ti_3O_7$ catalyst of monoclinic system. The Raman modes and their assignments were tabulated in Table 4.2.

Table 4.2: Assignment of Raman modes observed in all fresh catalysts

Our work (cm^{-1})	Silva (cm^{-1}) et al.	Bamber et al. (cm^{-1})
117 Ag	117	118
139 Ag	140	
157 Ag	155	
180 Bg	179	
202 Bg	201	202
230 Ag	230	230
258 Bg	260	261
283 Bg	283	286
301 Bg	302	304
344 Ag	346	345
386 Ag	386	386
399 Ag	400	399
449 Ag	449	450
487 Bg	488	489
588 Bg	587	589
656 Bg	655	658
684 Ag	684	684
740 Ag	742	742
849 Ag	849	852
883 Ag	884	884
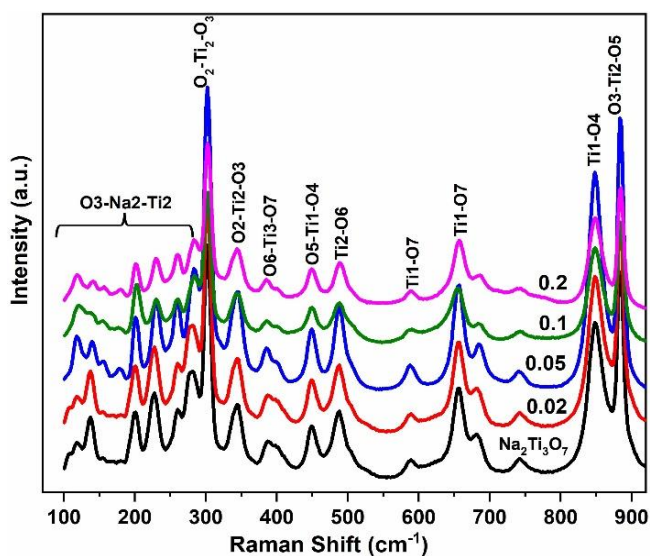
Figure 4.4: Raman spectrum of NTN002, NTN005, NTN01 and NTN02 catalysts

4.4.3 XPS Analysis of $Na_2Ti_{3-x}Ni_xO_7$ (X= 0.02, 0.05,0.1,0.2):

To investigate the electronic composition and surface environment of Ni-substituted NTO catalysts; x-ray photoelectron spectroscopy was employed. Figure 4.5 showed the Ti 2p spectrum of the NTO catalyst having peaks at 464.0 eV and 458.3 eV corresponding to Ti 2p3/2 and Ti 2p1/2 of Ti^{+4}. All Ni-substituted catalysts have Ti in +4 oxidation state. Interestingly, the NTN02 catalyst has an additional peak at around 459.9 eV corresponding to Ti^{+3}[22] along with Ti^{+4} peaks at 464.0 eV and 458.3 eV. Furthermore, a slight increase in the binding energy of Ti^{+4} peaks (464.3 eV and 458.44 eV) is also observed in the NTN02 catalyst, which may be due to the formation of surface oxygen species in the lattice [23]. In the NTN02 catalyst, higher Ni doping ascribed to a partial reduction of Ti^{+4} to Ti^{+3}, initiates defect formation and active oxygen species generation which is further corroborated by O 1s spectrum of NTN02 catalyst. The intensity of peak at 532. 2 eV corresponding to surface Ti-OH species is higher than other catalysts (Figure 4.5) [24]. The Ni 2p spectra reveal that all Ni-substituted catalysts have Ni in a +2 oxidation state. NTN002 and NTN01 catalysts have small peaks at around 857 eV and 867 eV corresponding to Ni hydroxide and satellite

peak respectively [25].
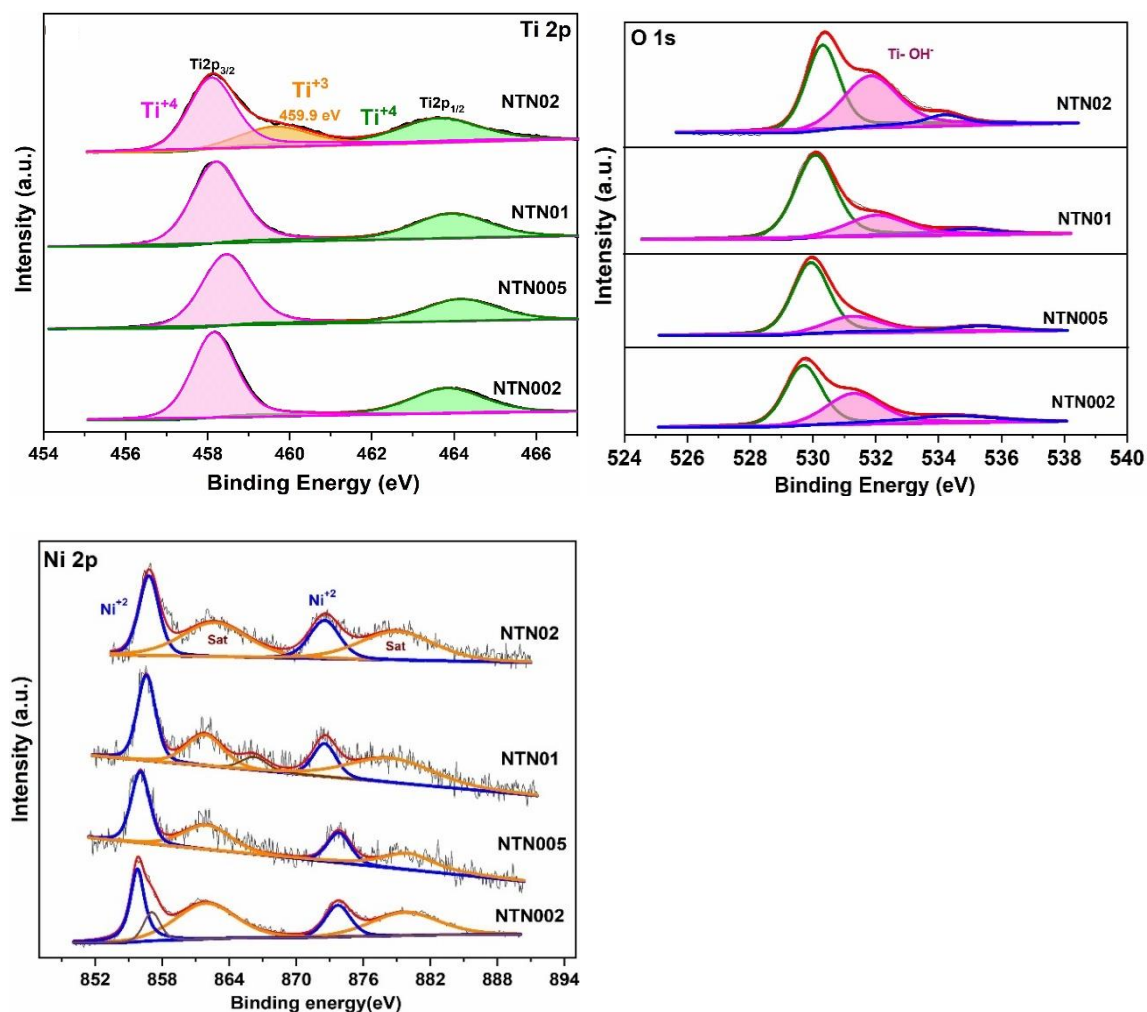
Figure 4.5: XPS spectrum of Ti 2p, O1s and Ni 2p of NTN002, NTN005, NTN01 and NTN02 catalysts

4.4.4 FESEM Analysis of $Na_2Ti_{3-x}Ni_xO_7$ (X= 0.02, 0.05,0.1,0.2):

The morphology of the catalysts was investigated by FESEM analysis. In the micrograph of

$Na_2Ti_3O_7$ parent catalyst (Figure 4.6 (E)), rod and whiskers-like structure were observed

which is similar to the reports by Y. Zhang et al where $Na_2Ti_3O_7$ was synthesized by sol-gel

method [26]. Ni substituted catalysts showed similar morphology as of parent catalysts

having rod-like structures sized in the range of 400-500nm length and 200-300 nm width

(Figure 4.6 A-D).
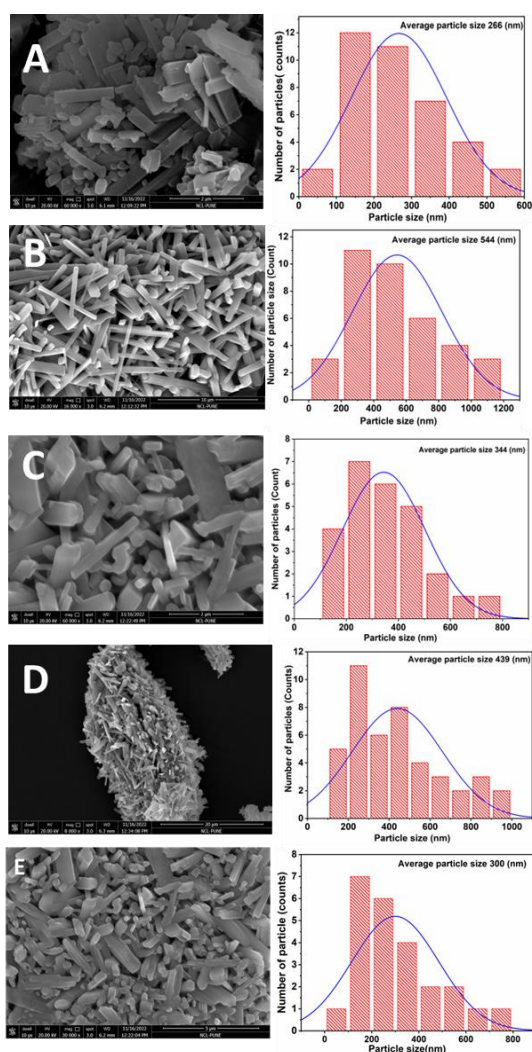
Figure 4.6: FESEM analysis of A) NTN002 B) NTN005 C) NTN01 D) NTN02 E) NTO catalysts

4.5 Catalytic activity of $Na_2Ti_{3-x}Ni_xO_7$ (X= 0.02, 0.05,0.1,0.2):

4.5.1 Dry reforming activity of $Na_2Ti_{3-x}Ni_xO_7$ (X= 0.02, 0.05,0.1,0.2):

All the above characterized catalysts were screened for dry reforming of methane. In a typical DRM run, pre-treatment steps comprising in situ calcination at 750 °C in air atmosphere for 6h and in situ reduction in the H_2 stream for 6h at 750 °C were carried out. After pre-treatment, a 1:1:1 ratio of CH_4: CO_2: N_2 with 80:80:80 ml/min gas mixture was sent in the reactor tube at 800 °C with 28800 h^{-1} GHSV at atmospheric pressure. Figure 4.7 shows that the NTN02 catalyst was superiorly active for DRM with 60% CH_4 conversion and 75 % CO_2 conversion among all the catalysts. The theoretical value of the H_2/CO ratio

is 1 but, in the case of the NTN01 catalyst slightly higher H_2/CO ratio was observed at the initial hours of reaction. During DRM, side reactions like RWGS reaction (5), are responsible for high CO_2 conversion resulting in more amount of CO. Apart from that partial oxidation of methane (3) also possible to occurs due to the presence of nascent O_2 in the reaction stream. Moreover, phase changes of $Na_2Ti_3O_7$ to $Na_2Ti_6O_{13}$ is also can be the source of oxygen in the DRM conditions resulting in increased H_2/CO ratio for initial hours. After some time of reaction DRM is dominating over the side reactions and H_2/CO stabilizes near unity.
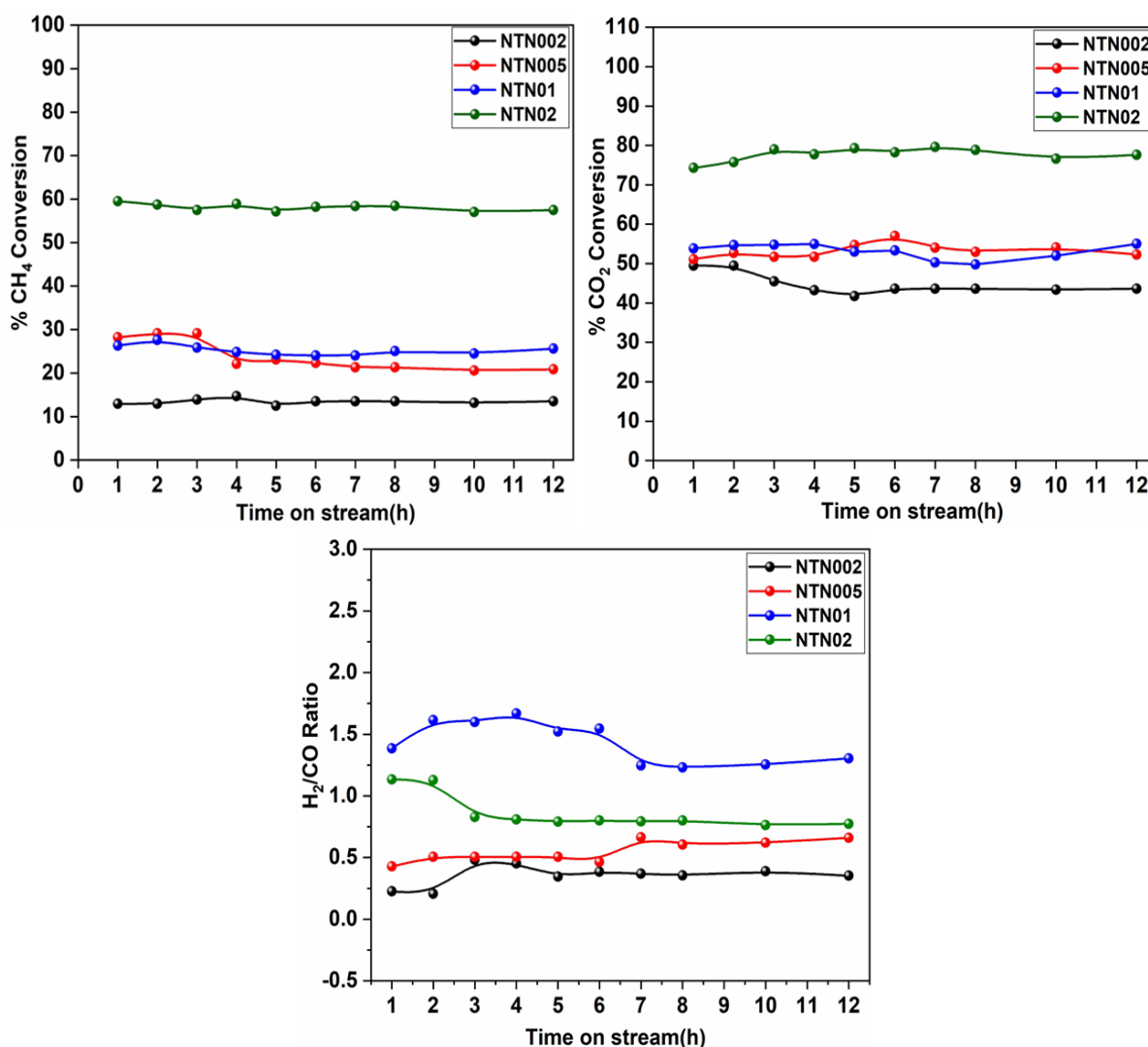
Figure 4.7: Dry reforming of methane activity of NTN002, NTN005, NTN01 and NTN02 catalyst

4.5.2 Durability Test of NTN02 catalyst:

After the screening of all Ni-substituted catalysts for 12 h, the NTN02 catalyst showed higher conversion in DRM. To check the prolonged activity and stability of this catalyst, a DRM run has been performed for 100 h time on stream. The conversion of methane was around ~ 56 % and CO_2 conversion was ~ 78% stable for 100 h and H_2/CO ratio is ~ 0.7 observed. Initially, the conversion was a little high but it got steady after 10-15 h of reaction. The stability in conversions confirmed the effect of OH^- species in simultaneous coke gasification and provided the superior activity of NTN02 catalysts for DRM.
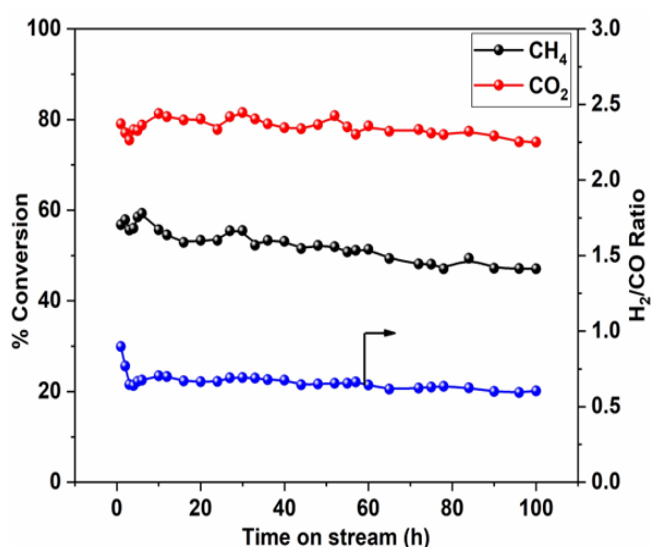
Figure 4.8: Durability test of NTN02 catalyst in DRM reaction

4.6 Spent Catalysts Characterization:

Dry reforming of methane reaction has major drawbacks like coke formation and dominance of side reactions at high reaction temperatures. Carbon formation occurs on metal surfaces during CH_4 activation. High temperature causes sintering of Ni resulting in agglomeration of carbon species over the metal surface. Side reactions like Boudouard (6) and methane decomposition (4) reactions are also having high possibilities of carbon formation.

To understand the quantity and morphology of carbon species formed after DRM, spent catalyst characterization is much needed. Apart from that, the structure stability of the parent catalyst after DRM is also an important part of the study. To consider this, spent catalysts

were evaluated by several analytical techniques like XRD, Raman, TGA, and FESEM.

4.6.1 XRD analysis of spent catalysts:

All Ni-substituted $Na_2Ti_3O_7$ catalysts screened in dry reforming conditions for 12 h are analyzed by XRD analysis shown in Figure 4.9. The diffraction pattern reveals that NTN002 and 005 have completely changed to $Na_2Ti_6O_{13}$ phase and in NTN01 and NTN02, parent structure is retained but presence of $Na_2Ti_6O_{13}$ phase is also observed (JCPDS No.15463)[27][28]. This impurity phase seems to arise only after long duration of exposure to reaction conditions. Apart from these peaks, a peak at around 26.4° 2θ position was also detected attributed to graphitic carbon. The intensity of the graphitic carbon peak and secondary phase is much higher in low-loading Ni catalysts that are NTN002, NTN005, and NTN01. In the NTN02 catalyst, the peaks of the $Na_2Ti_6O_{13}$ phase are less than in other catalysts. Moreover, the catalysts screened for 100 h also has a small peak of graphitic carbon and a secondary phase. From XRD, it can be concluded that the higher loading of Ni, is stabilizing the $Na_2Ti_3O_7$ structure and providing higher activity in DRM with less carbon formation.
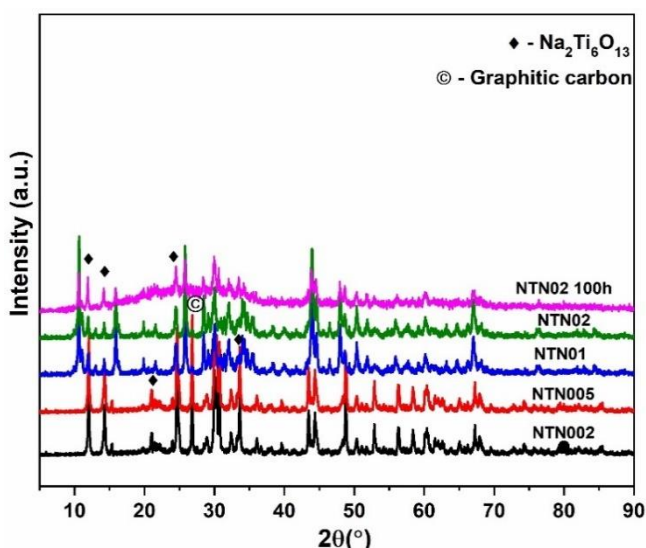
Figure 4.9: XRD pattern of Ni substituted spent catalysts
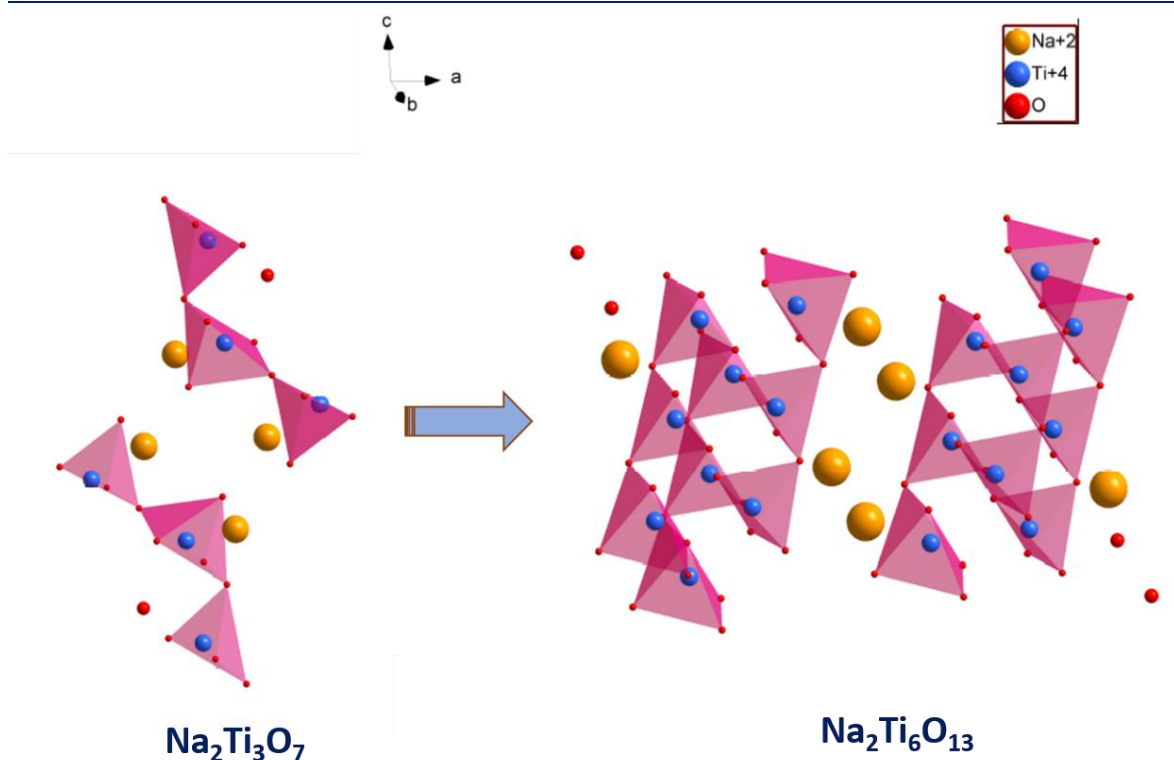
Figure 4.10: Structural representation of phase transformation $Na_2Ti_3O_7$ to $Na_2Ti_6O_{13}$

4.6.2 Raman analysis of spent catalysts:

To further understand the structural modifications in spent catalysts, Raman analysis has been performed. In figure 4.11 it is observed that the catalysts with a low concentration of Ni, like NTN002 and NTN005 have more vibrational modes representing the $Na_2Ti_6O_{13}$ phase [29]. It is well reported that at higher temperatures $Na_2Ti_3O_7$ tends to transform to $Na_2Ti_6O_{13}$ (Figure 4.10). Transformation can be observed by shifting Raman modes to higher wavenumber as well as some modes tend to disappear. During the transformation, modes at around 305, 769, and 883 cm^{-1} which correspond to stretching Ti-O and Na-O vibrations with terminal oxygen atoms of $Na_2Ti_3O_7$ structure, Ti-O-Ti and stretching vibration of Ti-O bond respectively, start disappearing. In NTN002 and NTN005 these modes are very weak and disappeared. In NTN01 and NTN02 catalysts modes representing the $Na_2Ti_3O_7$ structure are retained. This may be due to the increased amount of Ni in the B site of the structure, stabilizing the TiO_6 octahedron with a terminal oxygen atom and avoiding the condensation of terminal oxygen into two octahedra sharing linear oxygen atoms corresponding to the

$Na_2Ti_6O_{13}$ phase.
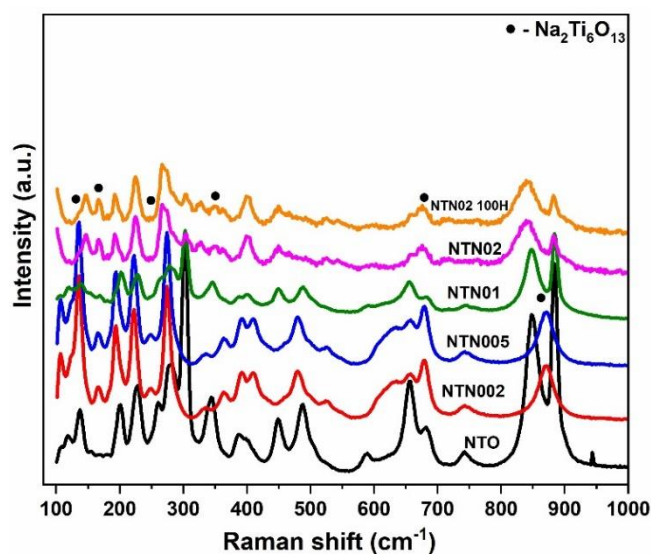
Figure 4.11: Raman Analysis of Ni substituted spent catalysts

4.6.3 Thermogravimetric analysis of spent catalysts:

TGA in the air atmosphere provides the quantitative extent of carbon formed over the surface of the catalyst during dry reforming of methane. In the particular experiment, the temperature was increased at a fixed rate in the air atmosphere, the carbon on the catalyst oxidized and weight loss was observed. The amount of carbon was calculated in moles of carbon per gram catalysts. Figure 4.12 showed the results of the TGA experiment done on all Ni-substituted catalysts. With the increased amount of Ni in the $Na_2Ti_3O_7$ catalyst, the trend of carbon accumulation is decreasing in an order of NTN002> NTN005>NTN01> NTN02. The NTN02 catalysts have a negligible amount of carbon formation in DRM for 12 h.
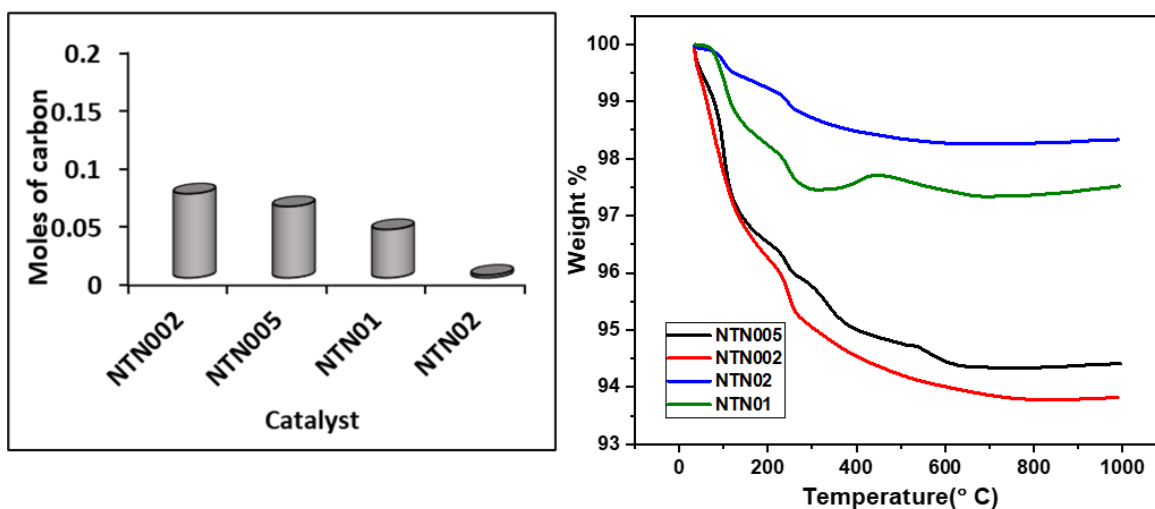
Figure 4.12: TGA Analysis of Ni substituted spent catalysts

4.6.4 FESEM Analysis of $Na_2Ti_{3-x}Ni_xO_7$ (X= 0.02, 0.05,0.1,0.2):

After evaluating the structural modifications and carbon formation by XRD, Raman, and TGA analysis of all spent catalysts, morphological changes have been studied by FESEM analysis. Micrographs of spent catalysts were shown in figure 4.13. Before DRM run, all catalysts were having rod-like structures with cross sections of 200nm $\times$ 600nm but in spent catalysts (A-D), morphological changes were observed. In the micrographs, it can be clearly observed that the rod-like structure is modified into sheets and agglomerated. While in the case of the NTN02 catalyst, still some initial rod-like morphology is retained (D). Figure 4.10 E shows the images of NTN02 catalysts after 100 h. Catalyst has remained in original morphology in 200 $\times$ 600 nm size with some agglomerates.
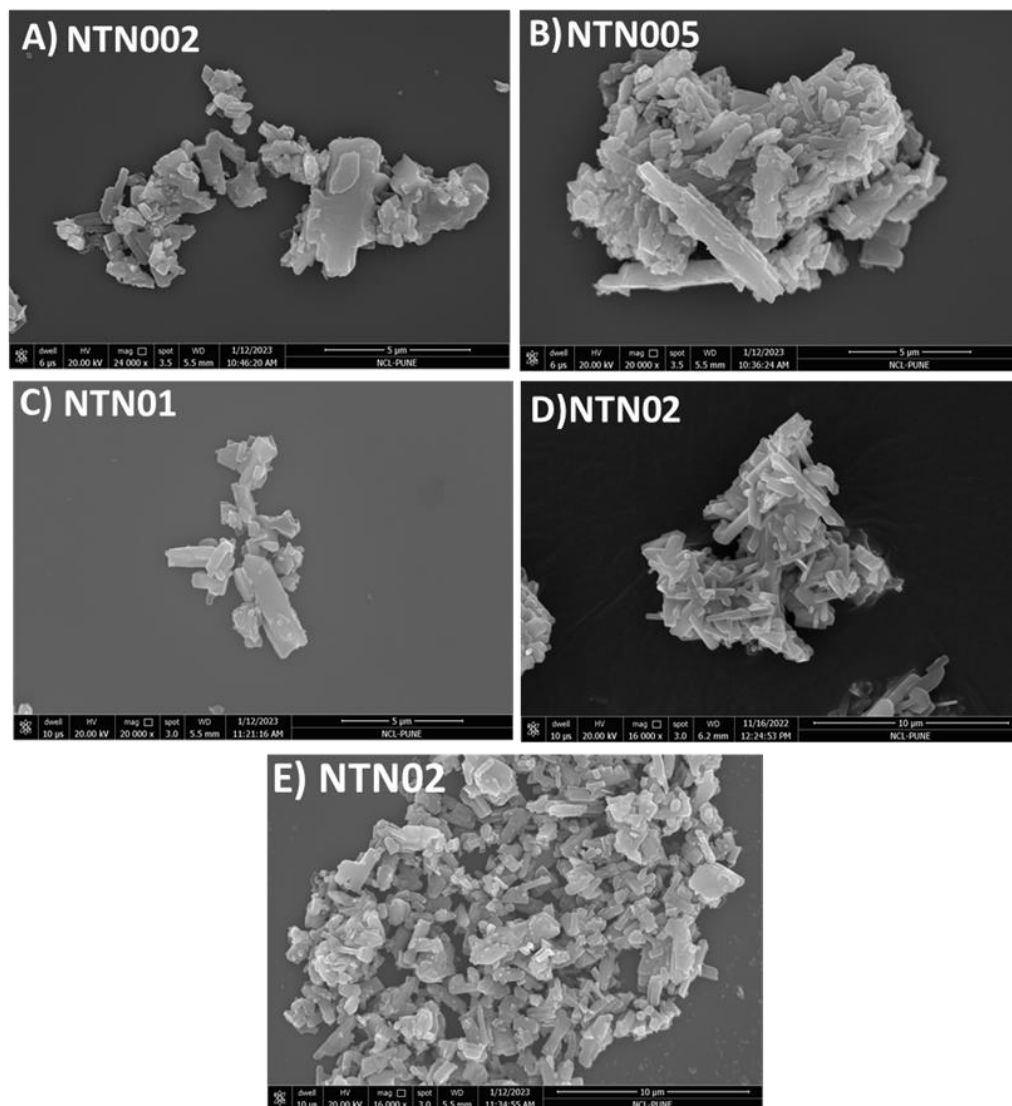
Figure 4.13: FESEM analysis of A) NTN002 B) NTN005 C) NTN01 D) NTN02 spent catalysts and FESEM analysis of E) NTN02 spent catalysts ran for 100 h DRM conditions

Part 2
Effect of transition metal substitution
$Na_2Ti_{2.96}Ni_{0.02}X_{0.02}O_7$ (x= Fe/ Co/ Cu) in DRM

4.7 Introduction:

In the first part of this chapter, a layered metal oxide $Na_2Ti_3O_7$ catalyst was synthesized, and optimization of Ni concentration has been carried out. The effect of Ni concentration on parent structure and DRM activity was investigated. In dry reforming of methane, Ni has been used extensively as active metal because of its low cost and abundance. However, Ni surface is more active for CH_4 decomposition and sintering at high reaction temperatures leading to carbon formation and deactivation of the catalyst. To overcome this, noble metal promoters like Pd, Pt, Ru, and Rh are studied in DRM with good conversions and activity with less carbon formation compared to non-promoted catalysts [30],[31],[32],[33],[34]. However, due to their high cost their application is difficult in DRM at industrial scale. Apart from noble metals, alkaline earth metals, rare earth, and transition metals as promoters are also studied in DRM as they provide basic strength to the support, which helps in the activation of CO_2 and formation of oxygenated species aiding in gasification of coke formed in DRM [35],[36],[37]. Especially, transition metals like Co, Cu, and Fe are added with Ni to synthesize bimetallic catalysts. Every transition metal has its own chemical properties which provide different pathways to gasify the carbon accumulated on the catalyst's surface while Ni metal facilitates CH_4 activation and provides superior activity in the dry reforming of methane; this is called the synergistic effect [38]. For instance, in Ni-Co system, Co has an affinity towards oxygen species and tends to oxidize by CO_2 but an appropriate amount of Co with Ni in the bimetallic system helps in the oxidation of carbon during DRM [39],[40]. In Ni-Fe bimetallic system, Fe tends to provide an alternate path for dry reforming by dealloying and alloying with Ni under different reaction conditions. During pre-treatment, on calcination, Fe tends to get oxidized, oxide species react with carbon formed on Ni metal by CH_4 decomposition to form CO and gets alloyed with Ni again. This redox behaviour of

Fe provides resistance toward carbon accumulation [41]. Moreover, Cu provides increased mobility to lattice oxygen species over the surface and activates the CO_2, and enhances the carbon gasification capacity of catalysts. However, several reports suggested that higher amount of Cu may not help in resisting the coke formation as it forms copper oxide and dealloys from Ni, so an appropriate Ni/Cu ratio is helpful in good conversions in DRM providing coke gasification [42][43]. Hence, in this part of the chapter we have substituted similar amounts of Co, Cu, and Fe with Ni in NTN002 catalyst to check the synergistic effect of bimetallic system in DRM activity. Since NTN002 has the lowest activity among all Ni substituted catalysts, it chosen for this study to clearly discern the improvement in activity, if any.

4.8 Experimental Section:

4.8.1 Synthesis of $Na_2Ti_{2.96}$ $Ni_{0.02}X_{0.02}O_7$ (X= Co, Cu, Fe):

The transition metals (Co, Cu, Fe) doping has been done in $Na_2Ti_{2.96}$ $Ni_{0.02}X_{0.02}O_7$ catalyst by adding 0.4, 0.39, 0.39 wt.% of Co, Cu, Fe respectively in NTN002 catalyst. The calculated amount of transition metal nitrate precursors was added to the reaction mixture along with other precursors. The obtained residue was calcined in air for 6 h at 800 °C. Synthesized catalysts were designated as NTN002Cu002O7, NTN002Co002O7, and NTN002Fe002O7.

4.9 Result and discussion:

4.9.1 X-Ray Diffraction and textural properties of $Na_2Ti_{2.96}Ni_{0.02}X_{0.02}O_7$ (X= Co, Cu, Fe)

PXRD patterns of transition metal substituted $NTN_{0.02}Co_{0.02}$, $NTN_{0.02}Cu_{0.02}$, and $NTN_{0.02}Fe_{0.02}$ catalysts are given in Figure 4.14. The XRD plots display that all substituted catalysts crystallized in a monoclinic structure with P21/m space group and confirmed with standard JCPDS No. 31-1329 structure [44]. The transition metal substituted catalysts have retained their parent structure with single phase monoclinic layered $Na_2Ti_3O_7$ structure. Any

other peaks corresponding to the transition metal oxides, and carbonates are not seen in the XRD plot. Textural properties have also been analyzed for all substituted catalysts. It can be observed that there is not much change in pore volume and surface area on substituting the Co, Cu, and Fe in the NTN002 catalyst.
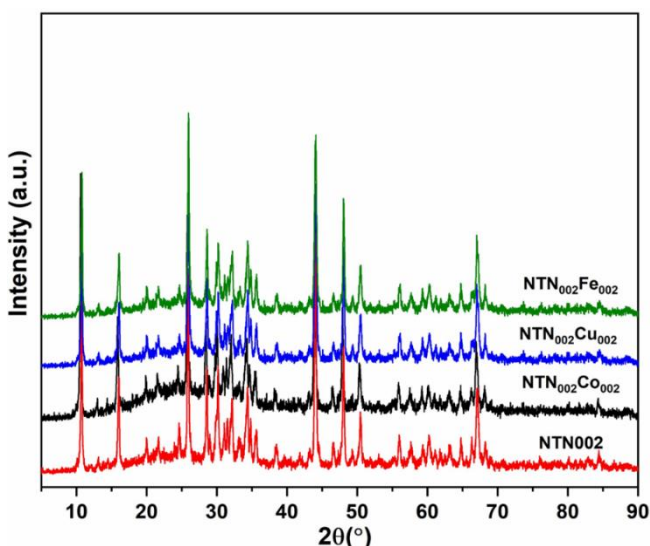
Figure 4.14: XRD of NTN002, NTN002Co002, NTN002Cu002 and NTN002Fe002 catalysts

Table 4.3 Textural properties of $Na_2Ti_{2.96} Ni_{0.02}X_{0.02}O_7$ (X= Co, Cu, Fe)

Catalyst	Ni wt.%	Transition metal wt.%	Surface area(m2/g)	Pore volume (cc/g)
NTO	-		8.2	0.032
NTN002	0.38	-	10.65	0.044
NTN002Co002	0.38	0.39	5.69	0.037
NTN002Cu002	0.38	0.40	4.95	0.023
NTN002Fe002	0.38	0.38	6.23	0.020

4.9.2 Raman Analysis of $Na_2Ti_{2.96} Ni_{0.02}X_{0.02}O_7$ (X= Co, Cu, Fe):

Co, Cu, and Fe substituted NTN002 catalysts have retained their parent structure showed by XRD analysis and corroborated by the Raman analysis. Figure 4.15 illustrates that all Raman modes are similar to Ni substituted catalyst NTN002 and parent $Na_2Ti_3O_7$. The three intense Raman modes at 301, 849, and 883 cm^{-1} correspond to B_g, A_g, and A_g modes due to vibrations of different Ti and O atoms and the modes between 107- 300 cm^{-1} are due to

stretching and bending between O, sodium and Ti atom. The observed assignments for all Raman modes are tabulated in Table 4.2[21].
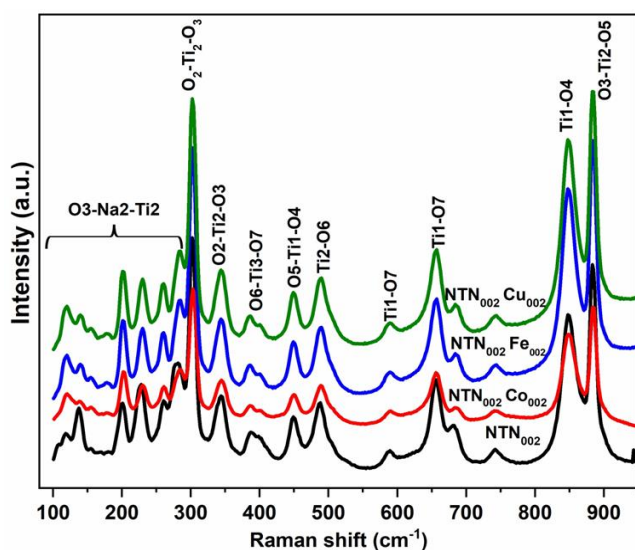
Figure 4.15: Raman spectrum of NTN002, NTN002Co002, NTN002Cu002 and NTN002Fe002 catalysts

4.9.3 XPS Analysis of $Na_2Ti_{2.96} Ni_{0.02}X_{0.02}O_7$ (X= Co, Cu, Fe):

X-ray photoelectron spectroscopy was employed to check the chemical state of elements in transition metal doped $Na_2Ti_{2.96} Ni_{0.02}X_{0.02}O_7$ (X= Co, Cu, Fe) catalysts. Figure 4.16 (A) shows that the Ti 2p spectrum has Ti 2p3/2 and Ti 2p1/2 peaks at 464.0 eV and 458.3 eV confirming the Ti^{+4} oxidation state in all substituted catalysts. In the Cu-based NTN0.02Cu0.02 catalyst, apart from peaks corresponding to Ti^{+4}, another small peak at around 458.9 eV attributed to the Ti^{+3} oxidation state. Presence of low valent Ti could lead to more O vacancies in the catalyst. In figure 4.16 (B), XPS spectrum of O 1s shows the presence of Ti-OH peak at 532.1 eV [22],[23],[24]. The intensity of the peak is much higher in Cu-doped catalysts among all catalysts. Confirming the defect formation in the lattice and more abundance of lattice OH^- species in the NTN0.02Cu0.02 catalyst. Apart from this, peaks at 529.8 eV and 535.8 eV are due to lattice oxygen species and chemisorbed oxygen species respectively. Moreover, the transition metal Co 2p, Cu 2p, and Fe 2p spectra confirm the oxidation state of all three transition metals is +2 [39],[43],[45].
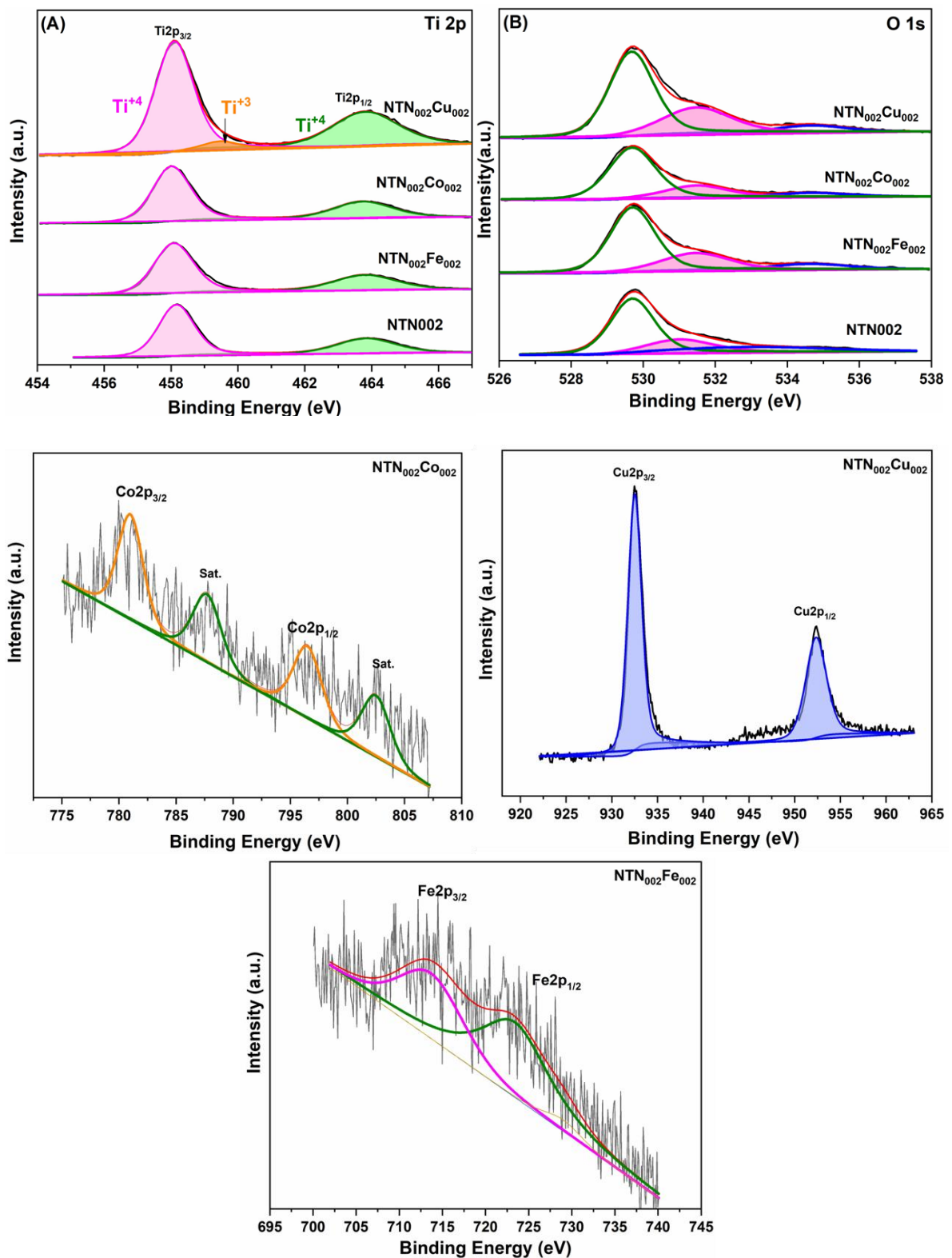
Figure 4.16: XPS spectrum of A) Ti 2p, B) O1s and dopant 2p spectra of NTN002, NTN002Co002, NTN002Cu002 and NTN002Fe002 catalysts

4.9.4 FESEM Analysis of $Na_2Ti_{2.96}$ $Ni_{0.02}X_{0.02}O_7$ (X= Co, Cu, Fe):

FESEM analysis of transition metal substituted NTN002 catalysts has been carried out and micrographs are shown in Figure 4.17. The morphology of Co, Cu, and Fe doped catalysts was retained in a rod-like structure. Some rods in the NTN002Fe002 catalyst have increased width as compared to Cu and Co substituted NTN002 catalyst. The cross-section of rods in NTN002Fe002 is 300×600 nm [26].
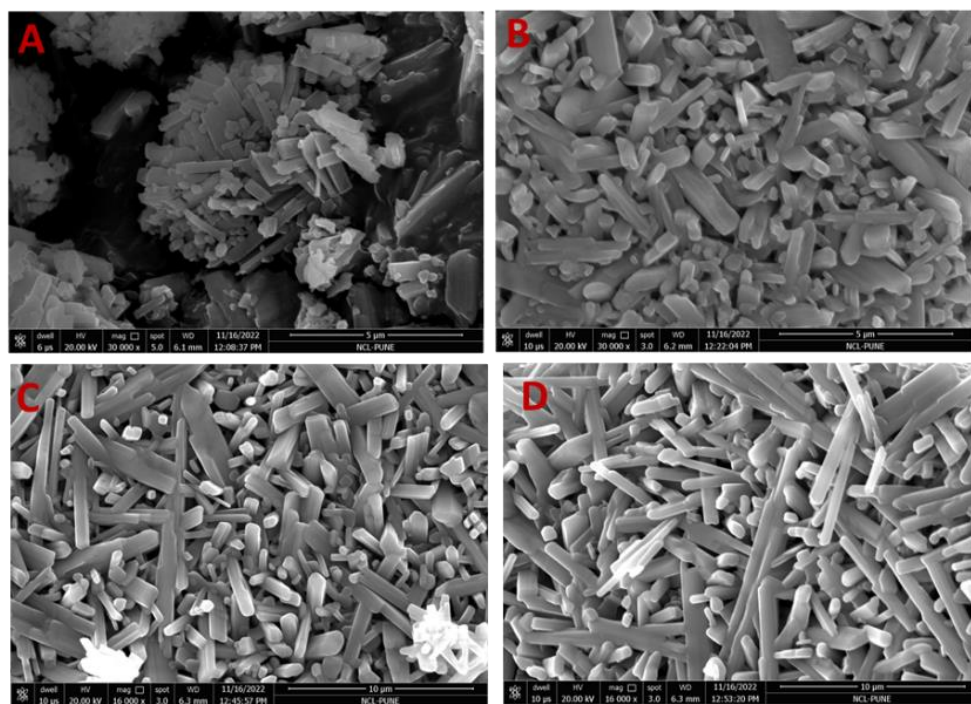
Figure 4.17: FESEM analysis of A) NTN002 B) NTN002Fe002 C) NTN002Co002 D) NTN002Cu002 catalysts

4.10 Catalytic activity of $Na_2Ti_{2.96}$ $Ni_{0.02}X_{0.02}O_7$ (X= Co, Cu, Fe):

All the catalysts are then evaluated for dry reforming of methane at 800 °C for 12 h. It has been observed that transition metal doped catalysts have increased methane conversion than NTN002 catalyst. The CH_4 conversion for NTN002 was around 15 % but after transition metal doping it has been enhanced to 25%. The bimetallic synergistic effect was observed between two metal systems in all the substituted catalysts, which helped in CH_4 decomposition and simultaneous coke gasification over the surface resulting in better activity for DRM. There is not much increase in CO_2 conversion observed in transition metal

substituted catalysts than NTN002 catalyst. The H_2/CO ratio for NTN002 was very low (~ 0.5), but in Co and Fe substituted catalysts, the H_2/CO ratio was higher around 2.5 -2.8 in the initial hours of the reaction; after 5 hours of reaction, it stabilized to 1-1.2 for further hours. This high H_2/CO ratio may be due to the dominance of side reactions like partial oxidation of methane (3) than the main dry reforming of methane initially, which slowly became predominant. For Cu substituted catalysts the H_2/CO ratio was 1.2-1.0 was observed for 12 h of Dry reforming reaction.
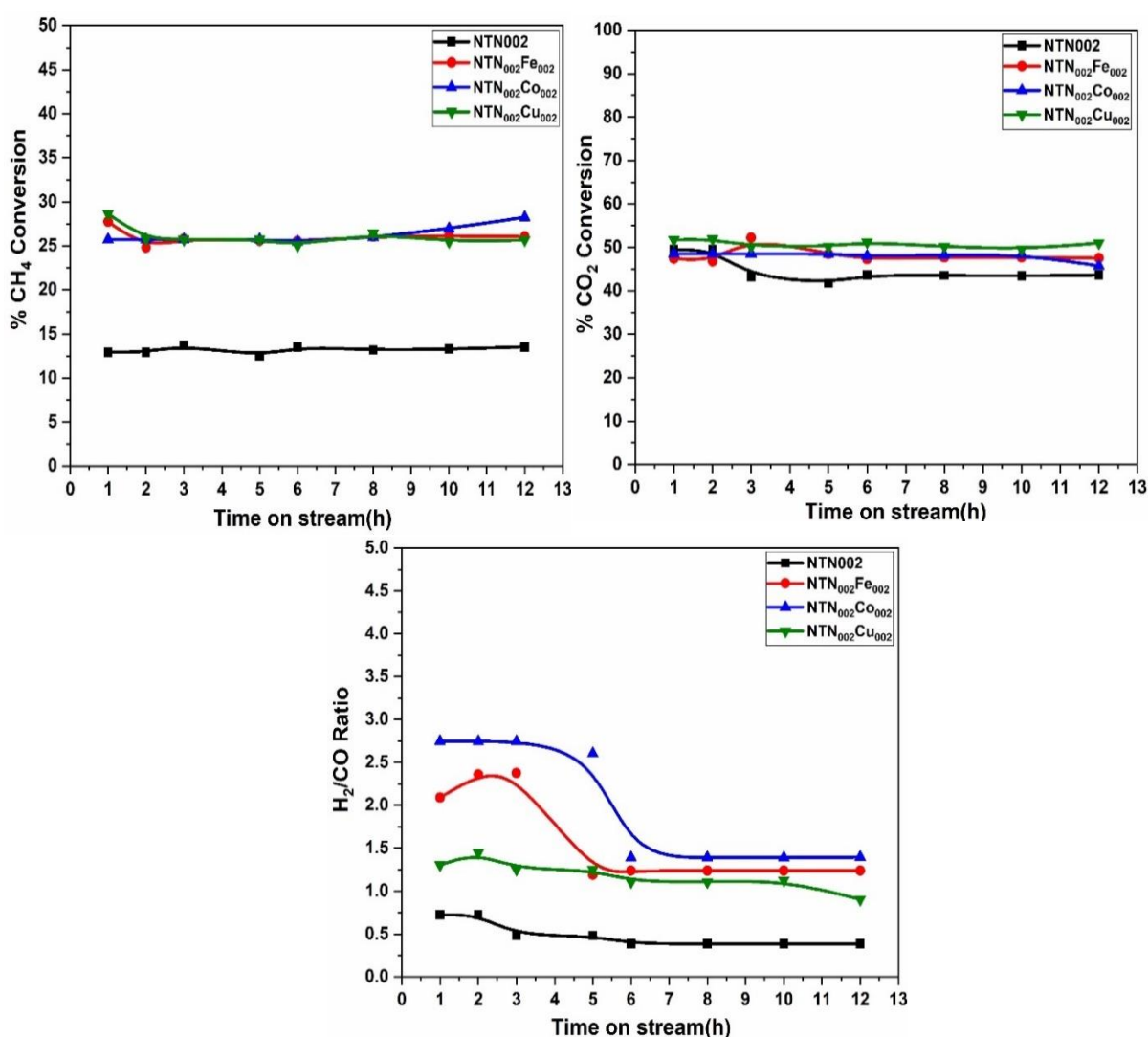
Figure 4.18: Dry reforming of methane activity of NTN002, NTN002Co002, NTN002Fe002 and NTN002Cu002

4.11 Spent Catalysts Characterization:

Transition metal doping has a positive impact on the DRM in the NTN002 catalyst. After

substitution of Co, Cu, and Fe, methane conversion increased, indicating enhanced CH_4 activation on the metal surface. As methane decomposition increases, hydrogen generation as well as carbon formation also will increase on the surface. The improved activity also leads to carbon formation and its simultaneous gasification. So, for all substituted catalysts used catalysts are thoroughly studied by XRD and TGA analysis.

4.11.1 X-Ray Diffraction Analysis of spent $Na_2Ti_{2.96}$ $Ni_{0.02}X_{0.02}O_7$ (X= Co, Cu, Fe):

XRD of spent catalysts has been taken after 12 h of DRM reaction. The XRD plot in figure 4.19 illustrates the formation of secondary phase $Na_2Ti_6O_{13}$ in all transition metal substituted catalysts [27]. Apart from this, peak at 26.4° 2θ position observed in all catalysts indicates formation of graphitic carbon. The intensity of carbon peak is less in Cu and Fe-substituted catalysts. In Cu substituted catalyst, $Na_2Ti_6O_{13}$ peaks are less as compared to other catalysts, the parent phase has been retained more in NTN002Cu002 catalyst. The XRD plot also suggests, there are no peaks corresponding to transition metal oxides were observed.
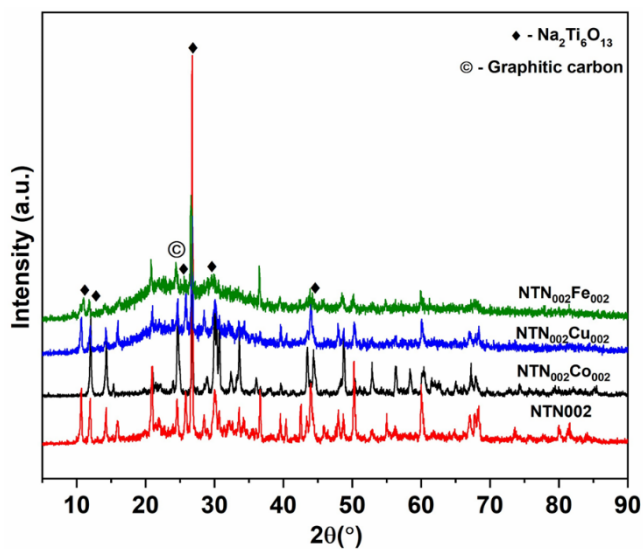
Figure 4.19: XRD of spent catalysts NTN002, NTN002Co002, NTN002Fe002 and NTN002Cu002

4.11.2 Thermogravimetric analysis of spent Na$_2$Ti$_{2.96}$ Ni$_{0.02}$X$_{0.02}$O$_7$ (X= Co, Cu, Fe):

TGA plots of all spent catalysts tested for 12 h in dry reforming of methane are shown in figure 4.20. Carbon formation was estimated by calculating the weight loss in the catalyst in air atmosphere up to 1000 ℃ with a 10 °/min ramp rate. After calculating the weight loss, moles of carbon per hour per gram of catalyst were estimated. It has been observed that the substitution of transition metal has an impact on carbon gasification over the surface of the catalyst. However, NTN002Cu002 catalysts have less amount of carbon than other catalysts. The less amount of carbon is possibly due to the stability of parent catalysts enhanced by the Cu substitution. CH$_4$ activation is improved in NTN002Cu002 catalysts as well as carbon gasification is also prone resulting in less carbon formation.
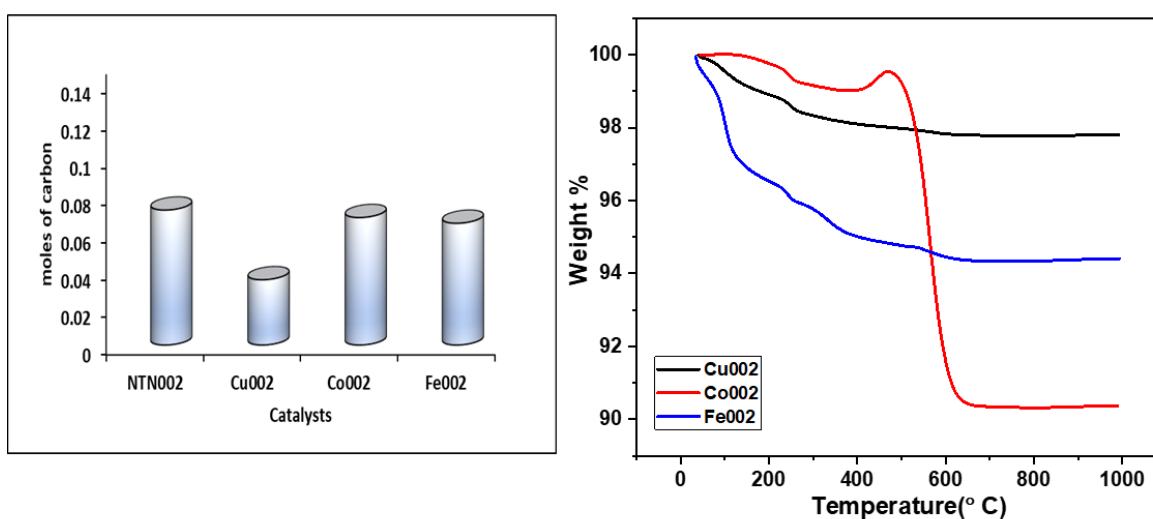
Figure 4.20: TGA analysis of spent catalysts NTN002, NTN002Co002, NTN002Fe002 and NTN002Cu002

4.12 Conclusions:

In this chapter, a new catalytic system, Na$_2$Ti$_3$O$_7$ has been studied in the dry reforming of methane. The chapter deals with the synthesis of Na$_2$Ti$_3$O$_7$ and Ni substituted Na$_2$Ti$_{2.96}$Ni$_{0.02}$O$_7$ catalysts by citrate gel method and characterized by XRD and Raman confirming the monoclinic phase with p21/m space group The effect of Ni concentration in DRM and on parent structure was also studied by increasing the Ni dopant concentration

gradually. XPS analysis revealed that the oxidation of Ti in the system is +4 and in the NTN02 catalyst, some Ti^{+3} species is present confirming the defect formation in the lattice. This has been further confirmed by a higher amount of OH^- species in NTN02 catalyst among all catalysts. Structure morphology was analyzed by FESEM studies and the rod-like structure of $Na_2Ti_3O_7$ was confirmed with a 200nm $\times$ 600 nm cross-section. NTN02 catalyst showed superior activity in dry reforming reaction for 12 h among all catalysts. The durability test performed with NTN02 catalyst for 100 h, without any drop in the activity and conversions indicates that NTN02 is a stable and durable catalyst for DRM. Spent catalysts were also examined by various characterization techniques. XRD and RAMAN data confirmed the retention of parent structure after DRM testing. However, carbon formation was observed in all catalysts by XRD, quantified by TGA analysis. NTN02 catalyst has a lower amount of coke on the surface revealing the role of increased OH- species in the catalyst for coke gasification.

Part 2 of this chapter studied the role of transition metals (Co, Cu, Fe) in NTN002 catalysts. Structure modifications were studied by XRD and RAMAN analysis in substituted catalysts. The catalytic activity of all catalysts revealed the transition metal substitution enhanced the CH_4 activation and conversion in DRM. NTN002Cu002 catalyst has an H_2/CO ratio near to equilibrium than other catalysts due to the dominance of DRM on other side reactions. Moreover, spent catalysts characterization illustrates the formation of the $Na_2Ti_6O_{13}$ phase with the parent $Na_2Ti_3O_7$ catalyst. It has been reported that heat treatment of $Na_2Ti_3O_7$ results in a phase change to $Na_2Ti_6O_{13}$ which is observed in all substituted catalysts. Although, NTN002Cu002 catalysts have fewer XRD peaks for the $Na_2Ti_6O_{13}$ phase confirming the retention of the $Na_2Ti_3O_7$ phase. XPS analysis of all catalysts revealed the formation of Ti $^{+3}$ species due to defect-generating oxygen vacancies in NTN002Cu002 catalysts further confirmed by more amount of OH^- species than other substituted catalysts. In Cu-based catalyst, the coke formation was less, quantified by TGA data. Fewer moles of

carbon in NTN002Cu002 catalyst gives the idea of simultaneous gasification of carbon by OH^- species on the surface, as well as increased CH_4 activation, confirming the synergistic effect of Bimetallic Ni-Cu in NTN002 catalyst.

4.13 References:

[1]   J. Zhu et al., "Perovskite Oxides: Preparation, Characterizations, and Applications in Heterogeneous Catalysis," ACS Catal, vol. 4, no. 9, pp. 2917–2940, Aug. 2014, doi: 10.1021/cs500606g.

[2]   B. S. N Ruddl and P. Popper, "New compounds of the K2NiF4 type," 1957.

[3]   S. N. Ruddlesden and P. Popper, "The compound $Sr_sTi_2O_7$ and its structure," 1958.

[4]   R. Uppuluri, A. Sen Gupta, A. S. Rosas, and T. E. Mallouk, "Soft chemistry of ion-exchangeable layered metal oxides," Chemical Society Reviews, vol. 47, no. 7. Royal Society of Chemistry, pp. 2401–2430, Apr. 07, 2018. doi: 10.1039/c7cs00290d.

[5]   W. C. Hansen, L. T. Brownmiller, and R. H. Bogue, "STUDIES ON THE SYSTEM CALCIUM OXIDE-ALUMINA-FERRIC OXIDE1," J Am Chem Soc, vol. 50, no. 2, pp. 396–406, May 2002, doi: 10.1021/ja01389a023.

[6]   G. G. C. Arizaga, K. G. Satyanarayana, and F. Wypych, "Layered hydroxide salts: Synthesis, properties and potential applications," Solid State Ion, vol. 178, no. 15–18, pp. 1143–1162, Jun. 2007, doi: 10.1016/J.SSI.2007.04.016.

[7]   "werthmann1984".

[8]   M. Shao-Yu and R. Xiao-Xia ZHOU Zhao-Hui, "Synthesis and Crystal Structure of Na 2 TiO 3," 2008.

[9]   P. J. P. Naeyaert, M. Avdeev, N. Sharma, H. Ben Yahia, and C. D. Ling, "Synthetic, Structural, and Electrochemical Study of Monoclinic $Na_4Ti_5O_{12}$ as a Sodium-Ion Battery Anode Material," Chemistry of Materials, vol. 26, no. 24, pp. 7067–7072, Dec. 2014, doi: 10.1021/cm5035358.

[10]   S. Andersson and A. D. Wadsley, "The Crystal Structure of $Na_2Ti_{30~}$," 1961.

[11]   Y. Zhang, J. Wu, Y. Zhang, W. Guo, and S. Ruan, "Characterization and humidity sensing properties of the sensor based on $Na_2Ti_3O_7$ nanotubes," J Nanosci Nanotechnol, vol. 14, no. 6, pp. 4303–4307, 2014, doi: 10.1166/jnn.2014.8038.

[12]   Y. Zhang et al., "A novel humidity sensor based on $Na_2Ti_3O_7$ nanowires with rapid response-recovery," Sens Actuators B Chem, vol. 135, no. 1, pp. 317–321, Dec. 2008, doi: 10.1016/J.SNB.2008.08.042.

[13]   H. Song, H. Jiang, T. Liu, X. Liu, and G. Meng, "Preparation and photocatalytic activity of alkali titanate nano materials $A_2Ti_nO_{2n+1}$ (A = Li, Na and K)," Mater Res Bull, vol. 42, no. 2, pp. 334–344, Feb. 2007, doi: 10.1016/J.MATERRESBULL.2006.05.025.

[14]   Y. Jiang, P. Zhang, H. Jin, X. Liu, and Y. Ding, "Flexible, nonflammable and Li-dendrite resistant $Na_2Ti_3O_7$ nanobelt-based separators for advanced Li storage," J Memb Sci, vol. 583, pp. 190–199, Aug. 2019, doi: 10.1016/J.MEMSCI.2019.04.032.

[15]   X. Zhu, D. Sun, B. Luo, Y. Hu, and L. Wang, "A stable high-power $Na_2Ti_3O_7/LiNi_{0.5}Mn_{1.5}O_4$ Li-ion hybrid energy storage device," Electrochim Acta, vol. 284, pp. 30–37, Sep. 2018, doi: 10.1016/J.ELECTACTA.2018.07.153.

[16]   T. Horiuchi, K. Sakuma, T. Fukui, Y. Kubo, T. Osaki, and T. Mori, "Suppression of carbon deposition in the CO_2-reforming of CH_4 by adding basic metal oxides to a Ni/Al_2O_3 catalyst," Appl Catal A Gen, vol. 144, no. 1–2, pp. 111–120, Sep. 1996, doi: 10.1016/0926-860X(96)00100-7.

[17]   J. Chen, X. Zhou, C. Mei, J. Xu, and C. P. Wong, "Improving the sodiation performance of $Na_2Ti_3O_7$ through Nb-doping," Electrochim Acta, vol. 224, pp. 446–451, Jan. 2017, doi: 10.1016/J.ELECTACTA.2016.12.094.

[18]   M. Németh et al., "Na-promoted Ni/ZrO_2 dry reforming catalyst with high efficiency: Details of Na_2O-ZrO_2-Ni interaction controlling activity and coke formation," Catal Sci Technol, vol. 7, no. 22, pp. 5386–5401, 2017, doi: 10.1039/c7cy01011g.

[19]   J. Ramírez-Salgado, E. Djurado, and P. Fabry, "Synthesis of sodium titanate

composites by sol-gel method for use in gas potentiometric sensors," J Eur Ceram Soc, vol. 24, no. 8, pp. 2477–2483, Jul. 2004, doi: 10.1016/J.JEURCERAMSOC.2003.07.014.

[20]   "bamberger1987".

[21]   F. L. R. e. Silva et al., "Polarized Raman, FTIR, and DFT study of $Na_2Ti_3O_7$ microcrystals," Journal of Raman Spectroscopy, vol. 49, no. 3, pp. 538–548, Mar. 2018, doi: 10.1002/jrs.5316.

[22]   D. S. Liu et al., "Phosphorus-Doping-Induced Surface Vacancies of 3D $Na_2Ti_3O_7$ Nanowire Arrays Enabling High-Rate and Long-Life Sodium Storage," Chemistry - A European Journal, vol. 25, no. 65, pp. 14881–14889, Nov. 2019, doi: 10.1002/chem.201902993.

[23]   J. Xia et al., "Lanthanide doping induced electrochemical enhancement of $Na_2Ti_3O_7$ anodes for sodium-ion batteries," Chem Sci, vol. 9, no. 14, pp. 3421–3425, 2018, doi: 10.1039/c7sc05185a.

[24]   P. Li et al., "Hydrogenated $Na_2Ti_3O_7$ Epitaxially Grown on Flexible N-Doped Carbon Sponge for Potassium-Ion Batteries," ACS Appl Mater Interfaces, vol. 10, no. 44, pp. 37974–37980, Nov. 2018, doi: 10.1021/acsami.8b11354.

[25]   A. P. Grosvenor, M. C. Biesinger, R. S. C. Smart, and N. S. McIntyre, "New interpretations of XPS spectra of nickel metal and oxides," Surf Sci, vol. 600, no. 9, pp. 1771–1779, May 2006, doi: 10.1016/j.susc.2006.01.041.

[26]   Y. Zhang et al., "Sodium titanate cuboid as advanced anode material for sodium ion batteries," J Power Sources, vol. 305, pp. 200–208, Feb. 2016, doi: 10.1016/J.JPOWSOUR.2015.11.101.

[27]   S. S. Costa et al., "Thermal and electrical properties of $Na_2Ti_3O_7$ /Na_2Ti_6 O_{13} /POMA composites." [Online]. Available: https://ssrn.com/abstract=4079488

[28]   C. Y. Xu et al., "Molten salt synthesis of $Na_2Ti_3O_7$ and $Na_2Ti_6O_{13}$ one-dimensional nanostructures and their photocatalytic and humidity sensing properties," CrystEngComm,

vol. 15, no. 17, pp. 3448–3454, May 2013, doi: 10.1039/c3ce27092k.

[29]   H. Liu et al., "A Raman spectroscopic and TEM study on the structural evolution of $Na_2Ti_3O_7$ during the transition to $Na_2Ti_6O_{13}$," Journal of Raman Spectroscopy, vol. 41, no. 10, pp. 1331–1337, 2010, doi: 10.1002/jrs.2561.

[30]   X. Gao, J. Ashok, and S. Kawi, "Smart Designs of Anti-Coking and Anti-Sintering Ni-Based Catalysts for Dry Reforming of Methane: A Recent Review," Reactions, vol. 1, no. 2, pp. 162–194, Dec. 2020, doi: 10.3390/reactions1020013.

[31]   L. Li et al., "Controlled surface segregation leads to efficient coke-resistant nickel/platinum bimetallic catalysts for the dry reforming of methane," ChemCatChem, vol. 7, no. 5, pp. 819–829, 2015, doi: 10.1002/cctc.201402965.

[32]   P. Ferreira-Aparicio, I. Rodríguez-Ramos, J. A. Anderson, and A. Guerrero-Ruiz, "Mechanistic aspects of the dry reforming of methane over ruthenium catalysts," Appl Catal A Gen, vol. 202, no. 2, pp. 183–196, Aug. 2000, doi: 10.1016/S0926-860X(00)00525-1.

[33]   J. Saleh et al., "Stability and Activity of Rhodium Promoted Nickel-Based Catalysts in Dry Reforming of Methane," Nanomaterials, vol. 13, no. 3, p. 547, Jan. 2023, doi: 10.3390/nano13030547.

[34]   C. Crisafulli, S. Scirè, R. Maggiore, S. Minicò, and S. Galvagno, "CO_2 reforming of methane over Ni-Ru and Ni-Pd bimetallic catalysts," 1999.

[35]   Z. Lian, S. O. Olanrele, C. Si, M. Yang, and B. Li, "Critical Role of Interfacial Sites between Nickel and CeO_2 Support in Dry Reforming of Methane: Revisit of Reaction Mechanism and Origin of Stability," The Journal of Physical Chemistry C, vol. 124, no. 9, pp. 5118–5124, Feb. 2020, doi: 10.1021/acs.jpcc.9b09856.

[36]   K. Sutthiumporn and S. Kawi, "Promotional effect of alkaline earth over Ni-La_2O_3 catalyst for CO_2 reforming of CH_4: Role of surface oxygen species on H_2 production and carbon suppression," Int J Hydrogen Energy, vol. 36, no. 22, pp. 14435–14446, Nov. 2011, doi: 10.1016/j.ijhydene.2011.08.022.

[37]   A. Tsoukalou, Q. Imtiaz, S. M. Kim, P. M. Abdala, S. Yoon, and C. R. Müller, "Dry-reforming of methane over bimetallic Ni–M/La$_2$O$_3$ (M = Co, Fe): The effect of the rate of La$_2$O$_2$CO$_3$ formation and phase stability on the catalytic activity and stability," J Catal, vol. 343, pp. 208–214, Nov. 2016, doi: 10.1016/J.JCAT.2016.03.018.

[38]   Z. Bian, S. Das, M. H. Wai, P. Hongmanorom, and S. Kawi, "A Review on Bimetallic Nickel-Based Catalysts for CO$_2$ Reforming of Methane," ChemPhysChem, vol. 18, no. 22. Wiley-VCH Verlag, pp. 3117–3134, Nov. 17, 2017. doi: 10.1002/cphc.201700529.

[39]   Z. Wu et al., "Lattice Strained Ni-Co alloy as a High-Performance Catalyst for Catalytic Dry Reforming of Methane," ACS Catal, vol. 9, no. 4, pp. 2693–2700, Jan. 2019, doi: 10.1021/acscatal.8b02821.

[40]   D. San-José-Alonso, J. Juan-Juan, M. J. Illán-Gómez, and M. C. Román-Martínez, "Ni, Co and bimetallic Ni–Co catalysts for the dry reforming of methane," Appl Catal A Gen, vol. 371, no. 1–2, pp. 54–59, Dec. 2009, doi: 10.1016/J.APCATA.2009.09.026.

[41]   L. Huang et al., "Optimization of Ni-Based Catalysts for Dry Reforming of Methane via Alloy Design: A Review," Energy & Fuels, vol. 36, no. 10, pp. 5102–5151, May 2022, doi: 10.1021/acs.energyfuels.2c00523.

[42]   M. A. Khan, M. S. Challiwala, A. V. Prakash, and N. O. Elbashir, "Conceptual modeling of a reactor bed of a nickel-copper bi-metallic catalyst for dry reforming of methane," Chem Eng Sci, vol. 267, p. 118315, Mar. 2023, doi: 10.1016/J.CES.2022.118315.

[43]   K. Han, S. Wang, Q. Liu, and F. Wang, "Optimizing the Ni/Cu Ratio in Ni–Cu Nanoparticle Catalysts for Methane Dry Reforming," ACS Appl Nano Mater, vol. 4, no. 5, pp. 5340–5348, May 2021, doi: 10.1021/acsanm.1c00673.

[44]   A. L. Sauvet, S. Baliteau, C. Lopez, and P. Fabry, "Synthesis and characterization of sodium titanates Na$_2$Ti$_3$O$_7$ and Na$_2$Ti$_6$O$_{13}$," J Solid State Chem, vol. 177, no. 12, pp. 4508–4515, Dec. 2004, doi: 10.1016/J.JSSC.2004.09.008.

[45]   H. Ali-Löytty et al., "Ambient-Pressure XPS Study of a Ni–Fe Electrocatalyst for the

Oxygen Evolution Reaction," The Journal of Physical Chemistry C, vol. 120, no. 4, pp. 2247–2253, Jan. 2016, doi: 10.1021/acs.jpcc.5b10931.

Chapter 5

Summary and Conclusions

5.1 Summary:

The first chapter concentrates on the negative influence of the greenhouse effect on the world's atmosphere, despite the fact that it plays a crucial function in keeping the globe warm for human and aquatic organism existence by trapping the heat of the sun through the jacketing of greenhouse gases such as CO_2, CH_4, NO_x, and other gases. Population growth and industrialization have elevated the concentrations of greenhouse gases, particularly CO_2, above their optimum levels. Physical and chemical techniques have been used to convert CO_2 into useful compounds such as methanol, DME, and high chain hydrocarbons, as well as syngas via various chemical processes. Dry reforming of methane has been widely used to transform two greenhouse gases, methane and CO_2, into syngas with an H_2/CO ratio close to unity. Several oxide-related materials, such as supported, structured oxides as catalysts, were tested for DRM conversion and durability. The effect of the catalyst's various components, such as active metal, support qualities, basic strength, metal support interaction, catalyst stability, and, most critically, carbon gasification capability, was thoroughly examined and explained in this chapter. The second chapter looks into the use of pyrochlore-based structured oxide catalysts in DRM reactions. Because of their stability and the existence of an oxygen vacancy in the structure, pyrochlore-related ternary oxide materials are being studied extensively in various catalytic reactions. Taking this into account, Ni substituted Gd-based pyrochlores were synthesized using the traditional Pechini process, characterized using several analytical techniques, and examined in dry reforming of methane. The first section of this chapter discusses the effect of B site substitution in the Gd-based ternary metal oxides catalyst $Gd_2B_{2-x}Ni_xO_{7-\delta}$ (B = Zr, Ti) in DRM. XRD and Rietveld analyses were used to investigate the structure stability and Ni concentrations inside and outside the lattice. Ti-based catalysts with high basic strength, reducibility, and hydroxyl species concentrations provide higher conversions of CO_2 and methane into syngas with high H_2/CO ratio near to equilibrium with carbon gasification capacity than Zr-based catalysts

providing superior activity and durability for 100 in DRM stream.

The Ni substituted $Gd_2Zr_2O_7$ catalyst was chosen for further examination in the second half of this chapter because to its lower activity performance in the DRM conditions observed in the first section. This study concentrated on the effect of Ni concentration in the structure. $Gd_2Zr_{2-x}Ni_xO_7$ (0.2, 0.5, 0.75) catalysts named GZN2, GZN5, and GZN75 with increased Ni content were synthesized, characterized, and tested in DRM. The results indicated that the GZN75 contains an optimal quantity of Ni both outside and inside the lattice as NiO. Furthermore, the greater reducibility of GZN75 catalyst among all catalysts demonstrated that the strong metal support interaction and higher amount of defect created OH^- species play a significant role in simultaneous gasification of carbon synthesized during DRM, which promotes methane activation for subsequent reaction. Although Ni in lattice and nicely dispersed surface NiO has a good impact on high DRM conversions because coke accumulation is also observed in GZN75 catalyst.

After observing enhanced coke formation in $Gd_2Zr_2O_7$ catalysts with optimized Ni concentration, the next part of this chapter focused on carbon gasification by substituting Ce in $Gd_2Zr_{1.8}Ni_{0.2}O_7$ catalyst with a series of catalysts as $Gd_2Zr_{1.8-x}Ni_{0.2}Ce_xO_{7-\delta}$ (x = 0.1, 0.2, 0.50.75) catalysts and comparing activity with parent GZN2 catalyst. Ce's redox behavior tends to form defects and active hydroxyl species, which provide a mechanism for oxidizing carbon into CO and increasing CO_2 activation. DRIFTS studies indicated that the optimal quantity of Ce in GZN2C2 catalysts initiates and maintains continuous CO_2 activation as CO through the creation of intermediates such as bi and monodentate carbonates, showing the presence of a basic site on the catalyst surface compared to other substituted catalysts. Furthermore, the presence of polydentate carbonate species in the parent catalyst demonstrates that an excess of acidic sites on the catalyst surface limits CO_2 adsorption and coke gasification. XRD, Raman, and TGA studies all show that the optimized Ce in GZN2C2 catalyst has less carbon on the surface. While the parent catalyst contains multiwalled carbon

nanotubes and excess graphitic carbon, the active sites for the subsequent DRM cycle are not covered.

Perovskite related oxide Ni substituted $SrMnO_3$ catalyst was synthesized and investigated in chapter 3. $SrMn_{1.8}Ni_{0.2}O_3$ catalysts was screened in DRM condition for 24 hours. Ni substituted $SrMnO_3$ crystalized in hexagonal phase with small impurities of $SrCO_3$ and Mn_2O_3.Furthermore, rare earth metal doping is well-known for improving the basic strength of the support, and substitution in the B site improves the synergetic effect with Ni and improves the production of defects, oxygen vacancies, and active OH- species owing to coke deposition mitigation. To demonstrate that rare earth metals (Nd, Sm, and Eu) doped in $SrMnO_3$ with a constant concentration of Ni were screened for DRM. Furthermore, Rare earth metal doping are famous for enhancing the basic strength of the support and substitution in B site enhances the synergetic effect with Ni and improves formation of defects, oxygen vacancies and active OH^- species owing to mitigate the coke deposition. To demonstrate that rare earth metals (Nd, Sm and Eu) with Ni in constant concentration was doped in $SrMnO_3$ and screened for DRM. Doping of rare earth metals in $SrMnO_3$ has improved the reducibility of all catalysts, among them Sm based catalysts have Dispersed NiO and Ni substituted in the bulk which generates hydroxyl species analysed by XPS analysis. DRM activity of all catalysts was tested for 24 hours, and Sm doped catalyst demonstrated the highest conversions among all catalysts. A durability test for 100 hours was also performed in DRM conditions. Catalyst has been shown to be stable and active for 100 hours, with less carbon production activity of all catalysts checked for 24 hours, Sm doped catalyst shown higher conversions among all catalysts, its durability test for 100 hours also conducted in DRM conditions. Catalyst has been proven to be stable and active for 100 hours and less carbon formation was observed.

In DRM, a family of stacked Ni substituted sodium titanates $Na_2Ti_3O_7$ was studied. The stability of a Ni substituted $Na_2Ti_3O_7$ catalyst was tested in DRM conditions in a tube furnace

at various temperatures and subsequently in a reactor tube for 12 hours. Phase changes in the parent structure were identified after 12 hours of running. The first section of this chapter discusses the influence of Ni concentration in $Na_2Ti_3O_7$ catalysts on DRM activity and parent compound stability. A series of $Na_2Ti_{3-x}Ni_xO_7$ catalysts (X= 0.02, 0.05,0.1,0.2) were synthesized and characterized using various approaches. NTN02 with 3.80 wt.% Ni catalyst was identified as a good catalyst with high conversions. After the reaction, spent catalyst analysis showed a phase change in all catalysts, with the $Na_2Ti_6O_{13}$ phase emerging as the secondary phase. However, XRD peaks corresponding to $Na_2Ti_6O_{13}$ catalyst were identified less frequently in NTN02 catalysts than in other catalysts. This suggests that the optimum Ni insertion aids in the retention of parent catalyst in NTN02 among all for 100 hours of reaction stream with the least amount of coke accumulation. The second section of this chapter is concerned with comprehending the effect of transition metals (Co, Cu, Fe) doping on NTN002 catalysts. Substitution of transition metals in the B site with Ni in NTN002 catalysts resulted in a beneficial structural change, as DRM activity rose after doping, and carbon resistance was also seen in doped catalysts. XRD and Raman studies were also used to get a look at structural changes in used catalyst.

5.2 Conclusions:

- ❖ Ti doping in a Gd-based pyrochlore catalyst shown more activity than the Zr equivalent in DRM.

- ❖ A larger concentration of format and hydroxyl species increases carbon resistance in the GTNO catalyst for 100 hours on stream in DRM.

- ❖ Optimal Ni concentration in GZN75 catalyst boosted reducibility and basic strength, resulting in high conversion into syngas with an H_2/CO ratio close to unity.

- ❖ Ce substitution in the parent catalyst $Gd_2Zr_{1.8}Ni_{0.2}O_7$ increases coke gasification during the DRM reaction. GZN2C2 catalyst with an appropriate amount of Ce

promotes CO_2 activation and formation of CO while also enhancing hydroxyl formation to reduce carbon production.

❖ Sm-doped perovskite type $SrMn_{1.8}Ni_{0.2}O_3$ catalysts demonstrated greater conversions, increased reducibility, and strong metal-support interaction.

❖ $Na_2Ti_3O_7$, the first-ever investigated in DRM has shown better activity with optimum concentrations of Ni as in NTN02 catalyst. Because of the synergetic impact of Cu and Ni with carbon resistance, Cu doping in NTN002 catalyst has a beneficial influence on structural stability and superior activity towards DRM.

5.3 Recommendations for Future Work:

The biggest challenge in front of whole world is to mitigate the emission of greenhouse gases mainly CO_2 and methane. Dry reforming of methane is one of the important reactions among all chemical reactions in utilizing the greenhouse gases. To achieve that formation of robust and durable catalyst is must among all aspects. In present work, the various aspects of structurally ordered catalysts like pyrochlores, perovskite and layered oxide catalysts are presented. Since the effect of synthesis, structural alterations and different metal substitutions were thoroughly studied. In the first chapter, by using cost effective metals like Gd, Zr, Ti was utilized as pyrochlore catalysts and their stability and activity was checked with most abundant Ni metal. Furthermore, trace amount of Ce in pyrochlore catalysts in coke gasification process also studied. Perovskite related $SrMnO_3$ and rare earth metals (Sm, Nd, Eu) substitution and their composition also studied and confirmed in activity. In the third chapter layered oxide catalysts wee first time checked for DRM for 100 hours of stream, role of transition metal substitution also studied in DRM. These catalysts must be checked with more different compositions to make them more stable for DRM reaction conditions. Moreover, their activity must be checked in pilot scale in DRM.

ABSTRACT

Name of the Student: Seema R. Ghodke   **Registration No.:** 10CC20A26072

Faculty of Study: Chemical Sciences   **Year of Submission:** 2023

AcSIR academic centre/CSIR Lab: CSIR-NCL Pune

Name of the Supervisor(s): Dr. R. Nandini Devi

 Title of the thesis: Study of structured oxide catalysts in Dry Reforming of Methane

----

Dry reforming of methane (DRM), reaction which utilizes two greenhouse gases CO_2 and CH_4 into syngas with H_2/CO ratio 1. Harsh reaction conditions like high operating temperature cause active metal sintering, agglomeration, coke formation and catalyst deactivation. Present thesis unveils the application of structured oxides like perovskite, pyrochlores and layered oxide catalyst in DRM. Thesis comprised of five chapters fleetingly described as follows: Chapter 1 covers the broad introduction of greenhouse effect, alarmed emission and utilization of CO_2 by various aspects explained widely and mainly focused on DRM. In chapter 2 effect of support, active metal concentration and Ce redox behavior was briefly studied in Gd based pyrochlore catalyst. Ti based $Gd_2Ti_{1.8}Ni_{0.2}O_{7-\delta}$, $Gd_2Zr_{1.25}Ni_{0.75}O_{7-\delta}$ and $Gd_2Zr_{1.8}Ni_{0.2}Ce_{0.2}O_{7-\delta}$ catalysts showed superior activity among all screened catalysts. Chapter 3 deals with screening of perovskite catalyst $SrMnO_3$ and effect of rare earth metals substitution (Sm, Nd, Eu) in A site of the catalyst in DRM. Sm doped $SrMn_{1.8}Ni_{0.2}O_3$ catalyst has showed less coke with high conversion. The 4th chapter put lights on layered $Na_2Ti_3O_7$ catalyst synthesized by sol gel method and screened first ever in DRM with Ni as active metal. First and second part of the work shown the effect of Ni concentration and transition metal (Co, Cu, Fe) doping in structure stability and modifications during DRM in $Na_2Ti_3O_7$ catalyst. $Na_2Ti_{3-x}Ni_xO_7$ (X= 0.2) and Cu doped catalysts showed high conversions and stability with less impurity phases in DRM. Chapter 5 summarize and conclude the findings of presented work in the thesis.

List of Publications

List of publication(s) in SCI Journal(s) (published & accepted) emanating from the thesis work, with complete bibliographic details.

- ➤ **Seema R. Ghodke**, S. Thundiyil, P. Dongapure, Nandini Devi R. Effect of B site substitution in $Gd_2B_{2-x}Ni_yO_{7-\delta}$ (B= Ti, Zr) ternary metal oxide catalysts in dry reforming of methane. *Molecular Catalysis* ,522 (2022) 112242. https://doi.org/10.1016/j.mcat.2022.112242

- ➤ **Seema R. Ghodke**, Akash Bhatkar, R. Nandini Devi. Understanding the effect of Ce substitution in $Gd_2Zr_{1.8}Ni_{0.2}O_{7-\delta}$ catalyst for dry reforming of methane. (To be communicated)

- ➤ **Seema R. Ghodke**, R. Nandini Devi. Layered metal oxide $Na_2Ti_3O_7$: Structural modifications and screening in Dry Reforming of Methane. (To be communicated)

List of publication(s) in SCI Journal(s) (published & accepted) other than the thesis work, with complete bibliographic details.

- ➤ S. Dama, **Seema R. Ghodke**, R. Bobade, HR. Gurav, S. Chilukuri. Active and durable alkaline earth metal substituted perovskite catalysts for dry reforming of methane. *Appl. Catal. B: Environ.,* 224 (2018) 146–58. https://doi.org/10.1016/j.apcatb.2017.10.048

- ➤ S. Dama, **Seema R. Ghodke**, R. Bobade, H. Gurav, S. Chilukuri. Tuning the dimensionality of layered $Sr_{n+1}Ti_{n-x}Ni_xO_{3n+1}$ perovskite structures for improved activity in syngas generation. *J. Catal.*, 360 (2018) 27–39. https://doi.org/10.1016/j.jcat.2018.01.015

Work Presented in Conferences

1) Science Day (Poster presentation) at CSIR-NCL Pune

Effect of Ni particle size in rare earth doped ceria catalysts on dry reforming of methane

Seema R. Ghodke, Srikanth Dama, Satyanarayana Chilukuri, R. Nandini Devi*

Abstract

Rare Earth (La Pr, Nd, Sm and Gd) doped ceria catalysts with 5 wt% Ni were synthesized by co-precipitation method and characterized by means of N_2 adsorption, X-ray diffraction (XRD), Raman spectroscopy, and temperature programmed (TP) techniques. All the synthesized samples crystallized to form stable cubic structures. Gd doped Ceria (GDC) catalyst showed good catalytic activity for dry reforming of methane (DRM) amongst all the catalysts. Effect of Ni particle size on DRM reaction in Ni/GDC samples were further studied by varying the synthesis methods as hydrothermal synthesis, solid state synthesis and citrate gel method.

2) 23rd National symposium on Applied Catalysis in Emerging Technologies for chemicals, (Poster presentation) at Bangalore

Effect of Ni particle size in rare earth doped ceria catalysts on dry reforming of methane

Seema R. Ghodke, Srikanth Dama, Satyanarayana Chilukuri, R. Nandini Devi*

Abstract

Rare Earth (La Pr, Nd, Sm and Gd) doped ceria catalysts with 5 wt.% Ni were synthesized by co-precipitation method and characterized by means of N_2 adsorption, X-ray diffraction (XRD), Raman spectroscopy, and temperature programmed (TP) techniques. All the synthesized samples crystallized to form stable cubic structures. Gd doped Ceria (GDC) catalyst showed good catalytic activity for dry reforming of methane (DRM) amongst all the catalysts. Effect of Ni particle size on DRM reaction in Ni/GDC samples were further studied by varying the synthesis methods as hydrothermal synthesis, solid state synthesis and citrate gel method.

3) Asia- Pacific Congress on Catalysis (Poster presentation) at Bangkok, Thailand

Scale Up of Perovskite material: An efficient catalyst for Dry reforming of Methane

Seema R. Ghodke, Akshay R. Kasar, R. Nandini Devi*
The world is preparing to overcome the possible effects of global warming attributed to greenhouse gas emissions particularly CO_2 and CH_4 emissions. Numerous initiatives are being taken for the development of capture and utilization technologies to reduce the level of greenhouse gases. In recent times various research activities are

proposed to utilize both the greenhouse gases to obtain fuels and chemicals. Dry reforming of methane is one such programme that utilizes both CO_2 and CH_4 to give valuable syngas. In this concern, Perovskite based catalysts (ABO_3) has been synthesized, in which alkaline earth metal used in A site, ZrO_2 as a support and nickel as an active metal. After success in small scale testing, catalyst has been used for scale up purpose. For large scale synthesis, different methods like sol-gel, paper dip and spray pyrolysis methods were implemented.

In every method citric acid has been used as a chelating agent. Rare earth substituted catalyst shows superior activity and stability towards dry reforming of methane. On the other hand, spent catalyst has been investigated by XRD and TGA. In the largescale platform, catalyst shows superior metal to support interactions and high surface area which helps the catalyst for dry reforming reaction activity with long life.

4) The 9th Tokyo Conference on Advanced Catalytic Science and Technology (Oral presentation) Fukuoka Japan

Effect of B site substitution in $Gd_2B_{2-x}Ni_yO_{7-\delta}$ (B= Ti, Zr) ternary metal oxide catalysts in dry reforming of methane

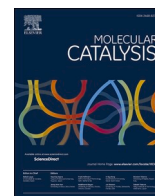Seema R. Ghodke, Shibin Thundiyil, R. Nandini Devi*

Abstract: Structured catalysts are emerging as stable and superiorly active catalysts in Dry reforming of methane. Substituted $Gd_2B_{1-0.2}Ni_{0.2}O_7$ (B= Ti, Zr) catalysts has been synthesized by Pechini method and characterized by XRD, Raman. Rietveld refinement, TPR and CO_2-TPD. All catalysts screened in Dry reforming of methane. Ti based $Gd_2B_{1-0.2}Ni_{0.2}O_7$ catalysts showed the stable and superior activity towards DRM for 100h. Surface analysis has been done by XPS and insitu IR. Presence and amount of graphitic carbon species in spent catalysts has been analysed by XRD and TGA analysis. The $Gd_2Ti_{1-0.2}Ni_{0.2}O_7$ catalysts lacks of carbon species, performed prolonged activity for DRM.

5) 4th International conference on recent advances in material chemistry, Tamil Nadu India (Poster presentation)

Scale Up of Perovskite material: An efficient catalyst for Dry reforming of Methane

Seema R. Ghodke, Akshay R. Kasar, R. Nandini Devi*

The world is preparing to overcome the possible effects of global warming attributed to greenhouse gas emissions particularly CO_2 and CH_4 emissions. Numerous initiatives are being taken for the development of capture and utilization technologies to reduce the level of greenhouse gases. In recent times various research activities are proposed to utilize both the greenhouse gases to obtain fuels and chemicals. Dry reforming of methane is one such programme that utilizes both CO_2 and CH_4 to give valuable syngas. In this concern, Perovskite based catalysts (ABO_3) has been synthesized, in which alkaline earth metal used in A site, ZrO_2 as a support and nickel as an active metal. After success in small scale testing, catalyst has been used for scale up purpose. For large scale synthesis, different methods like sol-gel, paper dip and spray pyrolysis methods were implemented. In every method citric acid has been used as a chelating agent. Rare earth substituted catalyst shows superior activity and stability towards dry reforming of methane. On the other hand, spent catalyst has been investigated by XRD and TGA. In the largescale platform, catalyst shows superior metal to support interactions and high surface area which helps the catalyst for dry reforming reaction activity with long life.

Effect of B site substitution in $Gd_2B_{2-x}Ni_yO_{7-\delta}$ (B= Ti, Zr) ternary metal oxide catalysts in dry reforming of methane

Seema R. Ghodke [a,b], Shibin Thundiyil [a,b], Pavan Dongapure [a,b], R. Nandini Devi [a,b,*]

[a] Catalysis and Inorganic Chemistry Division, CSIR-National Chemical Laboratory, Pune 411008, India
[b] Academy of Scientific and Innovative Research (AcSIR), Ghaziabad 201002, India

ARTICLE INFO

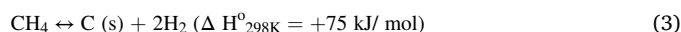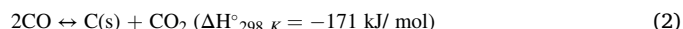## ABSTRACT

Structured catalysts are emerging as active and durable catalysts in dry reforming of methane due to their inherent characteristics like lattice insertion of active metals and consequent stability imparted. Here we report Ti and Zr substituted $Gd_2B_{2-x}Ni_yO_{7-\delta}$ (B = Ti, Zr) catalysts synthesized by citrate gel method, which are characterized and tested for dry reforming of methane. Structure and Ni substitution has been confirmed by Rietveld refinement of powder XRD patterns and Raman analysis. TPR and CO_2-TPD were performed to analyze the reducibility and effect of basic sites of catalysts in DRM activity. Ni doped Ti analogue shows stable and superior activity towards dry reforming of methane for 100 h. The in situ IR studies and XPS analysis confirmed the presence of surface hydroxyl species in this catalyst, which triggers the activation of CO_2 and provides higher and durable activity in dry reforming reaction. Absence of any C formation in this catalyst after durability test indicates the mechanism of C gasification by the surface hydroxyl species enhancing stable activity for long durations.

1. Introduction

The increase in global average temperature is attributed to an alarming upsurge in the greenhouse gas emissions, especially CO_2. To address this issue, several reactions converting CO_2 to useful products have been reported, viz., hydrogenation, reforming, methanation, carboxylation etc [1]. Among them, CO_2 reforming has attracted more attention since it utilizes two greenhouse gasses, CO_2 and methane, to generate valuable syngas (1). In particular, dry reforming of methane (DRM) generates syngas with $H_2/CO \approx 1$ at thermodynamic equilibrium using CO_2 and CH_4 [2]. Generated syngas can be further used for the synthesis of DME or long chain hydrocarbons by FT synthesis [3,4].

$$CH_4 + CO_2 \leftrightarrow 2CO + 2H_2 \ (\Delta H^\circ_{298\,K} = +247 \text{ kJ/mol}) \quad (1)$$
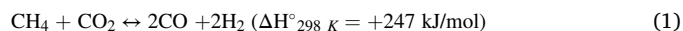
Most of the catalysts reported for this process are based on Ni supported on basic oxides, well known for steam reforming. Although, Ni based catalysts show superior activity at steam reforming conditions, they are prone to severe coke formation under dry reforming conditions, caused by two reactions, Boudouard reaction (2) and methane cracking (3) at temperatures around 550 °C and 700 °C respectively [5,6].

$$2CO \leftrightarrow C(s) + CO_2 \ (\Delta H^\circ_{298\,K} = -171 \text{ kJ/mol}) \quad (2)$$

$$CH_4 \leftrightarrow C\,(s) + 2H_2 \ (\Delta\,H^o_{298K} = +75 \text{ kJ/ mol}) \quad (3)$$

Another major drawback of supported metal catalysts, especially Ni, is the sintering of active metal nanoparticles at high temperature thereby compromising number of active sites in the catalyst [7]. Several suggestions to minimize these problems are documented and it has been observed that high dispersion and smaller particles of the active Ni with good metal support interaction can limit sintering as well as coke formation [8]. Support characteristics like redox property, basicity etc. also influence the activity and durability of the catalyst. Recently, the concept of stabilizing active metal sites as ionic lattice sites in stable structured oxides, to prevent sintering and coke formation has been attracting attention.

$A_2B_2O_7$ ternary oxides form a potential family of compounds for various reforming reactions due to their high thermal stability and tolerance to structural variations and lattice site doping. These analogous compounds are known to have various structure types like pyrochlores and defect fluorite. Effect of different parameters viz., A and B site substitutions in these structure types and oxygen vacancies have been studied for gasification, reforming and coupling reactions etc. Most of the reports are on lanthanum zirconate pyrochlore and noble metals

---

* Corresponding author.
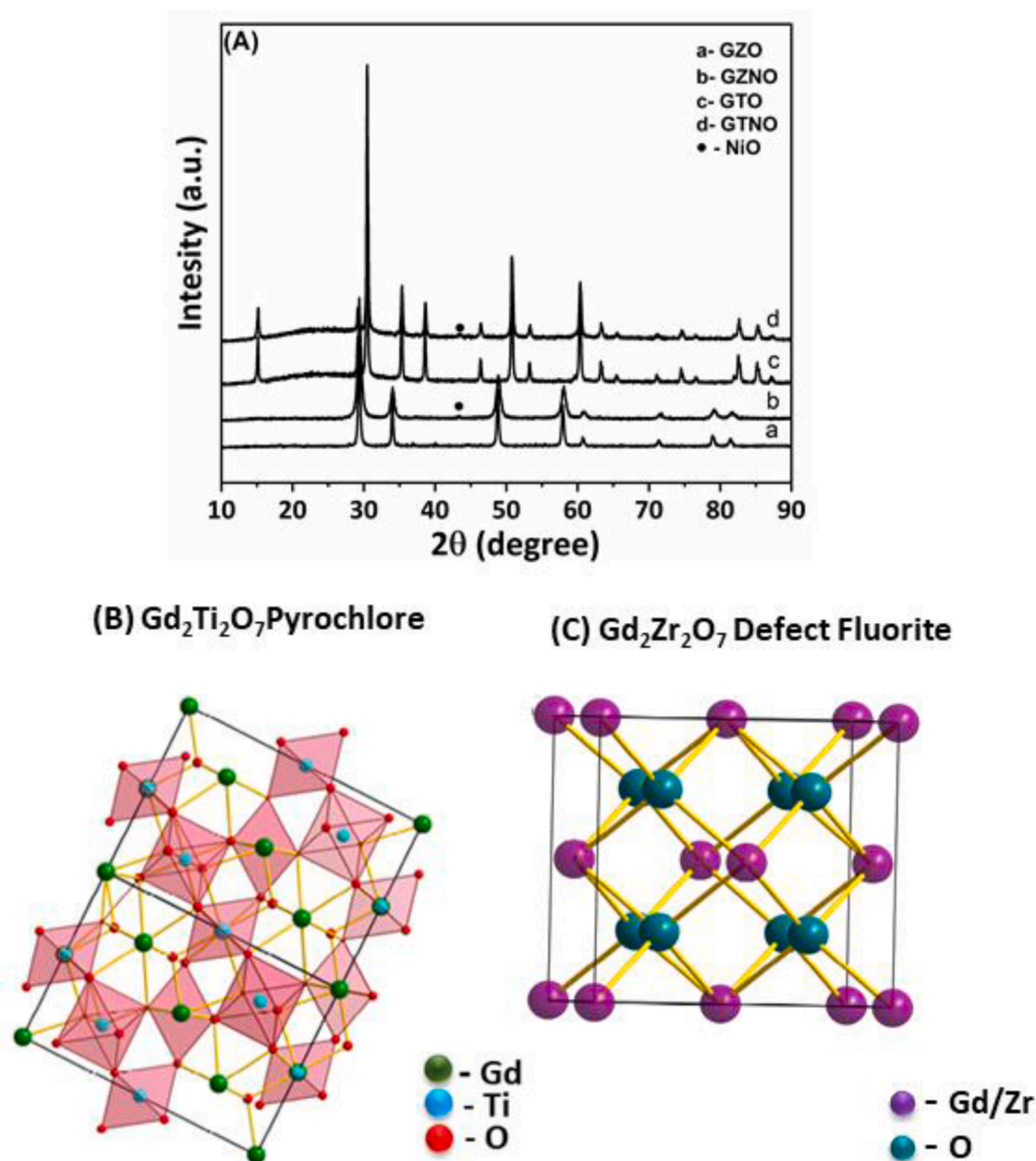*E-mail address:* nr.devi@ncl.res.in (R. Nandini Devi).

Fig. 1. (A) XRD pattern of a) GZO b) GZNO c) GTO d) GTNO. Peaks corresponding to NiO are marked with symbols (•) **(B)** Representative image of $Gd_2Ti_2O_7$ pyrochlore and **(C)** $Gd_2Zr_2O_7$ defect fluorite structure.

like Rh, Ru and Pt as well as Ni have been studied as active metal [9–14]. Apart from this, the effect of Rh doping in the kinetic parameters of dry and bi reforming of methane is also analysed [15–18].

In this paper, we report B site substituted Gd based ternary metal oxides and compared their activity and durability in dry reforming of methane. Unsubstituted and Ni substituted $Gd_2B_2O_7$ (B = Ti and Zr) have been synthesized by conventional citrate gel method. Structure-activity correlation by various characterization techniques and spent catalyst analysis suggests that structured ternary metal oxide catalyst with Ti has superior activity and is stable for dry reforming of methane.

2. Experimental

2.1. Synthesis

All structured catalysts were synthesized by conventional Pechini method. Metal nitrate precursors were dissolved in minimum amount of

distilled water separately, mixed together and then added to citric acid solution with the ratio of 3:1 (citric acid: nitrate precursors) under constant stirring at 80 °C. For Gd and Ti, Gd_2O_3 and Ti isopropoxide were dissolved in conc. HNO_3 before mixing with citric acid. Gd:B:Ni molar ratio in the solution was 1:0.96:0.099 for Ti compound whereas for Zr analogue, it was 1:0.898:0.099. Ethylene glycol was added to the solution as polymerizing agent with molar ratio of 1:1 (EG:CA). Formed gel was dried overnight at 180 °C to promote polyesterification and removal of water. The obtained fluffy material was crushed and calcined at 800 °C for 6 h in air to get the ternary metal oxides.

2.2. Characterizations

Powder x-ray diffraction (XRD) patterns of the parent and Ni substituted $Gd_2B_2O_7$ (B = Ti and Zr) catalysts were collected using PANanalytical X'pert Pro-dual goniometer diffractometer equipped with an X'celerator solid-state detector. Nickel filtered Cu Kα (1.5418 Å)

radiation was used for the data collection using a flat holder in Bragg-Brentano geometry with 1° slit at the source side. The data were recorded in 2θ range (10–90 °) in step size of 0.008 ° GSAS EXPGUI suit was used for Rietveld refinements of powder XRD pattern. First, refinement was carried out by fixing the stoichiometry of B site as in the synthesis and NiO secondary phase was quantified. Then refinement was done again by fixing the Ni occupancy based on the difference of Ni concentration added during synthesis and that present as NiO. The Brunauer-Emmett-Teller (BET) surface areas of the samples were measured by N_2 sorption at liquid nitrogen temperature (−196.15 °C) using a Quantachrome Autosorb iQ equipment. Prior to N_2 adsorption, the samples were degassed at 300 °C for 3 h to remove any residual moisture and other volatiles. Temperature programmed reduction (TPR) profiles were obtained using a Micromeritics Autochem 2920 catalyst characterization system, equipped with TCD detector. Freshly calcined samples were treated in 5% O_2-He gas mixture (30 mL min^{-1}) by ramping the temperature to 400 °C at a heating rate of 5 °C min^{-1}. Following this heat treatment for 1 h, the sample was cooled to 50 °C in Ar (purity 99.995%) flow. Subsequently, the gas was changed to 30 mL min^{-1} of 5% H_2 in Ar flow and the catalyst was heated to 1000 °C at a heating rate of 5 °C min^{-1}. The change in H_2 concentration at the outlet was monitored by TCD and plotted against temperature to get TPR profiles. Water produced during the reduction process was condensed and collected in a cold trap. Temperature programmed desorption of CO_2 (TPD- CO_2) was carried out on a Micromeritics Autochem 2920 equipped with a TCD detector. The samples were first degassed at 300 °C in 40 mL min^{-1} of He flow for 1 hour. Then the sample was cooled to 50 °C in He, and the gas was switched to 30 mL min^{-1} of 10% CO_2 in He for 30 min. Following this, the sample was purged with He for 30 min by ramping the temperature to 100 °C at 5 °C min^{-1} in order to remove the physisorbed CO_2. Subsequently, the sample was heated at 10 °C min^{-1} to 1000 °C under He flow (40 mL min^{-1}) while monitoring the TCD signal for desorbed CO_2. Raman spectra were recorded using Horiba JY Lab RAM HR 800 Czerny-Turner type spectrograph equipped with 800 mm focal length achromatic flat field monochromator and charge-couple device (CCD) detector. The wavenumber region (200–2000 cm^{-1}) was scanned using a He-Ne laser (632.8 nm, 20 mW). The in situ FTIR spectra were collected using Nicolet iS50 Analytical FTIR Spectrometer (Thermo Fisher Scientific) in diffuse reflectance mode (DRIFT) equipped with MCT detector. X-ray photoelectron spectroscopy (XPS) was carried out using K-Alpha+ model Thermo Fisher Scientific (UK) make XPS instrument with an Al Kα source. XPS data of all the compounds were fitted with the Shirley type background subtraction method using XPSPEAK41 software. Quantitative analysis of coke formation in spent catalysts performed by Thermogravimetric analysis in Perkin Elmer TGA/DTA model instruments by heating the sample to 1000 °C in air flow at 10 °C min^{-1}, using the weight loss in a defined region was used to estimate the coke content.

2.3. Catalysis

The dry reforming reactions were carried out in a packed-bed tubular down flow reactor made of Inconel HT, placing it in a programmable tubular furnace. All the gasses (CH_4, CO_2 and N_2) used for the reaction were regulated by mass flow controllers (Brooks Instruments). 0.5 cm^3 (0.6–0.75 g) of 0.3–0.5 mm range catalyst particles were mixed with 0.5 cc of same size quartz pieces and loaded in the reactor tube supported by ceramic wool plugs. The catalyst bed temperature was measured by chromel-alumel thermocouple centered in the catalyst bed. Prior to the reaction, the catalyst was calcined at 700 °C for 5 h and reduced in situ at 700 °C for 5 h using 20% H_2 in N_2 gas mixture. DRM reaction was carried out using a gas mixture consisting of CH_4, CO_2 and N_2 in the volume ratio of 1:1:1; with flow rate 80 mL min^{-1} with total gas hourly space velocity at 28,800 h^{-1}. The product gas mixture was analyzed by online gas chromatograph (Chemito 8610) equipped with a Spherocarb packed column (1/8″ OD and 8 feet length). CH_4 and CO_2 conversions

Table 1
Rietveld refinement data $A_2B_{2-x}Ni_yO_{7-\delta}$ (A= Gd and B = Zr, Ti).

	$Gd_2Zr_2O_7$	$Gd_2Zr_{1.8}Ni_{0.13}O_{7-\delta}$	$Gd_2Ti_2O_7$	$Gd_2Ti_{1.93}Ni_{0.08}O_{7-\delta}$
$\square 2^*$	3.09	2.32	3.63	3.22
wRp (%)**	4.91	3.77	4.86	4.80
Rp (%)**	3.67	2.99	3.84	3.58
Space group	Fm$\overline{3}$m	Fm$\overline{3}$m	Fd$\overline{3}$m	Fd$\overline{3}$m
a/°A	5.3008	5.2678	10.1861	10.1842
Occupancy	Zr= 0.5000	Zr = 0.4500 Ni = 0.0322	Ti = 1.0012	Ti = 0.8926 Ni = 0.0370
Impurity phase (wt %)		NiO = 0.68		NiO = 1.34
Crystallite Size (nm)	54.1	33.1	79.8	55.3

* $\chi^2 = \dfrac{M}{N_{obs} - N_{var}}$ where M is the minimized function during refinement, Nobs is the number of observed intensities and Nvar is the number of refined variables.

** Rp and wRp are the residual parameters defined as $R_p = \dfrac{\Sigma|Io - Ic|}{\sum^{Io}}$ and

$wR_p == \sqrt{\dfrac{Mp}{\Sigma wIo^2}}$, where Mp is the minimization powder diffraction function, IO and IC are observed and calculated intensities.

and the H_2/CO ratio were calculated using the gas composition analyzed by GC and conversions were calculated by the formulae,

CH_4 Conversion:

$$X_{CH4}\% = [(F_{CH4\ in} - F_{CH4\ out}/F_{CH4\ in}] \times 100$$

CO_2 Conversion:

$$X_{CO2}\% = [(F_{CO2\ in} - F_{CO2\ out}/F_{CO2\ in}] \times 100$$

H_2/CO ratio:

$$H_2/CO = [F_{out\ H2}/F_{out\ CO}]$$

3. Results and discussion

Our strategy was to identify structural frameworks with stable ions which form the basis for lattice insertion of active metals. $A_2B_2O_7$ compounds with B site occupied by Zr and Ti were anticipated to provide stable skeletal framework as well as provide catalytically active sites through a synergistic interaction of Zr and Ti with Ni ions. The materials were synthesized by conventional Pechini method and phase analysis was carried out by PXRD (Fig. 1(A)). $Gd_2Zr_2O_7$ (GZO) crystallized in defect fluorite structure with Fm$\overline{3}$m space group (PDF 01–080–0471), while $Gd_2Ti_2O_7$ (GTO) crystallized in pyrochlore structure with Fd$\overline{3}$m space group (PDF 01–073–1698). Ni doping (named as GTNO and GZNO for substitution in Ti and Zr compounds respectively) seems to have minimal effect on the structure type and parent structures are retained, with small amount of NiO present as impurity outside the lattice as indicated by the peak at 43.2° [19,20]. The XRD patterns also show a small shifting of peaks in Ni doped catalysts towards high 2θ values, pointing to a contraction of lattice. This is further confirmed by full pattern refinement by Rietveld method using GSAS-EXPGUI software [21]. For GZO, refinement was done with defect fluorite $Gd_2Zr_2O_7$ model, with Fm$\overline{3}$m space group (ICSD collection code - 068,265). Refinement went smoothly and resulted in a good fit with cell parameter a = 5.3008 Å, which is in agreement with the literature data [19]. For GTO, the refinement analysis confirmed a face centered cubic lattice system with Fd$\overline{3}$m space group (ICSD collection code- 024,207) with cell parameter a = 10.1861 Å. With Ni doped catalysts, quantitative analysis
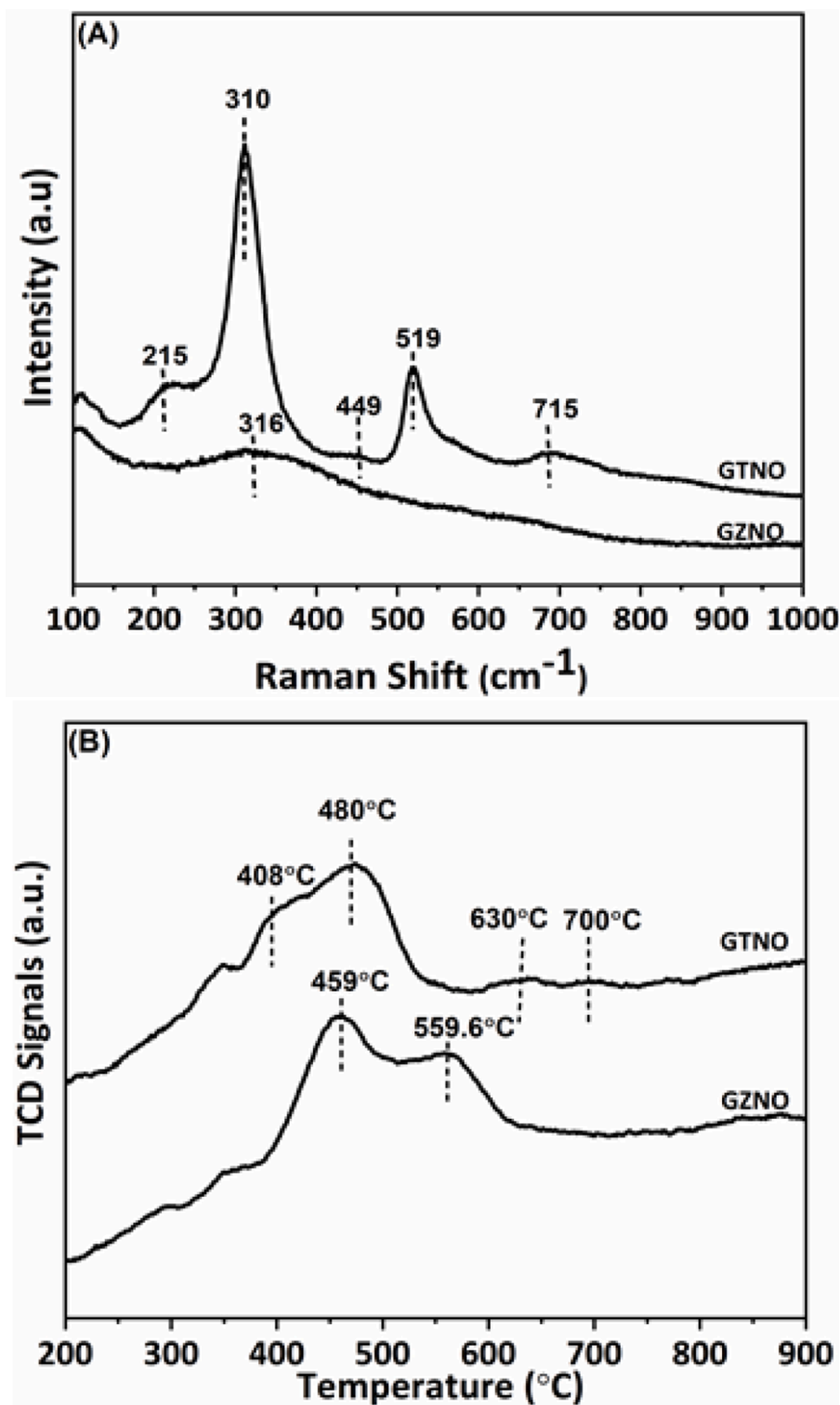
Fig. 2. (A) Raman spectra **(B)** TPR Analysis of GTNO and GZNO catalysts.

shows that 1.34 wt% and 0.68 wt% of Ni is present outside the lattice as NiO, in GTNO and GZNO respectively. Refinement studies were carried out by substituting appropriate concentrations of Ni (subtracting the Ni concentration present outside the lattice) in Zr and Ti sites and cell parameters were refined to be 5.2678 and 10.1842 Å for GZNO and GTNO respectively. The decrease in cell parameters of substituted catalysts confirms the incorporation of Ni in Ti and Zr sites. Lattice site substitution of Ni in Ti analogue is obviously lower due to the higher concentration of Ti added, which in turn has led to a higher

concentration of NiO outside the lattice, in a well dispersed manner. Crystallite size of main phases was calculated by Lorentian broadening of refined XRD peaks. Refined profiles and parameters are given in Fig. S1 (A-D) and Table 1 respectively. Atomic parameters are given in Table S1. In general, surface area of the materials is low as expected due to the high temperature synthesis (Table S2).

Substitution of lower valent Ni in the lattice is expected to affect the stoichiometry and hence form and redistribute O occupancy and vacancies. Since scattering parameters of O is low in x-ray diffraction
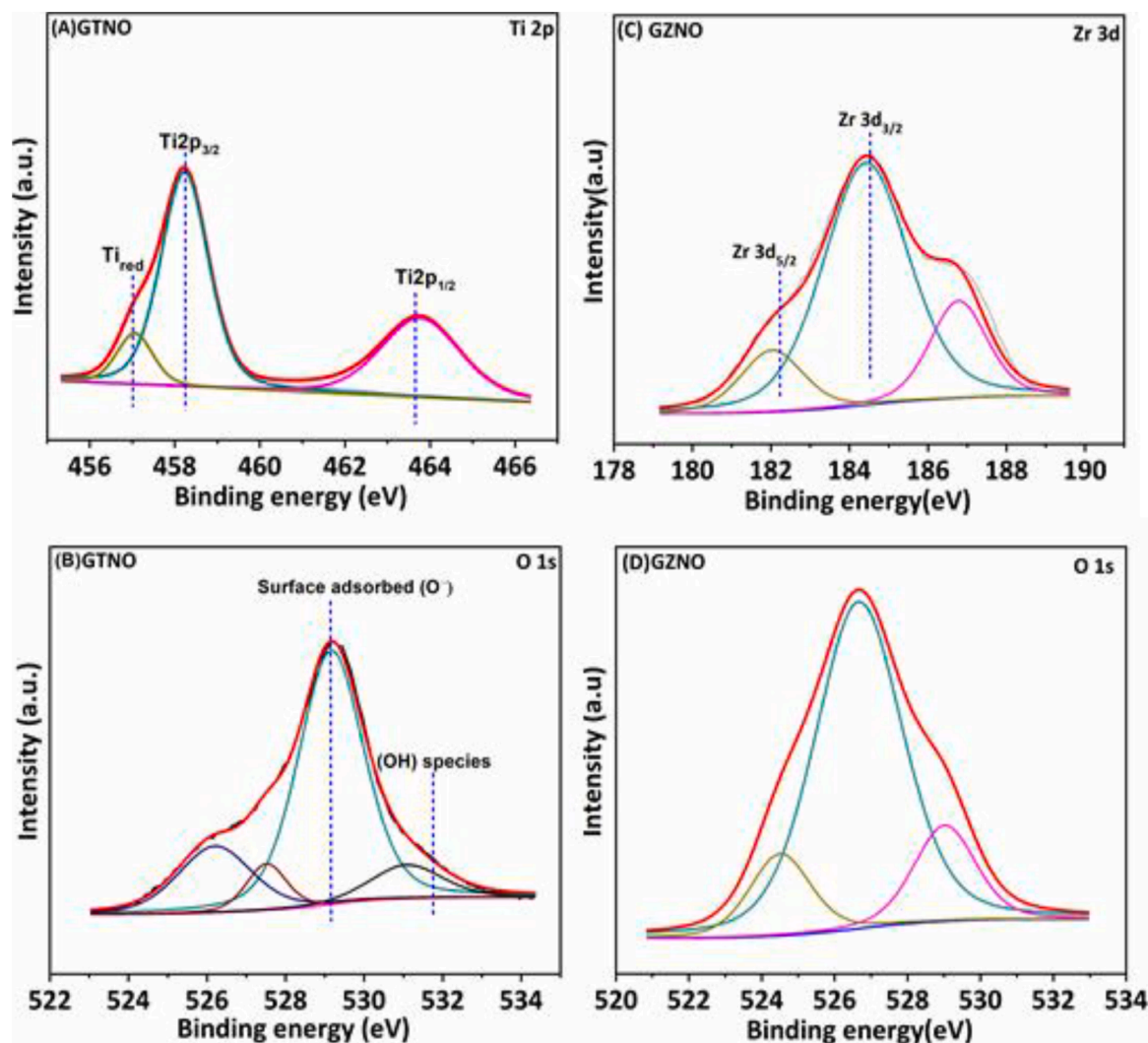
Fig. 3. Fitted XPS profile of GTNO catalyst (A) Ti 2p (B) O 1 s; GZNO catalyst (C) Zr 3d (D) O 1 s.

methods, we have refrained from refining O occupancy in Rietveld analysis. However, an attempt to understand O occupancy and vacancy distribution in the catalysts through Raman spectroscopy was carried out (Fig. 2(A)). Pyrochlore structure is known to have 6 active Raman modes distributed as A1g+Eg+4F2g irreducible presentations [22–24]. The A1g mode corresponds to Ti-O stretching, at higher frequencies (515–530 cm^{-1}) and Eg modes are due to O-Ti-O bending motion (330 – 340 cm^{-1}), while the F2g modes are due to O-Ti-O bending (300–320 cm^{-1}) and vibration of Gd-O' lattice (200–250 cm^{-1}). For GTNO catalyst, Raman modes around 215, 310, 449, 519 and 715 cm^{-1} were observed. Bands around 710–750 cm^{-1} are attributed to the defect originated oxygen disorder confirming the occurrence of oxygen vacancy in GTNO catalyst [22]. While in GZNO catalyst, broad Raman bands have been observed in the range of 300–350 cm^{-1}, the broadness of Raman modes confirm the defect fluorite structure of the catalyst [25]. According to Glerup et al., the absence of broad peak at 750 cm^{-1} confirms the lack of disorder generated oxygen vacancies in GZNO catalyst.

Difference in reducibility of both the catalysts was ascertained by TPR analysis. It can be seen from Fig. 2(B) that, in GZNO two reduction peaks were observed at around 459 °C and 559.6 °C. The first peak corresponds to the reduction of surface NiO particles and the second peak at 559.6 °C is owing to the lagged reduction of Ni^{+2} → Ni^0 present in the sub surface layers of the support [26,27]. In case of GTNO, the reduction of NiO particles on the support surface occurs at much lower

temperatures in the range of 350 – 410 °C, possibly due to better dispersion. The peak in the range of 480 - 500 °C corresponds to the reduction of NiO, which is strongly interacting with the support. Along with this, reduction peaks centered at 630 °C and 700 °C suggested the reduction of lattice Ni^{2+} into metallic Ni [28]. On comparing both the materials, it can be concluded that GTNO has more reducible Ni species over the surface as well as in sub layers of support. Surface acidic/basic nature also plays an important role in DRM, since CO$_2$ is acidic in nature; higher the basicity of support, more CO$_2$ is adsorbed activating CO formation and further dry reforming of methane. This was estimated by CO$_2$-TPD experiments (Fig. S2) and in GTNO, the desorption peaks are observed in lower temperatures as well as in higher temperature range which confirms the presence of weak, medium and strong basic sites facilitating activation of CO$_2$. While in GZNO catalysts, the broad peaks observed at around 200 °C indicates the presence of weak basic sites resulting in less desorption and activation of CO$_2$ [29,30].

To understand the surface composition of metals in the catalysts, XPS analysis has been carried out (Fig. 3). In GTO (Fig. S3) and GTNO catalyst, Ti 2p XPS spectrum showed the presence of Ti^{+4} through binding energy peaks at 458.1 and 463.8 eV [31]. Interestingly, we also observed a small peak at 456.6 eV which can be attributed to reduced Ti species [32]. The concentration of this reduced Ti species on the surface, however, decreased on Ni doping. The O 1 s spectrum of GTNO catalyst displays two peaks at 529.2 eV and 531.9 eV corresponding to the surface adsorbed oxygen (O^-) and hydroxyl oxygen (OH^-) species
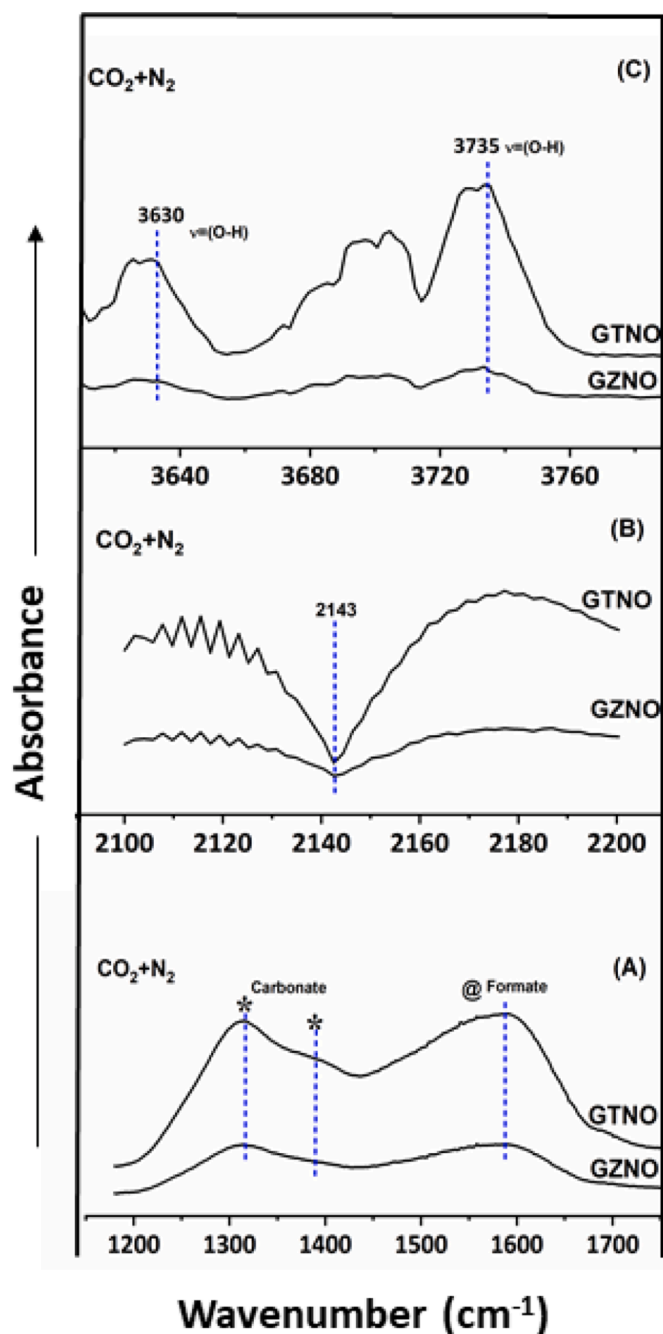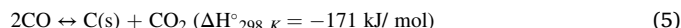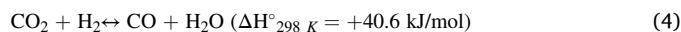
Fig. 4. in situ FTIR spectra of GTNO and GZNO catalysts with the feed gas 5 mL CO_2+ 20 mL N_2 at 400 °C (A) Formation of carbonate and formate species demonstrated by symbols, (B) Variation in desorbed CO intensities in GTNO and GZNO catalysts. (C) Formation of hydroxyl species over the catalysts surface.

respectively [31]. The ratio of surface adsorbed oxygen (O^-) and the hydroxyl species (O^-: OH^-) was estimated from the area under the peaks and is found to be 9:1 in GTO while in GTNO catalysts it is 7:3. This confirms the enhanced generation of hydroxyl species by Ni substitution in Ti site. In case of GZNO catalyst (Fig. 3), the Zr 3d XPS profile showed peaks at 182.5 eV and 184.9 eV confirming Zr in +4 valence state [33]. The O 1 s spectrum shows the binding energy at 529.1 eV indicating only loosely bound surface oxygen species and the lower binding energy peaks correspond to lattice oxygen atoms (Fig. S3). It is noteworthy that in GZNO, peak corresponding to hydroxyl oxygen species at 531.9 eV is missing.

Furthermore, we performed DRIFT experiments to understand the adsorbed species on the surface of these catalysts upon exposure to CO_2. Before the analysis, the sample was heated inside the DRIFT cell in N_2 at 400 °C to clean the surface. Following this, the sample was reduced in H_2 (20 mL min^{-1}) for 2 h and later the cell chamber was purged with N_2 at 400 °C for 30 min. H_2 is expected to be homolytically dissociated and adsorbed on the catalytically active sites and N_2 purge would sweep away any H_2 not anchored on the surface. Then a mixture of N_2 (20 mL min^{-1}) and CO_2 (5 mL min^{-1}) was passed over the sample and spectra were recorded at 400 °C in absorbance mode. The spectra show the presence of carbonates (symmetric stretching O—C-O and C—O) and formate species in the range of 1300–1600 cm^{-1} (Fig. 4(A)). Formate species are formed because of interaction between CO_2 and adsorbed H* on the surface Fig. 4.(C) shows the absorption bands at 3630 cm^{-1} and 3735 cm^{-1}, which correspond to the hydroxyl species; however, gaseous CO_2 also shows absorption in the same range and hence this cannot be conclusively assigned. The desorbed gaseous CO has been observed at 2143 cm^{-1} in Fig. 4(B) [34,35]. The peak at 2143 cm^{-1} is more intense in GTNO than GZNO catalyst, as the desorption of gaseous CO is more in GTNO catalyst which triggers the fast activation of CO_2. The less desorption of CO in GZNO shows lesser activation of CO_2.

The activity for dry reforming of methane of both the Ni substituted catalysts have been studied at various temperatures (Fig. S4) and durability was tested at optimized reaction conditions at 800 °C, 28,800 h^{-1} GHSV, CO_2: CH_4: N_2 = 80:80:80 mL min^{-1} and atmospheric pressure for 100 h time on stream (Fig. 5). Among the two catalysts, GTNO showed superior DRM activity. Initial activity of both the catalysts was poor and reached steady state conversions after 35–40 h. Initial poor activity was also accompanied by H_2/CO ratio much less than what is expected of DRM. It has been reported that, the decrease in H_2/CO ratio may be because of side reactions like reverse water gas shift reaction **(4)** and reverse Boudouard reaction at high reaction temperature (800 °C) **(5)** [36]. In case of GTNO, the activity recovers to 94% CO_2 and 88% CH_4 conversion and 0.96 (~1) H_2/CO ratio, whereas, GZNO exhibited much lower activity at maximum conversion.

$$CO_2 + H_2 \leftrightarrow CO + H_2O \ (\Delta H°_{298\ K} = +40.6 \text{ kJ/mol}) \quad (4)$$

$$2CO \leftrightarrow C(s) + CO_2 \ (\Delta H°_{298\ K} = -171 \text{ kJ/ mol}) \quad (5)$$

It is understood that the surface oxygen species play a key role in gasification of coke formed during the dry reforming reaction by converting it into CO. The XPS and in situ IR studies confirm the presence of these species, especially hydroxyl in GTNO catalysts. These active groups prevent blockage of active sites by carbonaceous species and make the active sites available for further reaction. We can anticipate this mechanism of coke removal from GTNO catalyst surface. The absence of hydroxyl species in GZNO catalyst may be the reason for its decreased activity by accumulation of carbonaceous compounds.

In order to check the structural change and the stability of Ni substituted catalysts after 100 h of reaction, the x-ray diffraction analysis of the spent catalysts was carried out. All two spent catalysts retained their parent structure after 100 h time on stream in DRM conditions (Fig. 6A). An extra peak in case of GZNO catalyst at 2θ, 26.2° (JCPDS No.75–1621) is attributed to graphitic carbon [36]. To further substantiate the presence of graphitic carbon, Raman analysis of spent GTNO and GZNO catalysts was done (Fig. 6B). Raman spectrum of GZNO catalyst showed bands at around 1350 cm^{-1} and shoulder peak at 1615 cm^{-1} corresponding to D and G bands of disordered graphitic carbonaceous species [36]. For the estimation of the amount of carbon formed during the dry reforming of reaction, thermogravimetric analysis was also done on the spent catalysts. The experiment was carried out under air and oxidized carbon was calculated in moles per gm of catalyst (Fig. 7). It has been observed that the GZNO showed more coke formation in comparison with GTNO.

From the above characterization studies, it can be inferred that structural and other factors like reducibility assist GTNO to be more
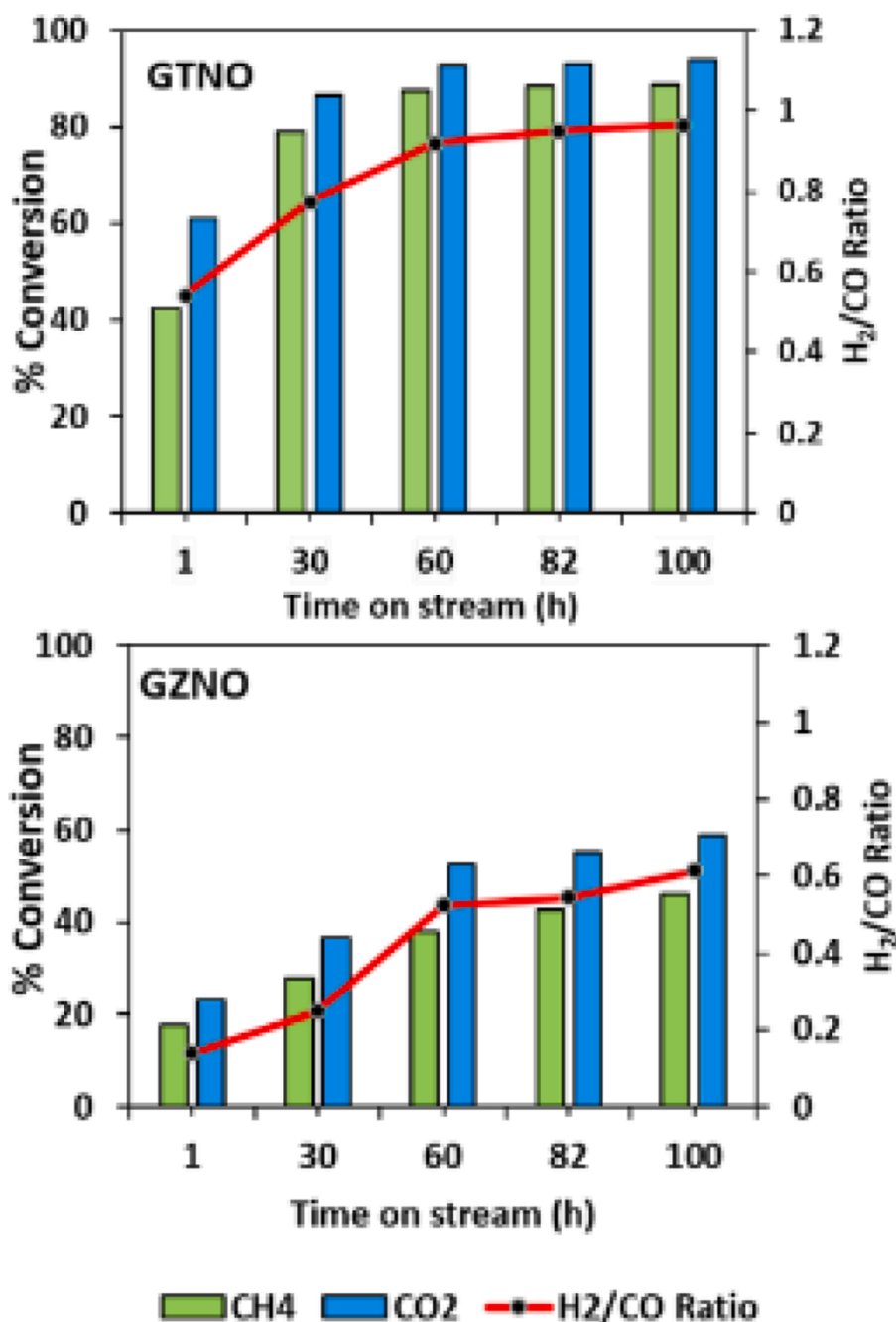
Fig. 5. Activity analysis of GTNO and GZNO catalysts in DRM conditions: CH_4: CO_2: N_2 = 80:80:80 mL/min, 28,800 h^{-1} GHSV at 800 °C for 100 h time on stream. Conversions and H_2/CO ratios are plotted against time on stream. Full TOS plots are given in Supporting Information Fig. S5.

active and stable in dry reforming conditions. Presence of more hydroxyl species as well as reduced Ti species possibly play very important roles in enhanced CO_2 activation. Presence of well dispersed NiO particles on the surface of GTNO could have enhanced the reducibility and hence activity. Surface hydroxyl groups on the surface could also influence gasification of the C formed resulting in further enhancement of activity and stability.

4. Conclusions

The Gd based Ni substituted ternary metal Ti and Zr oxide catalysts have been synthesized and tested for dry reforming of methane. The XRD analysis and refinement studies confirm the incorporation of Ni in the lattice as well as presence of reducible NiO over the surface resulting

in enhanced activity of the Ti based Ni doped catalyst. Temperature programmed reduction confirms that the reducibility of this catalyst is more than the Zr analogue, which substantiates the presence of well dispersed NiO particles over the surface and presence of stable active metal ions in the bulk. Strong basicity of GTNO catalyst also results in the promotion of CO_2 adsorption and activation than in GZNO catalyst towards DRM. This is corroborated by in situ IR studies which prove more reductive adsorption and desorption of CO_2 as CO on GTNO. Presence of loosely bound surface oxygen and hydroxyl oxygen species in GTNO catalyst may also be helpful in activation of CO_2 as well as simultaneous coke gasification on the GTNO catalyst surface. Amount of carbon formed in dry reforming of methane is less in GTNO than GZNO catalyst and absence of graphitic carbon shows the simultaneous removal of coke from the surface of GTNO catalyst and availability of
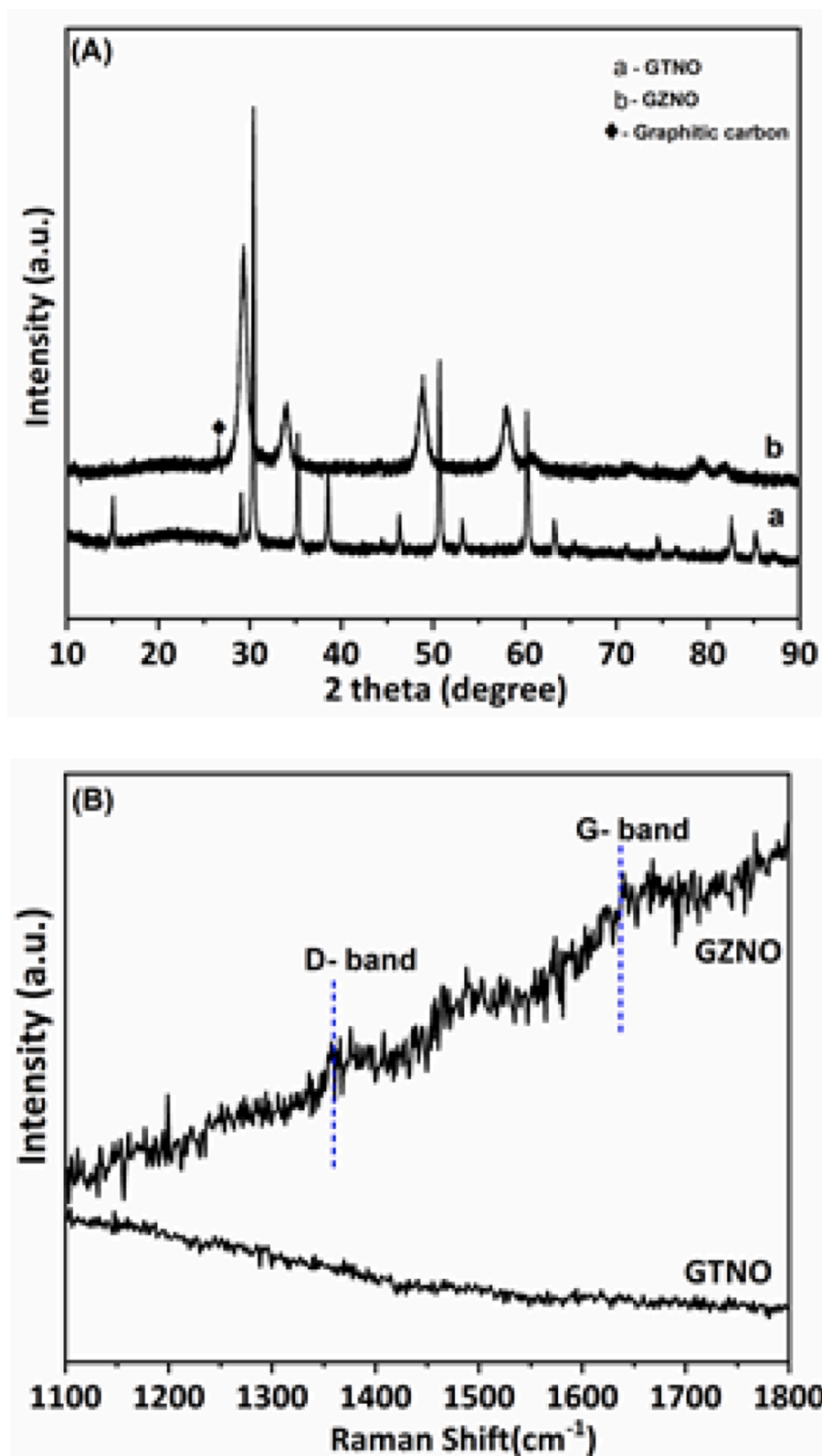
Fig. 6. (A) XRD pattern of spent GTNO and GZNO catalysts (B) Raman analysis of spent GTNO and GZNO catalysts.

active sites for DRM. This study unveils the influence of reducibility, basic strength of support and formation of defect modified oxygen as well as hydroxyl species for the superior and stable activity of GTNO catalyst towards dry reforming of methane.

Credit author statement

SRJ: Investigation, Methodology, Writing-Original draft; ST: Investigation, XRD and refinement; PD: Investigation, In-situ IR and interpretation; RND: Conceptualisation, Writing- review
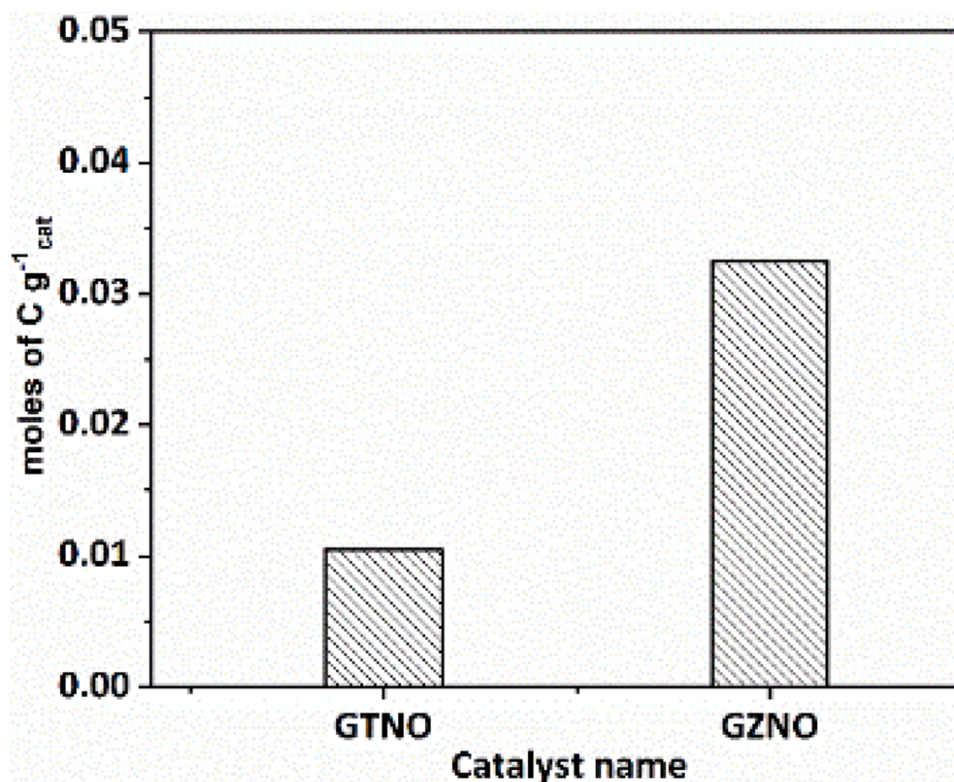
Fig. 7. TGA analysis of spent GTNO and GZNO catalysts after 100 h of DRM reaction. Moles of carbon formation is plotted per gram of catalyst.

Declaration of Competing Interest

The authors declare that they have no known competing financial interest to impact the work reported in this paper.

Acknowledgments

SRG thanks CSIR for research fellowship.

Supplementary materials

Supplementary material associated with this article can be found, in the online version, at doi:10.1016/j.mcat.2022.112242.

References

[1] A. Saravanan, P. Senthil kumar, Dai-Viet N. Vo, S. Jeevanantham, V. Bhuvaneswari, V. Anantha Narayanan, P.R. Yaashikaa, S. Swetha, B. Reshma, A comprehensive review on different approaches for CO_2 utilization and conversion pathways, Chem. Eng. Sci. 236 (2021), 116515, https://doi.org/10.1016/j.ces.2021.116515.
[2] L. Guczi, G. Stefler, O. Geszti, I. Sajo, Z. Paszti, A. Tompos, Z. Schay, Methane dry reforming with CO_2: a study on surface carbon species, Appl. Catal. A: Gen. 375 (2010) 236–246, https://doi.org/10.1016/j.apcata.2009.12.040.
[3] Z.L. Zhang, X.E. Verykios, Mechanistic aspects of carbon dioxide reforming of methane to synthesis gas over Ni catalysts, Catal. Lett. 38 (1996) 175–179. https://link.springer.com/journal/10562.
[4] L. Kapokova, S. Pavlova, R. Bunina, G. Alikina, T. Krieger, A. Ishchenko, V. Rogov, V. Sadykov, Dry reforming of methane over $LnFe_{0.7}Ni_{0.3}O_3$ perovskites: influence of Ln nature, Catal. Today 164 (2011) 227–233, https://doi.org/10.1016/j.cattod.2010.10.086.
[5] U. Olsbye, T. Wurzel, L. Mleczko, Kinetic and reaction engineering studies of dry reforming of methane over a $Ni/La/Al_2O_3$ catalyst, Ind. Eng. Chem. Res. 36 (1997) 5180–5188, https://doi.org/10.1021/ie970246l.
[6] J.R. Rostrup- Nielsen, Aspects of CO_2-reforming of Methane, Stud. Surf. Sci. Catal. 81 (1994) 25–41, https://doi.org/10.1016/S0167-2991(08)63847-1.
[7] A.J. Brungs, A.P.E. York, J.B. Claridge, C. Marquez-Alvarez, M.L.H. Green, Dry reforming of methane to synthesis gas over supported molybdenum carbide catalysts, Catal. Lett. 70 (2000) 117–122. https://link.springer.com/journal/10562.
[8] C.H. Bartholomew, Catal. Rev. Sci. Eng. 24 (1982) 67–112, https://doi.org/10.1080/03602458208079650.
[9] D.J. Haynes, D.A. Berry, D. Shekhawat, J.J. Spivey, Catalytic partial oxidation of n-tetradecane using Rh and Sr substituted pyrochlores: effects of sulfur, Catal Today 145 (2009) 121–126, https://doi.org/10.1016/j.cattod.2008.05.014.
[10] J. Xu, R. Xi, X. Xu, Y. Zhang, X. Feng, X. Fang, X. Wang, $A_2B_2O_7$ pyrochlore compounds: a category of potential materials for clean energy and environment protection catalysis, J. Rare Earths 38 (2020) 840–849, https://doi.org/10.1016/j.jre.2020.01.002.
[11] J. Xu, Y. Zhang, X. Xu, X. Fang, R. Xi, Y. Liu, R. Zheng, X. Wang, Constructing $La_2B_2O_7$ (B= Ti, Zr, Ce) compounds with three typical crystalline phases for the oxidative coupling of methane: the effect of phase structures, superoxide anions, and alkalinity on the reactivity, ACS Catal. 9 (2019) 4030–4045, https://doi.org/10.1021/acscatal.9b00022.
[12] A.C. Roger, C. Petit, A. Kiennemann, Effect of metallo-organic precursors on the synthesis of Sm-Sn pyrochlore catalysts: application to the oxidative coupling of methane, J. Catal. 167 (1997) 447–459, https://doi.org/10.1006/jcat.1997.1601.
[13] D. Pakhare, C. Shaw, Daniel Haynes, D. Shekhawat, J.J. Spivey, Effect of reaction temperature on activity of Pt- and Ru-substituted lanthanum zirconate pyrochlores ($La_2Zr_2O_7$) for dry (CO_2) reforming of methane (DRM), J. CO2 Util. 1 (2013) 37–42, https://doi.org/10.1016/j.jcou.2013.04.001.
[14] S. Bhattar, A. Krishnakumar, S. Kanitkar, A. Abedin, D. Shekhawat, D.J. Haynes, J.J. Spivey, 100th anniversary: dry reforming of methane over ni and sr substituted lanthanum zirconate pyrochlore catalysts – effect of Ni Loading, Ind. Eng. Chem. Res. 58 (2019) 19386–19396, https://doi.org/10.1016/j.jcou.2013.04.001.
[15] F. Polo-Garzon, M. He, D.A. Bruce, *Ab initio* derived reaction mechanism for the dry reforming of methane on Rh doped pyrochlore catalysts, J. Catal. 333 (2016) 59–70, https://doi.org/10.1016/j.jcat.2015.10.017.
[16] F. Polo-Garzon, D. Pakhare, J.J. Spivey, D.A. Bruce, Dry reforming of methane on Rh-doped pyrochlore catalysts: a steady-state isotopic transient kinetic study, ACS Catal 6 (2016) 3826–3833, https://doi.org/10.1021/acscatal.6b00666, 6.
[17] N. Kumar, A. Roy, Z. Wang, E.M. L'Abbate, D. Haynes, D. Shekhawat, J.J. Spivey, Bi-reforming of methane on Ni-based pyrochlore catalyst, Appl. Catal. A: Gen. 517 (2016) 211–216, https://doi.org/10.1016/j.apcata.2016.03.016.
[18] X. Fang, X. Zhang, Y. Guo, M. Chen, W. Liu, X. Xu, H. Peng, Z. Gao, X. Wang, C. Li, Highly active and stable $Ni/Y_2Zr_2O_7$ catalysts for methane steam reforming: on the nature and effective preparation method of the pyrochlore support, Int. J. Hydrog. Energy 41 (2016) 11141–11153, https://doi.org/10.1016/j.ijhydene.2016.04.038.
[19] Y. Wang, B. Gao, Q. Wang, X. Li, Z. Su, A. Chang, $A_2Zr_2O_7$ (A = Nd, Sm, Gd, Yb) zirconate ceramics with pyrochlore-type structure for high-temperature negative temperature coefficient thermistor, J Mater Sci 55 (2020) 15405–15414. https://link.springer.com/journal/10853.
[20] S. Culubrk, Z. Antic, V. Lojpur, M. Marinovic-Cincovic, M.D. Dramicanin, Sol-gel derived Eu^{3+}-doped $Gd_2Ti_2O_7$ pyrochlore, nanopowders, J. Nanomater. (2015), https://doi.org/10.1155/2015/514173.

[21] B.H. Toby, J. Appl. Cryst. 34 (2001) 210–213, https://doi.org/10.1107/S0021889801002242.

[22] M.T. Vandenborre, E. Husson, J.P. Chatry, D. Michel, Rare-earth titanates and stannates of pyrochlore structure; vibrational spectra and force fields, J. Raman Spectrosc. 14 (2) (1983) 63–71, https://doi.org/10.1002/JRS.1250140202.

[23] S. Saha, D.V.S. Muthu, C. Pascanut, N. Dragoe, R. Suryanarayanan, G. Dhalenne, A. Revcolevschi, S. Karmakar, S.M. Sharma, A.K. Sood, High-pressure Raman and x-ray study of the spin-frustrated pyrochlore $Gd_2Ti_2O_7$, Phys. Rev. B 74 (2006), 064109, https://doi.org/10.1103/PhysRevB.74.064109.

[24] S.P.S. Porto, P.A. Fleury, T.C. Dame, Raman spectra of TiO_2, MgF_2, ZnF_2, FeF_2, and MnF_2, Phys. Rev. 154 (1967) 522, https://doi.org/10.1103/PhysRev.154.522.

[25] A.F. Fuentes, S.M. Montemayor, M. Maczka, M. Lang, R.C. Ewing, U. Amador, A critical review of existing criteria for the prediction of pyrochlore formation and stability, Inorg. Chem. 57 (2018) 12093–12105, https://doi.org/10.1021/acs.inorgchem.8b01665.

[26] C. Ding, G. Ai, K. Zhang, Q. Yuan, Y. Han, X. Ma, J. Wang, S. Liu, Coking resistant $Ni/ZrO_2@SiO_2$ catalyst for the partial oxidation of methane to synthesis gas, Int. J. Hydrog. Energy. 40 (2015) 6835–6843, https://doi.org/10.1016/j.ijhydene.2015.03.094.

[27] M.A. Ebiad, D.R. Abd El-Hafiz, R.A. Elsalamony, L.S. Mohamed, Ni supported high surface area CeO_2–ZrO_2 catalysts for hydrogen production from ethanol steam reforming, RSC Adv 2 (2012) 8145–8156, https://doi.org/10.1039/C2RA20258A.

[28] Y. Lin, Y. Zhu, X. Pan, X. Bao, Modulating the methanation activity of Ni by the crystal phase of TiO_2, Catal. Sci.Technol. 7 (2017) 2813–2818, https://doi.org/10.1039/C7CY00124J.

[29] F. Meng, Y. Song, X. Li, Y. Cheng, Z. Li, Catalytic methanation performance in a low-temperature slurry-bed reactor over Ni–ZrO_2 catalyst: effect of the preparation method, J.Sol-Gel Sci. Technol 80 (2016) 759–768. https://link.springer.com/journal/10971.

[30] E.T. Kho, S. Jantarang, Z. Zheng, J. Scott, R. Amal, Harnessing the beneficial attributes of ceria and titania in a mixed-oxide support for nickel-catalyzed photothermal CO_2 methanation, Engineering 3 (2017) 393–401, https://doi.org/10.1016/J.ENG.2017.03.016.

[31] W. Zhang, Y. Tao, C. Li, Sol-gel synthesis of Gd2Ti2O7/HZSM-5 composite photocatalyst for ofloxacin degradation, J. Photochem. Photobiol. 364 (2018) 787–793, https://doi.org/10.1016/j.jphotochem.2018.07.022.

[32] J. Pouilleau, D. Devilliers, H. Groult, P. Marcus, Surface study of a titanium-based ceramic electrode material by X-ray photoelectron spectroscopy, J. Mater. Sci. 32 (1997) 5645–5651, https://doi.org/10.1023/A:1018645112465.

[33] J. Chen, X. Wang, Fabrication and characterization of novel excellent thermal-protection $Gd_2Zr_2O_7/ZrO_2$ composite ceramic fibers with different proportions of $Gd_2Zr_2O_7$, Ceram Int 46 (2020) 24029–24037, https://doi.org/10.1016/j.ceramint.2020.06.180.

[34] NIST Standard Reference Database 69: *NIST Chemistry WebBook*, https://doi.org/10.18434/T4D303.

[35] S. Xu, S. Chansai, S. Xu, C.E. Stere, Y. Jiao, S. Yang, C. Hardacre, X. Fan, CO Poisoning of Ru catalysts in CO_2 hydrogenation under thermal and plasma conditions: a combined kinetic and diffuse reflectance infrared fourier transform spectroscopy−mass spectrometry study, ACS Catal. 10 (2020) 12828–12840, https://doi.org/10.1021/acscatal.0c03620.

[36] S. Dama, S.R. Ghodke, R. Bobade, H.R. Gurav, S. Chilukuri, Active and durable alkaline earth metal substituted perovskite catalysts for dry reforming of methane, Appl. Catal. B 224 (2018) 146–158, https://doi.org/10.1016/j.apcatb.2017.10.048.